Diving deep into rocky exoplanets

Hakim, K.

DIVING DEEP INTO ROCKY EXOPLANETS

Kaustubh Hakim

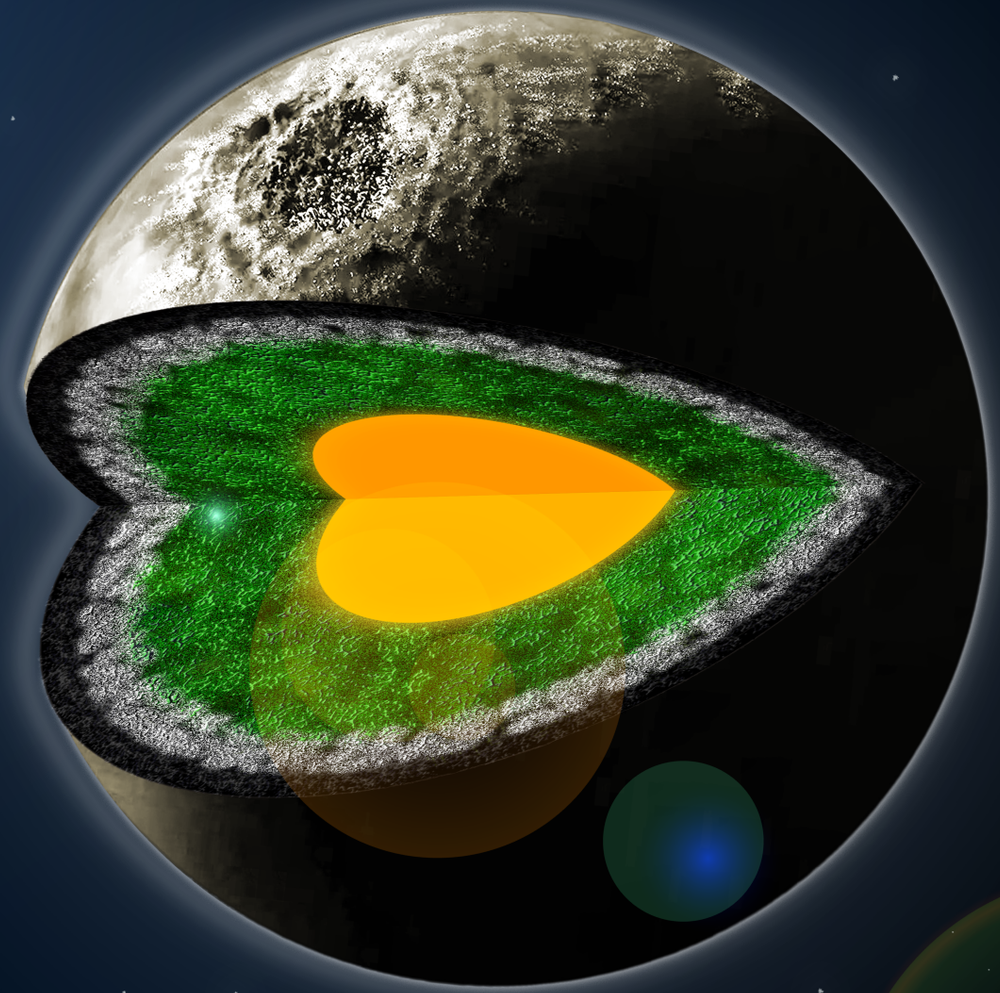

DIVING DEEP INTO ROCKY EXOPLANETS

Kaustubh Hakim

DIVING DEEP INTO ROCKY EXOPLANETS

Kaustubh Hakim

Contact: hakim.kaustubh@gmail.com

Diving Deep Into Rocky Exoplanets
Thesis, Anton Pannekoek Institute for Astronomy, University of Amsterdam

Printed by Gildeprint

ISBN: 978-94-6323-419-1

Cover and bookmark designed by Pankaj Kumar Chaukikar (pankmail2@gmail.com). Illustration of the exoplanetary surface adapted from the media coverage of Chapter 3 by New Scientist (`https://goo.gl/PFVA5z`).

UNIVERSITY OF AMSTERDAM

ANTON PANNEKOEK
INSTITUTE

VRIJE
UNIVERSITEIT
AMSTERDAM

This research has been financed by the Planetary and Exoplanetary Science (PEPSci) Network of the Netherlands Organization for Scientific Research (NWO) and carried out at the Anton Pannekoek Institute for Astronomy, University of Amsterdam and the Department of Earth Sciences, Vrije Universiteit Amsterdam.

Diving Deep Into Rocky Exoplanets

ACADEMISCH PROEFSCHRIFT

ter verkrijging van de graad van doctor
aan de Universiteit van Amsterdam
op gezag van de Rector Magnificus
prof. dr. ir. K.I.J. Maex
ten overstaan van een door het College voor Promoties ingestelde
commissie, in het openbaar te verdedigen in de Agnietenkapel
op dinsdag 18 december 2018, te 14:00 uur

door

Kaustubh Hakim

geboren te Jalgaon, India

Promotiecommissie:

Promotoren:	prof. dr. C. Dominik	Universiteit van Amsterdam
	prof. dr. W. van Westrenen	Vrije Universiteit Amsterdam
Overige leden:	prof. dr. L.B.F.M. Waters	Universiteit van Amsterdam
	prof. dr. T. Van Hoolst	Royal Observatory of Belgium
	dr. A.P. van den Berg	Universiteit Utrecht
	dr. J.M.L.B. Desert	Universiteit van Amsterdam
	prof. dr. I.A.G. Snellen	Universiteit Leiden
	dr. A. Vazan Shukrun	Universiteit van Amsterdam

Faculteit der Natuurwetenschappen, Wiskunde en Informatica

To my parents

Contents

Chapter 1

Introduction

1.1 History of planetary and exoplanetary science

Our galaxy is home to approximately 300 billion stars and at least as many planets, including the eight planets of our solar system and the extrasolar planets which are better known as exoplanets. In the past two and a half decades, about four thousand of these exoplanets have been discovered. Only in 2018, the first-ever image of a baby exoplanet, an exoplanet in the process of formation was taken (Fig. 1.1). Plenty more exoplanets are going to be discovered in the future and their characterization holds the key to exoplanetary exploration and to advance our understanding of our own planetary system as well as to fathom our identity in this universe. However, to make significant strides forward, it is essential to revisit what it took the human species to reach where we are today.

To ancient astronomers, all objects in the sky visible to the human eye consistently moved from the east to the west with the exception of five objects, the planets, Venus, Jupiter, Mars, Mercury and Saturn in decreasing order of their maximum brightness, which would undergo retrograde motion at times. In the 8^{th} century BC, the Indian sage Yajnavalkya recognized the spherical shape of the Sun, the Earth and the five planets in the sky and also propounded the idea of heliocentrism. The Greek philosopher Aristarchus of Samos also suggested a heliocentric system in the 4^{th} century BC. In contrast, Aristotle promoted an Earth-centric view, and a few centuries later, Ptolemy managed to explain the motion of planets using his concept of epicycles with the Earth at the center of universe. Because of the lack of precision in measurements of planetary motions and the dominance of state-sponsored astronomy and astrology with an Earth-centric belief, humanity had to wait for more than eighteen centuries for the Copernican revolution. Talents and hardships of Nicholas Copernicus, Giordano Bruno, Tycho Brahe, Johannes Kepler, Galileo Galilei, Issac Newton and several others were crucial in correctly establishing the heliocentric view of our planetary system. Copernicus was essentially the first-ever astrophysicist and hypothesized that the Earth and five other planets[1] orbit around the Sun, and Kepler was the first astrophysicist to discover a

[1] Uranus and Neptune, the seventh and the eighth planet of our solar system, were discovered much later in 1781 and 1846, respectively.

1

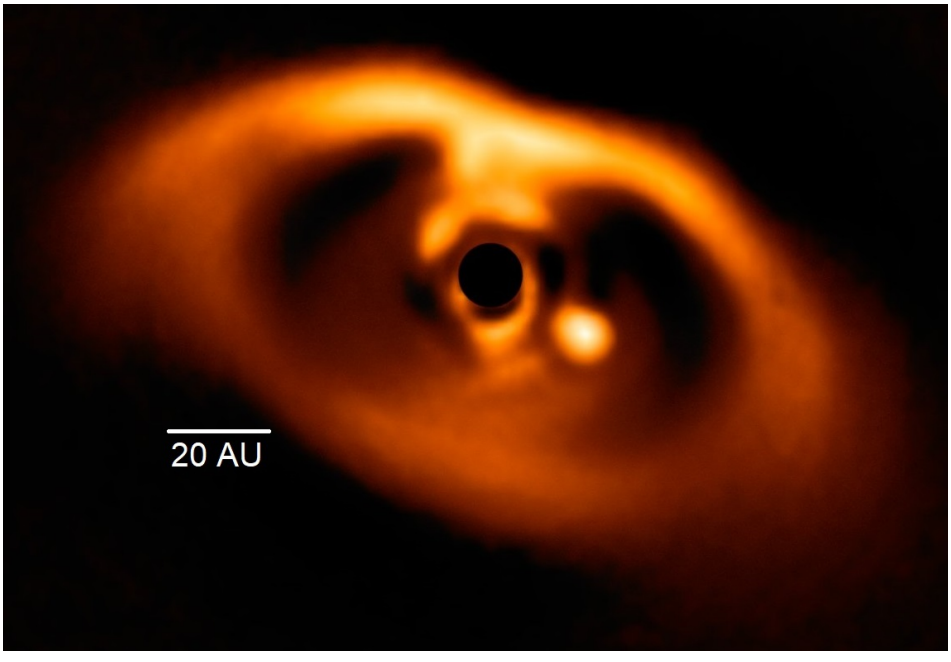

Figure 1.1: The first image of an exoplanet captured during the process of formation around the dwarf star PDS 70 with the help of SPHERE instrument on the European Southern Observatory's (ESO) Very Large Telescope (Müller et al., 2018). The planet is clearly seen as a bright point to the bottom-right of the center, which is blacked out by the coronagraph mask used to block the blinding light of the star. Figure taken from the ESO press release of Müller et al. (2018).

law of nature by fitting it to the observational data collected (without using a telescope) by Brahe.

The concept of many-worlds has been around since before the times of Aristotle. Scientific origins of this idea have their roots in the solar nebular disk theory of Immanuel Kant in 1755 and the measurement of distance to a star by Friedrich Bessel in 1843. The notion that the stars in our galaxy like our Sun, have a trail of planets was embraced by Camille Flammarion in his book "Astronomie Populaire" in 1880. Further evidence for the similarity between the Sun and stars came from the proposition of Arthur Eddington in 1920 that stars like our Sun burn hydrogen to helium using nuclear fusion and subsequent developments in nuclear physics and astronomy. In the 20^{th} century, when the hunt for solar system planets beyond the orbit of Neptune was ongoing, some astronomers started looking for signs of planets orbiting stars other than Sun. However, it is not easy to directly image exoplanets because of their proximity to their host stars in comparison to the large distances between two stars[1], and the enormous brightness contrast between planets and their host stars ($\sim 10^{-9}$ in

[1] The distance to our closest neighbor Proxima Centauri, which is now known to host an exoplanet, is about 270 000 astronomical units (AU), where 1 AU (149.6 million km) is the distance between the Earth and the Sun.

visible wavelengths). Therefore, the earliest searches for exoplanets (e.g., around Barnard's star, van de Kamp, 1963, 1982) implemented astrometry, which detects the motion of the star in the sky around the center of mass of the star-planet system. Several reports on the detection of exoplanets using astrometry were received between 1960s and 1980s. Unfortunately, all of them turned out to be false detections because of several technical challenges associated with astrometry. Nevertheless, the idea of exoplanets was already around in the fiction literature, from "The Skylark of Space" by Edward E. Smith originally published in 1928 to "The Hitchhiker's Guide To The Galaxy" by Douglas Adams published in 1979.

In the second half of the 20^{th} century, planetary science was essentially driven by a space-race between the USA and the Soviet Union who sent several space missions to and beyond low-Earth orbit. Unmanned missions to the Moon, Mars and Venus gathered invaluable observational data from these rocky bodies as well as helped to improve the technology for future missions. In the late 1960s and early 1970s, Apollo missions took humans to the Moon and facilitated bringing hundreds of kilograms of lunar rock samples back to Earth, a treasure trove for lunar and planetary scientists. In the 1970s, the Viking landers collected data on the surface of Mars for the first time. In the 1980s, the Voyager missions took the first close-up images of the giant planets of our solar system. Ambitious orbiter/impact missions to Jupiter, Saturn, asteroids and comets were launched in the 1990s and 2000s. Soon with the active involvement of more government space agencies and private companies, the future seemed bright for the exploration of our solar system.

Meanwhile in the 1990s, astronomers were exploring exoplanet detection methods such as radial velocity and transit photometry. The radial velocity method, or Doppler spectroscopy, involves measuring a periodic change in the radial velocity of the star, essentially the red- or blue-shift in the spectrum of the star, due to the gravitational pull of the planet. This method gives the minimum mass of the exoplanet. Transit photometry measures the decrease in the brightness of the host star due to an exoplanetary transit, and essentially gives the exoplanetary radius. Surprisingly, the first exoplanet was discovered around a millisecond pulsar (rapidly rotating neutron star) using another technique, pulse timing measurements (Wolszczan & Frail, 1992). Not long after this discovery, the first exoplanet around a main-sequence star (51 Pegasi b) was discovered (Mayor & Queloz, 1995), which paved the way for the radial velocity technique in coming decades. Five years later, transit photometry led to the discovery of HD 209458 b (Henry et al., 2000; Charbonneau et al., 2000). The real potential of this method was realized only after the launch of space-based telescopes, French and European space agencies' Convection, Rotation et Transits planétaires (CoRoT) in 2006 and NASA's Kepler in 2009, capable of detecting parts per million changes in stellar brightness. Several other detection methods such as imaging, gravitational microlensing, orbital brightness modulation, and eclipse, pulsation and transit timing variations have contributed to the search for exoplanets. Still, more than 95% share of exoplanet discoveries is attributed to transit photometry and radial velocity methods.

1

1.2 Diversity in exoplanetary systems

1.2.1 Physical diversity

The physical properties of exoplanets such as mass and radius as well as orbital parameters show a largely continuous trend in the whole range of observations to date, and no clear distinction exists between exoplanet types as in between the terrestrial and giant planets of the solar system (see below). The relation between the stellar metallicity and mass (e.g., Thorngren et al., 2016) as well as between the stellar metallicity and planet occurrence rates (e.g., Winn & Fabrycky, 2015; Petigura et al., 2018) have been investigated. Giant planet formation increases with stellar metallicity, whereas smaller planet occurrence seems to be independent of stellar metallicity (Petigura et al., 2018). Moreover, there is a huge diversity in planetary system architectures (e.g., Winn & Fabrycky, 2015). For example, HR 8799 consists of four Jupiter-size planets with orbital separations of more than 15 AU (Marois et al., 2008), whereas TRAPPIST-1 hosts seven Earth-size exoplanets within 0.06 AU (Gillon et al., 2017). Fig. 1.2 illustrates the diversity in orbital separations for the Solar System, TRAPPIST-1 and HR 8799. In addition to the diversity in planetary architectures, the types of host stars seem to vary from the more common main-sequence single and binary stars to the less common white dwarfs and pulsars. For main-sequence dwarfs, the main-sequence lifetime decreases with increasing luminosity or mass, implying that the main-sequence phase of M-dwarfs such as TRAPPIST-1 lasts up to a trillion years, whereas that of G-dwarfs such as Sun lasts for several billion years (Laughlin et al., 1997).

Since the radius is the only measured physical parameter for almost 80% of the known exoplanets, it makes sense to classify exoplanets based on their size. On the basis of host star metallicities, Buchhave et al. (2014) classify exoplanets as rocky at a radius up to 1.7 times that of the Earth ($R < 1.7$ $\mathrm{R}_\oplus$), gas dwarfs (1.7 $\mathrm{R}_\oplus < R < 3.9$ $\mathrm{R}_\oplus$) and gas giants ($R > 3.9$ $\mathrm{R}_\oplus$). Although the metallicity difference above and below the rocky-gas dwarf transition was questioned by Schlaufman (2015), this transition, which is not considered sharp ($1.5-2$ $\mathrm{R}_\oplus$, e.g., Rogers, 2015; Fulton et al., 2017; Van Eylen et al., 2018; Berger et al., 2018), marks a change in the bulk composition (see below). Although the physical reason behind the gas dwarf-gas giant transition is not clear, several studies have treated exoplanets with radii up to 4 $\mathrm{R}_\oplus$ as a different category, popularly termed as sub-Neptunes (e.g., Weiss & Marcy, 2014; Petigura et al., 2018). These categories can further be classified into sub-categories based on characteristics such as bulk density, surface temperature, core size (see Chapter 2), orbital separation and others. For instance, gas giants are called hot, warm or cool Jupiters based on their surface temperature, and lava planets and waterworlds, although different in their surface temperature and composition, can still fall into the broad category of rocky exoplanets. In this thesis, the term rocky (exo)planet does not imply that the planet contains only rock, it rather suggests that the atmospheres of these planets are insignificant in terms of the planetary mass.

For about 20% of the exoplanets with a known radius, the mass is also known, although for several of them only estimates on the minimum mass or an upper mass-limit are avail-

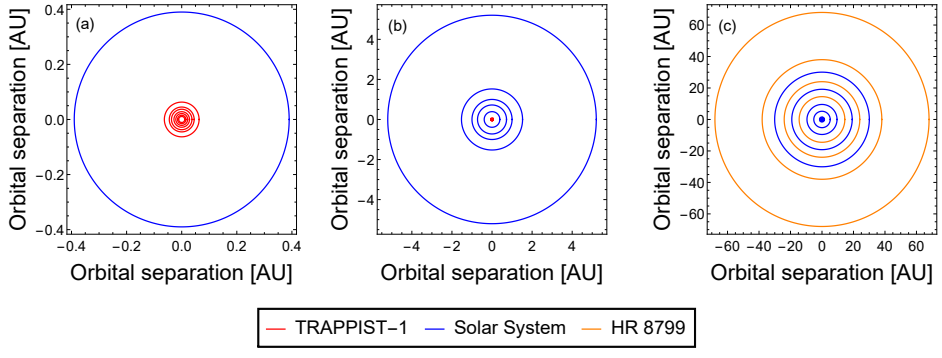

Figure 1.2: Comparison of the orbits of planets in the Solar System (blue) with those of the TRAPPIST-1 (red, Gillon et al., 2017) and HR 8799 (orange, Marois et al., 2008) systems. (a) The orbit of the innermost solar system planet Mercury easily encapsulates the tightly packed TRAPPIST-1 planets. (b) The outermost circle represents Jupiter's orbit and the TRAPPIST-1 system appears as a dot at the center. (c) Two outermost HR 8799 planets are at orbital separations beyond Neptune's orbit.

able[1]. The comparison of such exoplanets with the theoretical mass-radius relations of planets purely made of hydrogen, water, rock or iron reveals their composition to first order (Fig. 1.3). Gas giants mainly comprise hydrogen and helium, gas dwarfs contain volatiles other than hydrogen and helium as well as refractory material, and rocky exoplanets are mainly composed of refractories such as rock and iron and lack significant gas envelopes. In Fig. 1.3, some exoplanets seem more massive than the iron mass-radius relation because their masses represent upper-limits. Several gas giants lie above the hydrogen mass-radius relation because their radii are inflated likely due to ohmic dissipation in their atmospheres (e.g., Batygin & Stevenson, 2010; Thorngren & Fortney, 2018).

The physical diversity of planetary systems including that of the solar system has made it difficult to formulate a consistent planet formation theory. Early models were based on the classical core accretion theory where the solids are accreted only in the form of roughly 100 km-size planetesimals (Perri & Cameron, 1974; Mizuno, 1980; Bodenheimer & Pollack, 1986; Pollack et al., 1996). Models were also based on planet formation via gravitational instability (Kuiper, 1951; Cameron, 1978; Boss, 1997). More recently, core accretion with sub-millimeter to sub-meter-size pebbles[2] has become a more popular scenario of planet formation (Ormel & Klahr, 2010; Johansen & Lambrechts, 2017). Core accretion including pebbles is briefly discussed below.

Planet formation is a by-product of star formation which results from the collapse of a molecular cloud. This collapse leads to the formation of a protoplanetary disk providing the ingredients for planet formation, dust and gas. Coagulation of micrometer-size dust grains leads to the formation of sub-millimeter to sub-meter-size pebbles. The bouncing, fragmen-

[1] `https://exoplanetarchive.ipac.caltech.edu/`

[2] Not equivalent to the geological terminology of pebbles.

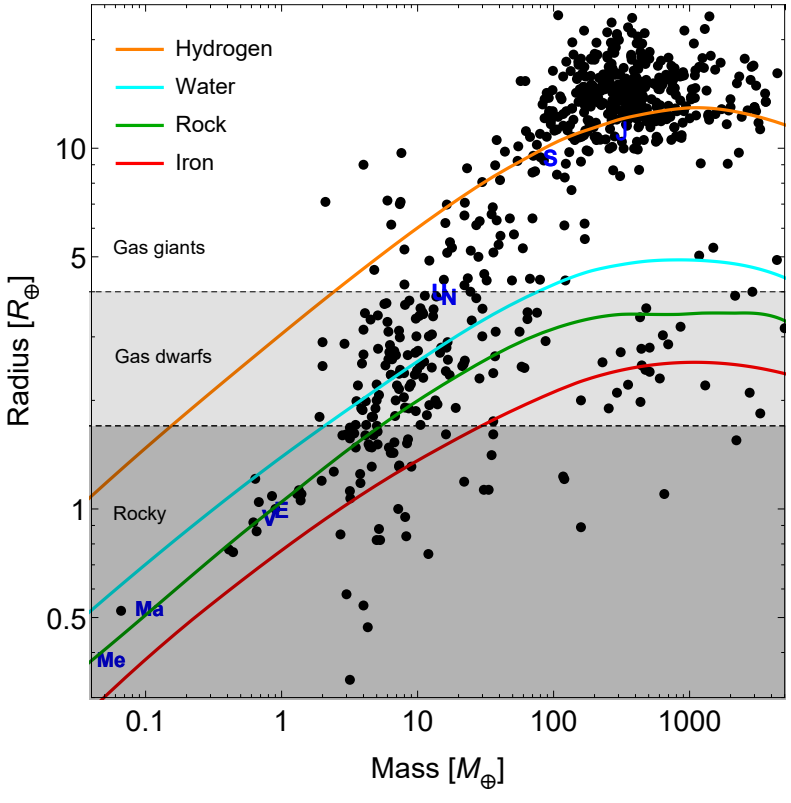

Figure 1.3: Masses and radii of exoplanets taken from `https://exoplanetarchive.ipac.caltech.edu/` (as of 31 August 2018) shown as black circles. Solar system planets are represented by letters, Me: Mercury, V: Venus, E: Earth, Ma: Mars, J: Jupiter, S: Saturn, U: Uranus, N: Neptune. Solid lines are mass-radius relations for pure hydrogen, water and rock ($MgSiO_3$) from Seager et al. (2007) and pure iron from Hakim et al. (2018a) (Chapter 2). Shaded regions represent rocky exoplanets, gas dwarfs and gas giants from bottom to top respectively.

tation and drift barriers, which hamper dust coagulation, also make protoplanetary disks efficient in producing pebbles of millimeter to centimeter sizes leading to concentration of pebbles in filaments (Johansen & Lambrechts, 2017). The gravitational collapse of these dense pebble filaments produces 100 km-size planetesimals (e.g., Johansen et al., 2015). Collisions with other planetesimals as well as pebble accretion lead to the growth of these planetesimals to 1000 km to 0.1 $\mathrm{M}_\oplus$ planetary embryos (Ormel et al., 2010). Pebbles are accreted by a planetary embryo more efficiently than planetesimals are, and therefore pebble accretion boosts the growth of planetary embryos (Ormel & Klahr, 2010). Collisions among planetary embryos, also known as giant impacts, lead to the formation of planetary cores[1] (e.g., Raymond et al., 2005; Walsh et al., 2011). These cores result in the formation of rocky

[1] Not to be confused with the geophysical definition of core given in Sect. 1.3.1

planets, gas dwarfs or gas giants depending on the core size and local constraints on gas in the protoplanetary disk (Johansen & Lambrechts, 2017, and references therein).

The orbital migration of giant planets, before (e.g., Grand Tack model, Walsh et al., 2011) and after (e.g., Nice model, Tsiganis et al., 2005; Gomes et al., 2005; Morbidelli et al., 2007) the dispersion of the gas disk, further complicates the formation of rocky planets. N-body simulations of planetesimals and planetary embryos including the effects of giant planet migration have been able to reproduce to a certain extent the physical configurations and masses of the rocky planets observed in our solar system (Grand Tack model, Walsh et al., 2011). The minimum-mass extrasolar nebula model (Chiang & Laughlin, 2013) is able to explain the observations of super-Earths extremely close to their host stars but cannot explain planet formation in a general sense. Other planet formation scenarios such as the many-seeds model (Schoonenberg & Ormel, 2017) are capable of explaining the formation of TRAPPIST-1 planets by forming them at the snowline (where water turns into ice) and growing them to their final mass during inward migration (Ormel et al., 2017). N-body simulations of Ogihara et al. (2018) explain super-Earth formation in a much broader sense than earlier attempts. Population synthesis models are based on the idea that the observed diversity of extrasolar planets is due to the diversity in initial conditions and the protoplanetary disks. These models account for planetary migration and provide a better way to constrain planet formation scenarios as well as to determine planetary evolution tracks especially for giant planets (Mordasini, 2018). Even with these developments, several regimes of planet formation such as the structure of protoplanetary disks, the formation of first planetesimals as well as the planetary migration mechanisms remain not fully understood (Morbidelli & Raymond, 2016).

1.2.2 Chemical diversity

Mass-radius relations reveal to first order that the composition of exoplanets is much more diverse than that of the planets in our solar system (Fig. 1.3). Chemical characterization of exoplanets using several different observational strategies reveals their atmospheric composition (e.g., Madhusudhan et al., 2016). After first detections of atomic Na (Charbonneau et al., 2002) and H (Lyman-α, Vidal-Madjar et al., 2003) in HD209458b, clouds, hazes as well as molecules such as H_2O, CO, CO_2, CH_4, VO, TiO_2 and even atomic Ti and Fe have been detected in the atmospheres of a variety of exoplanets ranging from cool gassy super-Earths to ultra-hot-Jupiters (e.g., Grillmair et al., 2007, 2008; Désert et al., 2008; de Kok et al., 2013; Birkby et al., 2013; Kreidberg et al., 2014; Todorov et al., 2016; Hoeijmakers et al., 2018). In contrast to gaseous exoplanets, there is no direct way to probe the composition of rocky exoplanets without detectable atmospheres. Nonetheless, spectral detections of exospheres of disintegrating exoplanets provide an indirect way to study their mineralogy (e.g., Rappaport et al., 2012; van Lieshout et al., 2014; Ridden-Harper et al., 2016; Bodman et al., 2018). Another unique tool to probe the interior composition of exoplanets is by studying the abundances of elements heavier than helium on the surface of polluted white dwarfs where the polluted surfaces are believed to come from the external accretion of disrupted rocky planets and planetesimals (e.g., Zuckerman et al., 2003, 2010; Veras et al., 2013).

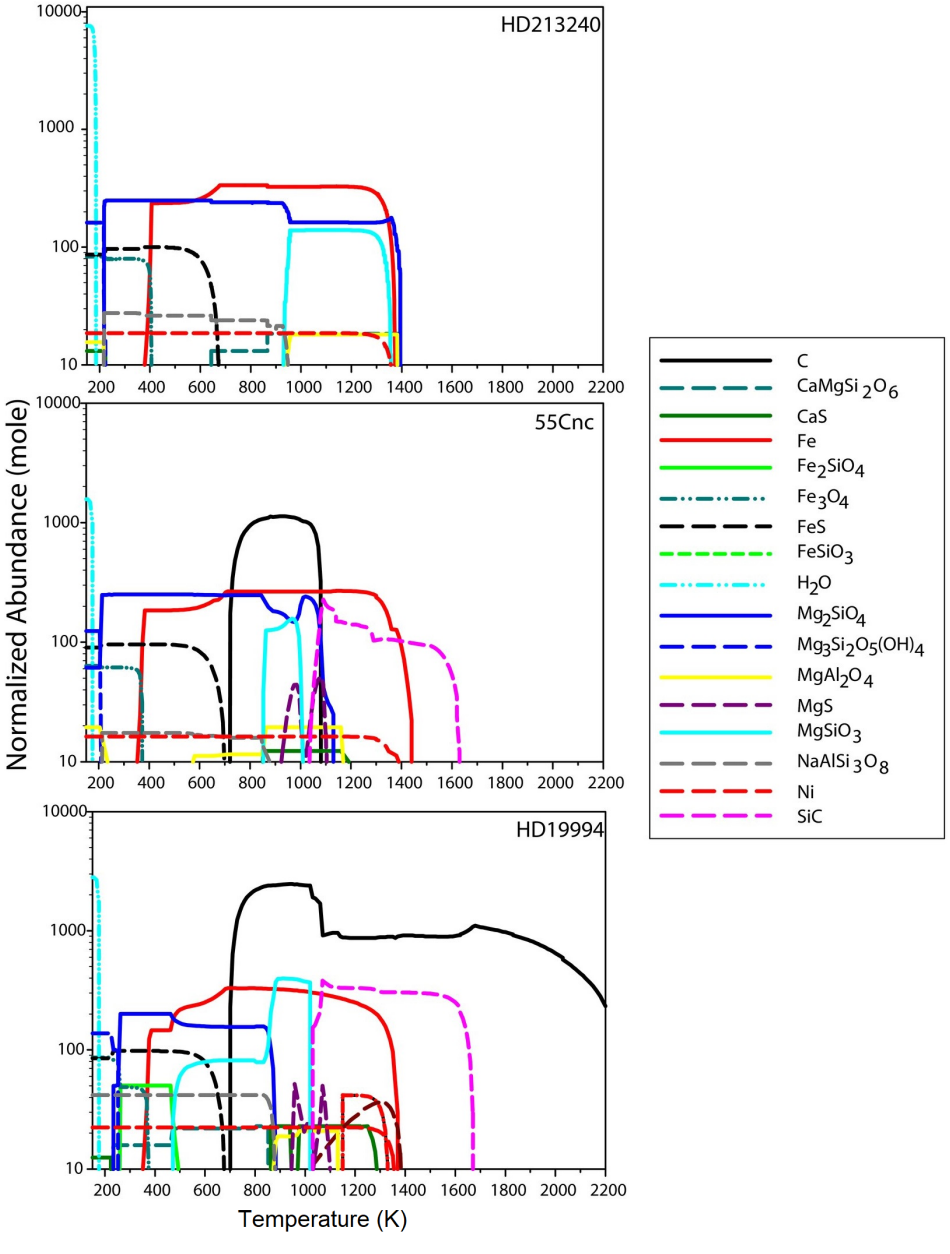

Figure 1.4: Relative abundances of different solid species obtained by Bond et al. (2010b) using the HSC Chemistry software for three representative systems: HD213240 (top), 55 Cancri (center) and HD19994 (bottom). The solid species towards the right side of the plots start forming first (at higher temperature) and as the disk cools down other species start condensing out depending on the temperature. Figure taken from Bond et al. (2010b).

About 95.7% of the Earth's total mass can be explained only by the presence of Mg, Si, Fe and O, and addition of Al, Ca and Ni makes the total 99.3% (e.g., Javoy et al., 2010). The bulk Mg/Si, Fe/Si and other refractory element ratios of the Earth reflect the solar photospheric element ratios (e.g., McDonough & Sun, 1995). Consequently, the bulk refractory element composition of rocky exoplanets is assumed to directly reflect the host star ratios such as Mg/Si, Fe/Si and others (e.g., Valencia et al., 2010; Wang et al., 2013). This assumption works for Earth and Mars but not for Mercury because of its anomalously high Fe content. Another approach is to assume that refractory material condenses from the protoplanetary disk in equilibrium (e.g., Lodders, 2003; Bond et al., 2010a; Elser et al., 2012). Using stellar photospheric elemental ratios as inputs for the initial composition of the protoplanetary disk, the abundances of a range of condensed solid phases are computed by iteratively minimizing the system's Gibbs free energy (e.g., Bond et al., 2010a). This gives robust information about the abundances of solid phases in different regions of the protoplanetary disk at a particular time as shown in Fig. 1.4 taken from Bond et al. (2010b). The solid phases with higher condensation temperatures form closer to the host star than the ones with lower condensation temperatures. Although the accuracy of estimated C/O ratios of stars in the solar neighborhood is being debated (see Introduction of Chapter 3), studies modeling protoplanetary disk chemistry have used these ratios to evaluate the extent of diversity in the composition of rocky exoplanets (see below). For stellar photospheric ratios of C/O > 0.8, Bond et al. (2010b) found that carbon-rich solid species such as graphite, silicon carbide and titanium carbide are produced in protoplanetary disks. Carbon is shown to be difficult to remove in protoplanetary disks by traditional mechanisms such as oxidation and photolysis (Klarmann et al., 2018). Moriarty et al. (2014) found that a sequential condensation model leads to the survival of solid phases in extended regions of inner protoplanetary disks and particularly increases the extent of refractory carbon.

Until 2010, only a few studies associated planet-formation N-body simulations with chemistry (e.g., water delivery, Raymond et al., 2004). Bond et al. (2010a) and Bond et al. (2010b) were the pioneering studies to combine dynamics and chemistry of rocky exoplanets for several planetary systems. Bond et al. (2010b) found that stellar Mg/Si and C/O ratios exert the strongest control on both the bulk mineralogy of the solid material present in the disk and the final composition of exoplanets, leading to a range of compositions from carbon-poor magnesium-rich to silicon-carbon-only (see Fig. 1.5). Carter-Bond et al. (2012b) took into account the effects of giant planet migration and found an increase in the frequency of rocky exoplanets with Earth-like silicate minerals with up to 47 wt% carbon as well as increase in the efficiency of delivery of hydrous phases to rocky exoplanets. Thiabaud et al. (2015) showed that the C/O ratios of rocky planets do not necessarily show a one-to-one correlation with the stellar photospheric C/O ratios, also evident in Fig. 1.5. Moreover, low Mg/Si stars tend to produce Mg-depleted and Ca-Al-enhanced planets (Carter-Bond et al., 2012a). Although such chemical-dynamical models are sensitive to the initial composition of solids in the disk, the feeding zone for each planet as well as the accretion time for each planet, these models present a robust way to study the composition of rocky planets in detail (Carter-Bond et al., 2012b). The effects of Mg/Si and C/O ratios on planetary composition and mineralogy are discussed in further detail in Chapters 2 and 3 of this thesis.

1

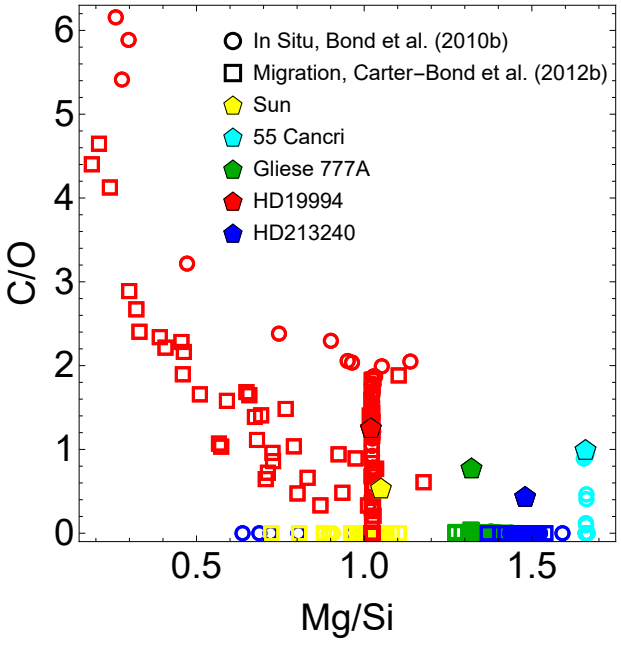

Figure 1.5: C/O vs Mg/Si ratios of planets produced in the in situ simulations of Bond et al. (2010b) and the migration simulations of Carter-Bond et al. (2012b) for five selected planetary systems. Also plotted are the stellar ratios used in these simulations. Most planets have Mg/Si ratios similar to their host star, however that is not the case for their C/O ratios.

1.3 Rocky exoplanets

1.3.1 Interior

Within a decade of the discovery of the first rocky exoplanet, CoRoT-7b (Léger et al., 2009), more than a thousand[1] exoplanets, which may be classified as rocky based on their radius ($R < 2$ R$_\oplus$) or mass ($M < 10$ M$_\oplus$), have been found. Rocky exoplanets are the most interesting extrasolar planets in terms of their potential for habitability because of the possibility of a solid surface, liquid water, a magnetic field to protect its surface and atmosphere from stellar radiation and other essential factors for life as we know it. Since rocky planets such as Earth are likely to lose their primordial atmospheres to space, the composition of their secondary atmospheres depends on coupled surface-interior processes such as outgassing, recycling and plate tectonics as well as external factors such as comet or asteroid impacts. To determine the surface dynamics and atmospheric composition of rocky exoplanets, it is essential to understand the processes in their interiors. At present there is little information about the interiors of specific rocky exoplanets but their physical and chemical diversity make it possible to probe their interior characteristics in a general sense. Although the Inter-

[1] https://exoplanetarchive.ipac.caltech.edu/

national Astronomical Union's definition[1] of a planet requires the neighborhood of its orbit to be cleared, the interiors of non-planet planetary bodies such as dwarf planets, larger satellites and asteroids are governed by the same principles as rocky planets. Knowledge of the interiors of solar system planetary bodies gives a logical starting point to build our understanding of rocky exoplanetary interiors.

The Earth's interior more than a few kilometers beneath the surface cannot be directly accessed. Nonetheless, the study of seismic surface waves and body (pressure and shear) waves, gravity and moment of inertia measurements, the study of plutonic and volcanic igneous rocks[2] and meteorites as well as computational modeling and laboratory experiments give insight into the structure and composition of the interior of the Earth. Some of these techniques such as gravity and moment of inertia measurements have also been carried out by fly-by and orbiter spacecrafts to explore the interiors of other planetary bodies in our solar system. The interiors of rocky planetary bodies in our solar system have a dense metallic core and a lighter rocky mantle which is a direct consequence of hydrostatic equilibrium (see below). Still, there is a diversity in their core and mantle sizes (Fig. 1.6). The Earth's mantle is stratified into an upper mantle and a lower mantle due to respective mineralogical transformations from olivine $(Mg,Fe)_2SiO_4$ to perovskite $(Mg,Fe)SiO_3$ and ferropericlase (Mg,Fe)O at a depth of 660 km, and perovskite to post-perovskite at a depth of 2700 km (Dziewonski & Anderson, 1981). The mantle of Mars is not thick enough to reach pressures high enough to form perovskite (e.g., Zuber et al., 2000). The Earth's core is divided into an outer molten core composed of iron and light elements, and a solid inner core comprising mainly iron and nickel (see Chapters 2 and 3 for details about the core and mantle mineralogy of rocky exoplanets). The Moon has a small core and Mercury, on the other hand, has a large core (Fig. 1.6). The effects of the core size on the planetary structure and mass-radius relations are discussed in Chapter 2. Although the rocky planets in the solar system are mainly composed of two layers (an iron core and a silicate mantle), rocky exoplanetary interiors may be characterized by multiple layers of different compositions. For instance, see Chapters 3 and 5 for rocky exoplanets covered by graphite.

The observed first-order density stratification or differentiation in planetary bodies is the result of chemical segregation and gravitational stratification during the magma ocean stage of planet formation. The refractory material acquired onto protoplanets from the protoplanetary disk is subjected to high pressures and high temperatures depending on the size of the protoplanet, the larger the protoplanet the higher the pressures and temperatures. The pressures[3] are high because of the self-compression of matter inside the protoplanet and the temperatures are high mainly due to the release of heat from the potential energy gained during accretion and radiogenic heating of short-lived radiogenic isotopes such as ^{26}Al[4]. These pressure-temperature-compositional conditions trigger geochemical reactions

[1] This 2006 definition disqualified Pluto to be a planet and put it in the category of dwarf planets. However, a case for Pluto to be re-classified as a planet is being made by Metzger et al. (2018).

[2] Rocks are defined as aggregates of minerals.

[3] The pressures in planetary interiors are 5−10 orders of magnitude higher than the protoplanetary disk pressures.

[4] This radioactive isotope is short-lived (half-life of 0.7 Myr), specific to the solar system and might not be present in other planetary systems.

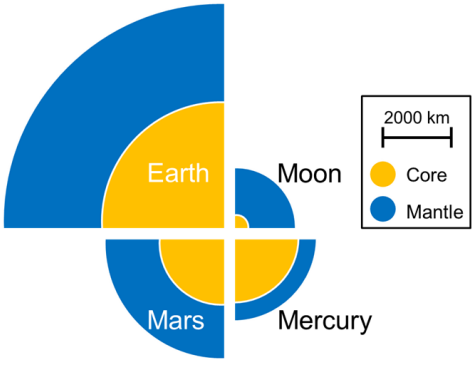

Figure 1.6: The diversity in the core and mantle sizes of four solar system rocky bodies.

transforming the refractory material in the protoplanet into a new set of coexisting minerals. For example, a carbonaceous chondritic composition subjected to a pressure of 1 GPa[1] and a temperature of 2000 K results in molten iron-rich metallic and silicate phases (e.g., Corgne et al., 2008). Such chemical differentiation of minerals happens fast compared to geological timescales (see Chapters 3 and 4). Hydrostatic equilibrium[2] conditions in the protoplanet favor it to go into a lower potential energy state by collecting the densest components at the center. If the minerals formed during chemical differentiation have different densities, heavier minerals such as iron alloys sink towards the center of the planet and form the core[3] and lighter minerals such as silicates rise towards the surface and form the mantle. Such a gravitational segregation concentrates siderophile elements such as Ni and S in the core and lithophile elements such as Mg, Si, Al, Ca, Na, K, U and Th in the mantle. Such differentiated planetesimals and protoplanets undergo multiple accretion events resulting in a range of possibilities for the final core and mantle composition and mineralogy of planets (e.g., Rubie et al., 2015).

After planet formation is complete, the planetary interior cools down over the course of evolution. Heat is transported from the interior of the planet to the surface via convection, conduction or radiation. In rocky planets, the temperatures are never high enough for radiative transfer to be important and the heat is transferred by convection and conduction. Internal heating slows down the cooling process. Primordial heat and radiogenic heat (arising from four radiogenic isotopes ^{238}U, ^{235}U, ^{232}Th and ^{40}K) contribute to internal heating. Both radioactive decay and remnant heat of formation decrease with time. Other sources of internal heating include tidal heating which becomes significant for exoplanets orbiting close to their host stars (e.g., Driscoll & Barnes, 2015).

[1] The pressure of 1 GPa is equivalent to 10 000 times of the atmospheric pressure.

[2] The state when the collapse due to self-gravitation is balanced by the internal pressure. Planetary bodies with a diameter larger than 600 km are capable of exhibiting hydrostatic equilibrium (Lineweaver & Norman, 2010).

[3] This is known as the core formation event in planetary science.

In rocky planets such as Earth and Mars, the silicate mantle solidifies soon after formation but shows plastic behavior on geological timescales. This allows for the silicate mantle to undergo slow creeping[1] motion as a result of convective currents carrying the heat from the planetary interior to the surface. Depending on the state of the core and the method of heat transfer in the mantle, it transfers heat via convection or conduction. A molten convective (outer) core is also capable of producing long-term planetary magnetism. In the case of Earth, the geodynamo produces a magnetosphere around the Earth which protects the atmosphere and life from the charged particles of the solar wind and cosmic rays. The thermal boundary layers formed at the top and the bottom of the silicate mantle transfer heat via conduction. The temperature inside a rocky exoplanet increases monotonically with the depth. Generally, the temperature profiles in the mantle of rocky planets are assumed to be close to adiabatic (e.g., Earth and Mars, Spohn, 1991). However, calculations of Tackley et al. (2013) for rocky super-Earths have shown that the temperature in their lower mantles may be super-adiabatic (see Chapter 2). The temperature profile in the core can be adiabatic or isothermal depending on the evolutionary state of the core. The surface temperature on a rocky exoplanet is generally assumed to be equal to the equilibrium temperature, which is calculated assuming the host star and the planet are blackbodies. But the surface temperature of rocky exoplanets may be governed by the amount of atmospheric greenhouse gases (or lack thereof). For example, Venus has a surface temperature of 740 K and an equilibrium temperature of 230 K. On the other hand, for a tidally-locked extrasolar planet with negligible greenhouse gases, there would be a large difference between day- and night-side surface temperatures. A high surface temperature can have important effects on the near surface heat flow and consequently on interior dynamics.

1.3.2 Habitability

The discovery of an Earth-size exoplanet in the habitable zone or the Goldilocks zone of our nearest star, Proxima Centauri (Anglada-Escudé et al., 2016) necessitates a comprehensible definition of habitability. The habitable zone is defined as a region with a minimum and a maximum distance from the host star where the planetary surface temperatures (and atmospheric pressures) allow for the presence of liquid water. Assuming the atmospheres of potentially habitable exoplanets are thin, similar to Earth, the distance from the host star, because of the stellar luminosity, plays an important role in determining the climates on these exoplanets. Small stars (e.g., M-dwarfs) have a habitable zone much closer to them as compared to Sun-like stars, owing to their lower luminosity. In the literature, the habitable zone was first discussed to understand the climate of early Earth and Mars (Huang, 1959; Hart, 1978), and was later associated with the planetary carbonate-silicate cycle as a climate-stabilizing mechanism (Walker et al., 1981; Kasting et al., 1993). Other requirements for habitability include, at present only qualitatively, low stellar variation, high stellar metallicity, plate tectonics, planetary magnetosphere, biogeochemical processes based on elements vital for life — C, H, O, and N, and several others. This implies that planet habitability

[1] Creep refers to the tendency of solids to move slowly or deform permanently under the influence of stresses.

is planet specific. Nonetheless, the potential for habitability is usually discussed in a general sense (see Chapters 3 and 5).

The first atmospheric detection of a rocky exoplanet marks the beginning of the atmospheric characterization of potentially habitable worlds (Southworth et al., 2017). As rocky exoplanets are likely to lose most of their primordial atmospheric gases to space, the composition and structure (pressure-temperature) of the secondary atmosphere depend on internal (interior degassing and recycling) as well as external (stellar radiation or cometary-asteroid bombardments) factors. To determine the climate on an exoplanet, it is of prime importance to take into account the effect of atmosphere-interior exchange through planetary volatile cycles as well as non-cyclical processes. Although the Earth contains less than 0.01 wt% carbon in total (e.g., Javoy et al., 2010), carbon plays a crucial role in biotic as well as abiotic processes on the planet. The carbonate–silicate cycle transforms silicate rocks to carbonate rocks by weathering and sedimentation on the surface and transforms carbonate rocks back into silicates by metamorphism and magmatism (Berner et al., 1983). It plays a large part in the overall carbon cycle, since the equilibrium point of the carbonate-silicate cycle dictates the pace of carbon release from the lithosphere. Interesting to note is that almost the total amount of carbon, which is present in the atmosphere of Venus, exists on Earth as well but is mainly deposited in carbonate rocks. The geosphere[1] of rocky exoplanets might accommodate planetary processes alien to those on Earth. For example, rocky exoplanets orbiting extremely close to their host star will have surface temperatures high enough to make their atmospheres silicate-rich and undergo a surface-interior evolution unlike any solar system body (Kite et al., 2016).

Plate tectonics, which is considered to be essential in sustaining the carbonate-silicate cycle over geological timescales, helps in stabilizing the climate and thereby is assumed to play a central role in determining the habitability of rocky planets (Walker et al., 1981; Kasting et al., 1993). Plate tectonics is specific to a planet, and the mantle thickness, gravity, composition and several other factors influence the heat transport mechanism and the tectonic mode (e.g., Valencia et al., 2007c; Höning et al., 2014; Tosi et al., 2017, also see Chapter 5). Arguments as to whether or not plate tectonics will occur in a planet more massive than Earth are still under debate (e.g., O'Neill & Lenardic, 2007; Valencia et al., 2007c; Kite et al., 2009; van Heck & Tackley, 2011; O'Neill et al., 2016). With a coupled interior-atmosphere evolution modeling, Tosi et al. (2017) have shown that a rocky planet with a stagnant lid (i.e., the absence of plate tectonics) is still potentially habitable.

Future remote-sensing observations of habitable exoplanets should be capable of detecting biogenic signatures. One way is to compare the observed reflectance spectra (e.g., vegetation red-edge, Seager et al., 2005) and geometric albedos (Madden & Kaltenegger, 2018) of exoplanets to those of the Earth. However, such observations are not possible yet. Biosignature gases produced by life which accumulate in atmospheres to high enough levels for remote detections are the most likely candidates for such a search. It will not be possible to detect all biosignature gases from such large distances. Only globally mixed, spectroscopi-

[1] The geosphere may be defined as a collective term for the lithosphere and the atmosphere including the hydrosphere, the cryosphere and life, if they exist.

cally active gases will be visible in an exoplanet spectrum (Seager, 2013). On Earth, the dominant global biosignature gases are O_2 (and its photolytic product O_3) produced by plants and photosynthetic bacteria, N_2O, and for early Earth possibly CH_4. However, the detectability of biosignatures of habitable exoplanets is likely to vary over time. Earth has undergone changes in its interior structure and atmospheric composition from the Archean eon until now, and it is likely that future observations will capture rocky exoplanets in various stages of evolution. For example, the Earth's unambiguous biosignature gases were detectable only for a quarter of the Earth's history (Palle, 2018). The partial pressure of O_2 in the atmosphere increased by two orders of magnitude (became detectable) only after the Great Oxidation Event, which occurred 2.45 billion years ago (Kasting et al., 1993). Additional processes such as degassing, asteroid or comet impacts and others can alter the atmospheric composition substantially. Many biosignature gases have a false positive interpretation because they can also be produced abiotically. Finally, planetary bodies outside the habitable zone can also host liquid water such as Europa and Enceladus. Overall, habitability is clearly complex and future studies are needed to obtain a better quantitative understanding of the requirements of habitability.

1.4 Geosciences for exoplanetary science

1.4.1 Geophysics

Modern geosciences cover several disciplines in earth and planetary sciences. Approximately two decades from now, observations of the surface of several Earth-size extrasolar worlds could become a reality. However, the observational data would be nowhere close to the data available for solar system bodies today. It will rather be roughly equivalent to the data planetary scientists collected in 1970s and 1980s the courtesy of first space missions to solar system planets. Extracting meaningful information about the surface and atmospheric processes on rocky exoplanets will be a challenge. There is no question that astronomers would turn to geoscientists to explain their observations. However, it is imperative that geoscientists as well as exoplanet scientists understand the current wide gap between the methods of modern geosciences and astronomy. Because of space missions to several solar system bodies, detailed numerical and analytical techniques in geosciences are being used to explain the abundant observational data. The goal of the application of techniques in geosciences to exoplanetary science should be to focus on developing a generalized theory for rocky exoplanets which has the right amount of detail to be matched with the sparse (future) observations of rocky exoplanets. Fig. 1.7 illustrates the dependency of computational modeling of rocky exoplanets on theory, experiments and astronomical observations, and provides a non-exhaustive list of aspects of study. This thesis focuses on the implementation of computational and experimental tools from geosciences to rocky exoplanets.

Geophysics is mainly concerned with the physical processes in the Earth and the implementation of numerical and analytical methods to understand them. The Earth and the Moon are the only rocky planetary bodies for which we have information about the interior structure from seismic observations. It is not surprising that the first studies focusing on the

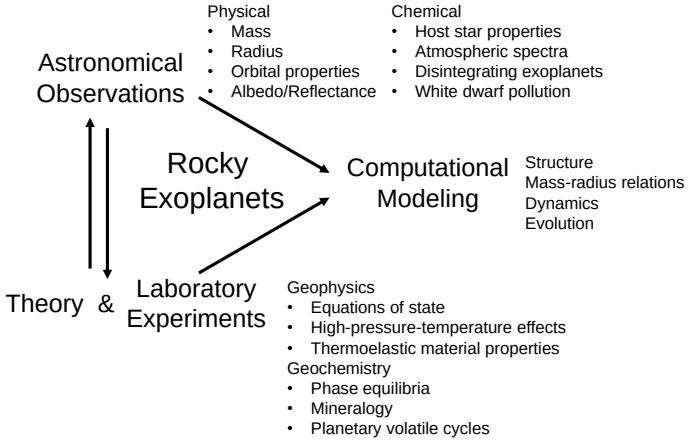

Figure 1.7: Different aspects involved in the study of rocky exoplanets. The interdependence of exoplanetary science and geosciences is evident.

interiors of rocky exoplanets extrapolated interior structure models of Earth (e.g., Valencia et al., 2006; Sotin et al., 2007). With assumptions on composition, these interior structure models are used to derive theoretical mass-radius relations, which are a valuable tool in determining the composition of rocky exoplanets to first order (e.g., Valencia et al., 2006; Seager et al., 2007; Wagner et al., 2011; Hakim et al., 2018a). To compute the structure of rocky exoplanets, the differential equations originating from the hydrostatic equilibrium assumption and the internal gravitational potential are integrated simultaneously (see Chapters 2, 3 and 5). The mass of a planet is integrated along the radius assuming that a planet can be described as a one-dimensional sphere, i.e., that the density depends only on the radius and does not vary significantly with longitude or latitude.

Interior structure models require a second equation relating the pressure and temperature of the material to its density, the equation of state. Since pressure and temperature increase monotonically with depth inside a planet, it is crucial to use an accurate equation of state. The ideal gas equation approximation, which holds in stellar interiors, does not work in solid or partially molten planets because solid silicates and solid/liquid metals are far less compressible than gas. Several techniques have been developed in the last century to describe the equation of state for solids based on thermodynamics and elasticity. The finite strain theory, also known as the Birch-Murnaghan equation, gives a temperature independent relation between the pressure and the density of solids (Birch, 1947). This equation is still widely used along with a temperature dependent term which comes from lattice dynamics theory (Mie-Grüneisen-Debye or Einstein equations, e.g., Ita & Stixrude, 1992). Due to a complex dependence of the thermoelastic properties of solids on pressure and temperature, it is not trivial to accurately determine the material density from these equations. It is common for material physicists to perform laboratory measurements on the material density

and fit the data to these equations (e.g., Stixrude & Lithgow-Bertelloni, 2005). However, laboratory data are not always available for a number of reasons including the technological inability to reach the required pressure. For example, the pressures at the center of rocky super-Earths are an order of magnitude higher than those achieved in laboratories (e.g., Hakim et al., 2018a). In such cases, studies modeling super-Earth interiors usually extrapolate equations of state validated at low pressures to high pressures (e.g., Valencia et al., 2006; Seager et al., 2007; Wagner et al., 2011). But extrapolations of the equations of state used in these studies lead to errors of up to 20% in the density of iron, which is the major constituent of the core of rocky planets (see Chapter 2). Quantum-mechanical calculations are the only way to accurately determine material density at such high pressures (Pisani, 2012). Several methods such as the density functional theory (DFT) have been developed over the years to investigate the electronic structure of many-body systems such as atoms and molecules (Cottenier, 2002). Chapter 2 in this thesis shows an implementation of DFT to derive an ab initio equation of state for solid iron at pressures up to 1.37 billion times the atmospheric pressure.

Another important aspect of rocky planetary interiors is their dynamics, which is again dependent on pressure, temperature and material properties. Moreover, understanding interior dynamics enables computation of the thermal evolution. The interior dynamics is driven by the heat transport mechanism in the mantle of the planet which also controls the cooling ability of the planet. The mantle of rocky planets in the solar system is mainly composed of silicates. As described in Sect. 1.3.1, convection in the silicate mantle transports heat from the interior to the surface. The convective material transport of heat is opposed by the viscosity of the material (Cole, 1984). The strength of the viscosity itself depends on the temperature (and on the pressure). The rise in temperature due to internal heating decreases the viscosity and so allows a creep motion to take place. The resulting flow of heat away from the region reduces the temperature, increasing the viscosity and reducing the advective heat flow. In a planetary layer, material transport is driven by differences in density at different depths in the presence of gravity. The buoyancy force is opposed by the viscous force and motion is caused if the buoyancy force exceeds the viscous force. The larger the motion, the stronger the convection. This vigor of convection can be written as the ratio of buoyancy and viscosity forces multiplied by the ratio of momentum and thermal diffusivities, which is essentially the Rayleigh number (Schubert et al., 2001). This is popularly known as the Rayleigh-Bénard convection. A planetary layer is in convection if its Rayleigh number significantly exceeds the critical Rayleigh number, which is a geometrical parameter of the order of 1000. The Rayleigh number can be associated with the Nusselt number, which gives the ratio of convective to conductive heat transfer, by a Nusselt-Rayleigh number power-law relationship (Schubert et al., 2001). Such a relationship provides a way to associate the heat transfer in a planetary layer to material properties such as viscosity and thermal diffusivity. In Chapter 5 of this thesis, we apply the Rayleigh-Bénard scheme to model the thermal evolution of rocky exoplanets with three layers: an iron core, a silicate inner shell and a graphite outer shell.

1.4.2 Geochemistry

Geochemistry largely deals with the chemical composition of the Earth, its rocks, and minerals. The rocks in the Earth's crust and upper mantle undergo weathering and recycling because of the combined action of the water cycle and plate tectonics. The weathering of all types of rocks due to water and wind produces sediments which over time cement together to form sedimentary rocks. These sedimentary rocks may be overlaid by other rocks and subjected to high pressure and temperature resulting in the formation of metamorphic rocks. Further increasing temperature at constant pressure can lead to partial melting of metamorphic rocks. Crystallization of these melts leads to the formation of igneous rocks, which when returned to the Earth's surface weather and restart the rock cycle. This molten material crystallizes to form igneous rocks again. The rock cycle plays an important role in geochemical cycling of volatile elements on the Earth. For example, during the carbonate-silicate cycle which involves cycling of carbon, silicate rocks undergo weathering and sedimentation to form carbonate rocks, which in turn undergo metamorphosis and magmatism to form silicate rocks.

Most of the rocks in the Earth's crust and upper mantle contain silicate mineral-series such as feldspar, pyroxene, olivine, garnet, mica and quartz (Schuiling et al., 1994). Common non-silicate mineral-series include spinel, carbonate, magnetite, hematite and others. Since changes in pressure, temperature, and bulk composition influence the stability of minerals in a given rock, it is essential to establish the conditions of stability through the study of phase equilibria. In a chemical system, a phase is a homogeneous substance that has a fixed composition and uniform chemical and physical properties. Goldschmidt's mineralogical phase rule, which is a corollary of the Gibbs' phase rule, states that in a system in equilibrium, the number of degrees of freedom is given by subtracting the number of phases from the sum of the minimum number of components required to constitute all phases and 2. For example, assuming olivine $(Mg_xFe_{1-x})_2SiO_4$ to be the only phase in the two-component system (Mg_2SiO_4 and Fe_2SiO_4) gives the number of degrees of freedom to be $2 + 2 - 1 = 3$. These three degrees of freedom are pressure, temperature and mole fraction x.

Oxygen is the most abundant element in silicate rocks, sharing bonds with almost all non-elemental minerals. Because oxygen exerts a huge influence on redox chemistry, it is of interest to quantify the bulk oxygen content in rocks and minerals by a single quantity. Oxygen fugacity is an equivalent of the partial pressure of oxygen in a particular environment (atmosphere, rocks, etc.) corrected for the non-ideal character of the gas. This does not mean that there is free oxygen in deep planetary interiors, but the oxygen fugacity is rather a measure of the oxygen partial pressure that the gas would have if it were in equilibrium with the rock. Oxygen fugacity, along with temperature and pressure, also controls chemical processes in planets, for example, metal-silicate partitioning which defines the amount of iron in the form of iron, essentially giving the relative core mass (see Chapter 3 for a discussion). Another important parameter is the partition coefficient, which gives the ratio of distribution of an element between metal and silicate, which are usually two most important phases for a planetary bulk composition. For example, because of the high metal-silicate partitioning coefficient of carbon ($500-5000$), it is evident that carbon preferentially partitions into a

planetary iron core rather than a silicate mantle (Chi et al., 2014). Water has an important role to play in the geochemical cycles on Earth, especially in the melting of mantle rocks by lowering their melting temperature (Wyllie, 1981), and would possibly be important for rocky exoplanetary interiors.

1.4.3 Experimental petrology

Historically, experimental petrology was concerned with experimentally determining the physical and chemical behavior of rocks and minerals, in the Earth's interior, at conditions that were not directly accessible. With the arrival of lunar rocks, the courtesy of the Apollo missions, and observational data for rocky bodies in our solar system, techniques in experimental petrology began to be applied in planetary science. With the prospects of detailed characterization of extrasolar planets in the near future, now the time is right to begin applying experimental petrology to exoplanetary science.

To simulate a planetary interior, chemical environments are subjected to controlled high pressures and temperatures in a laboratory. Such environments are created using high-pressure high-temperature devices including piston cylinder apparatuses, multi-anvil devices, laser-heated diamond anvil cells, and laser-driven shock wave experiment set ups. Piston-cylinder apparatuses (Boyd & England, 1960) are generally capable of reproducing deep interior conditions of planetary bodies of the size of the Moon or the uppermost mantle of the Earth ($P < 4$ GPa and $T < 2000$ K). Advantages of the piston-cylinder apparatus include a relatively large sample volume and relatively low costs (approximately 30000 per apparatus, and approximately 250 material costs per experiment). A variant of the piston cylinder apparatus may be mounted on a centrifuge to segregate denser phases from lighter phases (e.g., Solferino et al., 2006; Ardia et al., 2008). The top panel of Fig. 1.8 shows the end-loaded piston cylinder (along with the pressure and temperature controllers) at the High-Pressure-Temperature Laboratory, Vrije Universiteit Amsterdam (van Kan Parker et al., 2011). In this thesis, experiments have been performed using this device (see Chapters 3 and 4).

Starting materials for the experiments can be finely ground natural rock samples, or synthetic compounds mimicking the bulk composition of a particular rock or planet. In this thesis, experiments used synthetic starting materials (see Chapters 3 and 4). Before performing an experiment, simple chemicals are mixed in the required proportions (top-left panel, Fig. 1.9). If needed, a box furnace is used for melting the starting material at about 1800 K and quenching, thereby homogenizing the starting material (top-center panel, Fig. 1.9). Then the powdered starting material is inserted in a 0.5 inch diameter cylindrical sample assembly which has several concentric parts (a schematic of the sample assembly is shown in Fig. 3.6, Chapter 3). Images of some parts of the sample assembly are shown in the top-right panel of Fig. 1.9. Assembly parts such as alumina rods or graphite capsules are drilled and shaped using an industrial high-precision lathe (bottom panel, Fig. 1.9). The sample assembly is inserted in the cylindrical hole of a steel pressure plate with a tungsten carbide core. An end load is applied to the top of the pressure plate. A tungsten carbide piston is

1

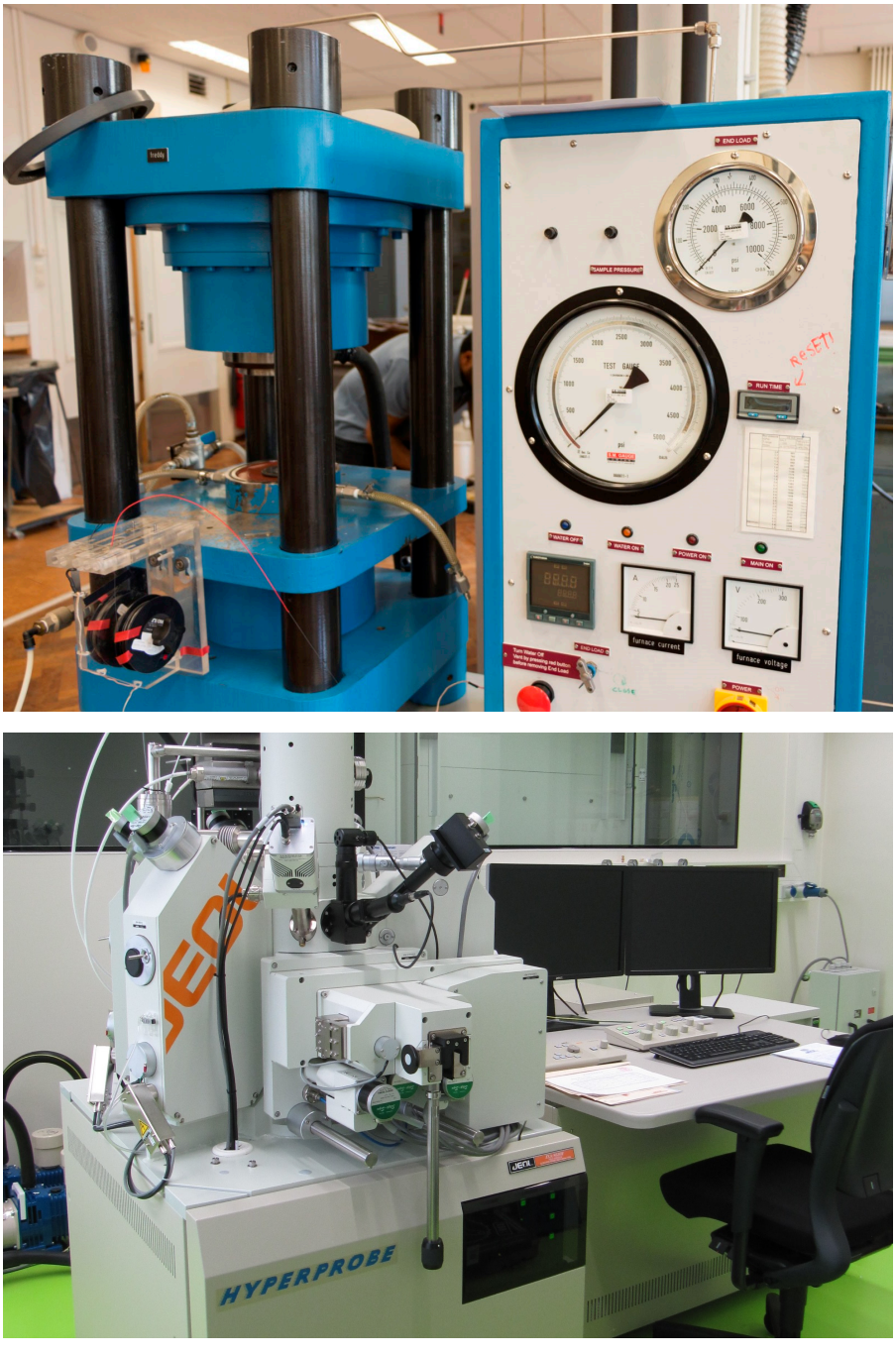

Figure 1.8: *Top*: End-loaded piston-cylinder apparatus (Freddy) in the High-Pressure-Temperature Laboratory of Vrije Universiteit Amsterdam (image credit: Esther Hanko). *Bottom*: Electron microprobe (JEOL JXA-8530F Hyperprobe) at the Dutch National Geological Facility, Utrecht University.

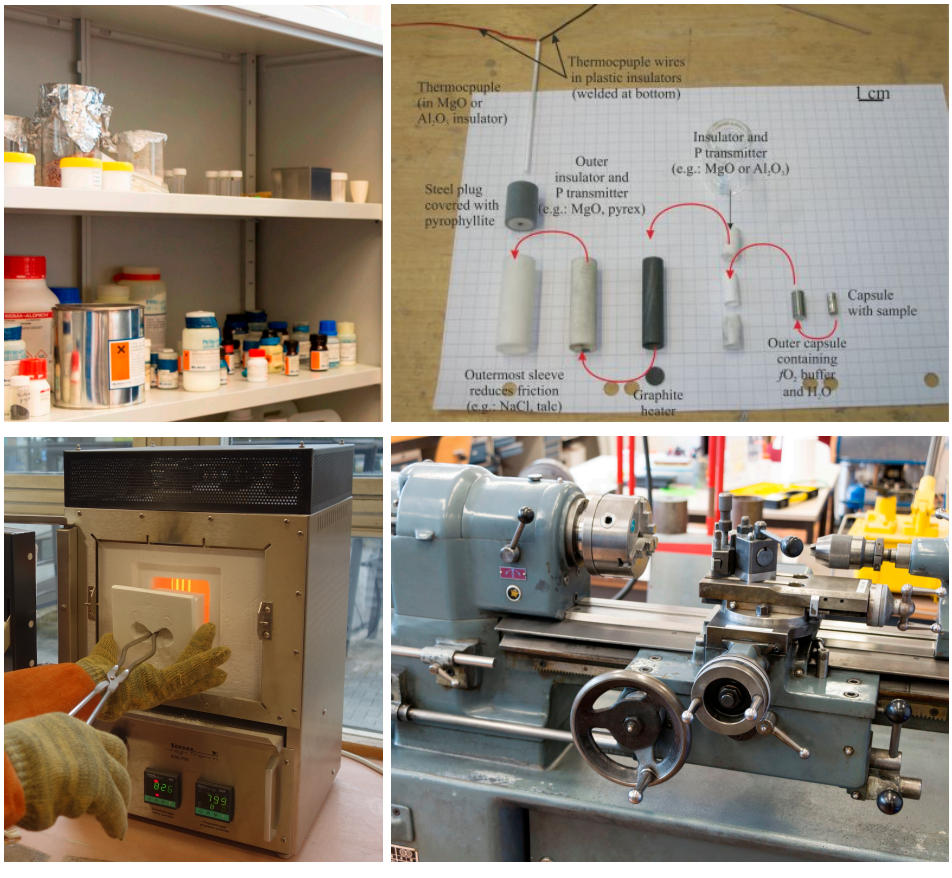

Figure 1.9: *Top-left*: Chemical powders used as starting materials for experiments. *Top-right*: Sample assembly parts shown to scale (image credit: Enikő Bali). A schematic of complete sample assembly is given in Appendices of Chapter 3. *Bottom-left*: An atmospheric pressure furnace for experimental steps such as glass formation. *Bottom-right*: An industrial high-precision lathe, the tool used for cutting, drilling and sanding several sample assembly parts (image credit: Esther Hanko).

Figure 1.10: *Top*: Multi-anvil device (Nina) in the High-Pressure-Temperature Laboratory, Vrije Universiteit Amsterdam. *Bottom-left*: Diamond-anvil cell at the Laboratory for Mineral Physics, University of Chicago. Two gem-quality diamonds inside the cell are visible through the hole. *Bottom-right*: Laser-driven shock wave experiment set up at the High-Pressure Mineral Physics Laboratory, New Mexico State University.

then pressed into the cylinder, pressurizing the solid materials in the pressure assembly. The sample is heated by running an electric current through the graphite sleeve of the sample assembly (see Sect. 3.2.3 for details).

Quantitative analyses of the experimental run products from the piston-cylinder apparatus are performed using an electron probe microanalyzer, or electron microprobe (bottom panel, Fig. 1.8). In an electron microprobe, if a solid material is bombarded by an accelerated and focused electron beam, the incident electron beam has sufficient energy to liberate both matter and energy from the sample. These electron-sample interactions mainly liberate heat, but they also yield both derivative electrons and X-rays. For the analysis of geological samples, secondary and back-scattered electrons are useful for imaging or obtaining an average composition of the material in terms of its mean atomic number (Reed, 2005). X-rays are generated by inelastic collisions of the incident electrons with electrons in the inner shells of atoms in the sample. When an inner-shell electron is ejected from its shell, leaving a vacancy, a higher-shell electron falls into this vacancy and sheds an X-ray characteristic to the element (Jansen & Slaughter, 1982). This quantitative analysis is largely non-destructive and it is possible to re-analyze the same materials more than one time. The size and current density of the electron beam determines the trade-off between resolution and scan time and/or analysis time.

Multi-anvil devices are capable of reaching core-mantle boundary conditions of Mars-size planets ($P < 25$ GPa and $T < 2500$ K). The multi-anvil device at the High-Pressure-Temperature Laboratory, Vrije Universiteit Amsterdam (Knibbe et al., 2018) is shown in the top panel of Fig. 1.10. A ceramic octahedron with holes for placing the furnace and sample acts as the sample assembly. Eight first stage tungsten carbide anvils (designs vary) press upon on octahedron. A set of second stage steel anvils presses upon these first stage anvils. As in the piston-cylinder, an electric current is passed through a furnace (graphite at low pressure, and rhenium and lanthanum chromate at high pressure) to heat the sample. Analyses for multi-anvil samples are performed ex situ as is the case for piston cylinder experiments. Another high-pressure device, a diamond-anvil cell, can reach pressures of the order of 100 GPa (the Earth's deep interior). The diamond anvil cell consists of two anvils made from gem-quality diamonds with a thin metal gasket containing a small sample hole in between (bottom-left panel, Fig. 1.10). A layer of the sample is pressed together between the polished diamond culets. The temperature of the sample is controlled by laser heating. Since diamond is transparent, a range of analytical techniques including X-ray diffraction can be performed in situ. Disadvantages are the small sample size (on the order of $10-50$ μm in diameter) and difficulty in measuring the experimental pressure and temperature accurately and precisely. The three high-pressure devices described above are becoming common in geoscience laboratories today. However, these devices are not capable of reaching the deep interiors of super-Earths. Pressures higher than 1 TPa can be achieved through shock compression at high-powered laser facilities such as the Laboratory for Laser Energetics (Lazicki et al., 2015). An experimental set up for laser-driven shock wave experiments is shown in the bottom-right panel of Fig. 1.10. The interaction of a high-power pulsed laser (above 1 GW/cm^2) with matter yields very high amplitude pressure loadings with very short

durations, initiating a strong short shock wave into solids. These characteristics offer the possibility to study the behaviour of matter under extreme dynamic conditions, with a possible recovery of the shocked samples presenting the effects of the passage of the shock in most cases (Boustie et al., 2008). Although shock wave experiments are useful for measurements of material equations of state at extreme pressures, mineralogical studies are not possible.

1.5 Future of exoplanetary science

The field of exoplanetary science has exploded with information in the past two and a half decades, thanks to several ground- and space-based telescopes focusing on exoplanet detection and characterization. With every discovery, there is something completely new to learn, raising more questions than answers. ESA's Gaia space telescope, which is expected to discover approximately 20 000 exoplanets through astrometry in its first five years of mission (Perryman et al., 2014), has already contributed to exoplanetary science by increasing the precision of data gathered by the Kepler mission (Berger et al., 2018). For spectroscopic observations of exoplanetary atmospheres, enormous amounts of time are currently being dedicated on the Hubble and Spitzer space telescopes, as well as major ground-based telescopes such as Keck, Gemini, Magellan, Very Large Telescope and Canada–France–Hawaii Telescope (e.g., Madhusudhan et al., 2016). NASA's Transiting Exoplanet Survey Satellite (TESS), launched earlier in 2018, has already begun its mission to discover 20 000 extrasolar planets around bright stars (see Fig. 1.11). Ground-based surveys such as NGTS, TRAPPIST, SPECULOOS, MEARTH, MASCARA and others are expected to find thousands of transiting exoplanets orbiting nearby bright stars within the next few years (e.g., Deeg & Alonso, 2018).

ESA's upcoming mission, CHaracterising ExOPlanets Satellite (CHEOPS) will characterize known transiting exoplanets orbiting bright and nearby stars (Broeg et al., 2014). During the same time, major ground-based direct imaging platforms such as SPHERE and GPI are also expected to find at least dozens of exoplanets at wide orbital separations orbiting nearby young stars (Madhusudhan et al., 2016). By the early 2020s, next generation telescopes, such as the James Webb Space Telescope (JWST) and the Extremely Large Telescope (ELT), will revolutionize the field. Future spectra obtained with JWST would be of unprecedented precision and resolution which will enable us to derive precise chemical abundances for transiting exoplanets and to observe atmospheres of much cooler low-mass planets than can be observed today. In the late 2020s, the ESA's PLAnetary Transits and Oscillations of stars (PLATO) (Rauer et al., 2014) and Atmospheric Remote-sensing Infrared Exoplanet Large-survey (ARIEL) (Tinetti et al., 2016) missions will discover numerous transiting exoplanets in habitable zones of nearby stars, and characterize their atmospheres, respectively. Space-based direct imaging is the prime way to find and identify a true Earth twin (Seager, 2013). In this regard, some mission concepts are currently under study by NASA such as the Large UV/Optical/IR Surveyor (LUVOIR) and the Habitable Exoplanet Observatory (HabEx).

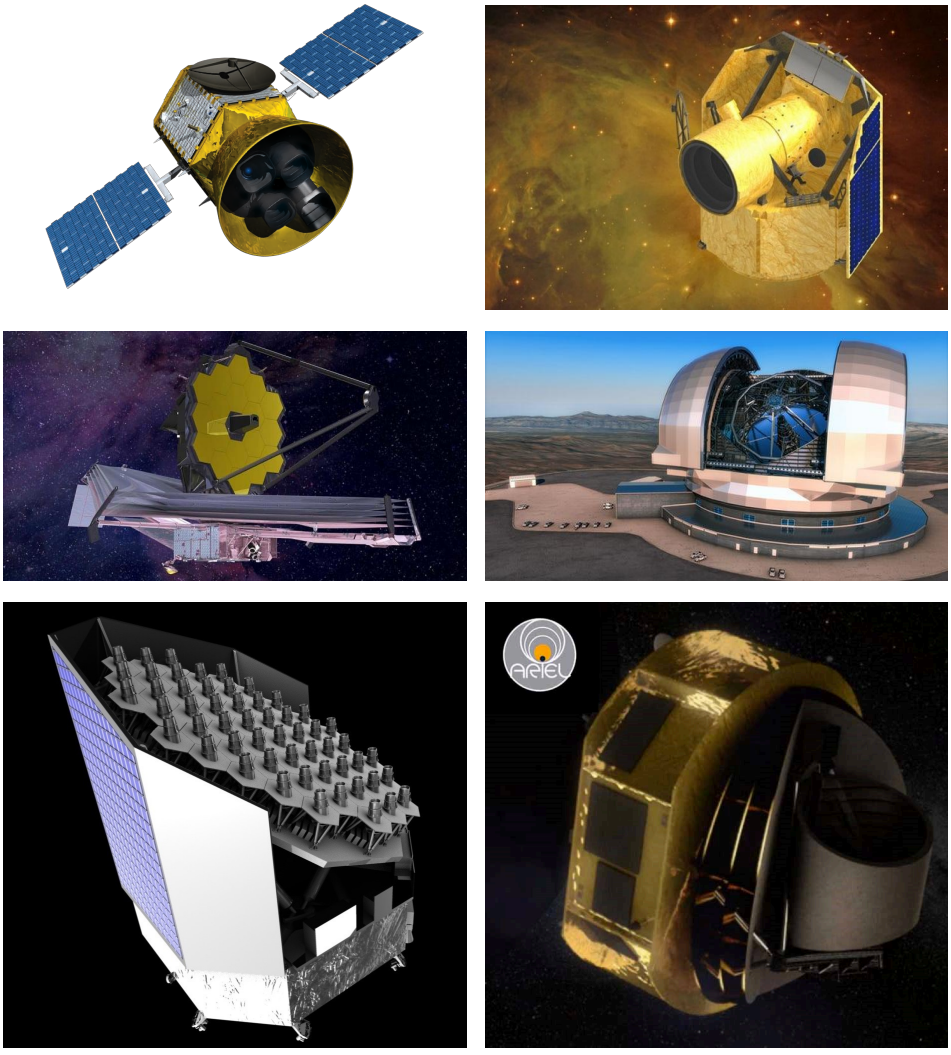

Figure 1.11: *Top-left*: NASA's TESS was launched in 2018 and will focus on the discovery of exoplanets around bright stars. *Top-right*: ESA's CHEOPS telescope will be launched in 2019 and will mainly study the known transiting exoplanets orbiting bright and nearby stars. *Center-left*: JWST is the successor of the Hubble Space Telescope (HST) which will, among several objectives, perform direct-imaging of exoplanets. *Center-right*: ESO's Extremely Large Telescope is the world's largest telescope, now under construction, and among several goals will also attempt to image Earth-size exoplanets. *Bottom-left*: ESA's PLATO space telescope would be launched in 2026 and will detect and characterize Earth-size exoplanets. *Bottom-right*: ESA's ARIEL space telescope will be launched in 2028 and aims at characterizing the atmospheres of about 1000 exoplanets.

Within the next two and a half decades, spectra of hundreds of rocky exoplanets will be available. The exoplanet community must be well prepared to decode these data in terms of the surface and atmospheric processes on these exoplanets. Among other factors, the accuracy of these interpretations depends on the collaboration between the exoplanet and geoscience communities in order to develop a generic understanding of interior and surface processes on rocky exoplanets. There is a need to understand planetary volatile cycles, the mineralogy of chemically diverse systems and the interior-atmosphere evolution, and making distinctions between biotic or abiotic origins of biosignature gases by doing laboratory experiments as well as developing theory. Information from studying solar system planetary bodies such as Pluto, icy satellites, asteroids or Mercury is also important because of the necessary diversity it brings in understanding extrasolar planets. Statistical studies of exoplanets on host star metallicity, star types, planet properties, etc. would further help in prioritizing the selection of candidates for detailed characterization. The future of exoplanetary science is as exciting as ever and it would be fitting to quote Carl Sagan: “Somewhere, something incredible is waiting to be known”.

1.6 Outline of this thesis

The following chapters in this thesis demonstrate the application of computational and laboratory tools from geosciences introduced in this chapter to understand the interior structure, mineralogy and evolution of chemically diverse rocky exoplanets.

In Chapter 2, we derive a new ultra-high-pressure equation of state of iron based on density functional theory valid at and beyond the core pressures of rocky super-Earths. We demonstrate the inaccuracies of previous equations of state in predicting the density of iron at pressures higher than their validity range. We compute the interior structure and mass-radius relations of rocky super-Earths without gas envelopes. We quantify the effect of a range of chemical compositions for the core and the mantle, equations of state of iron and temperature profiles on mass-radius relations.

In Chapter 3, we simulate interior conditions of carbon-enriched rocky exoplanets by performing high-pressure high-temperature laboratory experiments on carbon-enriched chemical mixtures. We identify the mineralogy of such exoplanets and demonstrate phase relations at different pressures and temperatures. We compute the resulting interior structure of these exoplanets and discuss their observations and habitability.

In Chapter 4, we perform a high-pressure high-temperature experiment between a silicon carbide layer and a layer representative of a carbon-enriched rocky exoplanet. By capturing the on going reaction between these two layers, we report the reactants and products taking part in the oxidation of silicon carbide under planetary interior conditions. We also discuss our results in terms of future observations of surfaces of rocky exoplanets.

In Chapter 5, we compute the thermal evolution of rocky exoplanets covered with a graphite layer. By implementing one-dimensional Rayleigh-Bénard convection scheme, we identify the heat transport mechanism in these exoplanets. We discuss the implication of our results in terms of planetary evolution and habitability.

Chapter 2

A new ab initio equation of state of hcp-Fe and its implication on the interior structure and mass-radius relations of rocky super-Earths

Kaustubh Hakim, Attilio Rivoldini, Tim Van Hoolst, Stefaan Cottenier, Jan Jaeken, Thomas Chust, Gerd Steinle-Neumann

Icarus, 2018, 313, 61−78

Abstract

More than a third of all exoplanets can be classified as super-Earths based on radius ($1-2$ $\mathrm{R}_\oplus$) and mass (< 10 $\mathrm{M}_\oplus$). Here we model mass-radius relations based on silicate mantle and iron core equations of state to infer to first order the structure and composition range of rocky super-Earths assuming insignificant gas envelopes. As their core pressures exceed those in the Earth by an order of magnitude, significant extrapolations of equations of state for iron are required. We develop a new equation of state of hexagonal close packed (hcp) iron for super-Earth conditions (SEOS) based on density functional theory results for pressures up to 137 TPa. A comparison of SEOS and extrapolated equations of state for iron from the literature reveals differences in density of up to 4% at 1 TPa and up to 20% at 10 TPa. Such density differences significantly affect mass-radius relations. On mass, the effect is as large as 10% for Earth-like super-Earths (core radius fraction of 0.5) and 20% for Mercury-like super-Earths (core radius fraction of 0.8). We also quantify the effects of other modeling assumptions such as temperature and composition by considering extreme cases. We find that the effect of temperature on mass ($< 5\%$) is smaller than that resulting from the extrapolation of the equations of state of iron and lower mantle temperatures are too low to allow for rock and iron miscibility for $R < 1.75$ $\mathrm{R}_\oplus$. Our end-member cases of core and mantle compositions create a spread in mass-radius curves reaching more than 50% in

terms of mass for a given planetary radius, implying that modeling uncertainties dominate over observational uncertainties for many observed super-Earths. We illustrate these uncertainties explicitly for Kepler-36b with well-constrained mass and radius. Assuming a core composition of 0.8ρ Fe (equivalent to 50 mol% S) instead of pure Fe leads to an increase of the core radius fraction from 0.53 to 0.64. Using a mantle composition of $Mg_{0.5}Fe_{0.5}SiO_3$ instead of $MgSiO_3$ leads to a decrease of the core radius fraction to 0.33. Effects of thermal structure and the choice of equation of state for the core material on the core radius of Kepler-36b are small but non-negligible, reaching 2% and 5%, respectively.

2.1 Introduction

With the discoveries of CoRoT-7b and Kepler-10b by ESA/CNES's and NASA's space telescopes, a new class of exoplanets known as super-Earths was introduced (Léger et al., 2009; Batalha et al., 2011). Borucki et al. (2011) classified super-Earths as rocky-type exoplanets in the size range $1.25-2\ \mathrm{R}_\oplus$ without a H/He envelope. Observational studies suggest an upper cut-off radius of super-Earths at around $1.5-1.7\ \mathrm{R}_\oplus$ (e.g., Weiss & Marcy, 2014; Buchhave et al., 2014; Rogers, 2015). The low occurrence rate of close-in (orbital period $<$ 100 d) planets between $1.5-2\ \mathrm{R}_\oplus$ introduces a radius gap in this size range, suggesting two distinct classes of exoplanets, super-Earths and sub-Neptunes (Fulton et al., 2017). This radius gap further supports an upper limit on the size of super-Earths. About a third of the four thousand[1] exoplanets known to this day have a radius between $1-2\ \mathrm{R}_\oplus$ or a mass of less than $10\ \mathrm{M}_\oplus$ and can potentially be classified as super-Earths.

Mass and radius, which are the only observable properties for most super-Earths, are used to infer internal structure as well as surface and internal dynamics of exoplanets (e.g., Valencia et al., 2006; Seager et al., 2007; Wagner et al., 2011). In such studies, the mass-radius relations of solid exoplanets are computed based on assumptions about structure, composition and equation of state. The equations of state used in these studies are usually obtained by fitting material properties measured or computed at pressures of the Earth ($<$ 300 GPa). Since the central pressure of a super-Earth with $10\ \mathrm{M}_\oplus$ is $\sim$4 TPa, the application of these equations of state require extrapolations into pressure domains where the predicted material properties are not reliable and their usage can introduce significant errors on the interior properties of super-Earths (Wagner et al., 2011). Consequently, such errors would produce uncertainties in mass-radius relations, the extent of which has not been studied previously. Due to the scarcity in experimental data and knowledge of the stability of iron at pressures beyond those in center of the Earth (Grasset et al., 2009), the choice of an appropriate equation of state of iron for modeling the interior structure of super-Earths is non-trivial. With the help of Density Functional Theory (DFT), it becomes possible to reliably determine the equation of state and stability of a material phase at such high pressures beyond experimental limits (e.g., Stixrude, 2014).

In this study, we assess the importance of various sources of uncertainty related to the equation of state of iron, to unknown core and mantle compositions and temperature in

[1] http://exoplanetarchive.ipac.caltech.edu

mass-radius relations of super-Earths. We assume a rocky composition for super-Earths, i.e., silicate minerals in the mantle and iron alloys in the core; we ignore water, ices or atmospheres. Our composition and structural modeling framework is given in Sect. 2.2. For mantle mineralogy, we apply a self-consistent approach to thermodynamics. In Sect. 2.3, we develop a new equation of state of iron based on ab initio calculations within DFT at pressures relevant to the core of super-Earths and compare it with other equations of state from the literature. In Sect. 2.4, we demonstrate the effects of using extrapolations of equations of state of iron on mass-radius relations of super-Earths. We quantify the effects of temperature and core and mantle composition in Sect. 2.5. Observed super-Earths are plotted in a mass-radius diagram in order to illustrate the extent of uncertainties in determining their structure and composition. As an example, we quantify the effects of the choice of an equation of state of iron, temperature, core and mantle composition on the interior structure of Kepler-36b, a super-Earth with well-constrained mass and radius, in Sect. 2.6. Summary and conclusions are given in Sect. 2.7.

2.2 Modeling of interior structure and composition

2.2.1 Structure

Structural modeling of a planet requires the computation of thermoelastic properties that depend on pressure P and temperature T. We assume a fully differentiated planetary interior having two concentric spherical shells, mantle and core, with homogeneous chemical composition. Super-Earths might not all be differentiated due to miscibility of iron and silicates at very high temperatures as suggested by Wahl & Militzer (2015), and we will briefly discuss that possibility in Sect. 2.5.1, but focus on the interpretation of mass and radius in terms of a differentiated interior structure. The shells in our models are considered to be spherically symmetric and isotropic such that the material properties depend only on radius r. To compute the planetary mass we integrate the equation describing the hydrostatic equilibrium and Poisson's equation from the center to the surface (with radius R). The equations are written as:

$$\frac{dP}{dr} = -\rho g, \tag{2.1}$$

$$\frac{dg}{dr} = 4\pi G\rho - 2\frac{g}{r}, \tag{2.2}$$

where g is gravity, G is the gravitational constant and the density $\rho(P,T)$ is calculated using an equation of state as described below. The planet's mass is then: $M = R^2 g(R)/G$.

The heat transport mechanism in the mantle is mainly controlled by viscosity, thermal conductivity and thermal expansivity (e.g., Schubert et al., 2001). Since both viscosity and conductivity increase and expansivity decreases with pressure, it is expected that the vigor of convection decreases with depth. Whether the mantle of super-Earths is convecting as a whole or only partially is still debated as relevant transport and thermoeleastic properties

are not known. However, parameterized thermal (Stamenković et al., 2012; Wagner et al., 2012) and 2d numerical convection (Tackley et al., 2013) studies, using plausible assumptions about the pressure dependence of material properties, suggest that the deep mantle of large super-Earths is convecting but with a depth-increasing sluggishness, implying a superheated lower mantle with a strong super-adiabatic thermal gradient. For our modeling we will either assume an isentrope in the whole mantle or a temperature profile that follows an isentrope in the upper mantle and a super-adiabatic gradient in the lower mantle. Since there are indications for a strong increase of the viscosity of post-perovskite (ppv) with pressure (Tackley et al., 2013), we pin the transition to the super-adiabatic temperature at the depth of the transition to ppv. The effect of these assumptions on the mass-radius relation will be discussed in Sect. 2.5.1. A vigorously convective layer is essentially isentropic and the gradient of the temperature is then given by

$$\frac{dT}{dP} = \frac{\gamma}{K_S} T, \tag{2.3}$$

where γ is the Grüneisen parameter and K_S is the adiabatic bulk modulus. For a given potential temperature, we compute the temperature in the mantle either by solving Eq. (2.3) or by computing a path of constant-entropy associated with the mantle's composition directly (see below). The thickness of the lithosphere is neglected and we use the footing temperature of the isentrope (1650 K) as the surface temperature T_{S}.

As can be seen in Fig. 2.1, the melting temperature of $\mathrm{MgSiO_3}$ (Belonoshko et al., 2005) is much higher than the isentropic temperature of the mantle for pure $\mathrm{MgSiO_3}$ at all pressures. This simple comparison suggests that the mantles of super-Earths are likely to be solid, although higher core temperatures might imply molten lower mantles. A strong viscosity increase in the lower mantle due to high pressure and the presence of ppv may inhibit convection. Less efficient cooling of the core and lower mantle may then lead to higher temperatures. Nevertheless, our calculations assume a solid mantle.

The thermal state of the core is mainly determined by the heat flow from the core to the mantle and thus depends on the capacity of the mantle to cool. If the heat flow out of the core is larger than what can be conducted along an adiabat, the whole core is convecting; if it is smaller, the core is at least partially thermally stratified. The extent of the stratified layer is mainly controlled by internal energy sources of the core (e.g., latent heat and chemical energy) that depend on poorly constrained material properties, on the composition of the core, and on its cooling rate. For this reason, we consider two end-member cases: a core convecting as a whole and an isothermal core.

At the core-mantle boundary (CMB), we consider two extreme scenarios for core temperature. In the first case, we assume that there is no thermal boundary, corresponding to very efficient cooling of the core. In the second case, we assume that the temperature of the core at the CMB (T_{CMB}) is equal to the melting temperature of $\mathrm{MgSiO_3}$ (e.g., Stixrude, 2014), $T_{\mathrm{CMB}} = 1831\ \mathrm{K}(1 + P/4.6\ \mathrm{GPa})^{0.33}$ (Belonoshko et al., 2005). Such an assumption combined with an isentropic mantle leads to an extreme temperature jump of $\sim$2500$-$7000 K

depending on the mantle temperature at the CMB. These values are higher than the temperature jumps of 800−2000 K used by Sotin et al. (2007); Valencia et al. (2007a); Wagner et al. (2011) and serve as upper bounds in our study.

We solve for P and g using Eqs. (2.1), (2.2) and an equation of state corresponding to the composition of the core or the mantle. We apply six boundary conditions: $g(0) = 0$, $P(R) = 0$ and $T_{\rm S} = 1650$ K, two conditions expressing the continuity of P and g at the CMB; T at the CMB is either continuous or equal to the melting temperature of the mantle. In calculations of model super-Earths, we fix R and the core radius fraction $r_{\rm CMB}$ to compute M. In calculations of a super-Earth with given M and R, we compute $r_{\rm CMB}$.

2.2.2 Mantle modeling

In the context of rocky exoplanets, the mantle is commonly assumed to be made of MgO end-member silicate minerals and the composition is usually assumed to be $\rm MgSiO_3$ or $\rm Mg_2SiO_4$ (e.g., Seager et al., 2007; Wagner et al., 2011). However, a mantle with only MgO and $\rm SiO_2$ is unlikely to appear in nature. Mantle minerals are expected to also incorporate oxides CaO, FeO and $\rm Al_2O_3$ in addition to MgO and $\rm SiO_2$, the CFMAS system, which makes up for about 99 wt% of the bulk silicate Earth (Javoy et al., 2010). Neglecting FeO, CaO and $\rm Al_2O_3$ bearing minerals that could be present in significant amounts and which mostly have higher densities than the end-member minerals in the MgO−$\rm SiO_2$ system, would create a bias in the inference of the exoplanet's interior structure from mass and radius. Valencia et al. (2006) therefore evaluated the effect of FeO on the planetary structure by adding up to 10 wt% of FeO to $\rm Mg_2SiO_4$ in the upper mantle and to $\rm MgSiO_3$ in the lower mantle.

The exact oxide content of the mantle depends on several factors including stellar composition, origin of the building blocks in the protoplanetary disk, planetary migration, the degree of differentiation in the planet and redox conditions in the mantle (e.g., Bond et al., 2010b; Carter-Bond et al., 2012b; Dorn et al., 2015; Schaefer et al., 2017; Santos et al., 2017). Although data are currently missing to accurately assess realistic ranges in compositions of exoplanetary mantles, significant deviations with respect to the mantle compositions of the terrestrial planets of the solar system are to be expected. Rocky exoplanets can for example be extremely depleted in Mg compared to the Earth, as has been shown by N-body simulations for the HD17051 and HD19994 planetary systems by Carter-Bond et al. (2012a). Here we consider five different end-member compositions: $\rm MgSiO_3$, $\rm FeSiO_3$, $\rm Mg_2SiO_4$, $\rm Fe_2SiO_4$ and $\rm SiO_2$, thereby extending the range of mantle compositions with respect to previous studies. The FeO end-members of olivine and bridgmanite, although much less likely than MgO end-members, represent an upper bound on the mantle density as they are the highest density minerals in the respective solid solutions (Stixrude & Lithgow-Bertelloni, 2011).

Phase relations and physical properties of mantle minerals are evaluated self-consistently using a new implementation (Chust et al., 2017) of the thermodynamic model of Stixrude & Lithgow-Bertelloni (2011) based on a Birch-Murnaghan Mie-Grüneisen equation of state formulation. At least for density, the central property we are interested in, the model shows ro-

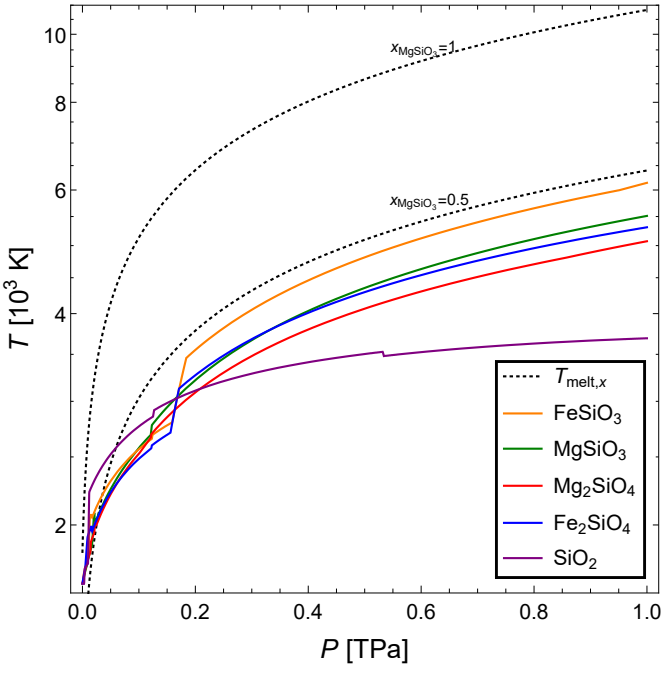

Figure 2.1: Isentropes of the mantle mineralogy computed thermodynamically self-consistently with $T_\mathrm{S} = 1650$ K. All relevant phases of Mg_2SiO_4, Fe_2SiO_4, $MgSiO_3$, $FeSiO_3$ and SiO_2 are taken into account. Dotted lines represent the melting temperature of $MgSiO_3$, $T_\mathrm{melt} = 1831\ \mathrm{K}(1 + P/4.6\ \mathrm{GPa})^{0.33}$ (Belonoshko et al., 2005) with the cryoscopic equation $T_{\mathrm{melt},x} = T_\mathrm{melt}(1 - \ln x_{\mathrm{MgSiO_3}})^{-1}$ (Atkins, 1994), where $x_{\mathrm{MgSiO_3}}$ is the mole fraction of pure $MgSiO_3$.

bust behavior beyond the $P-T$ conditions of the lowermost mantle (Connolly & Khan, 2016). From the database of Stixrude & Lithgow-Bertelloni (2011), we use MgO, the SiO_2 phases as well as the MgO- and FeO-bearing end-members of all silicate solid solutions to compute assemblages for the compositions given above. As the database of Stixrude & Lithgow-Bertelloni (2011) is only assessed for conditions (and minerals) of the Earth's mantle and ignores phase transitions at higher pressures, such as the dissociation of post-perovskite (ppv) (e.g., Umemoto & Wentzcovitch, 2011; Wu et al., 2014) or the B1-B2 transition in MgO (e.g., Cebulla & Redmer, 2014), we investigate an alternative scenario for mantle structure (Sect. 2.5.3), taking high-pressure phases and transitions from Umemoto & Wentzcovitch (2011) into account.

The isentropes associated with the five model compositions and the potential temperature of 1650 K are shown in Fig. 2.1. Isentropes show T-discontinuities at phase transitions with significant Clausius-Clapeyron slopes through volume changes and latent heat effects. Mostly, temperatures increase as different compositions undergo phase transitions with positive Clapeyron slopes. The perovskite$-$ppv transition in the $MgSiO_3$ and Mg_2SiO_4 composi-

tions in the vicinity of 100 GPa are such an example. The melting temperature of $MgSiO_3$ is higher than the temperatures along the isentropes of $MgSiO_3$ and Mg_2SiO_4, implying a solid mantle for super-Earths. The larger T-jumps for the FeO-bearing compositions at a pressure between 150−200 GPa stem from the formation of the $FeSiO_3$ ppv phase from a combination of SiO_2 seifertite and FeO wüstite, as the $FeSiO_3$ perovskite phase is predicted stable only at temperatures below 1500 K. For an SiO_2-only mantle, the stishovite-seifertite transition between 100−150 GPa leads to a temperature increase, but stishovite is then predicted to form again near 500 GPa with a negative Clapeyron slope and a slight temperature decrease. The re-appearance of stishovite is a numerical artifact of the database calibration, and a proper description of an SiO_2-based mantle would require an explicit consideration of the predicted high-pressure phases (Tsuchiya & Tsuchiya, 2011; Umemoto & Wentzcovitch, 2011). However, based on our discussion in Sect. 2.5.3, such a consideration will not strongly affect the overall structure of super-Earths.

2.2.3 Core modeling

Iron is ubiquitously assumed to be the major element in the core of super-Earths (e.g., Seager et al., 2007; Wagner et al., 2011). To compute the density of Fe at relevant conditions, previous studies have extrapolated different formulations of the equation of state of Fe which are strictly speaking only valid within the pressure range of their assessment (see Table 2.7). For instance, the Vinet formulations of Valencia et al. (2007a) and Seager et al. (2007) and the third-order Birch-Murnaghan (BM3) formulation of Dorn et al. (2015) are fitted to data of Fe up to pressures of 200−300 GPa but extrapolated to 5−20 TPa. Neither the Vinet nor BM3 equations have extrapolations that are thermodynamically consistent to infinite pressure (e.g., Holzapfel, 1996; Stacey, 2005). Seager et al. (2007) switch to a Thomas-Fermi-Dirac equation of state at 20.9 TPa that is valid at in the infinite pressure limit. Wagner et al. (2011) have used the modified Rydberg equation (Stacey, 2005) and fitted the data from Dewaele et al. (2006), obtained between 17 and 197 GPa. Extrapolation to several tens of TPa will result in significantly different density predictions, depending on the equation used, even when those equations approach a thermodynamically consistent limit at infinite pressure. For this reason, we calculated an equation of state of iron for super-Earths (SEOS) up to 137 TPa with ab initio methods. With this equation of state the core of Earth-mass and ultra-massive super-Earths can be modeled without using a biasing extrapolation scheme. Details are discussed in Sect. 2.3.1.

For the Earth's core, Fe accounts for about 85 wt% and the remainder consists of Ni and light elements. For the light elements in the Earth's core, there is no consensus on their amount and identity. A recent synthesis of different studies about the composition by Hirose et al. (2013) suggest: Si=6 wt%, O=3 wt% and S=1-2 wt%. Also, the possibility of C as a light element in the Earth's core cannot be ruled out (Fei & Brosh, 2014). In order to evaluate the effect of potentially important light elements in the core on mass-radius relations, we consider two approaches, reflecting the combined effects of Ni and light elements. First, we assume a decrease in density of the core with respect to pure iron by 10%, similar to the Earth's core; we also consider a decrease in density of 20%, i.e., we assume the core

density to be either 0.9ρ Fe or 0.8ρ Fe. Second, in order to be able to assess the effect of the presence of specific light elements, we assume that the core is made of either of the following Fe-alloys: FeS, FeSi, $Fe_{0.95}O$, Fe_3C (see Table 2.5). For details about the equations of state, see Appendix 2.D.

The melting curve of iron is steeper than a core isentrope at super-Earth pressures, suggesting that the core of massive super-Earths is solid if the temperature at the core-mantle boundary is below the melting temperature (Morard et al., 2011). The effect of light elements on the melting temperature of Fe at super-Earth core conditions is not known, but a maximal depression of 1500 K at 1.5 TPa has been proposed (Morard et al., 2011). The melting temperature of such an alloy is then above 13 000 K at 1.5 TPa and thus significantly above the predicted temperature at that pressure in super-Earth cores (Valencia et al., 2006; Wagner et al., 2012), indicating a solid core. Several factors including a sluggish or non-convecting lower mantle, warm initial conditions and a high temperature jump at the CMB (Stixrude, 2014) would allow for significantly higher core temperatures. Nevertheless, since the density deficit between the solid and the liquid state decreases with pressure (Alfè et al., 2002b) and is about 1−2% at the inner core boundary conditions of the Earth (Alfè et al., 2002a; Laio et al., 2000; Ichikawa et al., 2014), the use of an equation of state describing the density of solid iron has likely a negligible effect on mass-radius relations.

2.2.4 Mass-radius relations based on core size

Since mass and radius are currently the only observable parameters for most of the rocky exoplanets, mass-radius ($M-R$) relations are used to obtain a first-order estimate of their composition. Theoretical $M-R$ relations of rocky planets have been computed for isothermal planetary interiors (e.g., Zapolsky & Salpeter, 1969; Seager et al., 2007) and temperature increasing with depth (e.g., Valencia et al., 2006; Fortney et al., 2007; Sotin et al., 2007; Wagner et al., 2011). Simple power-law relations are generally used for super-Earths:

$$R = aM^{\beta}, \tag{2.4}$$

where R and M are in Earth units, β is the scaling exponent and a is the proportionality constant. β determines how the radius increases with mass: the larger β, the bigger are planets for the same mass. For small bodies whose internal density is not affected by pressure, $\beta = 1/3$. For larger planetary bodies, adiabatic self-compression leads to a slower increase of radius with mass and therefore smaller β.

Since the core size has a direct impact on planetary mass and bulk density, we calculate $M-R$ relations for three classes of rocky super-Earths: Mercury-like, Earth-like and Moon-like by fixing core radius fractions to 0.8, 0.5 and 0.2, respectively. These values are similar to those of Mercury (0.82), the Earth (0.54) and the Moon (0.21) (e.g., Dziewonski & Anderson, 1981; Garcia et al., 2011; Hauck et al., 2013; Rivoldini & Van Hoolst, 2013). Our definition of rocky super-Earth classes contrasts with most previous studies (e.g., Valencia et al., 2006; Wagner et al., 2011) in which the core mass fraction and essentially the bulk

elemental composition of an exoplanet class is constant but the relative core radius changes along a $M-R$ relationship. With our definition, the bulk composition of super-Earths of a given class slightly varies with mass (e.g., elemental abundance of Mg changes by <2 wt%) since the relative core radius is constant. This difference results in small differences of the order of $1-4$% in the β values of the $M-R$ relations. In order to be able to make consistent comparisons with the literature, we recompute β values for previous studies based on the same interior structure assumptions as in our work (see Table 2.2). We also compute $M-R$ relations for bare-core super-Earths since observations suggest their existence (Mocquet et al., 2014). Such a calculation provides an upper bound on the masses of super-Earths as a function of radius.

2.3 A new ab initio equation of state of hcp-Fe

2.3.1 Formulation of SEOS

Laser-heated diamond-anvil cell experiments (Sakai et al., 2011) show that the crystal structure of pure Fe at the conditions of the Earth's core is hexagonal close-packed (hcp). However, high core temperatures (Belonoshko et al., 2017), the presence of nickel (Dubrovinsky et al., 2007) and light elements in the core (Vočadlo et al., 2003) could stabilize the body-centered cubic (bcc) phase over hcp at the Earth's inner-core conditions. The exact crystal phase of the Earth's inner core remains a matter of extensive debate, but hcp-Fe is the most plausible candidate (e.g., Hirose et al., 2013).

Ab initio crystal structure predictions at zero temperature show that hcp-Fe is more stable than bcc and face-centered cubic (fcc) up to 8 TPa and between $24-35$ TPa (e.g., Pickard & Needs, 2009; Cottenier et al., 2011), and this remains true up to at least 10 000 K (Stixrude, 2012). Between $8-24$ TPa, the fcc phase is stable and above 35 TPa the bcc phase takes over. Since the expected core pressures in Earth-like super-Earths are likely below 10 TPa (Wagner et al., 2011), their cores would be dominated by hcp-Fe if they are pure Fe and at zero temperature. However, as already mentioned, high temperature and alloying elements will likely change the stability fields of different phases. The exact phase at TPa pressures is probably not very important for mass-radius relations of super-Earths since the density difference between the crystal phases of iron is expected to be small, especially for the closed-packed phases. According to the calculations in Cottenier et al. (2011), at 350 GPa fcc is 0.05% less dense than hcp, while bcc is 1.2% less dense. At higher pressures, density differences remain small: At 8 TPa, fcc and bcc are denser than hcp by less than 0.1%. For this reason, we approximate iron in the core of super-Earths as the hcp phase.

Here we perform Density Functional Theory (DFT)-based calculations for hcp-Fe in the volume range of $0.50-6.79$ $\mathrm{cm}^3/\mathrm{mol}$, to cover the whole compression range relevant for the cores of super-Earths. For high precision, we use the all-electron augmented plane wave method with local orbitals (APW+lo) (Sjöstedt et al., 2000; Madsen et al., 2001; Cottenier, 2002; Schwarz et al., 2010) with the PBE approximation to the exchange and correlation functional (Perdew et al., 1996). Within the APW+lo approach, we treat the $3s$, $3p$, $3d$, $4s$, $4p$ states as valence electrons. The muffin tin radius for the Fe-atoms was set to 1.6 au, and

the size of the APW+lo basis specified by $K_{\max}$ = 8.5/1.6 au = 5.31 au^{-1}. Brillouin zone integration used a mesh of 42 × 42 × 22 k-points. Calculations were performed both for non spin-polarized and spin-polarized charge densities, using the type II spin arrangement of Steinle-Neumann et al. (2004). At each volume, the c/a ratio was optimized and we found an increase with compression from 1.5858−1.6165 in the range from 0−2.5 TPa (1.6033 at 350 GPa).

From the energy-volume relation of 181 values (see Supplement) pressure is computed as the first derivative numerically. We employ an averaged 2-point backward and forward scheme that takes into account the uneven volume sampling. We chose this strategy, as the energy-volume range sampled by our calculations is too large to be adequately fit with a single closed expression (Fig. 2.10). Without a closed expression for the equation of state, we obtain volumes at given pressure by an interpolation scheme: this is done with a method that uses a sliding-window to locally fit a finite strain expression (see Appendix 2.C for a detailed description).

In previous studies, several methods within the framework of DFT have been applied to calculate the equation of state of hcp-Fe, almost always with the Perdew-Burke-Ernzerhof (PBE) exchange-correlation functional or closely related ones and with a variety of numerical solvers. Our results at zero pressure (Table 2.6) are in good agreement with published values, and the small differences are what can be expected when comparing different DFT codes (Lejaeghere et al., 2016a). Our density results are in excellent agreement with those of Pickard & Needs (2009) over a broad pressure range (cf. Fig. 1, Cottenier et al., 2011) and differ by less than 0.2% with the results of Stixrude (2012) at 6 and 38.3 TPa. The accuracy of DFT (PBE) predictions for a ground state equation of state (equilibrium volume or density, bulk modulus) have been assessed by Lejaeghere et al. (2013, 2016b). In particular when the bulk modulus is large, as in the present work, the uncertainty on the predicted density becomes negligibly small (Lejaeghere et al., 2016b).

Measurements of compression data at room temperature provide a reliable equation of state for iron up to almost 300 GPa (e.g., Fei et al., 2016): the third-order Birch-Murnaghan equation (BM3) used to summarize new and previous experimental data have pressure residuals that are not much larger than 2%. A fit of the same data to a Vinet equation (e.g., Poirier, 2000) results in similar residuals and the predicted bulk moduli from both equations are equivalent (see Fig. 2.9). The induced uncertainty on the parameters of the BM3 equation by the data uncertainties results in an error on density that is smaller than 0.5% and that on the bulk modulus is smaller than 1% at 300 GPa. In order to use the laboratory measurements together with the DFT results, the former have been extrapolated to 0 K (Fei et al., 2016) and zero-point vibration effects have been removed (Lejaeghere et al., 2014). The equations based on prior experimental data (e.g., Williams & Knittle, 1997; Anderson et al., 2001; Dewaele et al., 2006) show deviations from the equation of state of Fei et al. (2016) and SEOS (based on the same low pressure data) that are larger than 0.5% (Fig. 2.2) because they have either been deduced from smaller data sets or/and the uncertainties on those data were larger.

Our DFT results for hcp exhibit the well known pressure underestimation of about 8% at small compressions (Steinle-Neumann et al., 2004; Fei et al., 2016) (Fig. 2.11), an effect that cannot be explained by thermal pressure alone (less than 1%) and for which dynamical many-body effects beyond DFT need to be invoked (Pourovskii et al., 2014). This discrepancy is larger than what is usually obtained using DFT at the PBE level, including for bcc-Fe where the agreement with experiments is excellent (see Lejaeghere et al., 2014). After correcting laboratory data of hcp-Fe for thermal effects, densities become comparable to DFT results near 200 GPa. At pressures higher than 300 GPa, and depending on the formulation used to summarize the experimental data, extrapolated pressures grow weaker or stronger than our DFT results with compression (see Fig. 2.2 and discussion below). Therefore, we use the experimental equation of state of hcp iron for pressures up to 234 GPa, the pressure where laboratory data and our DFT results intersect, and our DFT results for pressures above. A discontinuity in K_T of $\sim$10% between the experimental equation of state and our DFT results has a negligible effect on mass-radius relations and a small effect on the thermal state of the core.

In addition to the numerical determination of SEOS that we have introduced above, we include, for convenience, a closed equation of state that is valid for pressures above 234 GPa. When the Holzapfel equation (Holzapfel, 1996) is fitted to our ab initio results in the pressure range 0.234$-$10 TPa, the volume residuals are below 1.1%, whereas fits with BM3 or Vinet equations have residuals that are 4 to 8 times larger. The Holzapfel equation is written as

$$P = P_0 + 3K_{T,0}x^{\frac{-5}{3}}(1-x^{\frac{1}{3}})[1+c_2x^{\frac{1}{3}}(1-x^{\frac{1}{3}})]\exp[c_0(1-x^{\frac{1}{3}})], \tag{2.5}$$

where $x = V/V_0$, $V_0 = 4.28575$ cm^3/mol, $P_0 = 234.4$ GPa, $K_{T,0} = 1145.7 \pm 3.6$ GPa, $c_0 = 3.19 \pm 0.08$ and $c_2 = -2.40 \pm 0.05$.

2.3.2 Thermal pressure

Total pressure can be divided into a cold (isothermal) part (discussed above), and two temperature-dependent (thermal) parts: $P(V,T) = P(V, 0\text{ K}) + P_{\rm harm}(V,T) + P_{\rm ae}(V,T)$, where $P_{\rm harm}$ is the quasiharmonic thermal pressure and $P_{\rm ae}$ is the anharmonic-electronic thermal pressure. For the quasiharmonic thermal pressure, phonon calculations can be performed (e.g., Vočadlo et al., 2008; Stixrude, 2012) or approximated by the Debye (e.g., Dewaele et al., 2006; Fei et al., 2016) or Einstein models (e.g., Bouchet et al., 2013). At high temperatures in the core of super-Earths, well above the Debye temperature, the Einstein and Debye models practically coincide (Poirier, 2000). Following Bouchet et al. (2013), we use the simpler Einstein model to compute $P_{\rm harm}$ and the Einstein temperature Θ:

$$P_{\rm harm}(V,T) = \frac{3R\gamma}{V}\left[\frac{\Theta}{2} + \frac{\Theta}{\exp(\Theta/T)-1}\right], \tag{2.6}$$

$$\Theta = \Theta_0 x^{-\gamma_\infty} \exp\left[\frac{\gamma_0 - \gamma_\infty}{b}(1 - x^b)\right], \tag{2.7}$$

with the Grüneisen parameter $\gamma = \gamma_\infty + (\gamma_0 - \gamma_\infty)x^b$, where R is the universal gas constant, b is a constant and $x = V/V_0$. The approach of Bouchet et al. (2013) reproduces the experimental P-V-T equation of Dewaele et al. (2006) well that is fit to static and shock wave experiments as well as ab initio simulations. The anharmonic-electronic thermal pressure is given as

$$P_{\mathrm{ae}}(V,T) = \frac{3R}{2V} m a_0 x^m T^2, \tag{2.8}$$

where m and a_0 are constants.

For both the harmonic and anharmonic-electronic thermal pressure we use the parameter values estimated by Bouchet et al. (2013) (see Table 2.7). Since our reference volume V_0 is not the same as that of Bouchet et al. (2013), we replace x in the equations for the quasiharmonic and anharmonic-electronic thermal pressures by $x(V_0/V_{0,\mathrm{Bouchet}})$. With this modification, the thermal pressure is equal to that of Bouchet et al. (2013) for a given volume V.

The isothermal bulk modulus K_T, the isobaric thermal expansivity α and the adiabatic bulk modulus K_S are given by

$$K_T = -V\left(\frac{\partial P(V,T)}{\partial V}\right)_T, \tag{2.9}$$

$$\alpha = \frac{1}{V}\left(\frac{\partial V}{\partial T}\right)_P, \tag{2.10}$$

$$K_S = K_T(1 + \alpha\gamma T). \tag{2.11}$$

2.3.3 Comparison of extrapolations of the equations of state of iron

We compare previously published equations of state of Fe (see Table 2.7) with our equation of state for super-Earths (SEOS) in the pressure range 0.234−10 TPa at 0 K. The various equations determined at a finite temperature were corrected to 0 K according to the method described in the respective articles and the zero-point vibration effects have been removed.

The BM3, Vinet, modified Rydberg and Holzapfel equations describe compression data with similar precision below 0.3 TPa if no prior assumption on equation parameters are made

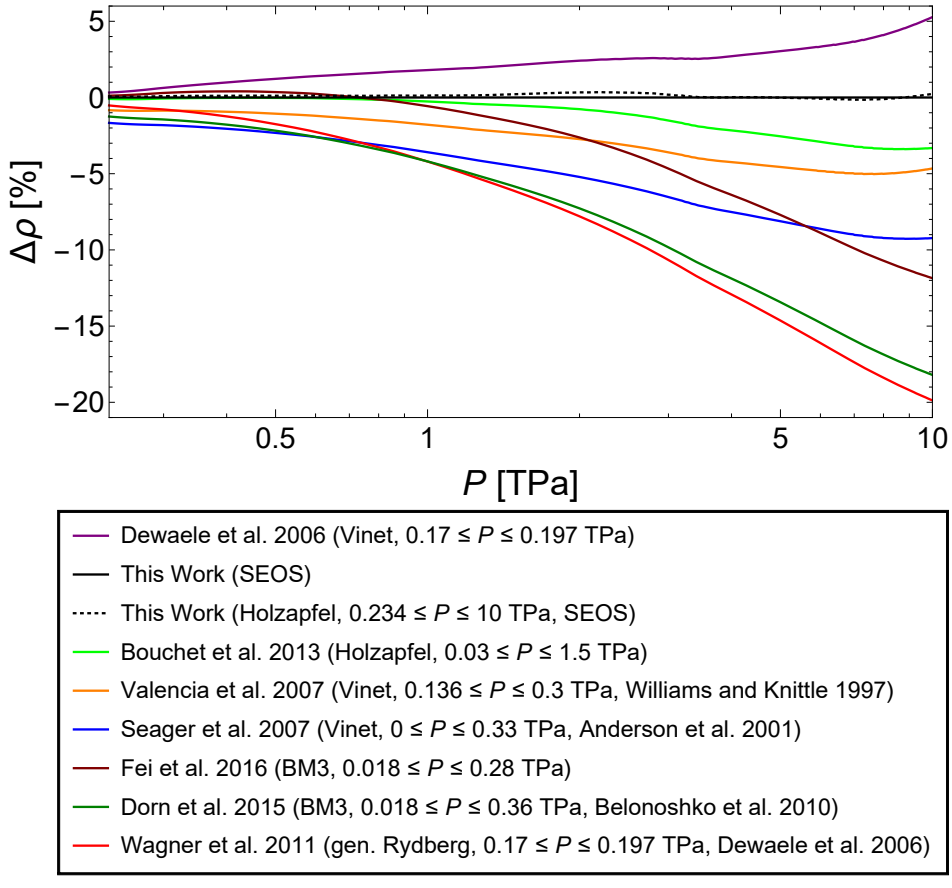

Figure 2.2: Comparison of the relative density difference in percent for equations of state of iron listed in Table 2.7 and for the Holzapfel fit to SEOS up to 10 TPa relative to SEOS at 0 K in the pressure range of 0.234−10 TPa. These equations of state are indicated by references, the form of the equation used, the pressure range of the fit and, if applicable, the source of the data.

(see Appendix 2.A), but extrapolation yields significantly different predictions at high pressures (see Fig. 2.2). Among those equations, the modified Rydberg and Holzapfel equations show a consistent thermodynamic behavior at infinite pressure and should therefore be used if large pressure extrapolations are required. The relevance of this behavior is illustrated by the equation of state from Bouchet et al. (2013) at 10 TPa (Fig. 2.2). Its density deviates by not much more than 3% from SEOS. In principle, a similar precision could be obtained with the modified Rydberg equation (see Appendix 2.B), but the large deviations exhibited by the equation of state from Wagner et al. (2011) at 10 TPa (Fig. 2.2) is the result of their choice of a specific value for the derivative of the bulk modulus at infinite pressure prior to fitting the laboratory data of Dewaele et al. (2006).

Table 2.1: Interior structure parameters and differences in planetary mass between SEOS and other equations of state of iron for different core sizes and planetary radii. Differences below 0.05% are not reported. Models assume an isentropic pure Fe core, an isentropic $MgSiO_3$ mantle, $T_S = 1650$ K and a zero CMB T-jump.

Ref.	Form.	Parameter	Bare-core	Mercury-like	Earth-like	Moon-like	Bare-core	Mercury-like	Earth-like	Moon-like
		$r_{\rm CMB}$	1	0.8	0.5	0.2	1	0.8	0.5	0.2
		R ($R_\oplus$)	1.25				1.75			
SEOS	–	$P_{\rm c}$ (TPa)	4.6	2.5	0.9	0.3	37.8	16.8	4.0	1.2
		$P_{\rm th,c}/P_{\rm c}$	3%	4%	7%	11%	1%	2%	4%	6%
		$P_{\rm ae,c}/P_{\rm th,c}$	14%	17%	20%	22%	8%	12%	16%	19%
		$T_{\rm c}$ (10^3 K)	8.6	7.2	5.1	3.7	18.2	15.4	9.1	5.8
		$\rho_{\rm c}$ ($\rm Mg/m^3$)	30.4	24.4	17.7	13.6	66.1	48.9	28.8	19.1
		M_{core}/M	100%	79.3%	31.0%	2.4%	100%	83.0%	33.7%	2.4%
		M ($M_\oplus$)	6.5	4.0	2.2	1.7	33.6	18.7	8.4	5.9
Dew	Vin	ΔM	+1%	+1%	+0.5%	–	+13%	+10%	+1.6%	+0.2%
Bou	Hol	ΔM	−1%	−1%	–	–	−6%	−5%	−0.8%	–
Val	Vin	ΔM	−2%	−1%	–	–	−7%	−7%	−1.7%	–
Sea	Vin	ΔM	−5%	−3%	–	–	−18%	−14%	−3.1%	–
Fei	BM3	ΔM	−3%	−1%	+0.5%	–	−22%	−14%	−1.9%	–
Dor	BM3	ΔM	−13%	−7%	−1.4%	–	−34%	−23%	−5.7%	−0.2%
Wag	Ryd	ΔM	−12%	−6%	−1.4%	–	−35%	−24%	−6.0%	−0.2%

Abbreviations: SEOS: Super-Earths equation of state, This Work, $P_{\rm th}$ from Bouchet et al. (2013); Dew: Dewaele et al. (2006); Bou: Bouchet et al. (2013); Val: Valencia et al. (2007a), data from Williams & Knittle (1997); Sea: Seager et al. (2007), data from Anderson et al. (2001); Fei: Fei et al. (2016); Dor: Dorn et al. (2015), data from Belonoshko et al. (2010); Wagner et al. (2011), data from Dewaele et al. (2006); Vin: Vinet; BM3: third-order Birch-Murnaghan; Hol: Holzapfel; Ryd: modified Rydberg.

Extrapolations with the Vinet formulation depart by more than 5% from SEOS at 10 TPa (Fig. 2.2) and deviations increase further with pressure. The large variations between the equations of state by Dewaele et al. (2006), Seager et al. (2007) and Valencia et al. (2007a) at high pressure are the result of the different data sets used (see Table 2.7). Among the equations considered, the BM3 equation is the least well suited for large pressure extrapolation (see Appendix 2.A) and should be avoided. Note, however, that extrapolation of the equation of state up of Fei et al. (2016) to 1 TPa results in a density less than 0.5% different from that of SEOS. This is a consequence of the extensive and precise data set used to fit the BM3 equation.

2.4 Effect of the iron equation of state on $M-R$ relations

To assess the effect of the choice of an equation of state of iron on the $M-R$ relations of rocky super-Earths, we have calculated the masses of Moon-like, Earth-like, Mercury-like and bare-core super-Earths with radius between $1-2$ $\mathrm{R}_\oplus$ by solving the interior structure equations (Table 2.1 and Fig. 2.3). For the purpose of this argument, the core and mantle compositions are approximated to be pure Fe and MgSiO_3. We use $T_\mathrm{S} = 1650$ K and ignore a temperature jump due to the thermal boundary layer at the CMB. Temperature profiles within the core and mantle are considered to be isentropic. We perform these calculations using SEOS and other equations of state of iron as discussed above.

Central density, temperature and pressure increase with the core radius fraction and with planetary radius (Table 2.1). The core mass fractions of Moon-like, Earth-like and Mercury-like super-Earths are in the range $2-3$%, $29-36$% and $76-83$%, respectively. Thermal contributions to total pressure decrease with increasing central pressure. Similarly, the anharmonic-electronic contribution to thermal pressure decreases, but remains at a 10% level. It decreases the density by 1.6% at zero pressure and by 0.1% at 10 TPa. The resulting effects on $M-R$ relations are not discernible.

Differences in computed planetary masses for different equations of state of iron are negligible for the Moon-like scenarios and R=1.25 $\mathrm{R}_\oplus$, but they generally increase with increasing central pressure (Table 2.1). For the same planetary radius and larger core size, the mass predicted with some equations (Dorn et al., 2015; Wagner et al., 2011) reach differences by as much as -12% for a bare core planet. When increasing the planetary radius from 1.25 to 1.75 $\mathrm{R}_\oplus$, differences are already noticeable for the smallest core radius fraction, and generally increase by a factor of 2-3 with core size; only for the equation of state by Dewaele et al. (2006) differences increase more strongly. All planetary models based on the equation of state of Dewaele et al. (2006) and some of the 1.25 $\mathrm{R}_\oplus$ Earth- and Mercury-type models (based on the equations from Bouchet et al. (2013), Fei et al. (2016) and Seager et al. (2007)) yield a larger planetary mass due to larger densities over the relevant $P-T$ range. This difference either stems from the isothermal equation of state (Fig. 2.2) or a smaller thermal pressure contribution than in SEOS. A comparison of differences in $M-R$ relation over a wider size range (Fig. 2.3) confirms this trend.

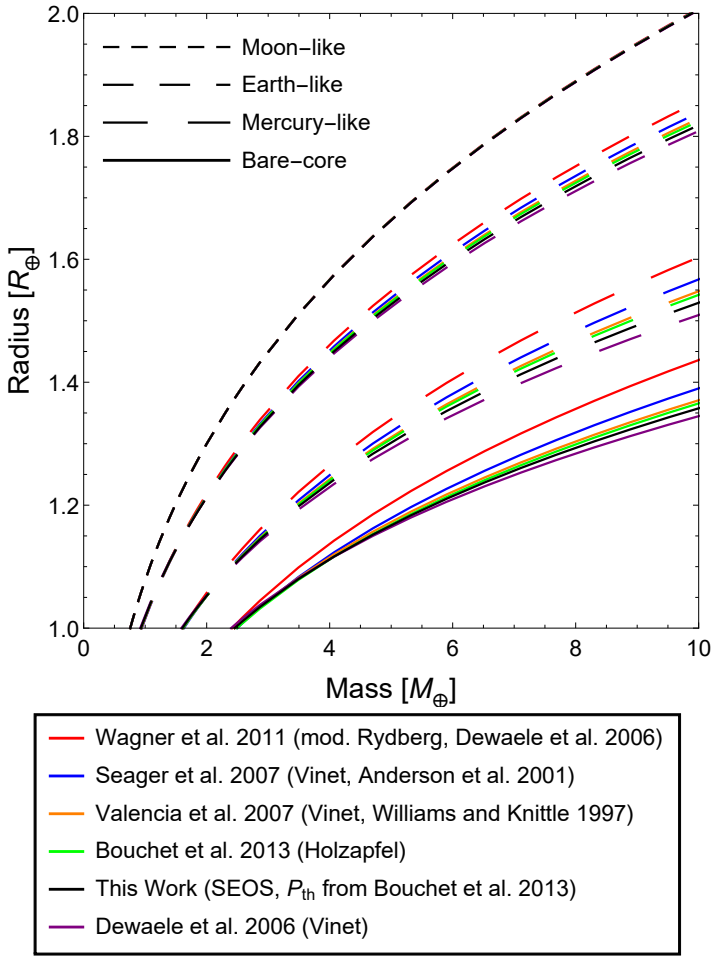

Figure 2.3: Effects of selected equations of state of Fe from Table 2.7 on the mass-radius relations of four classes of super-Earths with fixed core radius fractions.

Looking at the effect of different equation of state formulations for iron on the mass of super-Earths with an Earth-like core ratio, Wagner et al. (2011) found a difference of 2% in radius for 10 $\mathrm{M}_\oplus$, using modified Rydberg and Keane equations, based on the same experimental data of iron from Dewaele et al. (2006). Interestingly, we find that the use of the Vinet equation of Dewaele et al. (2006), still based on the same data, leads to a smaller radius by 3% compared to the modified Rydberg equation from Wagner et al. (2011) for a 10 $\mathrm{M}_\oplus$ Earth-like model. As explained above, this discrepancy stems from their choice of a specific value for the derivative of the bulk modulus at infinite pressure.

The differences in radii calculated using the two equations of state of iron with maximum density difference are 1% and 2% (M=1 $\mathrm{M}_\oplus$), 2% and 4% (M=5 $\mathrm{M}_\oplus$), and 3% and 6% (M=10 $\mathrm{M}_\oplus$) for Earth-like and Mercury-like super-Earths, respectively. Such differences result in significant variations for the exponent β in the mass-radius scaling law (Eq. 2.4), and values for β can vary by as much as 10% (Table 2.2). These differences are a consequence of extrapolations of the equations meant to be used up to the pressures of ∼0.3 TPa. Since the Holzapfel equation from Bouchet et al. (2013) needs to be extrapolated starting at 1.5 TPa, its $M-R$ curves diverge significantly from those based on SEOS for super-Earths with larger cores or larger planetary radii only (Fig. 2.3).

Table 2.2: Mass-radius relation scaling exponent β, calculated using different equations of state of Fe. Models assume an isentropic pure Fe core, an isentropic $\mathrm{MgSiO_3}$ mantle, T_S = 1650 K and a zero CMB T-jump. Our calculations for β values, using the equations of state from the studies listed below, are performed by fixing the core radius fraction. In the mass-radius relation, $R/R_\oplus = a(M/M_\oplus)^\beta$, a is 0.82, 0.89, 1.02 and 1.08 for bare-core, Mercury-like, Earth-like and Moon-like super-Earths, respectively.

Equation of state	Bare-core	Mercury-like	Earth-like	Moon-like
r_CMB	1	0.8	0.5	0.2
SEOS, P_th from Bouchet et al. (2013)	0.218	0.232	0.252	0.270
Dewaele et al. (2006), Vinet	0.207	0.224	0.248	0.269
Bouchet et al. (2013), Holzapfel	0.224	0.238	0.253	0.270
Valencia et al. (2007a), Vinet[a]	0.225	0.240	0.255	0.270
Seager et al. (2007), Vinet[b]	0.237	0.248	0.258	0.270
Fei et al. (2016), BM3	0.242	0.248	0.257	0.270
Dorn et al. (2015), BM3[c]	0.251	0.255	0.260	0.270
Wagner et al. (2011), mod. Rydberg[d]	0.255	0.259	0.262	0.270

Abbreviations: P_th: Thermal Pressure. BM3: third-order Birch-Murnaghan equation.
Data source: [a] Williams & Knittle (1997), [b] Anderson et al. (2001), [c] Belonoshko et al. (2010), [d] Dewaele et al. (2006).

2.5 Effects of temperature and composition on $M-R$ relations

2.5.1 Temperature

Since the temperature profile in super-Earths is not well constrained, it is important to assess the effect of uncertainties in temperature on the structure of super-Earths. Previous studies indicate a relatively minor effect (e.g., Sotin et al., 2007; Grasset et al., 2009). Here we re-evaluate this effect for some of the temperature assumptions described in Sect. 2.2.

For Moon-like models, a change in the temperature profile in the core from isentropic to isothermal reduces the central temperature by 200−600 K and has a negligible impact on mass. For Earth-like and Mercury-like models, the differences between the isentrope and isotherm in the center are 1000−4500 K and 2500−10000 K and masses by up to 1% and 2%, respectively.

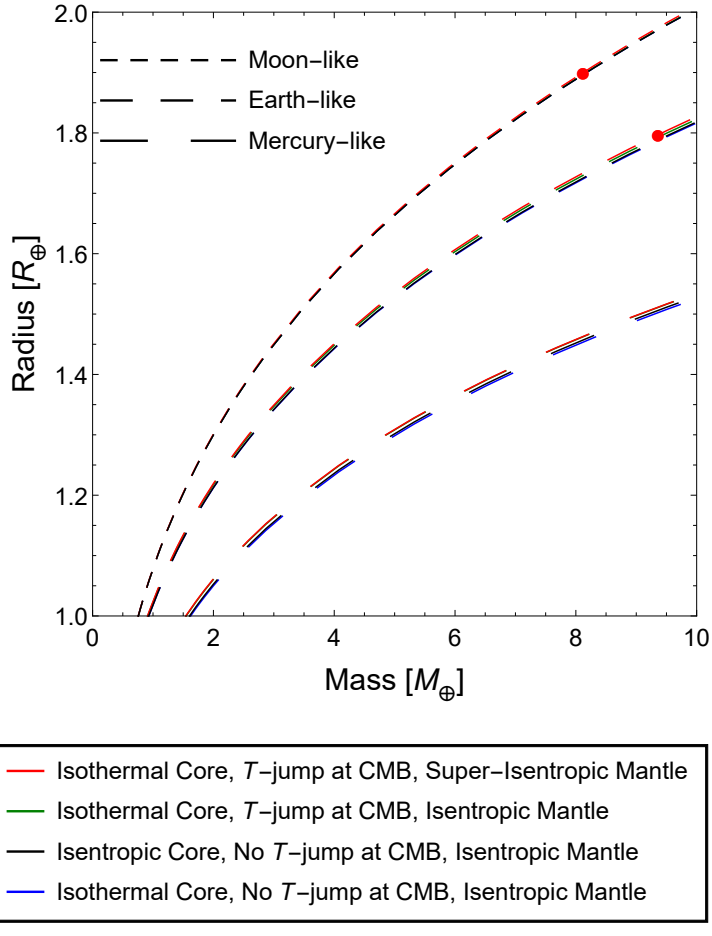

Figure 2.4: Effects of temperature on mass-radius relations of super-Earths with fixed core radius fractions. Red dots on red lines represent the mass and radius where the CMB temperature is at the solvus. For Mercury-like super-Earths, the cut-off occurs for planets with $M > 10$ $M_\oplus$.

An extreme CMB temperature jump of around 2500−7000 K (see Sect. 2.2) reduces the density of the core, it has a negligible impact on Moon-like models, but decreases the mass of Earth-like and Mercury-like super-Earths between 1−2% and 2−5%, respectively. This temperature jump effect decreases with planetary radius because thermal contribution to pressure decreases. Conversely, for a given planetary mass, the planetary radius increases by up to 1% and 1.5% for Earth-like and Mercury-like models (Fig. 2.4). These results are comparable to those of Grasset et al. (2009) who found a difference of up to 2% in radius when varying the planetary temperature profiles by 4000 K. To summarize, the effect of the

core thermal profile and the CMB temperature jump on $M-R$ relations increases with core size.

In the lower mantle, a super-adiabatic thermal gradient, starting at the transition to Mg-ppv, leads to a decrease in the mass of super-Earths by up to 3%. This effect is most prominent for moderate size cores (Earth-like) since smaller or larger cores lead to a smaller super-adiabatic profile in the mantle because the pressure either increases more slowly with depth or the mantle is thinner. In the super-adiabatic case, if the temperature in the lower mantle is higher than the solvus temperature of MgO, parts of the lower mantle might be soluble in the iron core (Wahl & Militzer, 2015). Our calculations for a pure Fe core show that the miscibility of rock and iron can occur when $R_{\mathrm{Moon-like}} > 1.9\ \mathrm{R}_{\oplus}$, $R_{\mathrm{Earth-like}} > 1.8\ \mathrm{R}_{\oplus}$ and $R_{\mathrm{Mercury-like}} > 1.75\ \mathrm{R}_{\oplus}$ (see Fig. 2.4). For such planets, the core size is defined by the solvus. If the core contains light elements, the pressure at the CMB for a given planet radius is lower than in a planet with a pure Fe core, therefore a dissolution of the lower mantle in the core occurs for planets with larger radii than for the pure Fe core case.

Overall, the effect of temperature on mass-radius relations is smaller than the effect of extrapolations of the equations of state of iron as seen in Figs. 2.3 and 2.4. Mass-radius relations due to changes in temperature profile differ only by $\Delta\beta < 0.003$ for all cases considered here. This confirms the results obtained by e.g., Sotin et al. (2007) and Grasset et al. (2009) and extends their validity range. Temperature, nevertheless, is important for many dynamic aspects of a planet, such as convection, volcanism as well as potential habitability.

2.5.2 Core composition

The composition of the core is one of the prime factors determining the mass of a super-Earth with a given radius (e.g., Unterborn et al., 2016). Valencia et al. (2007a) showed that the presence of a relatively small amount of light elements in the core, smaller than the amount in the Earth's core, can change the radius of large super-Earths with given mass by a non-negligible amount. Here we quantify this effect for prescribed density deficits with respect to pure iron and compare results obtained for different core compositions. The effect on mass-radius relations is negligible for Moon-like super-Earths, but significant for planets with larger cores (Fig. 2.5).

Models with Fe_3C cores are lighter than those with pure Fe cores resulting in smaller masses (Table 2.3). Super-Earths with 0.9ρ Fe cores are denser than FeS but lighter than Fe_3C. Models with FeS, FeSi or $Fe_{0.95}O$ cores have similar masses. Mass-radius curves with 0.8ρ Fe as core composition are almost overlapping with those of FeS, FeSi and $Fe_{0.95}O$ as core compositions, implying that the addition of 50 mol% (36 wt%) S, 50 mol% (33.5 wt%) Si or 51 mol% (23 wt%) O in the Fe-core is virtually equivalent to a 20% density deficit with respect to pure Fe. We do not show the overlapping $M-R$ curves of the FeSi and $Fe_{0.95}O$ cases in Fig. 2.5. It is interesting to note that the mass-radius curve of Mercury-like super-Earth with a pure Fe core and a $MgSiO_3$ mantle overlaps with that of FeS bare-core model, implying it is impossible to distinguish between the two with the knowledge of mass and radius only.

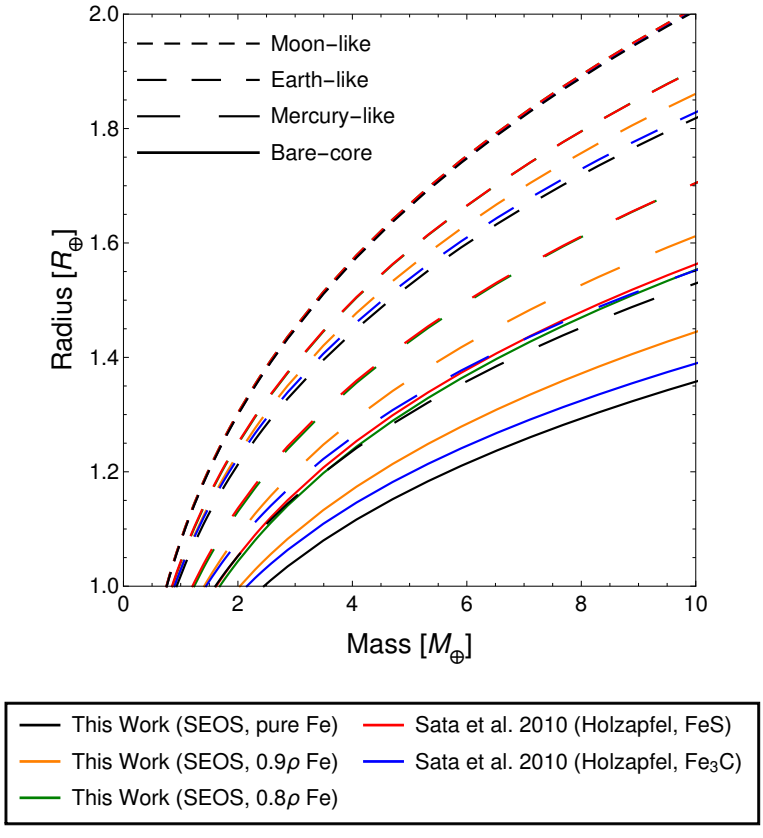

Figure 2.5: Effect of different core compositions on mass-radius relations of super-Earths with fixed core radius fractions. The Moon-like, Earth-like and Mercury-like models for our 0.8ρ Fe case and the FeS (Sata et al., 2010) case overlap with each other. Sata et al. (2010) measured the equation of state data of FeS and Fe_3C up to ∼200 GPa.

2.5.3 Mantle composition

Although mantle composition is mostly considered to be of lesser importance for the mass-radius relation of super-Earth exoplanets than core composition (e.g., Unterborn et al., 2016), only a limited range of mantle compositions has been considered previously. A reasonable range of mantle compositions based on stellar elemental ratios has been considered in Dorn et al. (2015), but these authors do not investigate their effect on mass-radius relations. As explained in Sect. 2.2, we here evaluate the effect of a wide range of mantle compositions and use the thermodynamic code of Chust et al. (2017) for the calculations of the various mineral phase transitions with increasing pressure. The effect of mantle composition on mass-radius relations increases with decreasing core size and increasing planetary

radius (Fig. 2.6). Moon-like and coreless models have almost indistinguishable mass-radius relations because of the small cores of Moon-like models.

Models with mantle compositions of $MgSiO_3$, Mg_2SiO_4 and SiO_2 differ by less than 2% (Table 2.4) because of the similarity in densities of MgO-SiO_2-based minerals. This finding extends that of Grasset et al. (2009) who showed that the effect of different Mg/Si ratios on planetary radius is < 2%, but did not consider high-pressure mineral phase transitions of

Table 2.3: Differences in planetary mass of super-Earths with R=1.25 $R_\oplus$ and R=1.75 $R_\oplus$ between different core compositions and core sizes. All differences in mass are calculated with respect to the model with a pure Fe core. Models assume an isentropic core, an isentropic $MgSiO_3$ mantle, T_S = 1650 K and a zero CMB T-jump.

Core comp.	Parameter r_{CMB}	Bare-core 1	Mercury-like 0.8	Earth-like 0.5	Moon-like 0.2
R = 1.25 $R_\oplus$					
0.9ρ Fe	ΔM	−21%	−16%	−6%	−0.5%
0.8ρ Fe	ΔM	−38%	−28%	−11%	−0.6%
FeS	ΔM	−40%	−29%	−11%	−0.6%
FeSi	ΔM	−40%	−30%	−11%	−0.6%
$Fe_{0.95}O$	ΔM	−43%	−31%	−12%	−1.2%
Fe_3C	ΔM	−11%	−9%	−4%	−0.3%
R = 1.75 $R_\oplus$					
0.9ρ Fe	ΔM	−29%	−22%	−8%	−0.5%
0.8ρ Fe	ΔM	−50%	−39%	−15%	−1.0%
FeS	ΔM	−52%	−39%	−15%	−1.0%
FeSi	ΔM	−51%	−39%	−15%	−1.0%
$Fe_{0.95}O$	ΔM	−49%	−37%	−14%	−1.0%
Fe_3C	ΔM	−8%	−5%	−2%	−0.2%

Table 2.4: Differences in planetary mass of super-Earths with R=1.25 $R_\oplus$ and R=1.75 $R_\oplus$ between different mantle compositions and core sizes. All differences in mass are calculated with respect to the model with a $MgSiO_3$ mantle. Models assume and isentropic pure Fe core, an isentropic mantle, T_S = 1650 K and a zero CMB T-jump.

Mantle comp.	Parameter r_{CMB}	Mercury-like 0.8	Earth-like 0.5	Moon-like 0.2	Coreless 0
R = 1.25 $R_\oplus$					
Mg_2SiO_4	ΔM	−0.8%	−1.4%	−2.4%	−2.4%
SiO_2	ΔM	+1.0%	+2.3%	+2.9%	+3.0%
$FeSiO_3$	ΔM	+11%	+32%	+44%	+58%
Fe_2SiO_4	ΔM	+15%	+44%	+44%	+59%
R = 1.75 $R_\oplus$					
Mg_2SiO_4	ΔM	−0.5%	−0.7%	−1.2%	−1.2%
SiO_2	ΔM	+3.0%	+1.2%	+1.5%	+1.7%
$FeSiO_3$	ΔM	+15%	+48%	+63%	+64%
Fe_2SiO_4	ΔM	+20%	+63%	+82%	+83%

perovskite. Our calculations show that post-perovskite is the most abundant mineral in all Mg-rich super-Earths larger than the Earth. The dissociated assemblages of Mg-ppv (Umemoto & Wentzcovitch, 2011), $MgSi_2O_5$ + MgO and Fe_2P-type SiO_2 + MgO, would be present in planets larger than $R \sim$1.7 $R_\oplus$ and $R \sim$1.9 $R_\oplus$, respectively. The inclusion of the dissociated phases of ppv has a negligible effect on the mass-radius relations of super-Earths.

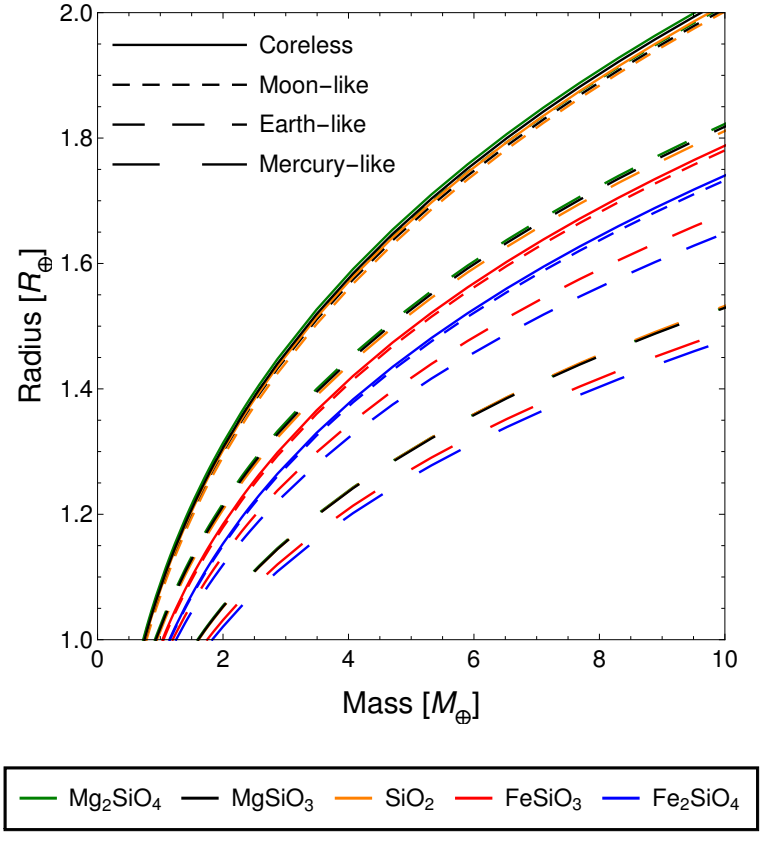

Figure 2.6: Effect of different mantle compositions on mass-radius relations of super-Earths with fixed core radius fractions. Lines corresponding to $MgSiO_3$, Mg_2SiO_4 and SiO_2 almost overlap with each other, with SiO_2 being the most dense and Mg_2SiO_4 being the least dense among these three compositions.

The presence of FeO end-member minerals in the mantle increases the mass of the planet by a large amount, depending on the core size and the planetary radius (Table 2.4). For an Earth-like planet with R=1 $R_\oplus$, switching the mantle composition from $MgSiO_3$ to $FeSiO_3$ leads to a higher mass by 26%, comparable to the result of Unterborn et al. (2016). Even though FeO end-members do not represent realistic mantles, they give an upper-limit and illustrate the large effect of the Fe-content of the mantle on mass-radius relations.

2.5.4 $M-R$ degeneracy and observed super-Earths

Uncertainties in mantle and core composition can introduce large errors in the determination of the core size of a rocky super-Earth without a gaseous envelope. In order to illustrate and quantify the combined effect of mantle and core compositions, we plot in Fig. 2.7 the mass-radius relations of bare-core, Mercury-like, Earth-like and Moon-like super-Earths with two extreme core compositions (pure Fe and 0.8ρ Fe) and two extreme mantle compositions ($\mathrm{MgSiO_3}$ and $\mathrm{FeSiO_3}$). Since the effect of temperature is small, we restrict ourselves to one temperature profile. We assume an isentropic core with no temperature jump at the CMB. We also plot observed $M-R$ curves for planets with $R < 1.5\ \mathrm{R_\oplus}$ from Weiss & Marcy (2014) and observed super-Earths[1], having uncertainties on radii and masses less than 10% and 50%, respectively.

In each of the four classes of super-Earths considered, the heaviest planets have a pure Fe core with a $\mathrm{FeSiO_3}$ mantle and the lightest planets have a 0.8ρ Fe core with a $\mathrm{MgSiO_3}$ mantle. The colored bands in the $M-R$ plane in Fig. 2.7 represent the spread due to variations in mantle and core compositions. For Mercury-like super-Earths, the planets with a pure Fe core and a $\mathrm{MgSiO_3}$ mantle are heavier than the planets with a 0.8ρ Fe core and a $\mathrm{FeSiO_3}$ mantle. However, the opposite is true for Earth-like and Moon-like planets which have smaller core size (Fig. 2.7a$-$c).

As an example of the degeneracy in estimating the core size due to uncertainties in mantle and core compositions we consider the case of CoRoT-7b. Its position in Fig. 2.7(b) on the Earth-like mass-radius curve with a pure Fe core and a $\mathrm{MgSiO_3}$ mantle suggests that the core radius fraction of CoRoT-7b is about $\sim$0.5, for a pure Fe core and a $\mathrm{MgSiO_3}$ mantle. A Mercury-like core size can be ruled out based on Fig. 2.7(c). On the other hand, given the position of CoRoT-7b in Fig. 2.7(a), it can also be Moon-like ($\mathrm{r_{CMB}}$ $\sim$0.2) with a pure Fe core and a mantle in composition close to $\mathrm{FeSiO_3}$. Uncertainties on the mass and radius of CoRoT-7b (15% and 4%, respectively) further contribute to the difficulty of constraining the core size. Additional information about composition, perhaps from the stellar composition as suggested by Dorn et al. (2015), is needed to lift the degeneracy.

For super-Earths with more extreme locations on the $M-R$ diagram, the degeneracy can be weaker. For example, HD 219134f, which is more massive than the Mercury-like or 0.8ρ Fe bare-core super-Earths (see Fig. 2.7(c) and (d)), is likely the stripped-off core of a giant planet as suggested for some other planets by Mocquet et al. (2014). Super-Earths that lie above the mass-radius bands, even with the lightest pure $\mathrm{MgSiO_3}$ composition, e.g., TRAPPIST-1f, have a lower density than a planet made purely of silicates (Fig. 2.7(a)) and likely contain significant amounts of lighter material such as ice or water in addition to rock. Another super-Earth in the same planetary system, TRAPPIST-1c, is situated in the denser part of the band of Earth-like models, and likely has a core radius fraction between that of the Earth and Mercury, assuming it has an Earth-like composition in the core and the mantle. The uncertainties on its mass, however, are too large to confidently make inferences on its interior.

[1] `http://exoplanetarchive.ipac.caltech.edu`

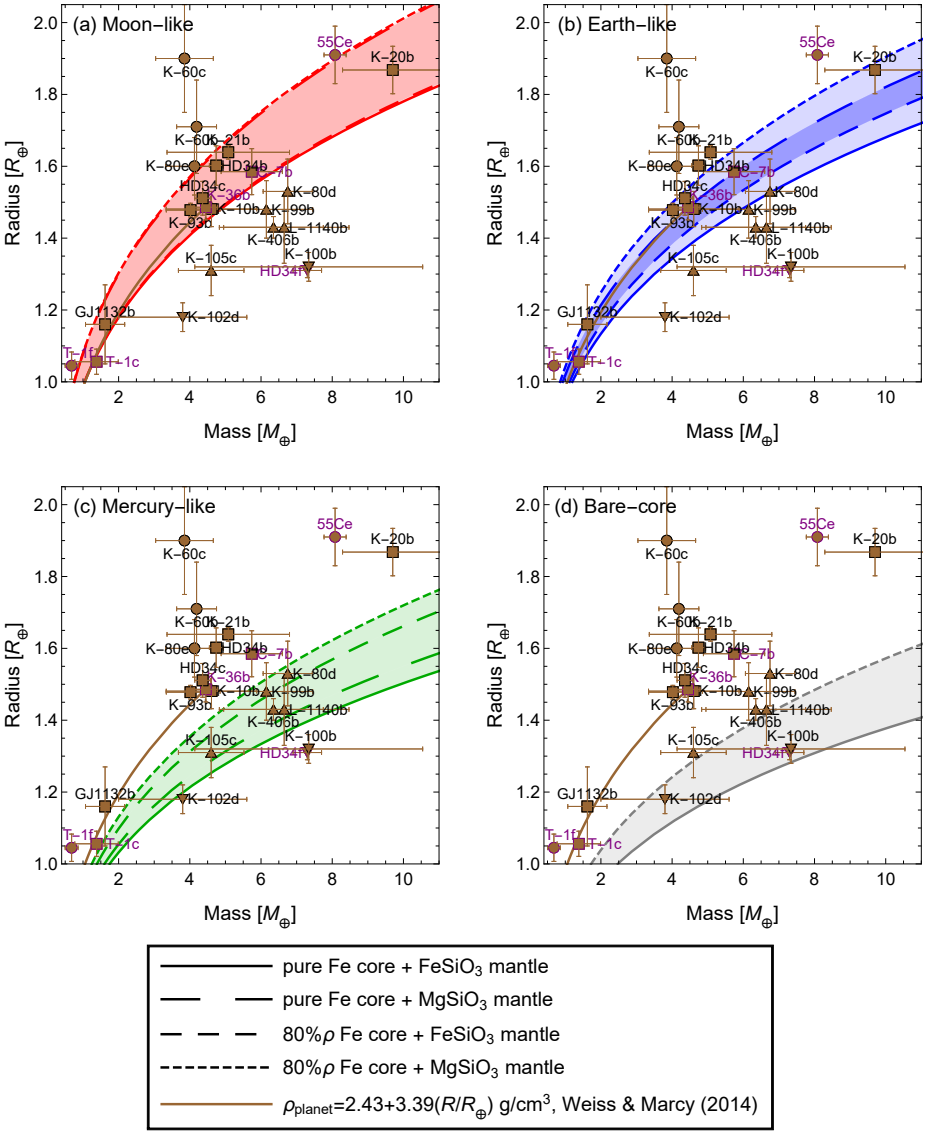

Figure 2.7: M-R relations of bare-core, Mercury-, Earth- and Moon-like super-Earths with fixed core radius fractions. Core compositions are 0.8ρ Fe or pure Fe and mantle compositions of $\mathrm{MgSiO_3}$ or $\mathrm{FeSiO_3}$, although $\mathrm{FeSiO_3}$ is much less likely. Observed exoplanets shown as squares have core radius fraction similar to the Earth or smaller, triangles have core radius fraction much larger than the Earth, inverted triangles have almost naked cores and circles are likely composed of significant amounts of volatile material or gas envelopes. Planets highlighted in violet are discussed in the text. Notation: T: TRAPPIST, K: Kepler, C: CoRoT, 55Ce: 55 Cancri e, HD34: HD 219134, L: LHS.

55 Cancri e and the planets in the Kepler-60 system are also lighter than the lightest rocky planets considered here (Fig. 2.7). This observation implies that such low-mass planets have thick atmospheres, which increase their radii by significant amounts as suggested by, e.g., Fortney et al. (2007). However, the presence of large amounts of lighter material such as water, ices or carbon compounds, not considered in this study, can also explain their low mean density, increasing the degeneracy (e.g., Seager et al., 2007; Valencia et al., 2007a; Grasset et al., 2009).

2.6 Uncertainties on the interior structure of Kepler-36b

In this section we compute in detail the interior density, pressure and temperature profiles and the core radius fraction ($r_{\rm CMB}$) for one example, Kepler-36b, a rocky super-Earth with the smallest uncertainty on its observed mass and radius, $M = 4.45^{+0.33}_{-0.27}$ $\rm M_\oplus$ and $R = 1.486 \pm 0.035$ $\rm R_\oplus$ (Carter et al., 2012). Assuming a pure Fe core and an $\rm MgSiO_3$ mantle and using the SEOS for Fe, $r_{\rm CMB}$ of Kepler-36b is $0.527^{+0.018}_{-0.012}$, implying it is an Earth-like planet by our definition (Fig. 2.8(d)). Use of equations of state of Fe other than SEOS changes $r_{\rm CMB}$ by -1% to 4% (see Fig. 2.12). The associated relative differences in density and pressure profiles reach 15%. Density increases monotonically from the surface to the center due to adiabatic self-compression, with discontinuous jumps at the mantle phase transitions, dominated by the perovskite and ppv forming transitions. Phases beyond ppv (Umemoto & Wentzcovitch, 2011) do not occur because the pressures in the mantle of Kepler-36b are not high enough for the dissociation.

A change of planetary temperature profiles has a small effect on the interior properties of Kepler-36b (Fig. 2.8(d)). Assuming an isothermal core with a CMB temperature jump of 9000 K, determined by the melting temperature of $\rm MgSiO_3$ at 0.6 TPa (Belonoshko et al., 2005), increases $r_{\rm CMB}$ by 1% (Fig. 2.8(d)). A super-adiabatic thermal gradient in the lower mantle further increases $r_{\rm CMB}$ by 2%. Core densities and pressures decrease by up to 2% because of a hotter and lighter interior. Since the super-adiabatic temperatures are below the solvus temperature of MgO (Wahl & Militzer, 2015), we do not expect high-temperature miscibility of iron and rock in the interior of Kepler-36b.

The presence of light elements in the core has a significant effect on the interior properties of Kepler-36b. Considering core compositions of 0.9ρ Fe and 0.8ρ Fe (equivalent to FeS), we predict $r_{\rm CMB}$ of Kepler-36b to increase by 9% and 22% compared to the case of pure Fe. The central density and pressure decrease by $\sim$13% ($\sim$25%) for 0.9ρ Fe (0.8ρ Fe). The combination of a $\rm MgSiO_3$ mantle and a 0.8ρ Fe core yields the largest core for Kepler-36b within our model scenarios.

Using different MgO-$\rm SiO_2$-based mantle compositions ($\rm Mg_2SiO_4$ and $\rm SiO_2$) show small effects on the core radius (1% and -2%, respectively). Switching to FeO-based end-members, i.e., $\rm FeSiO_3$ and $\rm Fe_2SiO_4$, the interior of Kepler-36b cannot be modeled successfully, because resulting densities are so high that the resulting mass exceeds the measured value for Kepler-36b. For instance, a pure $\rm FeSiO_3$ planet with no core and a radius of 1.486 $\rm R_\oplus$ would have a mass of 4.7 $\rm M_\oplus$ which exceeds the mass of Kepler-36b by 6%.

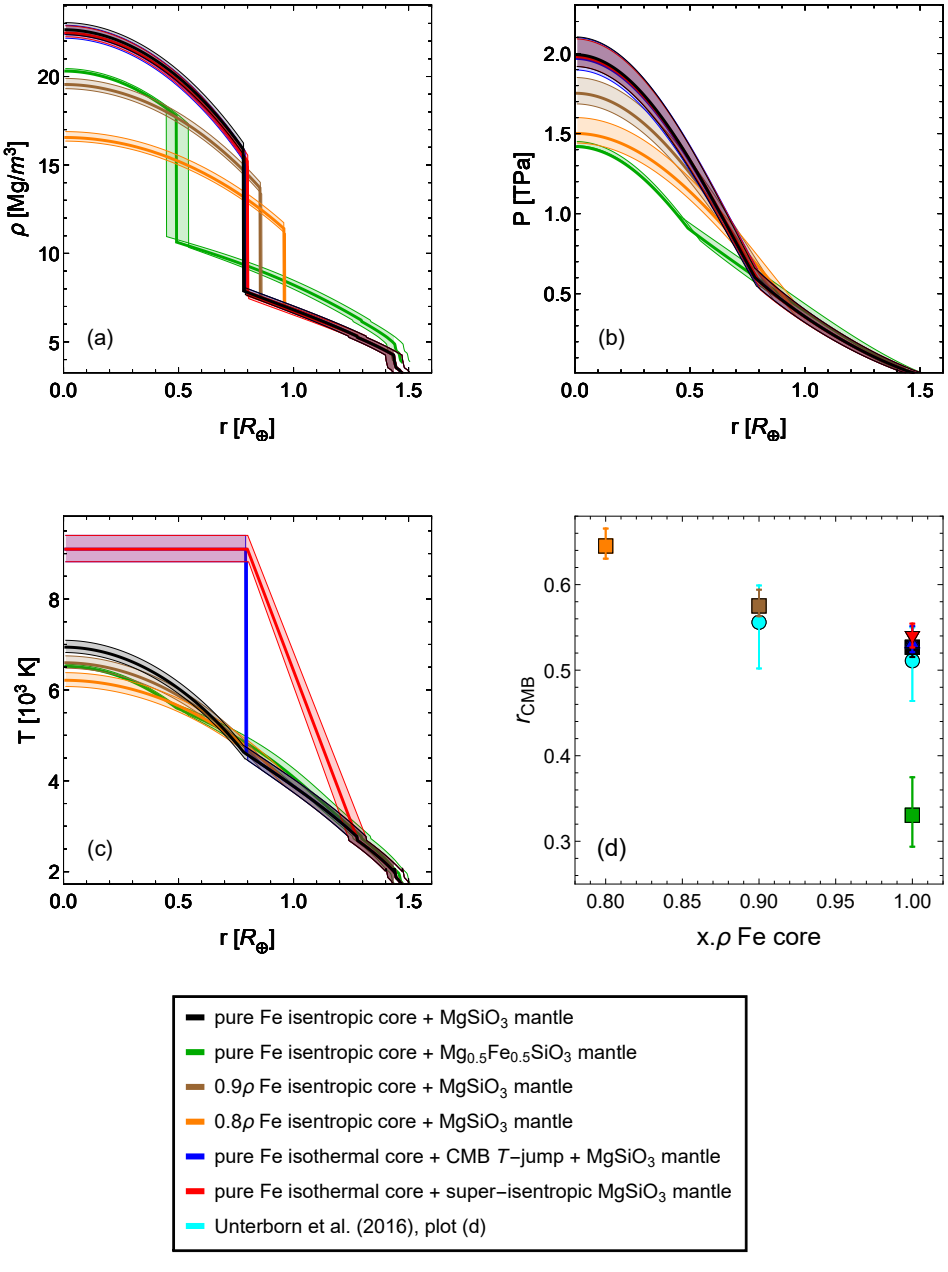

Figure 2.8: Density, pressure and temperature distribution, and the core radius fraction of Kepler-36b for selected modeling scenarios. Shaded areas represent uncertainties arising due to uncertainties in mass and radius of Kepler-36b.

With a mid-member mantle composition of $\mathrm{Mg_{0.5}Fe_{0.5}SiO_3}$ we find r_{CMB} to be $0.330^{+0.045}_{-0.036}$, which is smaller than the case of $\mathrm{MgSiO_3}$ by 37%. In the core, the density, pressure and temperature decrease by as much as 25%, while in the mantle there is a significant increase only in density, but not pressure or temperature (Fig. 2.8). Theoretically, the mass of Kepler-36b can be explained without any core, by considering an undifferentiated composition of about $\mathrm{Mg_{0.15}Fe_{0.85}SiO_3}$.

Taking all observational and modeling uncertainties into account, it is possible to give an upper bound to the core radius of Kepler-36b of $r_{\mathrm{CMB}} = 0.67$. For the models considered here with both the core and mantle, the central density and the central pressure belong in the range $16.3-22.9\ \mathrm{Mg/m^3}$ and 1.4−2.2 TPa. For our coreless model, the central density and the central pressure are $11.2\ \mathrm{Mg/m^3}$ and 1.0 TPa. The differences in the interior properties of Kepler-36b due to modeling uncertainties illustrate that temperature and equation of state of iron play a minor role on planetary interiors, compared to composition. As Fig. 2.8 clearly demonstrates, modeling uncertainties dominate over observational uncertainties on the interior properties of Kepler-36b.

2.7 Summary and conclusions

Previous studies (e.g., Seager et al., 2007; Grasset et al., 2009; Wagner et al., 2011) have pointed to the uncertainty of the equations of state of iron at pressures relevant to super-Earth cores (above 0.3 TPa) due to a lack of experimental data. In this paper, we derive a new ab initio equation of state of iron for super-Earths (SEOS) based on Density Functional Theory (DFT) calculations. In addition to the discrete set of ab initio results given in the supplement, we also provide a closed equation of state expression by fitting the DFT results to the Holzapfel equation to 10 TPa.

Density differences between SEOS and other equations of state of iron from the literature are restricted to $\pm$2% up to ∼0.5 TPa, but range between −20% and 5% at 10 TPa. The equation of state from Bouchet et al. (2013) based on the Holzapfel formulation has the smallest density difference with SEOS (< 3.5%) up to 10 TPa. These density differences have significant effects on mass-radius relations of rocky super-Earths without gaseous envelopes, in particular for planets with an iron-core large enough to reach pressures where extrapolations of equations of state of iron are required. For models with an Earth-like core radius fraction of 0.5, the use of an inadequate equation of state can result in a difference in the mass of up to 10% for a 2 $\mathrm{R_\oplus}$ super-Earth, and a difference in the radius of up to 3% for a 10 $\mathrm{M_\oplus}$ super-Earth. For models with Mercury-like core radius fraction of 0.8 and bare-core models, these effects are even larger, reaching 20% in mass and 6% in radius. For models with Moon-like core radius fraction of 0.2, the core pressures are not high enough to induce significant differences in mass-radius relations.

Although the effects of temperature on mass-radius relations are smaller than those of the equation of state for iron, assumptions of an extreme CMB temperature jump or a super-adiabatic temperature profile in the lower mantle can change the mass of super-Earths by up to 5%, depending on the core size. We find that mantle temperatures, when assuming

a super-adiabatic profile, are too low to allow for rock and iron to mix for planets smaller than 1.75 $R_\oplus$. Light elements in the core can strongly reduce the density in the core and therefore the mass of an exoplanet. By assuming a FeS core (equivalent to a reduction in density with respect to iron of 20%) instead of pure Fe, mass decreases by up to 13% and 33% for Earth- and Mercury-like super-Earths, respectively. The impact of the Mg/Si ratio on the mass-radius relations is very small because of the similarity in densities of MgO-SiO_2-based minerals. However, the presence of FeO in the mantle has a significant effect, as Fe-bearing minerals have higher densities than Mg-bearing minerals. Assuming a mantle composition of pure $FeSiO_3$, although much less likely than $MgSiO_3$, for a fixed mass, decreases the radius by up to 8% and 10% for Earth- and Moon-like super-Earths, respectively.

To quantify the effects of modeling uncertainties on the interior structure, we use Kepler-36b, a super-Earth with well-constrained mass and radius, as a test case. We demonstrate that the uncertainties due to the equation of state of iron (5%), temperature (2%), core and mantle composition (> 20%) on the core radius of Kepler-36b dominate over the observational uncertainties on its mass and radius, which are 7% and 2%, respectively. Similar modeling uncertainties are observed for other interior properties such as central density and pressure.

We show that the use of an appropriate equation of state of iron (Appendix 2.A) reduces the degeneracy in interpretations of mass and radius, but that uncertainties in composition, and to a minor extent temperature, lead to a spread of mass-radius curves into bands for Moon-, Earth- and Mercury-like exoplanets that can overlap. This significantly limits the ability to accurately infer the interior structure of rocky super-Earths. For example, the mass and radius of CoRoT-7b can equally be satisfied by a pure Fe core and a $MgSiO_3$ mantle for an Earth-like core or a pure Fe core and a $FeSiO_3$ mantle for a Moon-like core. This non-uniqueness adds to the large degeneracy that may result from not knowing if the planet has a substantial gaseous envelope. Since masses and radii of rocky super-Earths are expected to be determined with an accuracy as high as 3% in the planet radius and 10% in the planet mass (Hatzes et al., 2016) with upcoming missions such as TESS, CHEOPS, JWST and PLATO, modeling uncertainties will then dominate over observational uncertainties. Knowledge of the stellar composition, for example Fe/Si and Mg/Si ratios, would play an important role in mitigating the $M-R$ degeneracy (Dorn et al., 2015; Santos et al., 2017).

Acknowledgments

We thank Diana Valencia and an anonymous reviewer for their insightful comments in improving this manuscript. This research has been supported by the Planetary and Exoplanetary Science Network (PEPSci), funded by the Netherlands Organization for Scientific Research (NWO) Project no. 648.001.005, led by Carsten Dominik and Wim van Westrenen. TVH and AR acknowledge the financial support from the Belgian PRODEX program (grant no. 4000120791) managed by the European Space Agency in collaboration with the Belgian Federal Science Policy Office and from the BRAIN.be program of the Belgian Federal Science Policy Office. SC acknowledges financial support from OCAS NV by an OCAS-endowed chair

at Ghent University. Work by GSN is supported by Deutsche Forschungsgemeinschaft (DFG, German Science Foundation) through Research Unit 2440 (Matter Under Planetary Interior Conditions, STE1105/13-1).

Appendices

2.A Equation of state extrapolations

In order to assess which equation of state among the third-order Birch-Murnaghan (BM3), Vinet, modified Rydberg, and Holzapfel is more suitable for extrapolation, we fit them to the low pressure part (0−300 GPa) of our DFT calculated $P(V)$ set (see Supplement) and compare the pressures predicted with our set of results (up to 10 TPa). For all equations, every parameter has been estimated without any prior constraints except for the modified Rydberg equation where $K'_\infty > 5/3$ has been assumed.

The BM3 and Vinet equations have residuals below 0.4 GPa and those of the modified Rydberg and Holzapfel are below 0.05 GPa. This is significantly smaller than present day experimental error (< 2%) (Fei et al., 2016). Consequently, they are equally suitable for summarizing the low pressure data. Note that an unconstrained fit with the modified Rydberg equation has smaller residuals than the constrained fit, but the estimated value of K'_∞ is 1.43, smaller than the theoretical value of 5/3 (Stacey, 2005).

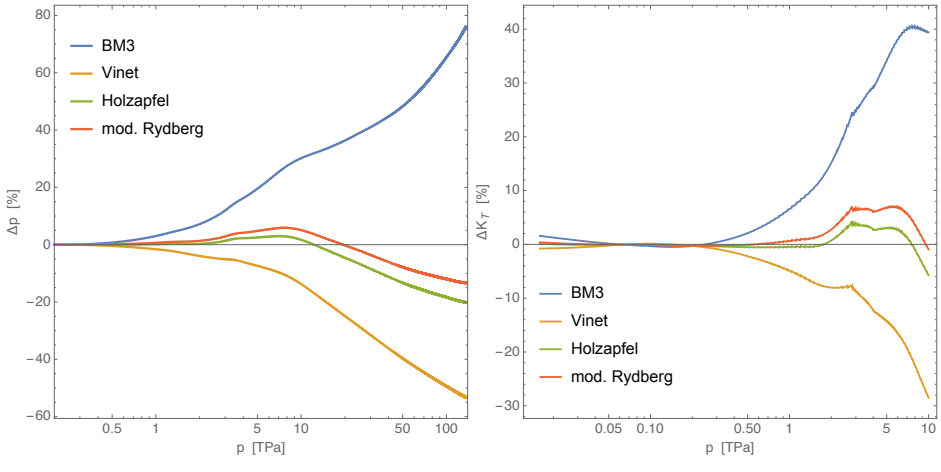

Figure 2.9: Relative differences in P and K_T between the DFT results and predictions obtained with the BM3, Vinet, modified Rydberg, and Holzapfel equation as a function of pressure.

Extrapolation with the Vinet and BM3 equation results in differences that are already above 2% at pressures that are not much larger than 1 TPa and above 14% at 10 TPa (Fig. 2.9). The pressures predicted by the modified Rydberg and Holzapfel equations differ significantly less from the DFT results (Fig. 2.9). Up to 10 TPa the difference are below 3% for the modified Rydberg (not shown) and Holzapfel equations. Differences with the 'constrained' modified Rydberg are about two times larger. Note that at 137 TPa the predicted pressures with the BM3 and Vinet equation differ from the DFT set by more than 50% and the modified Rydberg and Holzapfel equation by about 20%. For completeness we also compare K_T predicted by the equations of state and directly calculated from the DFT set (Fig. 2.9).

2.B Fitting residuals of DFT data

Fig. 2.10 demonstrates that the whole DFT result set (see Supplement) cannot be summarized accurately with one equation of state. However, a fit on a subset (0.234−10 TPa) with the Holzapfel equation has residuals that are below 2% if the reference volume is given (see main text). Comparable residuals are obtained for data at $P < 5$ TPa.

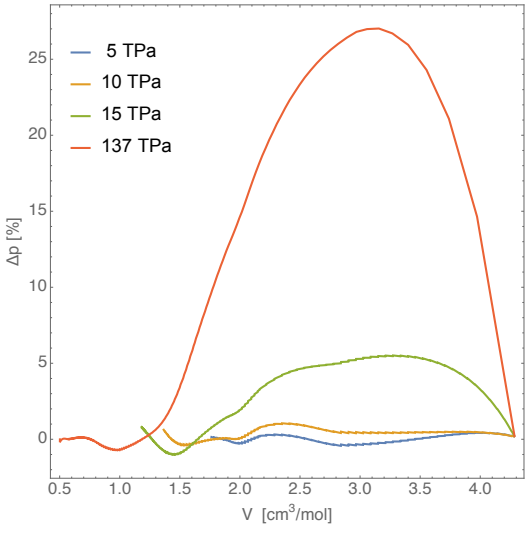

Figure 2.10: Fit residuals of the Holzapfel equation for different subsets of the DFT results.

2.C Sliding window interpolation scheme

To compute volumes at intermediate pressures we use a sliding-window local third-order Birch-Murnaghan (BM3) fitting scheme. Let $\{V_i, E_i, P_i\}_{1 \leqslant i \leqslant N}$ be the volume, energy, and pressure data set. The volume and bulk modulus at pressure $\tilde{P}$ is then calculated as follows:

1. locate the position of the pressure in $\{P_i\}_{1 \leqslant i \leqslant N}$ that is closest to $\tilde{P}$, say at k,
2. select a small subset of length $2l + 1$ of volumes and internal energies around P_k: $\{V_j, E_j\}_{k-l \leqslant j \leqslant k+l}$,
3. define a local enthalpy as: $H(V) = E(V) + \tilde{P}\, V$ (per construction H has a minima at $P = \tilde{P}$, since $\frac{dE}{dV} = -P$),
4. estimate V and K_T at $\tilde{P}$ by fitting the BM3 equation on $\{V_j, H_j\}_{k-l \leqslant j \leqslant k+l}$.

This scheme can be used to compute V and K_T on the fly or beforehand. In practice, the size of the local subset is chosen large enough to allow for a precise fit but not much larger. We have used $l = 7$.

2.D Equation of state of iron alloys

Sata et al. (2010) determined the density of FeS, FeSi, $Fe_{0.95}O$ and Fe_3C experimentally in a pressure range relevant for the Earth's core and fitted the data to a BM3 equation. In the absence of data in the high-pressure range of the super-Earth cores, extrapolations significantly beyond the experimental pressure range are needed. Such extrapolations can result in unreasonably large deviations (see Fig. 2.2). Since extrapolation with a Holzapfel equation leads to better results than with a BM3 equation (Fig. 2.10), we have refitted the density data from Sata et al. (2010) to a Holzapfel equation (Table 2.5).

Table 2.5: Thermoelastic parameters obtained by fitting the data of FeS, FeSi, $Fe_{0.95}O$ and Fe_3C from Sata et al. (2010) to a Holzapfel equation.

Fe-alloy	ρ_0 ($\frac{\text{kg}}{\text{m}^3}$)	$K_{T,0}$ (GPa)	$K'_{T,0}$	P_{FG0} (TPa)
FeS	6118	144.3	4.79	27.78
FeSi	6522	219.5	4.29	18.45
$Fe_{0.95}O$	5764	152.7	4.13	11.25
Fe_3C	7980	289.4	3.81	30.68

Key: ρ_0: reference density at $P_0 = 1$ bar and $T_0 = 300$ K, $K_{T,0}$: reference isothermal bulk modulus and its derivative $K'_{T,0}$, P_{FG0}: Fermi-gas pressure.

2.E DFT equations of state of iron

In Fig. 2.11, we compare our DFT results at low pressures (0−300 GPa) with similar DFT predictions and laboratory data from the literature. We compare our DFT results at zero pressure with studies from the literature in Table 2.6.

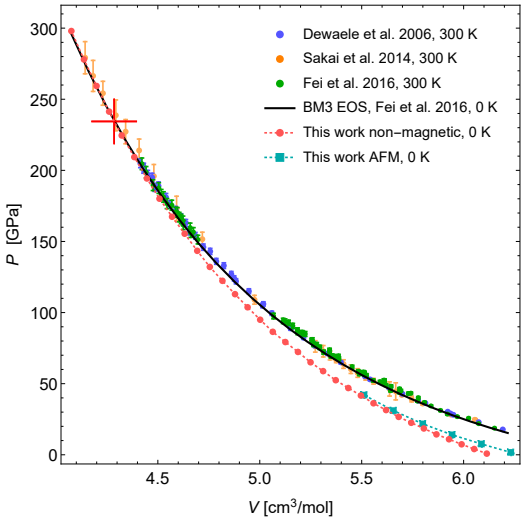

Figure 2.11: Pressure of hcp iron as a function of volume. Recent laboratory data with error-bars, DFT results for non-magnetic and anti-ferromagnetic phases, and the BM3 equation of state from Fei et al. (2016) corrected to 0 K and zero-point vibrational effects (Lejaeghere et al., 2014). The red plus denotes the pressure (234.4 GPa) and volume (4.28575 cm^3/mol) at which our DFT results match the experimental equation of state from Fei et al. (2016).

Table 2.6: Ab initio equations of state of hcp-Fe.

V_0 ($\frac{cm^3}{mol}$)	K_0 (GPa)	K_0'	XC	Reference
6.145	291	4.4	PW91	Stixrude et al. (1994), NM
6.136−6.250	287−296	4.2−4.5	PW91	Alfè et al. (2000), NM
6.175	293	−	PW91	Caspersen et al. (2004), NM
6.158	292	4.4	PBE	Steinle-Neumann et al. (1999), NM
6.078	296	−	PBE	Sha & Cohen (2010), NM
6.135	291	5.1	PBE	This Work, NM
6.315	224	5.5	PBE	Dewaele et al. (2006), AFM
6.354	209	5.2	PBE	Steinle-Neumann et al. (1999), AFM
6.306	222	5.7	PBE	This Work, AFM

Key: XC: Exchange correlation functional of hcp-Fe, NM: non-magnetic, AFM: antiferromagnetic, PW91: Perdew & Wang (1992), PBE: Perdew et al. (1996). Reference temperature and pressure are zero.

2.F Equations of state of iron and effects on Kepler-36b

Table 2.7 lists the thermoelastic parameters of various equations of state of iron from the literature used for modeling planetary cores. In Fig. 2.12, we illustrate the differences between our DFT-based equation of state and some equations of state from Table 2.7 on the internal properties of Kepler-36b.

Table 2.7: Thermoelastic parameters for various equations of state of iron from the literature.

Ref.	Form.	Isothermal				Harmonic				Anharmonic + Electronic				
		ρ_0 ($\frac{\mathrm{kg}}{\mathrm{m}^3}$)	$K_{T,0}$ (GPa)	$K'_{T,0}$	$K'_{T,\infty}$	Θ_0 (K)	γ_0	b [q]	γ_∞	a_0 ($\frac{1}{10^3\ \mathrm{K}}$)	m	e_0 ($\frac{1}{10^3\ \mathrm{K}}$)	g	P range (GPa)
Dew	Vin	8270	163.4	5.38	–	417	1.875	3.289	1.305	0.037	1.87	0.195	1.339	17−197
Bou	Hol	8878	253.8	4.719	–	44.574	1.408	0.826	0.827	0.2121	1.891	–	–	30−1500
Val	Vin	8300	160.2	5.82	–	998	1.36	[0.91]	–	–	–	–	–	136−300
Sea	Vin	8300	156.2	6.08	–	–	–	–	–	–	–	–	–	0−330
Fei	BM3	8269	172.7	4.79	–	422	1.74	[0.78]	–	–	–	–	–	18−280
Dor	BM3	8341	173.98	5.297	–	–	2.434	[0.489]	–	–	–	–	–	18−360
Wag	Ryd	8269	149.4	5.65	2.94	430	1.875	3.289	1.305	0.037	1.87	0.195	1.339	17−197

Key: ρ_0: reference density at ambient conditions, K_0: reference isothermal bulk modulus and its derivatives $K'_{T,0}$ and $K'_{T,\infty}$. Note: Fei et al. (2016) uses a different formulation for the electronic contribution to the specific heat, $C_{Ve} = \beta_0 x^{3k} T$, where $\beta_0 = 0.07$ J kg^{-1} K^{-2} and $k = 1.34$, and $\gamma_e = 2$.
Abbreviations: Dew: Dewaele et al. (2006); Bou: Bouchet et al. (2013); Val: Valencia et al. (2007a), data from Williams & Knittle (1997); Sea: Seager et al. (2007), data from Anderson et al. (2001); Fei: Fei et al. (2016); Dor: Dorn et al. (2015), data from Belonoshko et al. (2010); Wagner et al. (2011), data from Dewaele et al. (2006); Vin: Vinet; BM3: third-order Birch-Murnaghan; Hol: Holzapfel; Ryd: modified Rydberg.

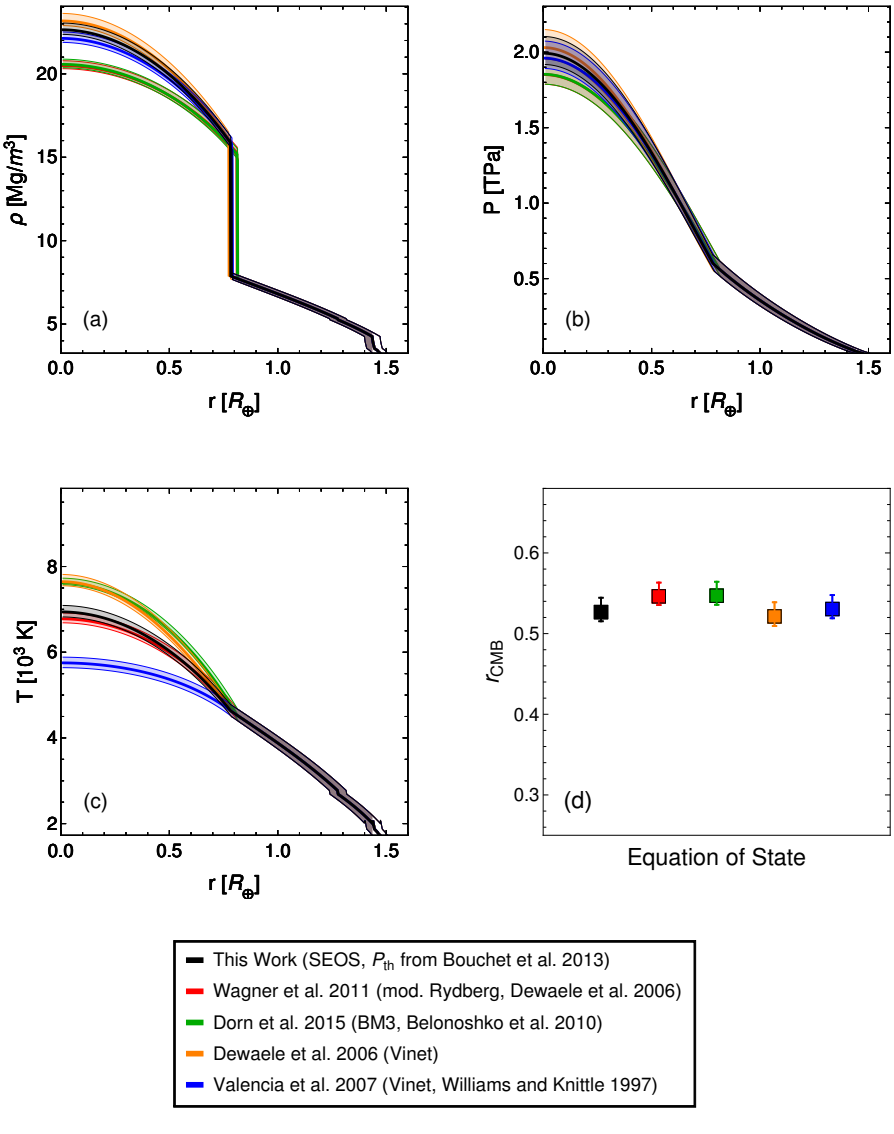

Figure 2.12: Density, pressure and temperature distribution, and the core radius fraction of Kepler-36b calculated using different equations of state of iron. Shaded areas represent uncertainties arising due to uncertainties in mass and radius of Kepler-36b.

Chapter 3

Mineralogy, structure and habitability of carbon-enriched rocky exoplanets: A laboratory approach

Kaustubh Hakim, Rob Spaargaren, Damanveer S. Grewal, Arno Rohrbach, Jasper Berndt, Carsten Dominik, Wim van Westrenen

under review in Astrobiology

Abstract

Carbon-enriched rocky exoplanets have been proposed around dwarf stars as well as around binary stars, white dwarfs and pulsars. However, the mineralogical make up of such planets is poorly constrained. We performed high-pressure high-temperature laboratory experiments on chemical mixtures representative of C-enriched rocky exoplanets according to protoplanetary disk modeling. Our results show that these exoplanets, when fully-differentiated, comprise a metallic core, a silicate mantle and a graphite layer on top of the silicate mantle. Graphite is the dominant carbon-bearing phase at the conditions of our experiments with no traces of silicon carbide or carbonates. The silicate mineralogy comprises olivine, orthopyroxene, clinopyroxene and spinel, similar to the mineralogy of the mantles of carbon-poor planets such as the Earth, and largely unaffected by the amount of carbon. Metals are either two immiscible iron-rich alloys (S-rich and S-poor) or a single iron-rich alloy in the Fe-C-S system with immiscibility depending on the S/Fe ratio and core pressure. We show that for our C-enriched compositions the minimum carbon abundance needed for C-saturation is 0.05−0.7 wt% (molar C/O$\sim$0.002−0.03). Fully differentiated rocky exoplanets with C/O ratios more than needed for C-saturation would contain graphite as an additional layer on top of the silicate mantle. For a thick enough graphite layer, diamonds would form at the bottom of this layer due to high pressures. We model the interior structure of Kepler-37b and show that a mere 10 wt% graphite layer would decrease its derived mass by 7%, suggesting future space missions that determine both radius and mass

of rocky exoplanets with insignificant gaseous envelopes could provide quantitative limits on their carbon content. Future observations of rocky exoplanets with graphite-rich surfaces would show low albedos due to the low reflectance of graphite. The absence of life-bearing elements other than carbon on the surface likely makes them uninhabitable.

3.1 Introduction

Since the discovery of the first rocky exoplanet, CoRoT-7b (Léger et al., 2009), more than a thousand such planets have been found[1]. The scatter in the mass-radius diagram of rocky exoplanets reveals a great diversity in their bulk composition and interior structure (e.g., Valencia et al., 2006; Seager et al., 2007; Wagner et al., 2011; Hakim et al., 2018a). Water/ices (e.g., GJ 876d, Valencia et al., 2007a), thick atmospheres (e.g., GJ 1132b, Southworth et al., 2017) as well as carbon-bearing minerals including graphite and silicon carbide (e.g., 55 Cancri e, Madhusudhan et al., 2012) have been suggested as dominant phases in these exoplanets, in addition to silicate minerals and iron alloys. Besides dwarf stars, carbon-enriched rocky exoplanets have been proposed around binary stars (e.g., Whitehouse et al., 2018) as well as pulsars and white dwarf stars (e.g., Kuchner & Seager, 2005).

Although life as we know it is largely based on carbon, the Earth contains less than 0.01 wt% carbon (e.g., Javoy et al., 2010). This is to some extent surprising, since many weakly processed planetary building blocks in solar system contain significant amounts of carbon in the form of organics (e.g., carbonaceous chondrites, Marty et al., 2013), and some larger, more evolved bodies such as the ureilite parent body contain significant amounts of refractory carbon (Nabiei et al., 2018). In order to explain the extremely low abundance of carbon in the Earth, carbon needs to be burned (oxidized and turned into CO/CO_2) or photolyzed away (broken out of the organic compounds by energetic photons) while the solid material is still present in the form of small grains with large surface-to-mass ratio (Lee et al., 2010; Anderson et al., 2017).

An alternative explanation is that planetesimal-sized parent bodies need to be subjected to igneous processing to degas carbon (Hashizume & Sugiura, 1998) which is tied to the presence of radioactive elements like ^{26}Al in the early solar nebula (Hevey & Sanders, 2006). Both these processes do not seem inevitable. Oxidation and photo-processing may be quenched by effects of dust growth and transport in disks (Klarmann et al., 2018). The presence of short-lived radioactive isotopes in significant amounts requires the fast (within a Myr) addition of the ejecta of a nearby supernova explosion or stellar wind material into the collapsing protosolar cloud, followed by rapid formation of planetesimals (Bizzarro et al., 2005). It is therefore likely that the conditions needed to decarbonize solids are absent in many planet-forming systems, and that rocky planets in such systems may contain significant levels of carbon up to 10 mass percent.

Even larger carbon abundance could be obtained in systems where the carbon-to-oxygen abundance ratio is higher than in the solar system. Modeling of the protoplanetary disk chemistry for planet-hosting stars with molar photospheric C/O > 0.65 (Moriarty et al.,

[1] http://exoplanetarchive.ipac.caltech.edu

2014) and C/O > 0.8 (Bond et al., 2010b; Carter-Bond et al., 2012b) (cf. $C/O_{Sun} \sim 0.54$) suggests that carbon acts as a refractory element mainly in the form of graphite and silicon carbide in the inner regions of such disks. Delgado Mena et al. (2010) and Petigura & Marcy (2011) reported spectroscopic observations of stars with photospheric C/O ratios greater than unity. However, Nakajima & Sorahana (2016) and Brewer et al. (2016) claim that the stars in solar neighborhood have largely solar-like C/O ratios. Although the debate over photospheric C/O ratios is not settled, the possibility of a substantial fraction of stars with C/O > 0.65 cannot be excluded.

Refractory elements in protoplanetary disks are the major building blocks of rocky planets. Bond et al. (2010b) found that the C/O ratio of the refractory material in inner disks of stars with C/O > 0.8 varies from zero to greater than one hundred as a function of distance from the star. Moriarty et al. (2014) found that, for high C/O stars, the extent of refractory carbon in the planetesimal disk increases using a sequential condensation model instead of a simple equilibrium condensation model. Thiabaud et al. (2015) showed that C/O ratios of rocky planets do not necessarily show a one-to-one correlation with the stellar photospheric C/O ratios. N-body simulations by Bond et al. (2010b) produce rocky exoplanets containing as high as 70 wt% carbon. The amount and nature of carbon-bearing minerals in carbon-enriched rocky exoplanets may directly impact geodynamical processes, carbon and water cycles and, in turn planetary habitability (Unterborn et al., 2014).

During the early stages of planet formation, refractory material in protoplanetary disks condenses out from the chemical reactions between gas molecules. Coagulation of refractory material leads to the formation of pebbles, which grow into sub-Ceres-size to Pluto-size planetesimals and later on form planets (Johansen et al., 2007; Schäfer et al., 2017). Such planetesimals are large enough to undergo large-scale differentiation at high-pressure-temperature conditions during the process of planet formation. Modeling studies such as Bond et al. (2010b) and Moriarty et al. (2014) derive proportions of chemical compounds condensing out from gas chemistry and perform N-body simulations on planetesimals to track the likely chemical composition of resulting planets. Since the pressures in interiors of planetesimals and planets are several orders of magnitude higher than the disk pressures, high-pressure high-temperature reactions are expected to reprocess their chemical composition and kick off large-scale differentiation processes in their interiors which lead to metal segregation and core formation (Kruijer et al., 2013). Current understanding of the mineralogy of exoplanets is based on extrapolation of the knowledge of rocky bodies in our solar system and lacks experimental evidence. There is a need to investigate the mineralogy and phase relations of carbon-rich planetesimals and exoplanets, which have no solar system analogs, in multi-component systems, and high-pressure high-temperature experiments make it possible (e.g., Valencia et al., 2009; Nisr et al., 2017).

C-enriched rocky exoplanets are speculated to contain large amounts of C-bearing minerals including silicon carbide and graphite (e.g., Bond et al., 2010b; Madhusudhan et al., 2012). Over the past decades, several laboratory studies have investigated the mineralogy of rocky planets in C-poor Earth-like conditions, but only a few studies are applicable to conditions relevant to C-enriched exoplanetary interiors. Corgne et al. (2008) used a CI-

chondrite-like composition to probe early planetesimal differentiation in carbon- and sulfur-enhanced environments and observed liquid metal immiscibility leading to the formation of C-rich and S-rich metals. The extent of liquid metal immiscibility has been explored in the simple Fe-C-S (e.g., Dasgupta et al., 2009), Fe-S-O (e.g., Tsuno et al., 2007) and Fe-S-Si (e.g., Morard & Katsura, 2010) systems. The solubility of carbon in iron alloys (e.g., Lord et al., 2009; Tsuno & Dasgupta, 2015) and silicate melts (e.g., Duncan et al., 2017), the partitioning of carbon between silicate melt and iron alloys (e.g., Chi et al., 2014; Li et al., 2015, 2016) and the stability of reduced versus oxidized carbon in the Earth's mantle (e.g., Rohrbach & Schmidt, 2011) have also been investigated. Phase relations have been studied in the carbon-saturated Fe-Mg-Si-C-O (FMS+CO) system with bulk compositions depleted in oxygen (Takahashi et al., 2013). The study by Takahashi et al. (2013) covers a range of oxygen fugacities resembling highly reducing conditions, however they did not consider the presence of S which can be a major component in the Fe cores of rocky bodies (e.g., Stewart et al., 2007; Rai & Westrenen, 2013; Steenstra et al., 2016). Moreover, they lack a discussion about the diversification of silicate minerals due to the absence of Al and Ca in their experiments. Finally, to our knowledge no experimental studies have used C-enriched starting compositions derived from modeling planet formation chemistry around stars other than our Sun, which is key for future exoplanetary exploration.

Here we probe the mineralogy and structure of small C-enriched rocky exoplanets by performing high-pressure high-temperature laboratory experiments on chemical mixtures in the Fe-Ca-Mg-Al-Si-C-S-O (FCMAS+CSO) system resembling the bulk compositions of C-enriched planetesimals from the models of Moriarty et al. (2014). In Sect. 3.2, we give our experimental and analytical methods. Phase relations and compositions of our experimental run products are given in Sect. 3.3. The mineralogy and structure of C-enriched rocky exoplanets and their dependence on several factors are discussed in Sect. 3.4. To illustrate the application of our findings, we discuss the implications of assuming a C-enriched interior on the derived mass, future observations and habitability of Kepler-37b, the smallest known exoplanet till date in Sect. 3.5. Finally, we summarize our findings and conclusions in Sect. 3.6.

3.2 Methods

3.2.1 Choice of bulk compositions

To prepare starting materials for our experiments, we used relative elemental abundances of C-enriched planetesimals at 1 AU and 0.15 Myr after disk formation in the HD19994 planetary system computed by Moriarty et al. (2014) for their equilibrium chemistry (EC) and sequential condensation chemistry (SC) cases. Two end-member compositions (SC and EC) were prepared using elemental proportions given in Table 4.1. The C/O ratios of SC and EC compositions are 0.35 and 1.38 respectively, about two-three orders of magnitude higher than that of the Earth. Since our experiments were performed in carbon-saturated conditions by enclosing samples in graphite capsules (see below), there is no upper limit on the amount of carbon in the resulting experiments, and hence these C/O ratios merely signify

lower limits. We also chose a third bulk composition (hereafter, TC) resembling solar system terrestrial planetesimals at 1 AU and 0.15 Myr after disk formation from the equilibrium chemistry model of Moriarty et al. (2014). The TC composition is also saturated with carbon.

Table 3.1: Planetesimal bulk compositions and starting materials

Element	SC	EC	TC	Material	SC	EC	TC
Si (mol%)	11.4	9.0	15.3	SiO_2 (wt%)	30.1	19.0	36.7
Mg (mol%)	11.4	9.3	15.3	MgO (wt%)	20.2	19.0	24.6
O (mol%)	45.8	30.0	51.2	FeO† (wt%)	27.3	23.1	8.1
Fe (mol%)	11.4	7.6	12.8	Fe (wt%)	2.2	0.0	14.2
S (mol%)	1.9	1.3	3.6	FeS (wt%)	7.0	8.8	12.6
Al (mol%)	1.4	0.9	1.0	Al_2O_3 (wt%)	3.1	2.4	2.1
Ca (mol%)	0.7	0.5	0.8	CaO† (wt%)	1.7	1.5	1.7
C (mol%)	16.0	41.4	–	C (wt%)	8.4	23.5	–
C/O (mol/mol)	0.35	1.38	–	SiC (wt%)	0.0	5.6	–

† CaO and FeO are obtained from $CaCO_3$ and Fe_2O_3 after decarbonation and reduction.

3.2.2 Starting materials

Starting materials were mixed in proportions shown in Table 4.1. In the first step, SiO_2 (99.9% SiO_2 powder from Alfa-Aesar), MgO (99.95% MgO powder from Alfa-Aesar), Al_2O_3 (99.95% min alpha Al_2O_3 powder from Alfa-Aesar), $CaCO_3$ (99.95-100.05% ACS chelometric standard $CaCO_3$ powder from Alfa-Aesar) and Fe_2O_3 (99.9% Fe_2O_3 powder from Alfa-Aesar) were homogenized in an agate mortar under ethanol. The oxide-carbonate mixture was decarbonated and reduced in a box furnace by first gradually increasing the temperature from 873 K to 1273 K in six hours. The decarbonated mixture, placed in a platinum crucible, was then heated to 1823 K in a box furnace for 30 minutes and then quenched to room temperature by immersing the bottom of the platinum crucible in water, leading to the formation of glassy material. It was then ground to a homogeneous powder using an agate mortar under ethanol. Fe (99.95% Fe powder, spherical, <10 micron from Alfa-Aesar), FeS (99.9% FeS powder from Alfa-Aesar), C (99.9995% Ultra F purity graphite from Alfa-Aesar) and SiC (⩾97.5% SiC powder from Sigma-Aldrich) were added to the powder. The final mixture was again homogenized by grinding in an agate mortar and stored in an oven at 383 K until use.

3.2.3 High-pressure high-temperature experiments

Experiments summarized in Table 3.2 were conducted in an end-loaded piston-cylinder apparatus at Vrije Universiteit Amsterdam in a 12.7 mm (half-inch) diameter cylindrical sample assembly. Details on sample assembly preparation are given in Appendix 3.A and Fig. 3.6.

Pressure and temperature conditions of 1−2 GPa and 1523−1823 K were chosen to represent the interior conditions of Pluto-mass planetesimals and planets. To reduce the porosity of the graphite capsules, the sample assembly was sintered at 1073 K and 1 GPa for 1 h before further heating and pressurization. During heating to the run temperature, the pressure was increased continuously with the hot-piston-in technique (McDade et al., 2002). The temperature was increased at a rate of 100 K/min. The experiments were run for the duration of 3.5−100 h (Table 3.2). All experiments were quenched to <450 K within ∼15 s by switching off the electric power to the heater.

3.2.4 Analytical procedure

The recovered samples were mounted in one-inch-diameter mounts using petropoxy resin, cut longitudinally, polished with grit-paper and fine-polished down to a 1/4 μm finish. The polished samples were carbon-coated to ensure electrical conductivity of the surface during electron probe micro-analysis. Major element contents of the experimental charges were

Table 3.2: Experimental conditions and run product phases

Run	P (GPa)	T (K)	t (h)	$\log f_{O_2}$ (ΔIW)	Run product phases (proportions in wt%) (Graphite is an additional phase in all runs)
SC					
1B1t	1	1823	3.5	−0.5	Olv (25%) + SiL (61%) + SrFeL2 (13%)
1B1p	2	1823	3.5	−0.7	Olv (27%) + SiL (56%) + SrFeL2 (18%)
1B1f	1	1723	4	−0.6	Olv (38%) + SiL (46%) + SrFeL2 (16%)
1B1j	2	1723	4	−0.4	Olv (44%) + SiL (46%) + SrFeL2 (10%)
1B1q	1	1623	20	−0.5	Olv (68%) + SiL (21%) + Spi (0.2%) + SrFeL2 (10.8%)
1B1w	2	1623	29	−0.3	Olv (47%) + SiL (41%) + SrFeL2 (11%)
1B1r	1	1545	20	*−0.5*	Olv (74%) + Spi (11%) + CPx (4%) + SrFeL2 (11%)
EC					
2C1a	1	1823	4	−1.2	Olv (41%) + SiL (36%) + SpFeL (9%) + SrFeL (14%)
2C1d	2	1823	4	−1.0	Olv (25%) + SiL (15%) + OPx (36%) + SpFeL (9%) + SrFeL (15%)
2C1e	1	1723	4	−1.2	Olv (30%) + SiL (13%) + OPx (31%) + SpFeL (9%) + SrFeL (17%)
2C1c	2	1723	6	*−0.9*	Olv (36%) + SiL† + CPx (41%) + SpFeL (9%) + SrFeL (14%)
TC					
1A2y	1	1823	3.5	−1.1	Olv (38%) + SiL (39%) + SpFeL (14%) + SrFeL (8%)
1A2zc	2	1823	6.5	−1.0	Olv (26%) + SiL (21%) + OPx (28%) + SpFeL (15%) + SrFeL (10%)
1A2zd	1	1723	8	−1.1	Olv (35%) + SiL (41%) + SpFeL (14%) + SrFeL (9%)
1A2a	2	1723	4	−1.0	Olv (22%) + SiL† + OPx (52%) + SpFeL (15%) + SrFeL (11%)
1A2c	1	1623	4	*−1.2*	Olv (18%) + SiL† + OPx (56%) + SpFeL (15%) + SrFeL (12%)
1A2za	2	1623	29	*−1.2*	Olv (28%) + OPx (46%) + SpFeL (15%) + SrFeL (11%)
1A2s	1	1523	100	*−1.0*	Olv (49%) + OPx (20%) + CPx (7%) + FeS (24%)

Note: Oxygen fugacity is calculated assuming a non-ideal solution behavior of S-rich Fe alloy and silicate melt (see Appendix 3.B for details). Numbers in italics are calculated using olivine instead of silicate melt.

† Silicate melt was present in small quantities which could not be measured using EPMA.

Abbreviations: Olv = Olivine, SiL = Silicate melt, OPx = Orthopyroxene, CPx = Clinopyroxene, Spi = Spinel, SpFeL = S-poor Fe melt, SrFeL = S-rich Fe melt, FeS = Fe-S solid (single alloy), SrFeL2 = S-rich Fe melt (single alloy).

determined using wavelength dispersive spectroscopy (WDS) on the 5-spectrometer JEOL JXA-8530F HyperProbe Electron Probe Micro-Analyzer (EPMA) at the Netherlands National Geological Facility, Utrecht University. We used a series of silicate, oxide and metal standards and conditions of 15 nA beam current and 15 kV accelerating voltage. Analyses were made with a defocused beam to obtain the compositions of metal (2−10 μm diameter) and silicate (5−20 μm diameter) phases. Standards for the quantitative analysis of Mg, Fe, Si, Al and Ca in silicate minerals were forsterite, hematite, forsterite, corundum and diopside, respectively and the standard for Fe in iron alloys was Fe-metal. Counting times were 30 s for Fe (hematite and Fe-metal), Si, Mg and Al, and 20 s for Ca and S. Quantitative analysis of Pt, with the help of a Pt-metal standard, was also performed to assess contamination from the Pt capsule. To measure light element abundances in iron alloys, the carbon coating was removed and the samples and standards (natural troilite for S, pure Si metal for Si, magnetite for O and experimentally synthesized Fe_3C for C) were Al-coated together for each run to keep the X-ray absorption uniform. These analyses were performed using a JEOL JXA 8530F Hyperprobe at Rice University, Houston following the analytical protocol of Dasgupta & Walker (2008). Detection limits (3σ) of all elements are less than 0.03 wt% except for Pt (0.07 wt%). Data reduction was performed using the ϕ(rZ) correction (Armstrong, 1995). Instrument calibrations were deemed successful when the composition of secondary standards was reproduced within the error margins defined by the counting statistics.

3.3 Experimental observations

3.3.1 Phase assemblages and texture

Run product phases are listed in Table 3.2. A clear segregation into silicate and iron-rich phases can be seen in all three series of run products (Fig. 3.1). Resulting phase diagrams for experiments with SC, EC and TC compositions are compared with each other in Fig. 3.2. Oxygen fugacities of EC are lower than those of SC runs by an average value of 0.6 log units (Table 3.2) since sequential condensation models of Moriarty et al. (2014) are richer in oxygen than equilibrium chemistry models. The oxygen fugacities of carbon-saturated experiments with EC and TC bulk compositions are similar because the relative elemental abundances of equilibrium chemistry models, excluding carbon, for HD19994 and the Sun are largely the same (Table 4.1). Mass-balance calculations on iron alloys and silicate phases, excluding graphite, result in 10−18 wt% of iron alloys in SC runs and 23−27 wt% of iron alloys in EC/TC runs.

In our run products, graphite grains <1−100 μm in diameter (see Fig. 3.1a,b,d) were identified with EDS analyses showing a clear peak of carbon with no other elements. In EC runs with 5 wt% SiC in their starting material we did not find any SiC grains, suggesting the formation of graphite via the oxidation of silicon in SiC. Since our experiments were conducted in graphite capsules, all our run products are graphite-saturated, and hence graphite is a stable phase in all runs.

Olivine crystals are present in all runs. Orthopyroxene is present in all EC runs except the run at 1 GPa and 1823 K, and all TC runs except the runs at 1 GPa and 1723−1823 K. The

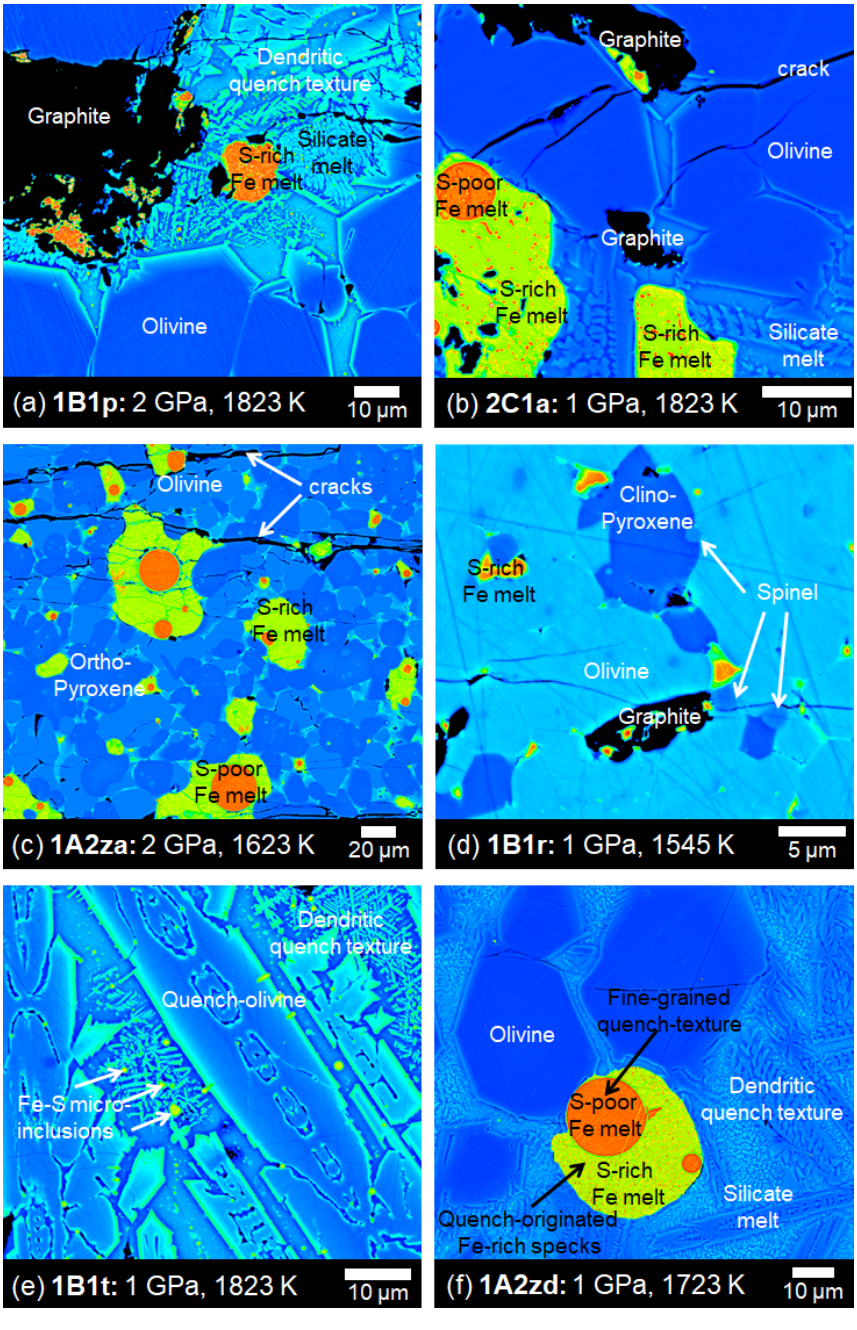

Figure 3.1: False-color backscattered electron images of six representative run products illustrating different phases and textural types. Phases can be broadly categorized into graphite, iron alloys and silicate phases. Silicate melts show a typical dendritic quench texture. Iron alloys show a fine-grained quench texture.

absence of orthopyroxene in SC runs is due to their higher oxygen fugacities and corresponding higher FeO content. Clinopyroxene is present only at 1 GPa and the lowest temperature in all three series. In SC runs at 1 GPa and 1545−1623 K, spinel is also identified. Silicate melts and iron alloys are usually concentrated between the boundaries of silicate crystals and at the top or edges of capsules. The proportion of silicate melt increases with temperature and decreases with pressure. The solidus of silicate melt in SC runs is lower than in EC/TC runs due to higher oxygen fugacities and corresponding higher FeO content.

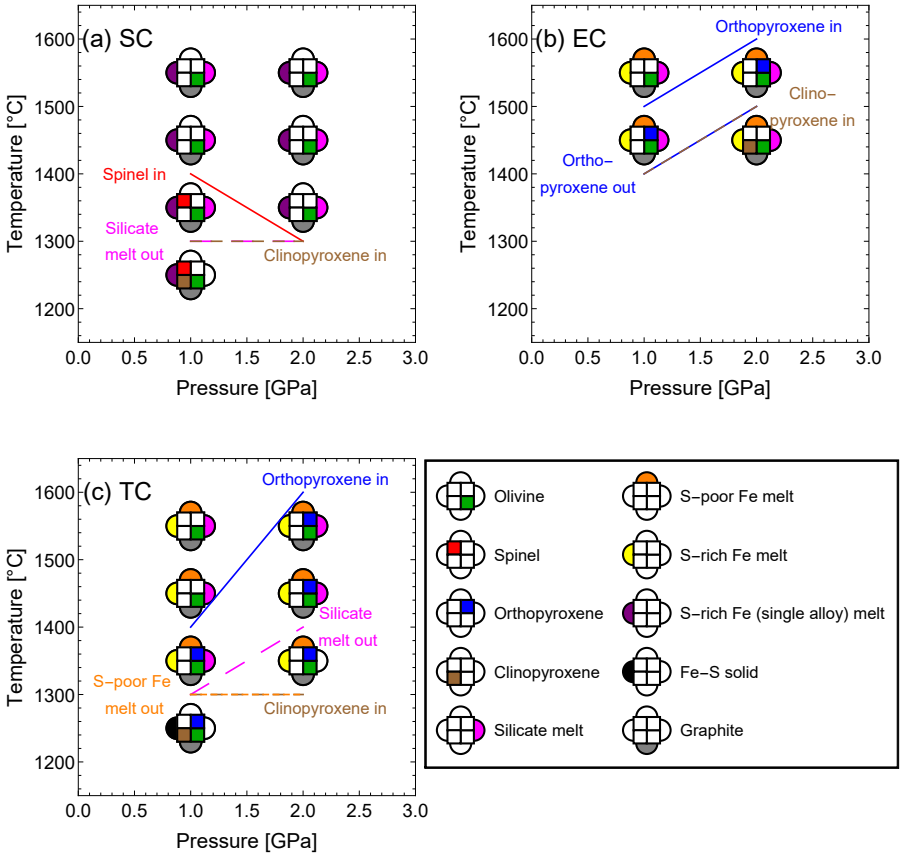

Figure 3.2: Phase diagrams of SC (a), EC (b) and TC (c) run products. Solid and dashed lines represent major phase changes in the direction of lower temperatures.

Iron alloys are present in all runs. In all EC/TC runs except TC run at 1 GPa and 1523 K containing solid Fe-S, two immiscible iron-rich melts (S-rich Fe melt and S-poor Fe melt) are identified. S-poor Fe melt is observed as almost spherical blebs usually surrounded by S-rich Fe melt (see Fig. 3.1b,c,f). This immiscibility is attributed to the chemical interactions

between carbon and sulfur. Such liquid metal immiscibility in Fe-C-S systems has been observed for a range of S/Fe ratios in previous studies (e.g. Wang et al., 1991; Corgne et al., 2008; Dasgupta et al., 2009). The S/Fe ratio in iron-rich melts of our EC/TC runs is within this range (see Sect. 3.3.2). In contrast, SC runs do not exhibit liquid metal immiscibility and contain a single alloy of S-rich Fe melt, since the S/Fe ratio in this series is beyond the range where immiscibility exists (see below).

As a result of quenching, the silicate melt exhibits a dendritic texture as shown in Fig. 3.1a,b,e,f. Dendrites in SC runs (e.g., Fig. 3.1a,e) are 5−10 times larger than in EC/TC runs (e.g., Fig. 3.1b,f). Quenching also results in the growth of thin rims at the boundaries of silicate crystals (e.g., Fig. 3.1a). These thin rims sometimes have a saw-toothed edge and are thicker in SC runs than in EC/TC runs, perhaps due to different viscosities and hence transport properties of the melts involved owing to different oxygen fugacities (e.g., Giordano et al., 2008). These textures are observed in melt regions because quenching is a non-instantaneous process leading to rapid exsolution and crystallization of melt. The silicate melt also contains Fe-S micro-inclusions resulting from the exsolution of the original melt upon quenching (see Fig. 3.1e), similar to observations made in the study of Boujibar et al. (2014).

The iron-rich melts show a fine-grained quench texture supporting the interpretation of a liquid state during the experiments. In EC/TC runs, the immiscibility of S-poor and S-rich Fe melts is evident from the sharp boundaries between them (see Fig. 3.1a,c,f). Sub-micron sized iron-rich specks seen in S-rich Fe melt, surrounding the S-poor Fe blebs, are likely a result of unmixing upon quenching.

3.3.2 Phase compositions

Tables 4.2 and 4.3 list the compositions of silicate and iron-rich phases, respectively. The lithophile elements, Mg, Si, Al and Ca are bonded to oxygen in silicate phases. O is largely present in silicate phases and to a smaller extent in iron-rich melts. S mainly partitions into iron-rich phases with smaller amounts present in silicate melts. Fe is distributed among silicate and iron-rich phases. Most of the carbon is present as graphite and a smaller amount is present in iron alloys.

Olivine crystals and silicate melts in EC/TC runs are richer in MgO and poorer in FeO than in SC runs. The Mg# , or Mg/(Mg+Fe) mol% of olivine in EC/TC and SC runs is between 75−87 and 55−75, respectively. Similarly, the Mg# of silicate melt in EC/TC and SC runs is between 60−65 and 25−50, respectively. Orthopyroxene, found only in certain EC/TC runs, has Mg# between 80−87. The SiO_2 content of silicate melt in EC/TC runs (44−50 wt%) is higher than in SC runs (33−41 wt%). These differences between EC/TC and SC runs are a direct consequence of lower oxygen fugacities of EC/TC runs ($\log f_{O_2}$ ∼IW−1.1) compared to SC runs ($\log f_{O_2}$ ∼IW−0.5) (see Table 3.2). The MgO content of olivine, orthopyroxene and silicate melt increases and the FeO content decreases with temperature.

Table 3.3: Composition of silicate phases

Run no.	n	SiO_2	MgO	FeO	Al_2O_3	CaO	S	Sum	K_D	K'_D
Olivine										
1B1t	19	38.5 (0.1)	39.9 (0.1)	21.3 (0.1)	0.1 (0.0)	0.1 (0.0)	<DL	99.9 (0.1)	0.26	0.26
1B1p	10	38.2 (0.1)	40.0 (0.1)	20.9 (0.2)	0.1 (0.0)	0.1 (0.0)	<DL	99.3 (0.1)	0.32	0.28
1B1f	12	37.6 (0.1)	37.7 (0.1)	23.7 (0.1)	0.1 (0.0)	0.1 (0.0)	<DL	99.3 (0.1)	0.27	0.26
1B1j	10	36.5 (0.1)	34.5 (0.3)	28.5 (0.5)	0.1 (0.0)	0.2 (0.0)	<DL	99.9 (0.3)	0.30	0.26
1B1q	10	35.3 (0.1)	29.8 (0.4)	34.0 (0.1)	0.2 (0.2)	0.3 (0.1)	<DL	99.5 (0.2)	0.25	0.27
1B1w	10	37.0 (0.1)	34.5 (0.2)	27.5 (0.2)	0.1 (0.0)	0.2 (0.0)	<DL	99.4 (0.1)	0.25	0.25
1B1r	9	35.4 (0.3)	28.2 (0.3)	35.0 (0.1)	0.6 (0.5)	0.4 (0.1)	<DL	99.5 (0.3)	–	–
2C1a	9	39.4 (0.1)	48.0 (0.1)	12.9 (0.1)	0.1 (0.0)	0.1 (0.0)	<DL	100.5 (0.1)	0.24	0.29
2C1d	10	39.7 (0.1)	43.7 (0.3)	17.6 (0.1)	0.2 (0.2)	0.2 (0.1)	<DL	100.5 (0.2)	0.38	0.28
2C1e	10	38.6 (0.1)	44.7 (0.6)	16.1 (0.7)	0.2 (0.2)	0.2 (0.0)	<DL	99.8 (0.4)	0.26	0.28
2C1c†	10	38.0 (0.2)	39.7 (0.2)	21.5 (0.3)	0.5 (0.2)	0.2 (0.0)	<DL	99.9 (0.2)	–	–
1A2y	10	40.3 (0.3)	44.7 (0.1)	15.0 (0.1)	0.0 (0.0)	0.1 (0.0)	<DL	100.2 (0.2)	0.31	0.28
1A2zc	9	39.9 (0.1)	42.8 (0.1)	16.7 (0.1)	0.1 (0.0)	0.1 (0.0)	<DL	99.5 (0.1)	0.35	0.28
1A2zd	11	39.9 (0.2)	45.2 (0.5)	14.3 (0.5)	0.0 (0.0)	0.1 (0.0)	<DL	99.6 (0.3)	0.31	0.28
1A2a†	8	38.4 (0.2)	41.9 (0.3)	19.6 (0.2)	0.1 (0.0)	0.2 (0.0)	<DL	100.2 (0.2)	–	–
1A2c†	7	37.5 (0.3)	42.4 (0.5)	19.5 (0.1)	0.1 (0.0)	0.3 (0.0)	<DL	99.9 (0.3)	–	–
1A2za	17	39.7 (0.1)	40.5 (0.2)	19.7 (0.1)	0.1 (0.0)	0.2 (0.0)	<DL	100.3 (0.1)	–	–
1A2s	8	38.6 (0.1)	40.7 (0.2)	20.3 (0.3)	0.1 (0.0)	0.2 (0.0)	<DL	99.8 (0.2)	–	–
Orthopyroxene										
2C1d	8	54.8 (0.2)	30.8 (0.4)	10.7 (0.4)	3.0 (0.4)	0.9 (0.1)	<DL	100.3 (0.3)	0.32	
2C1e	8	56.4 (0.6)	31.8 (0.2)	9.5 (0.1)	2.0 (0.4)	0.8 (0.0)	<DL	100.6 (0.3)	0.22	
1A2zc	10	56.4 (0.1)	30.8 (0.1)	10.9 (0.1)	0.9 (0.0)	0.7 (0.0)	<DL	99.8 (0.1)	0.32	
1A2a†	8	54.8 (0.1)	29.8 (0.5)	12.2 (0.1)	2.0 (0.2)	1.2 (0.1)	<DL	100.0 (0.2)	–	
1A2c†	8	53.7 (0.9)	30.4 (0.4)	12.1 (0.2)	2.3 (0.1)	1.3 (0.1)	<DL	99.8 (0.5)	–	
1A2za	17	55.8 (0.5)	28.6 (0.4)	12.4 (0.3)	2.3 (0.4)	1.5 (0.2)	<DL	100.7 (0.3)	–	
1A2s	7	53.3 (1.2)	28.9 (0.6)	12.1 (0.4)	3.1 (0.5)	2.1 (0.1)	<DL	99.5 (0.7)	–	
Clinopyroxene										
1B1r	10	48.6 (0.4)	20.0 (0.4)	21.1 (0.1)	7.3 (0.6)	2.4 (0.4)	<DL	99.4 (0.4)		
2C1c†	4	51.2 (0.4)	25.3 (0.4)	13.8 (0.4)	7.5 (0.6)	2.3 (0.1)	<DL	100.0 (0.4)		
1A2s	8	49.2 (0.5)	17.8 (1.0)	7.3 (0.2)	9.3 (0.9)	15.8 (1.0)	<DL	99.4 (0.8)		
Spinel										
1B1q	8	0.3 (0.1)	13.3 (0.1)	24.6 (0.2)	60.9 (0.3)	0.1 (0.0)	<DL	99.1 (0.2)		
1B1r	7	0.7 (0.4)	12.9 (0.2)	27.3 (0.1)	58.6 (0.6)	0.1 (0.0)	<DL	99.6 (0.4)		
Silicate melt										
1B1t	9	37.0 (0.5)	17.0 (1.2)	34.2 (1.1)	6.1 (0.7)	3.2 (0.3)	0.7 (0.2)	98.1 (0.8)		
1B1p	10	41.9 (0.4)	17.0 (0.5)	27.9 (0.5)	6.6 (0.3)	3.2 (0.1)	0.6 (0.1)	97.0 (0.3)		
1B1f	10	39.6 (0.3)	13.5 (0.4)	31.2 (0.4)	7.4 (0.2)	4.2 (0.1)	0.8 (0.1)	96.8 (0.3)		
1B1j	8	33.5 (0.5)	14.0 (1.8)	38.9 (1.5)	7.2 (1.3)	3.4 (0.6)	0.4 (0.0)	97.4 (1.1)		
1B1q	10	38.2 (0.3)	7.0 (0.7)	32.0 (0.3)	12.8 (0.3)	7.1 (0.2)	0.6 (0.0)	97.8 (0.4)		
1B1w	11	33.9 (0.3)	12.0 (1.4)	38.5 (0.6)	8.9 (1.0)	4.1 (0.5)	0.8 (0.2)	98.1 (0.8)		
2C1a	6	50.0 (1.4)	15.2 (2.5)	17.3 (1.4)	9.2 (1.2)	5.3 (0.6)	0.3 (0.1)	97.2 (1.4)		
2C1d	6	43.7 (1.9)	19.7 (3.7)	21.0 (1.3)	8.7 (2.1)	4.9 (1.0)	0.1 (0.0)	98.1 (2.0)		
2C1e	8	48.4 (1.0)	11.3 (2.5)	15.7 (1.1)	13.4 (1.6)	8.0 (0.8)	0.2 (0.0)	97.0 (1.4)		
1A2y	14	50.6 (0.5)	18.8 (1.7)	20.6 (0.8)	5.2 (0.3)	4.1 (0.3)	0.4 (0.1)	99.7 (0.8)		
1A2zc	11	45.4 (0.7)	19.9 (0.4)	22.1 (0.5)	6.1 (0.2)	4.8 (0.2)	0.3 (0.1)	98.7 (0.4)		
1A2zd	10	50.8 (0.5)	19.6 (0.9)	19.7 (0.4)	4.8 (0.3)	3.7 (0.3)	0.3 (0.1)	99.1 (0.5)		

Note: All compositions are in wt% with 1σ error given in parentheses. Sulfur in silicate melts is reported as S since oxygen fugacities are much lower than needed to form sulfates (Jugo et al., 2005, 2010). Runs marked † contain silicate melt in small quantities but could not be measured using EPMA. n is the number of analytical points. DL: detection limit. Pt is <DL in all silicate phases. K_D is the olivine-silicate melt FeO-MgO exchange coefficient and K'_D is the corrected exchange coefficient from Toplis (2005) (see Appendix 3.C for mineral-melt equilibrium calculations).

Table 3.4: Composition of iron-rich phases

Run no.	n/m	Fe	Pt	Si	C	S	O	Sum
S-rich Fe melt (single alloy)								
1B1t	10/4	62.7 (0.3)	0.4 (0.3)	0.4 (0.5)	0.7 (0.4)	29.1 (0.6)	5.7 (0.8)	98.9 (0.5)
1B1p	12/5	61.1 (0.6)	1.6 (0.4)	0.1 (0.1)	0.5 (0.2)	33.6 (1.3)	3.5 (2.9)	100.5 (0.7)
1B1f	8/10	62.6 (0.2)	0.3 (0.2)	0.1 (0.1)	0.4 (0.2)	30.3 (0.9)	5.1 (0.8)	98.8 (0.5)
1B1j	9/9	63.0 (0.8)	1.8 (0.4)	0.2 (0.1)	0.5 (0.2)	29.4 (1.2)	6.5 (1.0)	101.3 (0.7)
1B1q	8/8	64.0 (0.3)	0.4 (0.1)	0.1 (0.1)	0.2 (0.1)	28.5 (1.7)	6.0 (1.6)	99.3 (1.0)
1B1w	9/10	63.4 (0.2)	0.1 (0.1)	0.3 (0.1)	0.4 (0.2)	29.4 (0.9)	6.7 (0.6)	100.3 (0.5)
1B1r	8/9	61.9 (1.0)	0.9 (0.8)	<DL	0.3 (0.1)	37.3 (0.2)	0.7 (0.2)	101.1 (0.5)
S-rich Fe melt								
2C1a	5/10	69.2 (0.3)	<DL	<DL	1.0 (0.7)†	30.3 (0.2)	0.9 (0.3)†	101.4 (0.2)
2C1d	5/10	70.3 (1.4)	0.2 (0.1)	<DL	1.0 (0.7)	27.0 (0.4)	0.9 (0.3)	99.4 (0.6)
2C1e	5/4	68.8 (1.9)	0.1 (0.1)	<DL	1.6 (0.7)	30.2 (1.0)	1.3 (0.8)	102.0 (1.0)
2C1c	5/4	69.4 (1.0)	0.3 (0.1)	<DL	1.6 (0.7)†	28.9 (1.2)	1.3 (0.8)†	101.6 (0.8)
1A2y	10/10	68.4 (0.3)	<DL	<DL	0.4 (0.2)	29.8 (0.9)	1.0 (0.5)	99.6 (0.4)
1A2zc	7/7	68.6 (0.8)	0.3 (0.1)	<DL	0.6 (0.1)	29.7 (1.6)	1.1 (0.1)	100.3 (0.7)
1A2zd	15/11	69.2 (0.9)	0.3 (0.0)	<DL	0.4 (0.1)	30.2 (1.2)	0.6 (0.2)	101.6 (0.6)
1A2a	14/5	69.3 (1.2)	0.2 (0.1)	<DL	0.4 (0.1)	29.7 (1.4)	0.9 (0.4)	100.7 (0.8)
1A2c	8/10	68.9 (0.9)	0.1 (0.0)	<DL	0.6 (0.2)	30.2 (1.1)	0.6 (0.2)	100.4 (0.6)
1A2za	8/5	69.4 (0.6)	0.3 (0.1)	<DL	0.8 (0.5)	29.4 (0.6)	1.1 (0.2)	100.9 (0.4)
S-poor Fe melt								
2C1a	5/20	94.0 (0.5)	0.5 (0.1)	<DL	3.6 (0.2)	0.9 (0.1)	0.4 (0.0)	99.4 (0.2)
2C1d	5/16	89.0 (0.5)	3.5 (0.1)	<DL	3.2 (0.2)	1.9 (0.1)	0.4 (0.0)	98.0 (0.2)
2C1e	4/5	93.8 (0.5)	0.2 (0.0)	<DL	5.4 (1.0)	1.7 (0.3)	0.4 (0.0)	101.4 (0.5)
2C1c	4/12	88.3 (0.2)	4.4 (0.2)	<DL	4.5 (0.3)	1.1 (0.1)	0.2 (0.0)	98.5 (0.2)
1A2y	13/10	90.9 (0.4)	3.6 (0.4)	<DL	2.1 (0.1)	1.0 (0.1)	0.3 (0.0)	97.8 (0.2)
1A2zc	13/9	87.4 (0.6)	6.4 (0.4)	<DL	3.6 (0.6)	1.4 (0.2)	0.3 (0.0)	99.2 (0.4)
1A2zd	9/11	87.1 (0.3)	6.4 (0.2)	<DL	3.3 (0.2)	1.0 (0.2)	0.2 (0.0)	98.1 (0.2)
1A2a	7/10	88.2 (0.7)	6.4 (0.5)	<DL	4.3 (0.4)	1.3 (0.2)	0.3 (0.0)	100.4 (0.4)
1A2c	10/10	89.1 (0.8)	5.1 (0.8)	<DL	4.5 (0.5)	1.0 (0.2)	0.3 (0.1)	100.0 (0.5)
1A2za	17/13	86.2 (0.5)	8.3 (0.3)	<DL	4.5 (0.9)	1.6 (0.2)	0.2 (0.1)	100.9 (0.4)
Fe-S solid								
1A2s	9/5	61.3 (0.1)	0.2 (0.1)	<DL	0.5 (0.2)	38.9 (0.1)	0.3 (0.1)	101.1 (0.1)

Note: All compositions are in wt% with 1σ error given in parentheses. n is the number of analytical points for Fe and Pt, and m is the number of analytical points for other elements. DL means below detection limit. Mg, Ca and Al are <DL in all iron-rich phases. The Pt contamination is 0−2.2 mol% in S-poor Fe melt, negligible in S-rich Fe melt and 0−0.4 mol% in S-rich Fe melt (single alloy). The numbers marked with † were not measured for that phase and have been taken from the same phase of another run product at similar conditions.

Since olivines do not accommodate significant amounts of the oxides of Ca and Al, they are present only in silicate melt and/or pyroxenes. Orthopyroxenes and clinopyroxenes contain a combined 2−5 wt% and 10−25 wt% of CaO and Al_2O_3, respectively. The similarity in CaO and Al_2O_3 contents of clinopyroxenes between SC and EC runs and their differences from TC runs are due to the differences in starting Ca/Si and Al/Si ratios. Silicate melts contain 0.1−0.8 wt% S, with higher values of S seen mainly in SC runs, which is likely due to their higher FeO contents than in the EC/TC runs (e.g., Smythe et al., 2017). The formation of spinel in the SC run at 1 GPa and 1545−1623 K and its absence in TC runs is likely due to a higher Al/Si ratio of the SC composition.

Across EC/TC runs exhibiting liquid metal immiscibility, the S-poor Fe melt contains 86−94 wt% Fe, 3.9 ± 0.9 wt% C, 1.3 ± 0.3 wt% S and 0.3 ± 0.1 wt% O. The variable Fe content is a result of the variable Pt contamination of 0−8 wt% (0−2 mol%) from the outer Pt capsules surrounding the inner graphite capsules. The S-rich Fe melt contains 69.2 ± 0.5 wt% Fe, 0.8 ± 0.5 wt% C, 29.5 ± 1.1 wt% S and 1.0 ± 0.3 wt% O. The S-rich Fe melt (single alloy) in SC runs contains 62.7 ± 0.9 wt% Fe, 0.4 ± 0.1 wt% C, 29−37 wt% S and 1−7 wt% O (∼36 wt% S+O, equivalent to sulfur's composition in iron sulfide). The higher amount of oxygen in SC iron alloys is likely due to their higher oxygen fugacity with respect to EC/TC iron alloys.

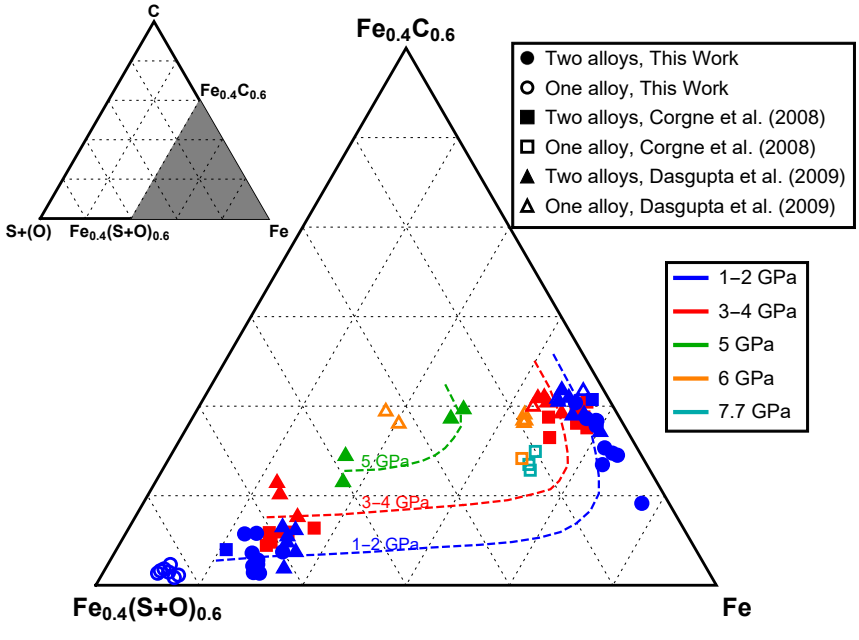

Figure 3.3: Liquid metal immiscibility in the Fe-C-S system compared with results from previous studies. For all studies, O measurements are added to S. For Corgne et al. (2008), Ni measurements are added to Fe. The hand-drawn dashed lines based on the experiments considered here represent the compositional variation of immiscible S-poor and S-rich Fe melts with pressure.

Fig. 3.3 illustrates that our measurements of S-rich and S-poor Fe melts exhibiting immiscibility are in excellent agreement with the studies of Corgne et al. (2008) and Dasgupta et al. (2009). The single alloys from our SC runs are clustered together in the lower left corner of Fig. 3.3 and their composition is a reflection of the starting composition, as is the case for single alloys reported in Corgne et al. (2008) and Dasgupta et al. (2009).

The molar S/Fe ratio in bulk iron-rich melts of our SC runs is $\sim$0.85, which is higher than that of our EC and TC runs having $\sim$0.4 and $\sim$0.25, respectively. Up to pressures of 4$-$6 GPa, Dasgupta et al. (2009) observed immiscibility for S/Fe ratios of $\sim$0.1 and $\sim$0.33 and miscibility for S/Fe ratios of 0.02 and 0.06. Corgne et al. (2008) also found immiscibility at S/Fe$\sim$0.15. Since the miscibility gap closes above 4$-$6 GPa, some runs contain single alloys despite having characteristic S/Fe ratios. Combined with our results this implies that immiscibility is observed in the Fe-C-S system for moderate S/Fe ratios between $\sim$0.1$-$0.8 up to pressures of 4$-$6 GPa. For lower or higher S/Fe ratios, a single iron-rich melt is expected.

3.4 Mineralogy and structure of C-enriched rocky exoplanets

3.4.1 Mineralogy

Our experiments show that silicate minerals, iron-rich alloys and graphite dominate the mineralogy in differentiated C-enriched planetary interiors. In addition to the C/O ratio, the oxygen fugacity and the Mg/Si, Al/Si, Ca/Si and S/Fe ratios play an important role in determining the mineralogy in carbon-rich conditions. Our oxygen fugacity conditions (IW$-$0.3$<\log f_{O_2}<$IW$-$1.2) are a direct reflection of the chemical modeling calculations of Moriarty et al. (2014) who derived the bulk composition of planetesimals in protoplanetary disks. However, oxygen fugacity can vary over a larger range either because of its dependence on pressure implying its change with depth in planetary interiors, or due to the formation in protoplanetary disks of more reducing bulk compositions than the ones we used in this study. Here we place our results in a broader context of C-enriched planetary interiors by combining our results with previous studies.

At IW$<\log f_{O_2}<$IW$-$2 and up to $\sim$4$-$6 GPa, our study and previous studies (e.g., Dasgupta et al., 2009, 2013) show that iron-rich melts are composed of single alloys or two immiscible alloys in the Fe-C-S system depending on the S/Fe ratio. The immiscible S-poor and S-rich Fe melts show characteristic solubilities with $\sim$5 wt% C and $\sim$1 wt% S, and $\sim$1 wt% C and $\sim$30 wt% S, respectively. At pressures higher than $\sim$4$-$6 GPa, a closure of the miscibility gap will allow only single Fe-C-S alloys (Corgne et al., 2008; Dasgupta et al., 2009). With decreasing $\log f_{O_2}$ from IW$-$2 to IW$-$6, the solubility of C in Fe decreases and the solubility of Si in Fe increases (Deng et al., 2013; Li et al., 2016). At even lower oxygen fugacities ($\log f_{O_2}\sim$IW$-$6.2), C is not soluble in Fe and about $\sim$20 wt% Si is present (Takahashi et al., 2013). Morard & Katsura (2010) show that the Fe-S-Si system also exhibits liquid metal immiscibility similar to the Fe-C-S system at $\log f_{O_2}\sim$IW$-$10, although this miscibility gap closes at approximately 25 GPa. If the temperature is lower than the liquidus in the Fe-C$\pm$S$\pm$Si system, solids such as Fe, FeS, Fe_3C, Fe_7C_3 and Fe-Si can form depending on pressure and f_{O_2} (Deng et al., 2013).

Takahashi et al. (2013) found olivine to be a dominant silicate mineral in the FMS+CO system at IW$-1<\log f_{O_2}<$IW-3.3 and 4 GPa. Our experiments in the FCMAS+CSO system at IW$-0.3<\log f_{O_2}<$IW-1.2 and $1-2$ GPa showed a larger variety in silicate minerals such as orthopyroxene, clinopyroxene and spinel, in addition to olivine. The diversity in silicates increases with decreasing temperature. The compositions of these silicate minerals are sensitive to f_{O_2} and Mg/Si, Ca/Si and Al/Si ratios. At their lowest $\log f_{O_2}$ ~IW-6.2, Takahashi et al. (2013) find periclase to be a dominant mineral because of decreased concentration of SiO_2. At pressures above 25 GPa, olivine polymorphs break down to form perovskite and ferropericlase (Hirose & Fei, 2002).

We do not observe any carbonates in our runs since magnesite and calcite are stable only in very oxidizing conditions, $\log f_{O_2}>$IW$+1$ (Rohrbach & Schmidt, 2011; Lazar et al., 2014). We also do not find silicon carbide in our runs, as it forms only at extremely reducing conditions, $\log f_{O_2}$ ~IW-6.2 (Takahashi et al., 2013). Our starting compositions, which represent realistic elemental abundances of C-enriched planetesimals, do not present such extremes in oxygen fugacity and these minerals seem unlikely to form in the magma ocean stage of the type of planets we have considered. However, highly reduced planets with depleted oxygen relative to major rock-forming elements such as Si and Mg may stabilize silicon carbide in their magma ocean stage.

Carbon solubility in the interior of the Earth is key in driving the terrestrial carbon cycle (Dasgupta, 2013). Similarly, carbon solubility is expected to impact the carbon cycles and habitability on C-enriched rocky exoplanets (Unterborn et al., 2014). Although we do not measure the carbon abundance in silicate melts of our experiments, Li et al. (2015, 2016) give an upper limit of ~200 ppm C in silicate melts at oxygen fugacity conditions similar to our experiments. The C-solubility in S-poor Fe melts is $3-9$ wt% (Rohrbach et al., 2014; Boujibar et al., 2014; Li et al., 2015, 2016, and this study), which is more than two orders of magnitude larger than the C-solubility in silicates.

In Fig. 3.4, we plot the C-solubility in the mantle and core against core mass percent (excluding graphite) for our experiments and those from Corgne et al. (2008) and Takahashi et al. (2013). Since all experiments are carbon-saturated, this figure essentially gives the minimum amount of carbon in a planet that is necessary to achieve carbon-saturation in the planet during its magma ocean stage. For a C-enriched exoplanet with a EC/TC-like composition and 25% of its mass in the core, ~0.7 wt% C (molar C/O~0.03) is sufficient for carbon-saturation. For a C-enriched exoplanet with a SC-like composition and 10% of its mass in the core, ~0.05 wt% C (C/O~0.002) is sufficient for carbon-saturation. For an extreme case with a zero core mass, the minimum amount of carbon needed for carbon-saturation is 200 ppm (C/O~0.001). In contrast, if the core mass percent is Mercury-like (70%), assuming 9 wt% C in the core, 6 wt% C (C/O~0.5) is needed for carbon-saturation. Once carbon-saturation is achieved, an increase in C/O ratio increases only the amount of graphite produced, and has a negligible impact on the mineralogy of silicates or iron-alloys. The solubilities of carbon for the experiments considered in Fig. 3.4 is lower than the 9 wt% C-solubility from Boujibar et al. (2014) because of the difference in oxygen fugacities and/or the presence of two Fe alloys where S-rich Fe melts have lower C-solubility than S-poor Fe

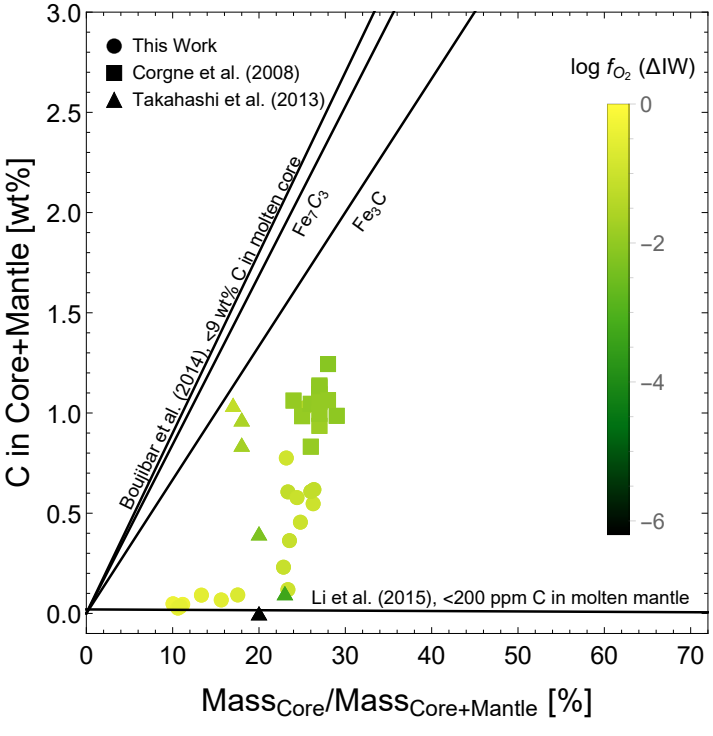

Figure 3.4: Experimental measurements of carbon solubility in iron alloys is plotted against the core mass percent. Solid lines give upper bounds on carbon solubility in a molten iron-rich core and a molten silicate mantle.

melts, which decreases the net C-solubility in the iron-rich core. The C-solubility in the core is more or less the same for $\log f_{O_2}$ from IW to IW$-$2, whereas it decreases with a further decrease in $\log f_{O_2}$ from IW$-$2 to IW$-$6.2, where it becomes negligible.

3.4.2 Interior structure

High temperatures during planet formation enable melting and chemical segregation of several minerals (Elkins-Tanton, 2012). These minerals eventually undergo gravitational stratification. For C-enriched rocky exoplanets, iron alloys, silicates and graphite are the main categories of minerals based on densities. Due to density contrasts of more than 40% between graphite and silicates and more than 50% between silicates and iron alloys, three major gravitationally stable layers are expected to form in these exoplanets: an iron-rich core, a silicate mantle and a graphite layer on top of the silicate mantle.

For smaller C-enriched rocky exoplanets (with interior pressures < 4 GPa) showing Fe-C-S liquid metal immiscibility, S-poor Fe alloy will form the inner core and S-rich Fe alloy will form the outer core because of the density contrasts between the two alloys. Our mass-balance calculations show that the core/mantle mass ratio would be $\sim$0.33 for planets with EC/TC compositions and $\sim$0.15 for planets with SC composition. Even though the core/-mantle ratio is similar for EC and TC compositions, the S-poor Fe inner-core to the S-rich Fe outer-core mass ratio would be about 0.7 for TC planets and about 1.6 for EC planets owing to a difference in the S/Fe ratio. For C-enriched exoplanets with core pressures larger than 6 GPa, there would be no stratification in the core because of the closure of the miscibility gap. For planets with extremely reducing cores showing Fe-S-Si immiscibility, again an inner and an outer core would exist (e.g., Morard & Katsura, 2010). Depending on composition, pressure, temperature and f_{O_2}, cores may stratify into multiple metal-rich layers, for instance, a solid Fe_3C inner core with a liquid S-rich Fe outer core, or a solid Fe inner core surrounded by a solid Fe_3C middle core and a liquid FeS outer core (e.g., Deng et al., 2013).

Even though C-enriched rocky exoplanets are expected to contain large amounts of carbon, olivine and pyroxenes would be the common mantle minerals, similar to C-poor rocky planets. Additionally, minerals such as spinel and garnet may be abundant in the upper mantle for planets depending on Al/Si and Ca/Si ratios, which might also vary as shown by the models of Carter-Bond et al. (2012a). For larger C-enriched rocky exoplanets, high-pressure phases of these minerals, ferropericlase and perovskite and/or post-perovskite would be the most abundant minerals in the lower mantle.

Graphite will likely form a flotation layer on top of the magma ocean or silicates such as olivine because of its lower density. Graphite is expected to be in its solid state because the melting temperature of the graphite-diamond system exceeds 4500 K for all pressures in a planetary interior (Kerley & Chhabildas, 2001). If the graphite layer extends deep into the planet exceeding pressures of 2$-$15 GPa and depending on the temperature, diamond would form beneath graphite. Since diamond is denser than graphite with a density comparable to some silicate minerals, convection, if it exists, in the mantle may strip off diamonds from

beneath the graphite layer. This would result in a diamond-silicate mantle similar to the mantle discussed by Unterborn et al. (2014).

3.5 A C-enriched interior for Kepler-37b

3.5.1 Effect of a graphite layer on the derived mass

Transit photometry is used to measure the radius of exoplanets (Batalha, 2014). Follow-up stellar radial velocity measurements help to put constraints on their masses, but for most of the rocky exoplanets, masses are currently unknown. Due to graphite's significantly lower density compared to silicate minerals and iron-rich alloys, the mass of an exoplanet in the presence of significant amounts of graphite would be lower than expected for a given radius. To quantify the effect of graphite on a planet's mass, we compute the interior structure and mass of the smallest known exoplanet till date, Kepler-37b with radius of 0.34 $\mathrm{R}_{\oplus}$ (Stassun et al., 2017), by following the isothermal recipe to solve the hydrostatic and Poisson's gravitational gradient equations and keeping the radius fixed (e.g., Unterborn et al., 2016). We implement the third-order Birch-Murnaghan equation of state in order to provide a relation between density and pressure (Birch, 1947). Since we are interested in the effect of graphite on its total mass, we assume Kepler-37b is fully differentiated with a pure iron or iron sulfide core, an enstatite mantle and a graphite layer. To model the equations of state, we use the thermoelastic data of graphite (Colonna et al., 2011), enstatite (Stixrude & Lithgow-Bertelloni, 2005), iron (Fei et al., 2016) and iron sulfide (Sata et al., 2010).

Applying a core/mantle mass ratio of 0.33, similar to our EC/TC results, and assuming a pure Fe core and an enstatite mantle to the interior structure model of Kepler-37b, the derived mass is 0.26 times the martian mass (0.26 $\mathrm{M}_{\male}$). When a 33.3 wt% graphite layer is assumed on top of its mantle keeping the core/mantle mass ratio at 0.33, the total mass becomes 0.21 $\mathrm{M}_{\male}$ (about 19% less). In fact, a graphite layer of 10 wt% of the planet's total mass is sufficient to decrease the derived mass of Kepler-102b by 7% (see Fig. 3.5.1). Assuming a hypothetical 100 wt% graphite-only planet gives a mass of 0.16 $\mathrm{M}_{\male}$ (about 40% less). For models with a FeS core instead of pure Fe, a similar trend can be seen (Fig. 3.5.1). With future missions such as TESS (Ricker et al., 2014), CHEOPS (Fortier et al., 2014) and PLATO (Ragazzoni et al., 2016), the masses and radii of rocky exoplanets will be measured with higher accuracy. This will allow better constraints on the presence of low density C-bearing minerals such as graphite in their interior of rocky exoplanets such as Kepler-37b.

We also show the internal pressure distribution of Kepler-37b in Fig. 3.5.1 for the cases of 0, 10, 33.3, 66.7 and 100 wt% graphite. The central pressure of Kepler-37b decreases with the amount of graphite. For our models of Kepler-37b, pressures at the bottom of graphite layers are <4 GPa, making phase transformation to diamond impossible at temperatures above 1000 K (Kerley & Chhabildas, 2001). C-enriched rocky exoplanets larger than Kepler-37b with thick graphite layers are likely to form diamonds beneath these graphite layers. If the amount of diamond is significantly larger than that of graphite, the effect on the derived mass of the planet would be smaller since the density of diamond is higher than graphite and comparable to silicates.

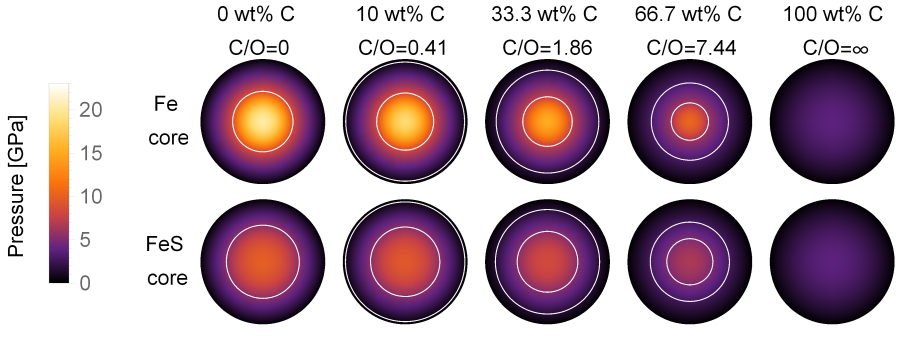

(a)

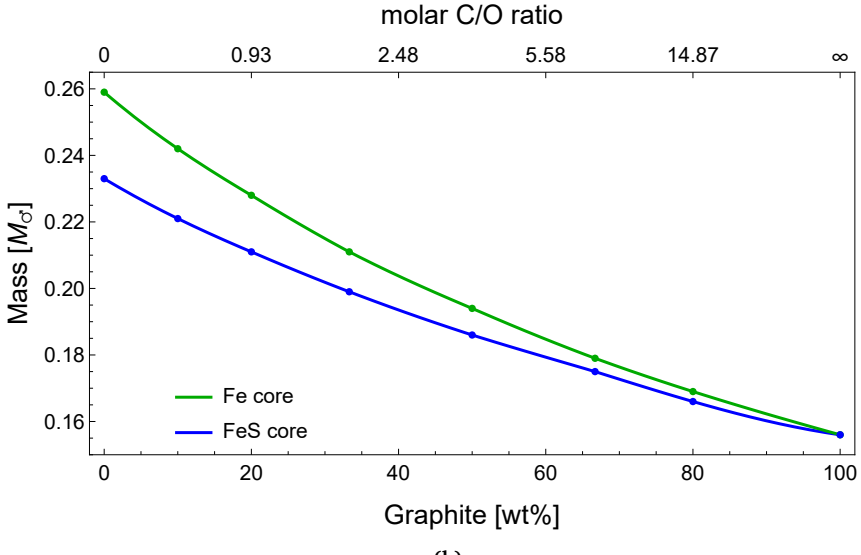

(b)

Figure 3.5: (Bottom) Solid lines represent the derived mass of Kepler-37b assuming a pure iron or an iron sulfide core, an enstatite mantle and a graphite crust with a core/mantle mass ratio of 0.33 and different mass fractions of graphite for a fixed planet's radius of 0.34 $R_\oplus$ (Stassun et al., 2017). (Top) The internal pressure distribution of Kepler-37b is also shown for five cases where white contours represent the core-mantle and mantle-crust boundaries.

much lower than expected for a C-poor planet. Similarly, a darkening agent discovered on Mercury's surface has been speculated to be graphite (Peplowski et al., 2016).

Small C-enriched exoplanets are unlikely to retain a primary atmosphere. Secondary atmospheres of graphite-layered planets might be non-existent if the graphite layers are able to completely isolate the silicate mantles. For planets with relatively thin graphite layers, outgassing processes from the silicate mantle may allow for an atmosphere to exist. Atmospheres of C-enriched rocky exoplanets are believed to be devoid of oxygen-rich gases (e.g., Kuchner & Seager, 2005). Carbon is dissolved in silicate melts mainly as CO_2 at $\log f_{O_2}$ >IW−1 and mainly as CH_4 and partially as CO_2 at $\log f_{O_2}$ <IW−1 (Li et al., 2015). Future observations of exoplanetary atmospheric gases such as CO/CO_2 or CH_4 will not imply existence or absence of graphite-rich surfaces.

If the graphite layer is several hundreds of kilometers thick, it might not allow direct recycling of the mantle material to the surface. Such a graphite surface without essential life-bearing elements other than carbon will make the planet potentially uninhabitable. However, deep silicate volcanism, along with the presence of water, may still alter the surface composition of a C-enriched rocky exoplanet during the course of its evolution. To comment more on this topic, detailed studies on planetary evolution need to be conducted.

3.6 Summary and conclusions

We performed the first high-pressure high-temperature experiments on chemical mixtures representing bulk compositions of small C-enriched rocky exoplanets at 1 AU from their host star computed by a study modeling the chemistry in the protoplanetary disk of a high C/O star. Our results show that fully differentiated C-enriched rocky exoplanets consist of three major types of phases forming an iron-rich core, a silicate mantle and a graphite (and diamond) layer on top of the silicate mantle. Their mineralogy depends on oxygen fugacity and Mg/Si, Al/Si, Ca/Si, S/Fe and C/O ratios. For S/Fe ratios in iron alloys between 0.1 and 0.8 and at pressures below ∼4−6 GPa, the core stratifies into a S-poor Fe inner core surrounded by a S-rich Fe outer core. The variety in mantle silicate minerals is largely independent of the C/O ratio. The sequential condensation model from Moriarty et al. (2014) at 1 AU from the host star result in C-enriched rocky exoplanets with higher oxygen fugacity conditions compared to the equilibrium condensation model. High C/O ratios in planet-forming refractory material do not necessarily imply reducing conditions as the amount of C has no direct impact on the oxygen fugacity. Extremely reducing (<IW−6) or oxidizing conditions (>IW+1) would be able to stabilize silicon carbide or carbonates such as calcite and magnesite, respectively, in C-enriched planetary interiors. The minimum amount of carbon needed for carbon-saturation in the type of C-enriched rocky exoplanets considered in this study is 0.05−0.7 wt% (molar C/O∼0.002−0.03), which lies between the upper bounds of 200 ppm and 9 wt% for mantle-only and core-only planets, respectively. Any amounts of carbon exceeding the carbon-saturation limit would be in the form of graphite. If the graphite layer is deep enough to exceed pressures of 2−15 GPa, depending on the temperature profile, a diamond layer would exist beneath the graphite layer. Carbon in the form of graphite can

significantly affect the mass of an exoplanet for a fixed radius. For example, only a 10 wt% graphite crust is sufficient to decrease the derived mass of Kepler-37b by 7%, a difference detectable by future space missions focusing on determinations of both mass and radius of rocky exoplanets with insignificant gaseous envelopes. Rocky exoplanets with graphite-rich surfaces would appear dark in future observations because of low albedos due to graphite. Atmospheres of such planets are likely thin or non-existent and detection of CO/CO_2 or CH_4 on its own cannot confirm the presence or absence of a graphite-rich surface. Surfaces of such planets are less likely to be hospitable for life because of the lack of life-bearing elements other than carbon.

Acknowledgements

This work is part of the Planetary and Exoplanetary Science Network (PEPSci), funded by the Netherlands Organization for Scientific Research (NWO, Project no. 648.001.005). We are grateful to Sergei Matveev and Tilly Bouten from Utrecht University for their technical assistance during EPMA measurements at Utrecht University. We thank Rajdeep Dasgupta for facilitating analyses of light elements in metals in the EPMA Laboratory at Rice University. We are also thankful to Jack Moriarty for providing data from the (Moriarty et al., 2014) study.

Appendices

3.A Experimental sample assembly

Sample powder was inserted in a 1.6 mm-wide graphite capsule with a graphite lid (Fig. 3.6). This graphite capsule was put into a 2 mm-wide Pt capsule which was sealed and arc-welded on both ends using a Lampert PUK 3 welder. The Pt capsule was placed in a MgO rod sealed with MgO cement. The MgO rod was introduced in a graphite furnace, thermally insulated by surrounding it with an inner pyrex sleeve and an outer talc sleeve. A four-bore Al_2O_3 rod through which thermocouple wires were threaded, was placed on the top of MgO rod. Pressure calibration of the assembly was performed by bracketing the albite to jadeite plus quartz and fayalite to ferrosilite plus quartz transitions (van Kan Parker et al., 2011). The resulting pressure correction of 3% is consistent with literature data (McDade et al., 2002). On top of the talc-pyrex assembly, a hardened silver steel plug with a pyrophillite ring and a hole for thermocouple was placed. A $W_{97}Re_3/W_{75}Re_{25}$ (type D) thermocouple was placed in the thermocouple hole directly above the Pt capsule. The distance of $1-3.5$ mm between the thermocouple tip and the sample produced a temperature difference of 10 K (Watson et al., 2002).

3.B Oxygen fugacity calculations

We computed oxygen fugacity (f_{O_2}) in our experiments with respect to the iron-wüstite (IW) buffer by using the following equation:

$$\log f_{O_2}(\Delta\mathrm{IW}) = 2\log \frac{X_{\mathrm{FeO}}^{\mathrm{sil}} \cdot \gamma_{\mathrm{FeO}}^{\mathrm{sil}}}{X_{\mathrm{Fe}}^{\mathrm{alloy}} \cdot \gamma_{\mathrm{Fe}}^{\mathrm{alloy}}}, \tag{3.1}$$

where $X_{\mathrm{FeO}}^{\mathrm{sil}}$ and $\gamma_{\mathrm{FeO}}^{\mathrm{sil}}$ are the mole fraction and the activity of FeO in silicate melt, and $X_{\mathrm{Fe}}^{\mathrm{alloy}}$ and $\gamma_{\mathrm{Fe}}^{\mathrm{alloy}}$ are the mole fraction and the activity of Fe in S-rich Fe alloy. We assumed a non-ideal solution behavior of silicate melt and iron alloy, which implies non-unity values for $\gamma_{\mathrm{FeO}}^{\mathrm{sil}}$ and $\gamma_{\mathrm{Fe}}^{\mathrm{alloy}}$. A fixed value of $\gamma_{\mathrm{FeO}}^{\mathrm{sil}} = 1.5$, the average from the two studies that determined $\gamma_{\mathrm{FeO}}^{\mathrm{sil}}$ for a wide range of melt compositions were used (Holzheid et al., 1997;

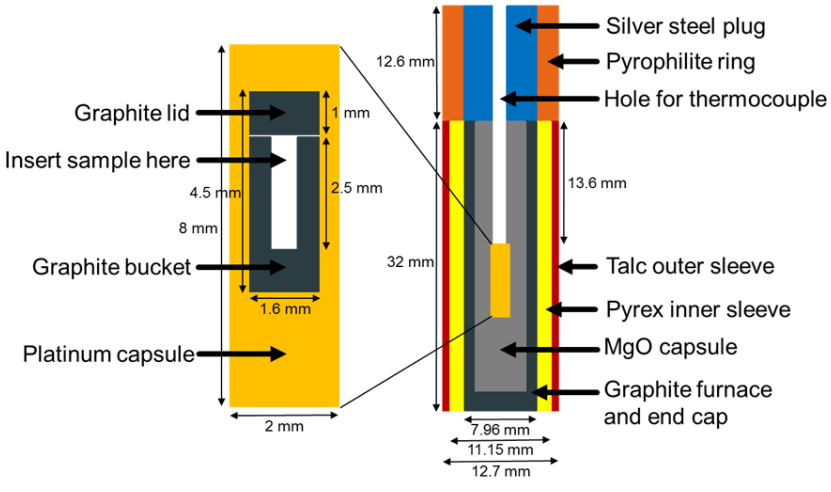

Figure 3.6: Components of the assembly used to perform high-pressure experiments.

O'Neill & Eggins, 2002), assuming no significant pressure effect on $\gamma_{\mathrm{FeO}}^{\mathrm{sil}}$ (Toplis, 2005). For $\gamma_{\mathrm{Fe}}^{\mathrm{alloy}}$, we computed $\gamma_{\mathrm{Fe}}^{\mathrm{alloy}}$ from Lee & Morita (2002) using

$$\ln \gamma_{\mathrm{Fe}}^{\mathrm{alloy}} = \frac{\alpha_2}{2}(1 - X_{\mathrm{Fe}}^{\mathrm{alloy}})^2 + \frac{\alpha_3}{3}(1 - X_{\mathrm{Fe}}^{\mathrm{alloy}})^3 + \frac{\alpha_4}{4}(1 - X_{\mathrm{Fe}}^{\mathrm{alloy}})^4, \tag{3.2}$$

where $\alpha_2 = 3.80$, $\alpha_3 = -5.24$ and $\alpha_4 = 2.58$ at 1623 K, $\alpha_2 = 4.01$, $\alpha_3 = -5.52$ and $\alpha_4 = 2.71$ at 1723 K and $\alpha_2 = 4.25$, $\alpha_3 = -5.84$ and $\alpha_4 = 2.87$ at 1823 K. In the absence of silicate melts, as in some of our experiments, we used X_{FeO} of olivine instead. Our oxygen fugacity calculations are given in Table 3.2.

3.C Mineral-melt equilibrium

To assess mineral-melt equilibrium, we calculated olivine-melt and orthopyroxene-melt Fe-Mg exchange coefficients, K_D and K'_D, following Kushiro & Walter (1998) and Toplis (2005), respectively.

$$K_{D\ \mathrm{Olv-Melt}}^{\mathrm{Mg-Fe}} = \frac{X_{\mathrm{Melt}}^{\mathrm{Mg}} / X_{\mathrm{Olv}}^{\mathrm{Mg}}}{X_{\mathrm{Melt}}^{\mathrm{Fe}} / X_{\mathrm{Olv}}^{\mathrm{Fe}}} \tag{3.3}$$

$$K'_{D\ \mathrm{Olv-Melt}}^{\mathrm{Mg-Fe}} = \exp\left[\left(\frac{-6766}{RT} - \frac{7.34}{R}\right) + \ln[0.036 X_{\mathrm{Melt}}^{\mathrm{SiO_2}} - 0.22] + \left(\frac{3000(1 - 2Y_{\mathrm{Olv}}^{\mathrm{Mg/(Mg+Fe)}})}{RT}\right) + \left(\frac{0.035(P-1)}{RT}\right)\right] \tag{3.4}$$

where $X_{\mathrm{b}}^{\mathrm{a}}$ is mol% of a in b, $Y_{\mathrm{Olv}}^{\mathrm{Mg/(Mg+Fe)}}$ is molar Mg/(Mg+Fe) in olivine, R is the gas constant, T is temperature in K and P is pressure in bar. Our calculations of K_D and K'_D for all runs result in values between 0.22−0.38 and 0.24−0.28, respectively (see Table 4.2). According to Toplis (2005), this range is consistent with equilibrium. For orthopyroxene in the TC run at 2 GPa and 1823 K, and the EC runs at 1 GPa and 1723 K and 2 GPa and 1823 K, K_D ranges between 0.21−0.32, also within the acceptable range for equilibrated systems.

Chapter 4

Capturing the oxidation of silicon carbide in rocky exoplanetary interiors

Kaustubh Hakim, Wim van Westrenen, Carsten Dominik

Astronomy & Astrophysics, 2018, 618, L6

Abstract

Theoretical models predict the condensation of silicon carbide around host stars with C/O ratios higher than 0.65 (cf. $C/O_{Sun} = 0.54$), in addition to its observations in meteorites, inter-stellar medium and protoplanetary disks. Consequently, the interiors of rocky exoplanets born from carbon-enriched refractory material are often assumed to contain large amounts of silicon carbide. Here we aim to investigate the stability of silicon carbide in the interior of carbon-enriched rocky exoplanets and to derive the reaction leading to its transformation. We perform a high-pressure high-temperature experiment to investigate the reaction between a silicon carbide layer and a layer representative of a carbon-enriched rocky exoplanet's bulk composition. We report the reaction leading to oxidation of silicon carbide producing quartz, graphite and molten iron silicide. Combined with previous studies, we show that in order to stabilize silicon carbide, carbon-saturation is not sufficient, and a complete reduction of Fe^{2+} to Fe^{0} in a planetary mantle is required, suggesting that future spectroscopic detection of Fe^{2+} or Fe^{3+} on the surface of rocky exoplanets would imply the absence of silicon carbide in their interiors.

4.1 Introduction

Silicon carbide grains have been observed in meteorites (Huss et al., 2003), in the interstellar medium (Min et al., 2007), and in protoplanetary disks (Fujiyoshi et al., 2015). Although the Earth is poor in carbon, carbon-rich carbonaceous chondrite meteorites, diamonds discovered in the ureilite parent body (Nabiei et al., 2018), and the proposed presence of graphite on Mercury's surface (Peplowski et al., 2016) suggest locally carbon-rich environments in

the early solar system. Moreover, chemical simulations of protoplanetary disks around host stars with C/O ratios higher than 0.65 (cf. $C/O_{Sun} = 0.54$) result in the condensation of refractory minerals ranging from oxides, silicates, and metals to silicon carbide and graphite (Bond et al., 2010b; Carter-Bond et al., 2012b; Moriarty et al., 2014). Dynamical simulations show that these refractory minerals end up in the interiors of rocky exoplanets in different proportions with up to 47 wt% carbon (Carter-Bond et al., 2012b). Because of the low density of the carbon-bearing minerals, silicon carbide and graphite are used to explain the low-density rocky exoplanets in the mass-radius diagram with insignificant gas envelopes (Seager et al., 2007; Madhusudhan et al., 2012).

Because of speculations of silicon carbide in exoplanetary interiors, physical properties of silicon carbide are being studied extensively at high pressures and temperatures (Wilson & Militzer, 2014; Nisr et al., 2017; Daviau & Lee, 2017; Miozzi et al., 2018). Significant amounts of silicon carbide in exoplanetary interiors would have a major impact on the thermal evolution and geodynamical processes on such exoplanets because its thermal conductivity is abnormally high (Nisr et al., 2017). There is no question that silicon carbide is highly refractory in nature because its extremely high melting temperatures facilitate its survival in protoplanetary disks once formed. However, the pressures in the interior of planets are orders of magnitude higher than those in protoplanetary disks, which strongly affects its stability.

Laboratory experiments suggest that SiC is not stable at high-pressure high-temperature conditions resembling those in carbon-enriched exoplanetary interiors (Hakim et al., 2018b). Moissanite (naturally occurring SiC), a rare mineral in the Earth, is known to be unstable in the carbon-poor conditions dominating Earth's mantle and crust, and its formation in Earth is attributed to extremely reducing local conditions (Schmidt et al., 2014; Golubkova et al., 2016). Experiments in the Fe-Mg-Si-C-O (FMS+CO) system show that silicon carbide is stable only at extremely low oxygen fugacities of about 6 log units below the iron-wüstite (IW) buffer ($\log f_{O_2}$=IW−6) (Takahashi et al., 2013). At oxygen fugacities above IW−6, silicon carbide becomes oxidized, but it is not clear which reaction drives the instability of silicon carbide in a carbon-enriched exoplanetary interior. In this study, we performed an experiment at 1 GPa and 1823 K by juxtaposing an SiC layer and a bulk composition representative of a small carbon-enriched rocky exoplanet (Hakim et al., 2018b) (see Table 4.1).

4.2 Experimental and analytical method

4.2.1 Starting materials

We prepared a mixture of eight major elements (Fe, O, Si, Mg, Al, Ca, S, and C) representative of the bulk composition of a carbon-enriched exoplanet. The proportions of elements in these mixtures are based on the sequential condensation modeling of the protoplanetary disk of HD19994 at 1 astronomical unit (AU) and 0.15 Myr from the study by Moriarty et al. (2014) (see Table 4.1). To prepare the chemical mixtures, the starting materials were mixed in proportions shown in Table 4.1. In the first step, SiO_2 (99.9% SiO_2 powder from Alfa-Aesar), MgO (99.95% MgO powder from Alfa-Aesar), Al_2O_3 (99.95% min alpha Al_2O_3 powder from

Alfa-Aesar), $CaCO_3$ (99.95-100.05% ACS chelometric standard $CaCO_3$ powder from Alfa-Aesar), and Fe_2O_3 (99.9% Fe_2O_3 powder from Alfa-Aesar) were homogenized with an agate mortar under ethanol. The oxide-carbonate mixture was decarbonated in a box furnace by gradually increasing the temperature from 873 K to 1273 K in six hours. The decarbonated mixture, placed in a Pt-crucible, was first subjected to 1873 K in a box furnace for 30 minutes and then quenched to room temperature by immersing the bottom of the Pt-crucible in water, leading to the formation of glass. The glass was ground to a homogeneous powder using an agate mortar under ethanol. Fe (99.95% Fe powder, spherical, <10 microns from Alfa-Aesar) and FeS (99.9% FeS powder from Alfa-Aesar) were then added to the glass powder. In the carbon-enriched case, C (99.9995% Ultra F purity graphite powder from Alfa-Aesar) was also added to the glass powder. The final mixture was again homogeneously ground with an agate mortar and stored in an oven at 383 K until use. SiC (-400 mesh particle size, $\geqslant$ 97.5% SiC from Alfa-Aesar) was also ground with an agate mortar and stored separately.

Table 4.1: Bulk composition of a carbon-enriched planetesimal based on protoplanetary disk evolution modeling around high C/O stars from Moriarty et al. (2014)

Element	mol%	Material	wt%
Si	11.4	SiO_2	30.1
Mg	11.4	MgO	20.2
O	45.8	FeO†	27.3
Fe	11.4	Fe	2.2
S	1.9	FeS	7.0
Al	1.4	Al_2O_3	3.1
Ca	0.7	CaO†	1.7
C	16.0	C	8.4

† CaO and FeO are obtained from $CaCO_3$ and Fe_2O_3 after decarbonation. The starting composition reflects the composition of the powder after the decarbonation.

4.2.2 High-pressure high-temperature experiments

The experiment was conducted in an end-loaded piston-cylinder apparatus at a pressure of 1 GPa and temperature of 1823 K in a 12.7 mm (half-inch) sample assembly. Carbon-enriched composition powder was inserted in a 1.6 mm wide graphite capsule, filling the capsule approximately 60 percent by volume. Silicon carbide powder was inserted on top of the carbon-enriched planetary bulk composition, filling the remaining 40 percent by volume of the capsule. The capsule was then sealed with a stepped graphite lid. This graphite capsule was put into a 2 mm wide Pt capsule that was sealed and arc-welded on both ends using a Lampert PUK 3 welder. The Pt capsule was placed in a MgO rod sealed with MgO cement to hold the Pt capsule in place. The MgO rod was introduced in a graphite furnace, thermally insulated by surrounding it with an inner pyrex sleeve and an outer talc sleeve. A four-bore Al_2O_3 rod through which thermocouple wires were threaded was placed on the top of MgO

rod. Pressure calibration of the assembly was performed by bracketing the albite to jadeite plus quartz and fayalite to ferrosilite plus quartz transitions (van Kan Parker et al., 2011). The resulting pressure correction of 3% is consistent with literature data (McDade et al., 2002). A hardened silver steel plug with a pyrophillite ring and a hole for thermocouple were placed on top of the talc-pyrex assembly. A $W_{97}Re_3/W75Re_{25}$ (type D) thermocouple was placed in the thermocouple hole directly above the Pt capsule. The distance of $1-3.5$ mm between the thermocouple tip and the sample produced a temperature difference of $\sim$10 K (Watson et al., 2002). To reduce the porosity of the graphite capsule, the sample assembly was sintered at 1073 K and 1 GPa for 1 h before further heating and pressurization. During heating to run temperature, the pressure was increased continuously using the hot-piston-in technique. The temperature was increased at a rate of 100 K/min. The experiment was run for the duration of 3.5 h and was subsequently quenched to $<$500 K within $\sim$15 s by switching off the electric power to the heater.

4.2.3 Analytical procedure

The recovered samples were mounted in one-inch diameter mounts using petropoxy resin, cut longitudinally, polished with grit-paper and fine-polished down to a 1/4 μm finish. The polished samples were carbon-coated to ensure electrical conductivity of the surface during electron probe micro-analysis (EPMA). Major element contents of the experimental charges were determined using wavelength dispersive spectroscopy on the five-spectrometer JEOL JXA-8530F Hyperprobe Field Emission Electron probe micro-analyzer at the Netherlands National Geological Facility, Utrecht University. For Fe-C and Fe-Si alloys, samples were coated with aluminum instead of carbon, and analyses were performed using a JEOL JXA 8530F Hyperprobe at Rice University, Houston following the analytical protocol (Dasgupta & Walker, 2008). We used a series of silicate, oxide, and metal standards and conditions of 15 nA beam current and 15 kV accelerating voltage. Analyses were made with a defocused beam to obtain the compositions of the metal ($2-10$ μm diameter) and silicate ($5-20$ μm diameter) phases. Standards for the quantitative analysis of Mg, Fe, Si, Al, and Ca in silicate minerals were forsterite, hematite, forsterite, corundum, and diopside, respectively. Standards used for measuring Fe, Si, C, S, and O were Fe-metal, Si-metal, experimentally synthesized Fe_3C, natural troilite, and magnetite, respectively. Counting times were 30 s for Fe (hematite and Fe-metal), Si, C, O, Mg, and Al, and 20 s for Ca and S. Data reduction was performed using the Φ(rZ) correction (Armstrong, 1995). The instrument calibration was deemed successful when the composition of secondary standards was reproduced within the error margins defined by the counting statistics.

4.3 Results and discussion

The backscattered electron image (Fig. 4.1a) of the experimental run product shows a clear reaction zone between the SiC layer (top) and the silicate-rich layer representing a carbon-enriched rocky exoplanet (bottom). Tables 4.2 and 4.3 give the compositions of the phases analyzed using wavelength-dispersive spectroscopy, whereas graphite was identified using

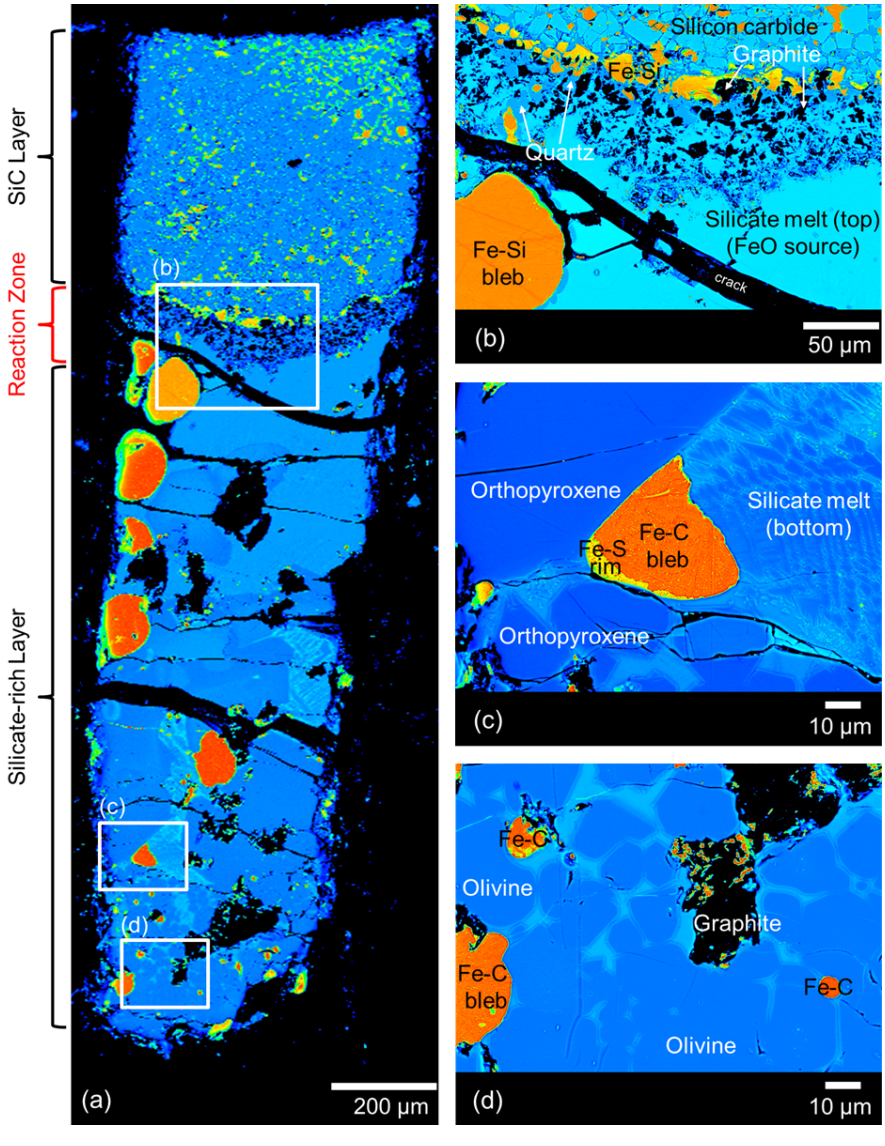

Figure 4.1: False-color backscattered electron images of the run product at 1 GPa and 1823 K. (a) A cross-section of the whole capsule is shown. The reaction zone lies between the silicon carbide layer and the silicate-rich layer representing a carbon-enriched rocky exoplanet. (b) The reactants (SiC and FeO from silicate melt) and the products (quartz, graphite, and Fe-Si alloy) are clearly visible. (c) One of the Fe-C blebs has a Fe-S rim, surrounded by orthopyroxene crystals and silicate melt. (d) At the bottom of the capsule, olivine crystals are present instead of orthopyroxene.

energy-dispersive spectroscopy. The reaction zone contains grains of C (graphite) and SiO_2 (quartz), and molten Fe-Si alloy (iron silicide) (Fig. 4.1b). SiC grains become oxidized in the reaction zone and no SiC is present in or below the reaction zone. Although most of Fe-Si alloy moves to the silicate-rich layer, a small portion of it moves up through the silicon carbide layer. The silicate melt pool present below the reaction zone is enriched in SiO_2 compared to the silicate melt at the bottom of the capsule because of the progressive dissolution of quartz formed in the reaction zone.

Table 4.2: Composition of silicate phases

Phase	n	SiO_2	MgO	FeO	Al_2O_3	CaO	S	Sum
Quartz specks	4	99.64 (0.49)	0.20 (0.17)	1.06 (0.17)	0.15 (0.06)	0.05 (0.03)	0.07 (0.05)	101.15 (0.23)
Silicate melt specks	9	62.86 (0.08)	19.92 (0.15)	5.02 (0.05)	6.44 (0.05)	4.46 (0.03)	0.13 (0.01)	98.84 (0.08)
Silicate melt pool	20	61.81 (0.21)	20.60 (0.44)	5.01 (0.15)	6.77 (0.08)	4.47 (0.24)	0.14 (0.00)	98.79 (0.23)
Orthopyroxene	10	58.31 (0.22)	36.38 (0.11)	4.12 (0.15)	0.56 (0.02)	0.37 (0.01)	<DL	99.73 (0.12)
Olivine (bottom)	12	41.47 (0.29)	52.95 (0.26)	5.48 (0.24)	0.12 (0.05)	0.11 (0.02)	<DL	100.13 (0.19)
Silicate melt (bottom)	8	53.37 (0.42)	26.45 (1.63)	6.16 (0.52)	8.21 (0.55)	4.28 (0.88)	0.10 (0.03)	98.58 (0.83)

Note: All compositions are in wt% with 1σ error given in parentheses. n is the number of analytical points. <DL implies the measurements were below the detection limit. Pt contamination in all metallic phases was below the detection limit of approximately 0.07 wt%. At these levels the activity of iron in these metal phases is unaffected (e.g., Steenstra et al., 2018, and references therein).

Table 4.3: Composition of metallic phases

Phase	n	Fe	Si	C	S	O	Sum
SiC specks	7	0.38 (0.03)	73.30 (0.18)	26.32 (0.09)†	<DL	–	100
Fe-Si specks	7	78.40 (0.09)	19.83 (0.29)	0.94 (0.18)‡	0.12 (0.01)	–	99.29 (0.18)
Fe-Si bleb	10	79.66 (0.10)	18.82 (0.24)	1.01 (0.15)‡	0.15 (0.01)	–	99.64 (0.15)
Fe-C bleb	11	93.75 (0.41)	<DL	4.33 (0.10)	0.79 (0.14)	0.64 (0.07)	98.87 (0.23)
Fe-S rim	8	65.90 (2.01)	<DL	1.66 (0.79)	31.22 (2.03)	0.74 (0.59)	98.78 (1.51)

Note: All compositions are in wt% with 1σ error given in parantheses. n is the number of analytical points. <DL implies the measurements were below the detection limit. – implies lack of measurements. † Calculated by subtracting the total from 100. ‡ C-abundance calculated using a model for C-solubility in Fe-Si from Steenstra et al. (submitted).

Previous experiments by Hakim et al. (2018b) have shown that the equilibrium phases for the bottom silicate-rich layer representing a carbon-enriched rocky exoplanet comprise graphite, olivine, silicate melt, and a S-rich Fe-C-S alloy. In the presence of SiC grains, the silicate phases in the silicate-rich layer become richer in MgO and poorer in FeO compared to compositions formed in the absence of the initial SiC layer. Quartz produced during the process reacts with olivine to produce orthopyroxene. The FeO contents of olivine and silicate melt in the previous study (Hakim et al., 2018b) were 34.2 ± 1.1 wt% and 21.3 ± 0.1 wt%, respectively, whereas we find the FeO content of olivine, orthopyroxene, and silicate melt to

be 4−6 wt%. There is about five times less FeO in the silicate-rich layer of our experiment than its equilibrium state in the absence of the SiC layer. Moreover, the formation of Fe-Si and S-poor Fe-C alloy melts implies that most of the Fe^{2+} initially bonded to oxygen is reduced to Fe^0 in this reaction. Since the reaction products observed in the reaction zone are quartz, iron silicide melt, and graphite, we report the following reaction consuming silicon carbide:

$$3\ \mathrm{SiC(s)} + 2\ \mathrm{Fe\text{-}O(l)} \rightarrow \mathrm{SiO_2(s)} + 2\ \mathrm{Fe\text{-}Si(l)} + 3\ \mathrm{C(s)}. \tag{4.1}$$

In the equation, Fe-O (l) denotes Fe^{2+} bonded to oxygen in silicate melt, and Fe-Si (l) denotes Fe^0 bonded to Si^0 in metallic liquid. An important consequence of the reduction of Fe^{2+} is that the molar Mg/(Mg+Fe) of olivine and other silicates (X_{Mg}) are very high because of the lack of FeO. In our experiment we find $X_{\mathrm{Mg}} \sim 0.95$ for olivine and orthopyroxene and $X_{\mathrm{Mg}} \sim 0.88$ for the silicate melt, which are significantly higher than the equilibrium state (Hakim et al., 2018b), $X_{\mathrm{Mg}} \sim 0.77$ for olivine and $X_{\mathrm{Mg}} \sim 0.47$ for the silicate melt. Experiments and theoretical modeling have shown that SiC and Fe-Si alloy can be equilibrated with olivine only when its $X_{\mathrm{Mg}} > 0.99$ (Schmidt et al., 2014; Golubkova et al., 2016). Experiments in carbon-saturated FMS+CO system also find SiC to be stable only when olivines have a very high X_{Mg} of 0.992 (Takahashi et al., 2013). We conclude that almost all Fe^{2+} should be in its reduced state, Fe^0, to stabilize SiC even in a carbon-enriched rocky exoplanetary interior.

Since the reaction is still in progress, the conditions at the top of the silicate-rich layer are more reducing than at its bottom. Therefore, Fe-Si alloy is only present within the original SiC layer and at the top of the silicate-rich layer, whereas the remainder of the silicate layer contains Fe±C±S alloys only. One Fe-C bleb at the bottom of the capsule is surrounded by a Fe-S alloy showing liquid metal immiscibility because of the lowered local S/Fe ratio, as shown in the previous study by Hakim et al. (2018b) (Fig. 4.1c). Similarly, orthopyroxene, which is relatively oxygen-poorer than olivine, is found in most of the silicate-rich layer except at the bottom where olivine is present. We do not find any SiC below the reaction zone, which also contains a large Fe-Si bleb. This suggests that SiC forms at even more reducing conditions than needed for the formation of the Fe-Si alloy, which is in contrast to previous modeling studies in the context of moissanite stability in the Earth's mantle, which suggested that SiC and Fe-Si alloy form together at the same oxygen fugacities (Schmidt et al., 2014; Golubkova et al., 2016).

The backscattered electron image (Fig. 4.1a) of the experimental run product shows a clear reaction zone between the SiC layer (top) and the silicate-rich layer representing a carbon-enriched rocky exoplanet (bottom). Tables 4.2 and 4.3 give the compositions of the phases analyzed using wavelength-dispersive spectroscopy, whereas graphite was identified using energy-dispersive spectroscopy. The reaction zone contains grains of C (graphite) and SiO_2 (quartz), and molten Fe-Si alloy (iron silicide) (Fig. 4.1b). SiC grains become oxidized in the reaction zone and no SiC is present in or below the reaction zone. Although most of Fe-Si alloy moves to the silicate-rich layer, a small portion of it moves up through the

silicon carbide layer. The silicate melt pool present below the reaction zone is enriched in SiO_2 compared to the silicate melt at the bottom of the capsule because of the progressive dissolution of quartz formed in the reaction zone.

Our experimental conditions are applicable to the magma ocean stage of Ceres- to Pluto-size exoplanets and planetesimals. Larger rocky exoplanets form from the collision and accretion of such planetesimals. Since silicon carbide is not stable in exoplanetary building blocks and based on the rapid pace of the reaction in our experiment, SiC is expected to completely disappear before the formation of larger exoplanets. There may still be cases where an exoplanetary interior is reducing, for example, through a bombardment of SiC-rich meteorites onto the protoplanet. In such a case, the core of the exoplanet will become larger because FeO in the mantle is reduced to Fe and formation of Fe-Si alloy, which will move to the core. This will enrich the core with Si, and the mantle will be deficient in FeO in this case.

In order for SiC to become a dominant mineral in a rocky exoplanet, our experiment indicates that the conditions should be so reducing that such a planet would already contain a Fe-Si alloy core, contrary to the assumption of a pure Fe core with a SiC-C mantle in previous studies (Madhusudhan et al., 2012; Nisr et al., 2017). Our results show that SiC is unstable until the conditions are extremely reducing, allowing only for traces of Fe^{2+}, and previous studies (Takahashi et al., 2013; Hakim et al., 2018b) show that graphite/diamond is the dominant carbon-bearing mineral. Hence, care should be taken when assuming SiC in the interior modeling of a carbon-enriched rocky exoplanet. Assuming no effects of atmosphere or water on the composition of the surface of a rocky exoplanet, if Fe^{2+} or even more oxidizing Fe^{3+} is present in the mantle, it should also be present on the surface. Since the presence of Fe^{2+} or Fe^{3+} implies the absence of SiC, future spectroscopic detections of Fe^{2+} or even more oxidizing Fe^{3+} on the surface of a rocky exoplanet would mean that its interior is devoid of SiC. The conversion of SiC into graphite as well as the presence of graphite in carbon-saturated but not extremely reduced rocky exoplanets would have important consequences for the surface composition and therefore for the habitability of such planets.

Acknowledgements

This work is part of the Planetary and Exoplanetary Science Network (PEPSci), funded by the Netherlands Organization for Scientific Research (NWO, Project no. 648.001.005). We are grateful to Sergei Matveev and Tilly Bouten from Utrecht University for their technical assistance during EPMA measurements at Utrecht University. We thank Damanveer Grewal and Rajdeep Dasgupta for performing and facilitating analyses of metals in the EPMA Laboratory at Rice University.

Chapter 5

Thermal evolution of rocky exoplanets with a graphite outer shell

Kaustubh Hakim, Arie van den Berg, Allona Vazan, Dennis Höning, Wim van Westrenen, Carsten Dominik

in preparation

Abstract

Both simulations of the chemical evolution of protoplanetary disks for stars with photospheric C/O ratios > 0.65 and laboratory experiments indicate that carbon-enriched rocky exoplanets contain large amounts of refractory carbon in the form of graphite, in addition to silicates and iron. Because graphite has the lowest density and iron has the highest density among graphite, silicates and iron, graphite is likely to form an outer shell on top of the silicate mantle and the iron core in rocky exoplanets, assuming differentiation. Here we apply a parameterized model of mantle convection to determine the heat transport in the graphite shell and the thermal evolution of rocky exoplanets with a graphite outer shell up to 25% of the total radius or 50% of the total mass. For the long-term evolution (> 200 Myr), we find conduction as the dominant heat transport mechanism in graphite shells. Our results show that the graphite outer shell produces a thermal shielding effect which reduces the cooling rate of the planetary interior. For planets with a graphite outer shell thickness < 500 km, thermal shielding is strong in the early evolution but has a small effect over several billion years of evolution. For planets with a graphite outer shell thickness > 500 km, the planetary mantles end up hotter by about 500 K after 1 Gyr and 200 K after 5 Gyr of their evolution compared to a similar planet not covered by graphite. Our application to a known exoplanet, Kepler-37b, assuming that it is covered by a graphite shell, shows that the thermal shielding effect dominates over the effect of reduced internal heating. Since the maximum possible graphite-shell thickness (i.e., the thickness beyond which graphite at the bottom of the shell would transform to diamond) for Earth-size and super-Earth-size planets

is less than 500 km, we do not expect a significant effect of a graphite outer shell on their long-term thermal evolution.

5.1 Introduction

Rocky exoplanets appear to be ubiquitous around all types of planet-hosting stars in our galaxy (Petigura et al., 2018). Mass-radius relations of rocky exoplanets hint at a large variety in their composition ranging from rock-iron compositions to ice-waterworlds (e.g., Valencia et al., 2006; Seager et al., 2007; Wagner et al., 2011; Hakim et al., 2018a). Other indications about their compositional diversity come from spectroscopic observations of their host stars which show a range in photospheric elemental ratios, especially Mg/Si and C/O (e.g., Bond et al., 2008; Delgado Mena et al., 2010). Chemical evolution simulations of the refractory material, the building blocks of rocky planets, in protoplanetary disks of these planet-hosting stars widen their compositional diversity even further, in particular in terms of their refractory C/O ratio (e.g., Bond et al., 2010b; Carter-Bond et al., 2012b; Moriarty et al., 2014).

Planet-hosting stars with molar C/O > 0.65 (cf. $\mathrm{C/O_{Sun}} \sim 0.54$) are capable of producing rocky exoplanets abundant in carbon (Moriarty et al., 2014). Although the accuracy of photospheric C/O ratio measurements of stars in the solar neighborhood is being debated (e.g., Delgado Mena et al., 2010; Petigura & Marcy, 2011; Nakajima & Sorahana, 2016; Brewer et al., 2016), there is a large spread in the reported C/O ratios ranging from 0.2 to 1.6. This hints that a substantial fraction of stars still may have photospheric C/O ratios exceeding 0.65 and consequently they are likely to host carbon-enriched rocky exoplanets. Even in our solar system, refractory carbon is not rare. Graphite and diamond have been observed in the ureilite parent body meteorites (Nabiei et al., 2018). Graphite is also speculated to be present on the surface of Mercury (Peplowski et al., 2016). The chemical-dynamical simulations of Carter-Bond et al. (2012b) accounting for giant planet migration show that the rocky planets around high C/O stars can contain up to 47 wt% carbon in addition to iron and silicates.

Because pressures in planetary interiors are orders of magnitude higher than pressures in protoplanetary disks, the refractory material formed in protoplanetary disks undergoes high-pressure high-temperature processing ensuing changes in mineralogy. Laboratory experiments of Hakim et al. (2018b) investigated the mineralogy and phase relations of carbon-enriched rocky exoplanets with compositions derived from the chemical simulations of Moriarty et al. (2014) of carbon-enriched protoplanetary disks. Hakim et al. (2018b) found that an iron-rich core and a silicate-rich mantle can dissolve carbon only up to an order of a per cent by weight and graphite (and diamond depending on the pressure) is the dominant carbon-bearing mineral in carbon-enriched rocky exoplanets. Since graphite is 40% less dense than regular silicate minerals and silicate melts, graphite is expected to form an outer shell on top of the silicate mantle in such planets assuming efficient buoyancy-driven segregation.

After planet formation and differentiation, the heat locked up in rocky planetary interiors (stemming both from accretion/differentiation processes and radioactive decay) is gradually released to space. From studies of the thermal evolution of the Earth and other solar system planets, it is clear that the outermost shell determines the efficiency of heat transfer from the interior to the surface and subsequently affects the interior dynamics including the tectonic mode, volcanism, deep volatile cycles as well as the presence of a magnetic field (e.g., Schubert et al., 2001). In turn, these processes greatly affect the habitability of the surface of a planet.

Physical properties, such as the planet radius and the interior layer thicknesses, as well as rock and mineral properties, such as thermal conductivity and viscosity, control the heat transport through convection, conduction or radiation. The contribution of convective heat transport is expressed by the Nusselt number, which increases with the vigor of thermal convection from a value of unity for purely conductive heat transport (Schubert et al., 2001).

The thermal evolution and interior dynamics in solar and extrasolar planetary bodies have been studied in detail for Earth-like compositions (e.g., Schubert et al., 1979; Spohn, 1991; Valencia et al., 2007c; van den Berg et al., 2010; Höning & Spohn, 2016). Several studies have focused on the thermal evolution in planetary layers with non-Earth-like mineralogies such as ice (e.g., Deschamps & Sotin, 2001; Deschamps & Lin, 2014, for icy satellites and dwarf planets), water and ice (e.g., Noack et al., 2016, for extrasolar waterworlds) and diamond (e.g., Unterborn et al., 2014, for carbon-enriched exoplanets). These studies found that composition has a direct impact on the heat transport and interior dynamics of planetary bodies and consequently on the potential for habitability.

The presence of graphite as an outer shell in carbon-enriched rocky exoplanets presents a unique problem and is likely to influence the planetary dynamics and habitability. In addition to its low density compared to silicate and iron-rich materials, graphite has other peculiar properties such as an order of magnitude higher thermal conductivity ($20-200\,\mathrm{W\,m^{-1}\,K^{-1}}$, Tyler & Wilson, 1953; Boylan, 1996; Hofmeister et al., 2014) than silicates ($3-6\,\mathrm{W\,m^{-1}\,K^{-1}}$, Kobayashi, 1974), a high melting temperature of about 4500 K at all pressures of its stability (Kerley & Chhabildas, 2001; Ghiringhelli et al., 2005) and metal-like specific heat of about $700\,\mathrm{J\,kg^{-1}\,K^{-1}}$ (Boylan, 1996). Unterborn et al. (2014) found that the high thermal conductivity of diamond ($\sim 3000\,\mathrm{W\,m^{-1}\,K^{-1}}$, Wei et al., 1993) has a significant impact on the cooling of the planet, although they assume diamond to be homogeneously mixed with the silicates due to their similar densities. To our knowledge, no study has focused on the thermal evolution of planets with a graphite shell.

In this paper, our goal is to evaluate to first order the effects of a graphite outer shell on the thermal evolution of rocky exoplanets. Graphite transforms into diamond at pressures between $2-15$ GPa depending on the temperature (Kerley & Chhabildas, 2001; Ghiringhelli et al., 2005). Here, we first apply our modeling scheme to small rocky planets where the pressure in the graphite shell remains below the graphite-diamond transition pressure. Then we discuss implications of our results for larger planets where diamond possibly mixes with the silicate mantle (Unterborn et al., 2014). In Sect. 5.2, we describe our one-dimensional parameterized thermal evolution model applied to the main layered reservoirs in these planets.

In Sect. 5.3, we first compare the duration of convective cooling for the silicate and graphite layers and establish the nature of heat transport in the graphite shell. Next we compute the thermal evolution of a generic planet consisting of an iron core and a silicate mantle by adding graphite shells of different thicknesses on top of the silicate mantle. Then we apply our modeling strategy to a known exoplanet, Kepler-37b and evaluate the effect of different amounts of carbon on the cooling rate of the planet. We summarize our results and discuss the implications on the potential for habitability of such planets in Sect. 5.4.

5.2 Modeling methods

5.2.1 Interior structure

To model the thermal evolution, realistic values of input parameters such as the average density of a layer, the surface gravity and others are needed (see Sect. 5.2.2). These values are determined by computing the planetary interior structure by integrating the equation describing the hydrostatic equilibrium and the Poisson's equation from the center to the surface as a function of the radial distance r, assuming a spherically symmetric and isotropic dependence of material properties. The equations are written as

$$\frac{dP}{dr} = -\rho g, \tag{5.1}$$

$$\frac{dg}{dr} = 4\pi G\rho - 2\frac{g}{r}, \tag{5.2}$$

where P is pressure, g is gravity, G is the gravitational constant and the density $\rho(P)$ is calculated using an equation of state. Although temperature has a small effect of the order of a few per cent on the density (e.g., Hakim et al., 2018a), we ignore the effect of temperature on material density for interior structure calculations. For a three-layered planet with a radius $R_{\rm surf}$ (see Fig. 5.1), three sets of these equations need to be solved and six boundary conditions are required: $P(R_{\rm surf}) = 0$, $g(0) = 0$ and four continuity conditions for P and g at the two interfaces of this three-layered planet. For material equations of state, we implement the equations of state of graphite (Colonna et al., 2011) for the graphite outer shell, $MgSiO_3$ (enstatite for $P < 25$ GPa and Mg-perovskite for $P > 25$ GPa, Stixrude & Lithgow-Bertelloni, 2011) for the silicate mantle, and hcp-Fe (Fei et al. (2016) for $P < 234$ GPa and Hakim et al. (2018a) for $P > 234$ GPa) for the iron core.

5.2.2 Thermal evolution model

In Sect. 5.3.1 we will show that convection in graphite shells is restricted to the very early evolution and conduction is the dominant heat transport mechanism for all but the earliest times of the planet history. Ignoring convection, we model the graphite shell as a purely conductive subdomain of the layered planet model. We combine the graphite shell with a heat reservoir representing an iron core and a convective silicate mantle. To couple the

thermal evolution of these three layers, we implement the following equations (see Fig. 5.1 for a schematic representation).

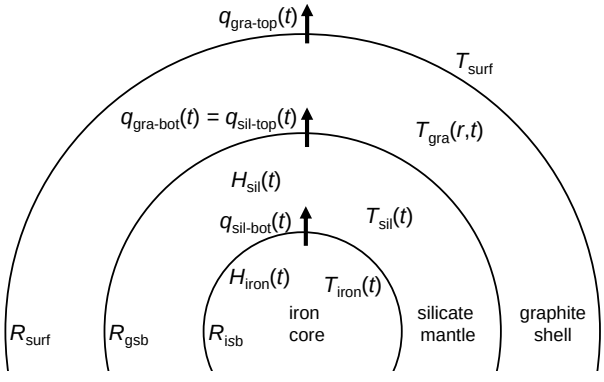

Figure 5.1: Three-layer thermal evolution model to model the coupled evolution of a planet with an iron core, a silicate mantle and a graphite shell.

The iron core is modeled as a heat reservoir with temperature T_{iron} described by an equation for the conservation of thermal energy (Schubert et al., 2001),

$$V_{\text{iron}}\rho_{\text{iron}}C_{P,\text{iron}}\frac{dT_{\text{iron}}}{dt} = V_{\text{iron}}\rho_{\text{iron}}H_{\text{iron}}(t) - A_{\text{isb}}q_{\text{sil-bot}}(t), \tag{5.3}$$

where $H_{\text{iron}}(t) = H_{\text{iron},0}\exp(-t/\tau_{\text{iron}})$ is the internal heating rate per unit mass due to radioactive decay in the core with a half-life τ_{iron}, $q_{\text{sil-bot}}(t)$ is the heat flux through the iron core-silicate mantle boundary (isb) at the bottom of the silicate mantle, A_{isb} is the area of the isb, V_{iron} is the volume of the core, ρ_{iron} is the average core density and $C_{P,\text{iron}}$ is the specific heat of the core.

The temperature of the silicate mantle, T_{sil}, is described by the equation for the conservation of thermal energy,

$$V_{\text{sil}}\rho_{\text{sil}}C_{P,\text{sil}}\frac{dT_{\text{sil}}}{dt} = V_{\text{sil}}\rho_{\text{sil}}H_{\text{sil}}(t) - A_{\text{gsb}}q_{\text{sil-top}}(t) + A_{\text{isb}}q_{\text{sil-bot}}(t), \tag{5.4}$$

where $H_{\text{sil}}(t) = H_{\text{sil},0}\exp(-t/\tau_{\text{sil}})$ is the internal heating rate per unit mass due to the radioactive decay with a half-life τ_{sil}, $q_{\text{sil-top}}(t)$ is the heat flux through the graphite-silicate boundary (gsb) at the top of the silicate mantle, A_{gsb} is the area of the gsb, V_{sil} is the volume of the silicate mantle, ρ_{sil} is the average mantle density and $C_{P,\text{sil}}$ is the specific heat of the mantle.
The heat flow density $q_{\text{sil-bot}}$ and $q_{\text{sil-top}}$ in Eqs. (5.3) and (5.4) can be expressed using the Nusselt number Nu, which gives the ratio of convective to conductive heat transfer,

$$q_{\text{sil}-j}(t) = \text{Nu}_j\frac{k\Delta T_j(t)}{h}, \quad j = \text{top}, \text{bot}, \tag{5.5}$$

where k is the thermal conductivity of the silicate mantle, h is the height of the silicate mantle and $\Delta T_j = 2\delta T_j$ are temperature contrast values across the convecting layer related to temperature contrasts δT_j across the thermal boundary layers respectively at the top and bottom of the convecting mantle.

The top/bottom Nusselt numbers are parameterized in terms of the Rayleigh number Ra by a power-law relation derived from thermal boundary layer analysis of Rayleigh-Bénard thermal convection (Schubert et al., 2001),

$$\mathrm{Nu}_j = f_N \mathrm{Ra}_j^{\beta}, \quad j = \mathrm{top}, \mathrm{bot}. \tag{5.6}$$

Several values between 0.19−0.35 have been proposed for the power-law exponent β depending on geometry, theory and experiments (Wolstencroft et al., 2009, and references

Table 5.1: Input parameters for thermal evolution modeling

Parameter	Value	Description
Material properties		
$\rho_{0,\mathrm{gra}}$ (kg/m^3)	2300	Average graphite density (Sect. 5.2.1)
$\rho_{0,\mathrm{sil}}$ (kg/m^3)	3300	Average enstatite density (Sect. 5.2.1)
$\rho_{0,\mathrm{iron}}$ (kg/m^3)	9000	Average iron density (Sect. 5.2.1)
$C_{P,\mathrm{gra}}$ (J K^{-1} kg^{-1})	700	Specific heat of graphite (Boylan, 1996)
$C_{P,\mathrm{sil}}$ (J K^{-1} kg^{-1})	1250	Specific heat of silicate (Schubert et al., 2001)
$C_{P,\mathrm{iron}}$ (J K^{-1} kg^{-1})	550	Specific heat of iron (Schubert et al., 2001)
α_{gra} (K^{-1})	3×10^{-5}	Thermal expansivity of graphite (Morgan, 1972)
α_{sil} (K^{-1})	3×10^{-5}	Thermal expansivity of silicate (Schubert et al., 2001)
k_{gra} (W m^{-1} K^{-1})	40	Thermal conductivity of graphite (Hofmeister et al., 2014)
k_{sil} (W m^{-1} K^{-1})	5	Thermal conductivity of silicate (Schubert et al., 2001)
E_{gra} (kJ mol^{-1})	209	Activation energy of graphite (Wagner & Driesner, 1959)
E_{sil} (kJ mol^{-1})	300	Activation energy of silicate (Schubert et al., 2001)
$\eta_{0,\mathrm{gra,min.}}$ (10^9 Pa s)	5.3	Ref. viscosity of graphite (min. shear modulus, Cost et al., 1968)
$\eta_{0,\mathrm{gra,max.}}$ (10^9 Pa s)	185	Ref. viscosity of graphite (max. shear modulus, Min & Aluru, 2011)
$\eta_{0,\mathrm{sil}}$ (10^9 Pa s)	160	Ref. viscosity of silicate (assuming η (1600 K) = 10^{21} Pa s)
Model Properties		
T_{surf} (K)	700	Planet surface temperature (Kepler-37b, Barclay et al., 2013)
$T_{0,\mathrm{int}}$ (K)	1700	Initial graphite-silicate interface temperature
$T_{0,\mathrm{sil}}$ (K)	2000	Initial silicate mantle temperature
$T_{0,\mathrm{iron}}$ (K)	3000	Initial iron core temperature
$H_{0,\mathrm{sil}}$ (10^{-12} W kg^{-1})	15	Initial internal heating rate of the silicate mantle
τ_{sil} (Gyr)	2.4	Half-life of radioactive sources in the silicate mantle
$H_{0,\mathrm{iron}}$ (10^{-12} W kg^{-1})	1.5	Initial internal heating rate of the iron core
τ_{iron} (Gyr)	2.4	Half-life of radioactive sources in the iron core

therein). Here we assume the classical boundary layer theory exponent $\beta = 1/3$ from Turcotte & Oxburgh (1967) which is similar to the β for internally heated systems (0.337±0.009) from Wolstencroft et al. (2009). We take the prefactor value $f_N = 0.164$ from Wolstencroft et al. (2009). The top/bottom Rayleigh numbers are defined in terms of the layer properties as

$$\mathrm{Ra}_j(t) = \frac{\alpha g \rho^2 C_P \Delta T_j(t) h^3}{k\, \eta(T)}, \quad j = \mathrm{top}, \mathrm{bot}, \tag{5.7}$$

where α is the thermal expansivity and $\eta(T)$ is temperature-dependent viscosity. The viscosity is given by the Arrhenius law (Schubert et al., 2001),

$$\eta(T) = \eta_0 \exp\left(\frac{E + PV}{RT}\right), \tag{5.8}$$

where η_0 is the reference viscosity, E is the activation energy, V is the activation volume, P is the pressure and R is the universal gas constant. For simplicity, we assume a pressure-independent ($P = 0$) description of the Arrhenius law here, a reasonable approximation in view of other approximations and the limited pressure range considered. The pressure-dependent term PV is small for small planets. For example, for a planet with the radius of 2500 km, PV is about 10% of E.

Table 5.2: Planet parameters

Model	R_{surf} (km)	R_{gsb} (km)	R_{isb} (km)	g (m/s^2)
Hypothetical (100 km C-shell)	1600	–	1500	3.7
Hypothetical (200 km C-shell)	1700	–	1500	3.7
Hypothetical (500 km C-shell)	2000	–	1500	3.7
Hypothetical (1000 km C-shell)	2500	–	1500	3.7
Generic (1 km C-shell)	3001	3000	1500	3.5
Generic (100 km C-shell)	3100	3000	1500	3.5
Generic (200 km C-shell)	3200	3000	1500	3.5
Generic (500 km C-shell)	3500	3000	1500	3.5
Generic (1000 km C-shell)	4000	3000	1500	3.5
Kepler-37b (0.1 wt% C)	2166	2165	1038	2.35
Kepler-37b (10 wt% C)	2166	2045	981	2.2
Kepler-37b (20 wt% C)	2166	1925	926	2.07
Kepler-37b (33 wt% C)	2166	1767	851	1.92
Kepler-37b (50 wt% C)	2166	1558	754	1.77

All relevant parameters concerning Eqs. (5.3)−(5.8) for graphite and silicate are given in Table 5.1. For the viscosity of graphite, the strain rate equation from Wagner & Driesner (1959) is implemented, which gives η_0 in terms of the shear modulus μ and prefactor $A = 1.75$ as $\eta_0 = \mu/2A$. The shear modulus of graphite has been reported to be as low as 10 GPa (Cost et al., 1968) and as high as 350 GPa (Min & Aluru, 2011). For this reason we implement two reference viscosities for graphite as given in Table 5.1. However, we also show in Sect. 5.3.1 that there is a negligible impact of these upper- and lower-limits of the shear modulus on the duration of convective cooling of the graphite layer.

In Table 5.2, we list the three types of models implemented in Sect. 5.3. 'Hypothetical' planets refer to the models which have a shell composed of either graphite or silicate surrounding a core . 'Generic' planets are the three-layered models shown in Fig. 5.1 with fixed iron core and silicate mantle radii (resulting in an approximate mantle to core mass ratio of 2.5) and only the graphite shell thickness is allowed to vary. 'Kepler-37b' planets are similar to 'Generic' planets but the planetary radius is fixed and the amount of graphite (and therefore the graphite shell thickness) in the planet varies. For Kepler-37b, Hakim et al. (2018b) assumed a silicate mantle to iron core mass ratio of 3 (compared to 2 for Earth) in accordance with their experimental results for certain exoplanetary compositions. Here we assume the same mantle to core mass ratio as Hakim et al. (2018b). Consequently, the iron core and silicate mantle radii decrease with increasing graphite content.

As we will show in Sect. 5.3.1, graphite shells transfer heat mainly via conduction for all but the earliest times of the planet history, here we model the graphite shell as a purely conductive static medium. Assuming a spherically symmetric temperature distribution of the shell, the partial differential equation (PDE) for time-dependent conductive heat transport (Schubert et al., 2001) can be written as

$$\rho_{\rm gra} C_{P,\rm gra} \frac{\partial T_{\rm gra}}{\partial t} = \frac{1}{r^2}\frac{\partial}{\partial r}\left(r^2 k_{\rm gra}\frac{\partial T_{\rm gra}}{\partial r}\right) + \rho_{\rm gra} H_{\rm gra}, \tag{5.9}$$

where the subscript 'gra' refers to material properties specific to the graphite shell. The boundary conditions applied here are: 1) a prescribed fixed temperature at the outer surface of the shell, $T_{\rm gra}(R_{\rm surf}, t) = T_{\rm surf}$ and 2) a prescribed time-dependent heat flow density at the interface between the shell and underlying mantle, $-k_{\rm gra}\frac{\partial T_{\rm gra}}{\partial r} = q_{\rm gra-bot}(t)$.

The conductive shell is thermally coupled to the underlying convective mantle through the thermal boundary conditions, where the bottom heat flow is obtained from the convection model for the mantle. The time dependent bottom temperature of the conductive shell, on the other hand, is applied as a boundary condition for the convecting mantle part of the domain. Eq. (5.9) is solved numerically by a finite difference discretization method using 100 grid points in the radial direction (van Kan et al., 2014). Time discretization then results in a system of algebraic equations that are solved in a time stepping algorithm that combines the solution of the conductive shell and the convecting mantle coupled through the boundary conditions.

5.3 Results

5.3.1 Duration of convective cooling

We first establish the nature of heat transport in the graphite shell of rocky exoplanets. For this purpose, we define the duration of convective cooling as the time required to bring the top Nusselt number ($\mathrm{Nu_{top}}$) down to a value of unity (Sect. 5.2.2). Then we compare the duration of convective cooling of shells composed of either graphite or silicate. The temperature of the shell is computed by integrating the ordinary differential equation, Eq. (5.4) supplemented by Eqs. (5.5)−(5.8) and using parameter values for graphite or silicate from Table 5.1. Here we isolate the effects of planet properties such as the planet size, surface area, and gravity or internal heating and initial temperature on our model outcomes. To achieve that, we keep the core size of our model fixed at 1500 km, keep the shell thickness the same for the graphite and silicate cases (see 'Hypothetical' rows in Table 5.2), and assume identical initial shell temperatures of 2500 K, a surface temperature of 700 K and no radiogenic heating.

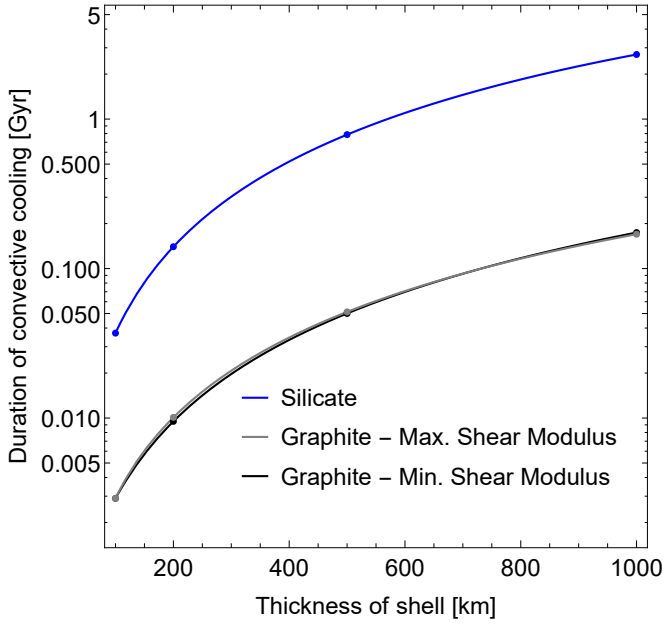

Figure 5.2: Comparison of the convective cooling duration of graphite and silicate shells for hypothetical planets with a core radius of 1500 km and a shell thickness of 100−1000 km. For planets with a graphite shell, two cases of viscosity based on the minimum and maximum values of shear modulus are also compared.

Fig. 5.2 shows that the convective cooling duration for silicate-shell planets with shell thicknesses between 100−1000 km is between 0.04−2.7 Gyr. In contrast, the convective cooling duration for graphite-shell planets is more than an order of magnitude lower (3−170

Myr). The cases of minimum and maximum shear modulus (see Sect. 5.2.2) for graphite-shell planets differ by only 5%, implying a negligible effect of the shear modulus on the cooling of the planet. Assuming an initial shell temperature of 4000 K increases this duration for the silicate and graphite cases by only 10−120 Myr and 0.3−5 Myr, respectively. By switching on the internal heating ($H_0 = 15 \times 10^{-12}$ W kg^{-1}), we find that the 2500 km silicate-shell planets take up to 9.8 Gyr to reach $\mathrm{Nu}_{\mathrm{top}} = 1$. As the main radiogenic heat producing elements in rocky planets (U, Th, and K) are highly incompatible in graphite, it is unlikely that significant internal heating in a graphite layer would occur under any circumstances. Even if radiogenic heating in the graphite layer is made equal to that in silicate, the duration of convective cooling for our largest C-shell model with a 2500 km radius is still about 220 Myr. The effect of internal heating on planets with thin shells (∼100 km) is negligible. Although we ignore the pressure-dependent term in viscosity, we extend our calculations to larger planets up to the size of Earth. Our calculations show that for large planets the duration of convective cooling increases by less than 20% compared to the planets shown in Fig. 5.2 for layer thicknesses up to a few hundred kilometers. Such a fast cooling of the graphite shell is the result of its high thermal conductivity. Because of the extremely short duration of convection in the graphite shell compared to the lifetime of rocky exoplanets, hereafter we assume conduction to be the heat transport mechanism in the graphite shell of the models considered here.

5.3.2 Effects of the thickness of a graphite outer shell on thermal evolution

We solve the equations given in Sect. 5.2.2 to calculate the coupled three-layered thermal evolution of carbon-enriched rocky exoplanets. To assess the effects of the thickness of the graphite shell on planetary evolution, we fix the iron core and silicate mantle radii of our generic model planets to 1500 km and 3000 km respectively and only vary the outer C-shell thickness. Across different models, we also assume the same surface temperature ($T_{\mathrm{surf}} = 700$ K), the same initial layer temperatures for the core ($T_{0,\mathrm{cor}} = 3000$ K), the mantle ($T_{0,\mathrm{sil}} = 2000$ K) and the graphite-mantle interface ($T_{0,\mathrm{int}} = 1700$ K), and the same heating rates for the silicate mantle ($H_{0,\mathrm{sil}} = 15 \times 10^{-12}$ W kg^{-1}) and the iron core ($H_{0,\mathrm{iron}} = 1.5 \times 10^{-12}$ W kg^{-1}). The internal heating of the graphite shell is assumed to be zero (see Sect. 5.3.1). We perform thermal evolution calculations for models with a 100 km C-shell and a 1000 km C-shell and compare them with our reference case of 1 km C-shell. We choose an extremely thin C-shell as our reference case instead of a 2-layer iron-silicate model in order to avoid model-specific effects such as the initial temperature of the graphite-silicate interface.

Fig. 5.3 compares several properties related to the thermal evolution of models spanning 5 Gyr for the reference model (1 km) and the 100 km and 1000 km C-shell models, respectively. The silicate mantle of the 100 km C-shell model cools slower than that of the reference model because of several effects. First, the thermal inertia of the shell, which is related to its heat capacity, smoothens a rapid temperature drop in the early stages. Second, the shell presents a thermal resistance that reduces the surface heat flux for a given temperature contrast (van den Berg et al., 2005). Third, the presence of the shell reduces the temperature

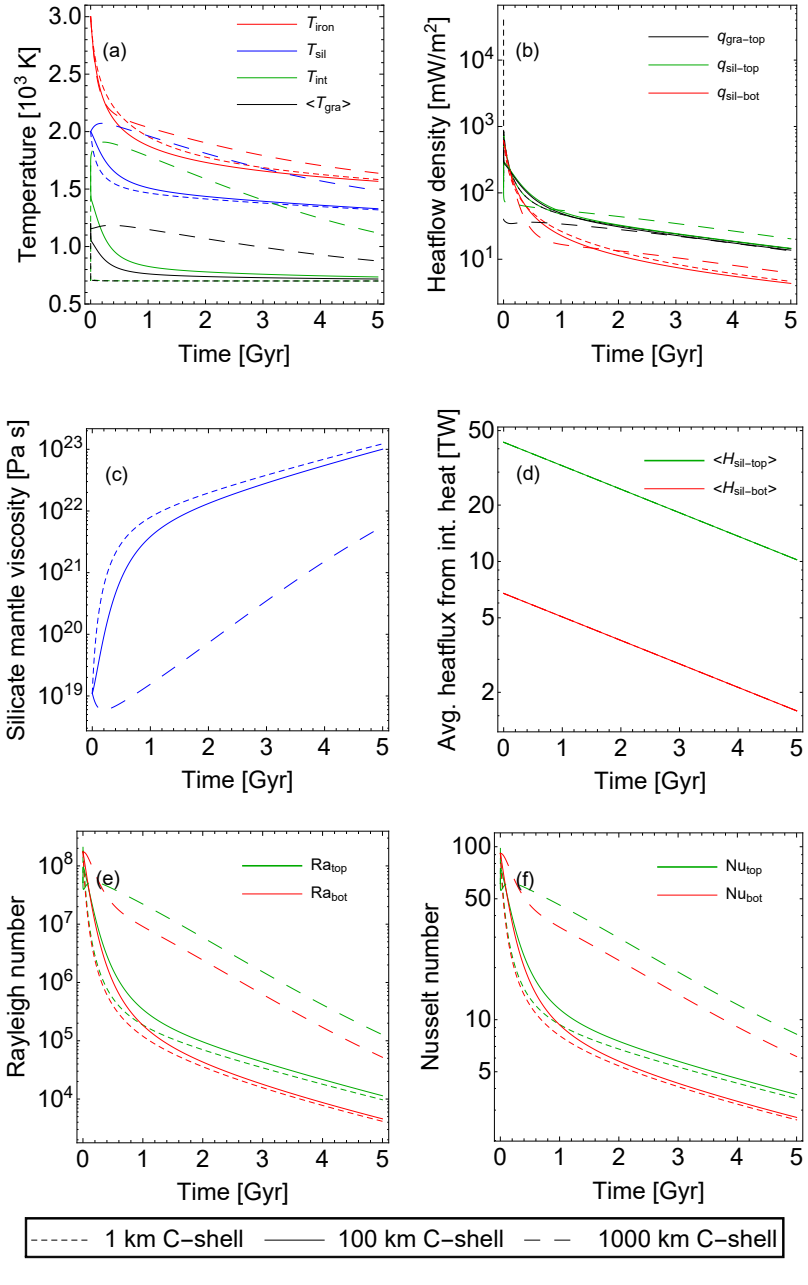

Figure 5.3: Thermal evolution of generic planets with core and mantle radii of 1500 km and 3000 km, respectively and thicknesses of graphite shells of 100 km and 1000 km. Also plotted is the reference case with 1 km graphite shell.

contrast at the top of the mantle that drives thermal convection. The 1000 km C-shell provides both a much larger thermal inertia and thermal resistance resulting in a stronger delay in the cooling of the mantle. Although the mantle temperature of the 1000 km C-shell model also approaches that of the reference model after 5 Gyr, it is still higher than the other two models by almost 200 K at 5 Gyr (Fig. 5.3(a)). The trends in the silicate mantle temperature corroborate to the trends in the silicate mantle viscosity and the top and bottom Rayleigh and Nusselt numbers as seen in Fig. 5.3(c,e,f).

On the other hand, the core of the 100 km C-shell model cools down faster than the reference model. This is the result of a higher heat flux at the top of the graphite-shell for the 100 km C-shell model between 0.12−1.25 Gyr, which allows for a higher heat flux at the top as well as at the bottom of the silicate mantle. Although the initial (between 0−0.12 Gyr) heat flux at the top of the graphite shell of the reference model is higher than that of the 100 km C-shell model due to initial conditions, it does not affect the result. Nonetheless, at 5 Gyr the core temperature of the 100 km C-shell model approaches that of the reference model. Similarly, for the 1000 km C-shell model, the core keeps cooling faster than the reference model during the first 0.6 Gyr due to the same effect. However, during the later stages of evolution the core temperature decreases more gradually due to the thermal shielding effect of the thick C-shell and the heat cannot escape the core efficiently. This results in a higher core temperature (higher by almost 100 K) for the 1000 km C-shell model at 5 Gyr than in the other two models. Essentially, our calculations indicate that a thin graphite shell (<500 km) does not significantly affect the long-term thermal evolution of the planetary layers interior to the shell.

5.3.3 Application to Kepler-37b

In this section, we apply our methods to the case of Kepler-37b, the smallest known exoplanet identified to date with a radius of 2166 km (Stassun et al., 2017). Since there are no estimates on its mass, there are no constraints on its bulk composition. Here we revisit two cases considered by Hakim et al. (2018b), assuming a bulk composition with 10 wt% C and 50 wt% C and compare with the reference model of 0.1 wt% C (equivalent to a C-shell thickness of 1 km, see Table 5.2). These models are different from each other in several aspects. Apart from the change in planet properties such as the core and silicate mantle radii, the C-shell thickness, and others, an important difference is the total internal heating. Since our internal heating rate assumption is per unit mass of silicates and iron, the total internal heating in the reference model with 0.01 wt% C is much higher than that with 50 wt% C, because in the latter the planet must contain less silicate and iron to yield the overall radius of 2166 km (Fig. 5.4(d)).

The mantle temperatures of the three models of Kepler-37b follow trends similar to those of the generic planet, although the effects are less pronounced (Fig. 5.4(a)). The core temperatures for models with 10 wt% and 50 wt% outer graphite shells are cooler than the reference model, which is similar to the generic planet comparison between the 100 km C-shell and reference models as discussed in Sect. 5.3.2. Here, this result is the combination

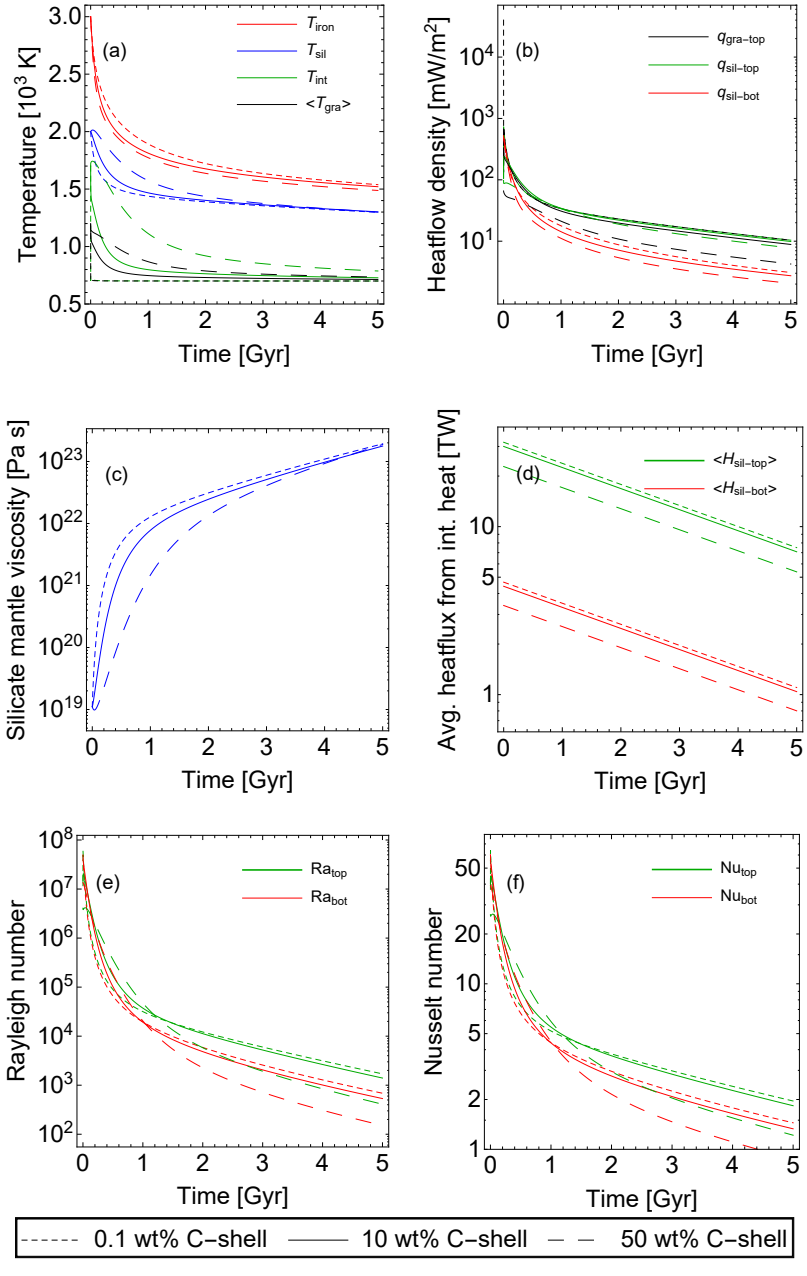

Figure 5.4: Thermal evolution of Kepler-37b assuming silicate mantle to iron core mass ratio of 3. Two cases with 10 wt% and 50 wt% graphite-shells are compared with the reference case with 0.1 wt% graphite-shell.

of two effects, the thermal shielding effect as well as the effect of a much lower total internal heating in the 50 wt% C model compared to the 10 wt% C model. The higher internal temperatures, for the 10 and 50 wt% C-shell cases, show that the effect of thermal shielding dominates over the effect of reduced internal heating. The mantle viscosity shows a simple trend, lower for models with higher carbon content, because of its direct dependence on the mantle temperature (Fig. 5.4(c)). However, the Rayleigh and Nusselt numbers do not show a simple trend because of their strong dependence on the silicate layer thickness which is smaller for the 50 wt% C model compared to the 0 and 10 wt% C models (Fig. 5.4(e,f)). Nevertheless, the mantle of Kepler-37b can be in a convective regime for at least 5 Gyr, in particular for graphite budgets of less than 50 wt%.

5.4 Discussion and conclusions

Our results show that conduction is the dominant heat transfer mechanism in the graphite outer shell of carbon-enriched rocky planets regardless of graphite viscosity. This is mainly the result of an order of magnitude higher thermal conductivity of graphite than that of common mantle silicates. The impact of a graphite outer shell on the thermal evolution of a planet depends on the thickness of the shell. This is because the thermal inertia and the thermal resistance increase with the thickness of the shell. The thermal inertia is mostly important in the initial stages of the first $\sim$100 Myr of planetary evolution when the thermal profile of the C-shell changes fast. For the long term effect, the thermal resistance of the C-shell (van den Berg et al., 2005) determines the thermal evolution. For the models tested here, we find that a thin outer graphite shell ($<$500 km in thickness) has a small effect on the heat release from the deep interior of the planet. This implies that the addition of a thin graphite shell on the top of the silicate mantle does not significantly impact the evolution of the interior, even though the total radius and mass of the model planet increase. However, if the graphite layer thickness exceeds 500 km, the thermal shielding effect of the C-shell becomes sufficient to delay the cooling of the planet by several billion years. For planets with a known radius, if the radioactively dead graphite shell is added by removing the radiogenic heat producing iron and silicates, although the total internal heating is reduced the thermal shielding effect still dominates over internal heating resulting in higher mantle and core temperatures for planets with thicker graphite shells.

In this paper, we do not take into account the temperature and pressure effects on material properties such as thermal conductivity and heat capacity, or pressure effects on viscosity. To assess high-temperature effects, our chosen parameter values are either based on ambient temperature data or measurements in a temperature range relevant to our models depending on the availability of temperature-dependent values of the parameter. Since the interior pressures of planets considered in this study are small, we expect these effects to be small and to not change our conclusions in a qualitative way. For example, the pressure-dependent silicate viscosity for Kepler-37b-size planets is only 10% higher than the pressure-independent one. On the other hand, to our knowledge, there are no experimental studies focusing on the effect of high-pressure on the properties of graphite. In order to account for the pressure-temperature effects of a deep planetary interior, experimental studies in

the future need to focus on determining the high-pressure high-temperature properties of graphite such as thermal conductivity, heat capacity and activation parameters.

Here our calculations focus on small planets where the pressures at the bottom of the graphite shell are not high enough to form diamond (graphite-diamond phase diagram, Kerley & Chhabildas, 2001; Ghiringhelli et al., 2005). For larger planets, there is a steeper increase in the pressure with increasing depth allowing diamond-forming pressures to be reached at shallower depths. For example, if we assume a temperature-independent graphite-diamond transition pressure at 10 GPa, the maximum allowed outer graphite shell thicknesses for a planet with radius of 3500 km, an Earth-size planet and a planet twice the size of Earth would be about 1500 km, 400 km and 100 km, respectively. For planets with a bulk carbon content exceeding the maximum carbon content possible in the graphite shell, a diamond layer would form beneath the graphite shell. Such a diamond layer would become part of the silicate mantle because the density of diamond is similar to common mantle silicates making it more difficult for diamond to form a physically separate layer from silicates.

For Earth-size planets, Unterborn et al. (2014) have shown that the mixing of diamond with the silicate mantle accelerates the cooling process because of diamond's extremely high thermal conductivity. Even if such planets have a graphite outer shell, the allowed shell thickness of 400 km would be small enough to be in the regime where the graphite shell only has a small effect on the cooling of the planet. The presence of a graphite outer shell is therefore unlikely to affect the thermal evolution of Earth-size planets. However, for smaller planets with a thicker graphite shell (> 500 km), which exhibits sufficient thermal shielding effects, diamond mixing in the silicate-rich mantle will cool the planet faster while the thermal shielding effect of the graphite outer shell will slow down the cooling. The net planetary cooling rate would be faster or slower depending on the effect that dominates.

Plate tectonics and the presence of water have been associated with the potential of habitability for rocky exoplanets (e.g., Valencia et al., 2007c; Tackley et al., 2013; Noack et al., 2016). Although this study does not focus on the tectonic mode or the presence of water, it is possible that the rocky planets with a thin graphite shell behave similar to iron-silicate planets because of the minimal effect of the thin shell on planetary evolution. If the silicate mantle allows plate tectonics, the thin graphite shell might break because of its brittle nature. With the presence of water, formation of graphite continents surrounded by oceans could be possible. In contrast, for thick graphite shells, even if the mantle is convecting, stresses developed during tectonics may not lead to fractures propagating to the surface and the thick shell would likely isolate the silicate mantle from the surface. If the planet's silicate mantle is in a stagnant lid mode, graphite shells would likely be part of the stagnant lid. If plate tectonics is important to keep the planet habitable, out of the two cases, thick graphite shells are more likely to hamper habitability. However, studies such as Tosi et al. (2017) have shown that stagnant lid planets are also potentially habitable. Nonetheless, the tectonic mode of a planet is a more complicated problem and a more detailed modeling of the evolution of planets than discussed here is required to convincingly state the nature of tectonic mode on planets with a graphite outer shell.

Acknowledgments

This work is part of the Planetary and Exoplanetary Science Network (PEPSci), funded by the Netherlands Organization for Scientific Research (NWO, Project no. 648.001.005).

Bibliography

Alfè, D., Gillan, M. J., & Price, G. D. 2002a, *Composition and temperature of the Earth's core constrained by combining ab initio calculations and seismic data*, Earth and Planetary Science Letters, 195, 91

Alfè, D., Kresse, G., & Gillan, M. J. 2000, *Structure and dynamics of liquid iron under Earth's core conditions*, Physical Review B, 61, 132

Alfè, D., Price, G. D., & Gillan, M. J. 2002b, *Iron under Earth's core conditions: Liquid-state thermodynamics and high-pressure melting curve from ab initio calculations*, Physical Review B, 65, 165118

Anderson, D. E., Bergin, E. A., Blake, G. A., et al. 2017, *Destruction of refractory carbon in protoplanetary disks*, The Astrophysical Journal, 845, 13

Anderson, O. L., Dubrovinsky, L., Saxena, S. K., & LeBihan, T. 2001, *Experimental vibrational Grüneisen ratio values for ϵ-iron up to 330 GPa at 300 K*, Geophysical Research Letters, 28, 399

Anglada-Escudé, G., Amado, P. J., Barnes, J., et al. 2016, *A terrestrial planet candidate in a temperate orbit around Proxima Centauri*, Nature, 536, 437

Ardia, P., Giordano, D., & Schmidt, M. W. 2008, *A model for the viscosity of rhyolite as a function of H_2O-content and pressure: A calibration based on centrifuge piston cylinder experiments*, Geochimica et Cosmochimica Acta, 72, 6103

Armstrong, J. T. 1995, *CITZAF: A package of correction programs for the quantitative electron microbeam X-ray analysis of thick polished materials, thin films, and particles*, Microbeam Analysis, 4, 177

Atkins, P. W. 1994, *Physical Chemistry* (W.H. Freeman)

Barclay, T., Rowe, J. F., Lissauer, J. J., et al. 2013, *A sub-Mercury-sized exoplanet*, Nature, 494, 452

Batalha, N. M. 2014, *Exploring exoplanet populations with NASA's Kepler Mission*, Proceedings of the National Academy of Science, 111, 12647

Batalha, N. M., Borucki, W. J., Bryson, S. T., et al. 2011, *Kepler's first rocky planet: Kepler-10b*, The Astrophysical Journal, 729, 27

Batygin, K. & Stevenson, D. J. 2010, *Inflating hot Jupiters with ohmic dissipation*, The Astrophysical Journal Letters, 714, L238

Belonoshko, A. B., Bryk, T., & Rosengren, A. 2010, *Shear relaxation in iron under the conditions of Earth's inner core*, Physical Review Letters, 104, 245703

Belonoshko, A. B., Lukinov, T., Fu, J., et al. 2017, *Stabilization of body-centred cubic iron under inner-core conditions*, Nature Geoscience, 10, 312

Belonoshko, A. B., Skorodumova, N. V., Rosengren, A., et al. 2005, *High-pressure melting of $MgSiO_3$*, Physical Review Letters, 94, 195701

Berger, T. A., Huber, D., Gaidos, E., & van Saders, J. L. 2018, *Revised radii of Kepler stars and planets using Gaia data release 2*, ArXiv e-prints

Berner, R. A., Lasaga, A. C., & Garrels, R. M. 1983, *The carbonate-silicate geochemical cycle and its effect on atmospheric carbon dioxide over the past 100 million years*, American Journal of Science, 283, 641

Birch, F. 1947, *Finite elastic strain of cubic crystals*, Physical Review, 71, 809

Birkby, J. L., de Kok, R. J., Brogi, M., et al. 2013, *Detection of water absorption in the day side atmosphere of HD 189733 b using ground-based high-resolution spectroscopy at 3.2 μm*, Monthly Notices of the Royal Astronomical Society, 436, L35

Bizzarro, M., Baker, J. A., Haack, H., & Lundgaard, K. L. 2005, *Rapid timescales for accretion and melting of differentiated planetesimals inferred from ^{26}Al-^{26}Mg chronometry*, The Astrophysical Journal Letters, 632, L41

Bodenheimer, P. & Pollack, J. B. 1986, *Calculations of the accretion and evolution of giant planets The effects of solid cores*, Icarus, 67, 391

Bodman, E. H. L., Wright, J. T., Desch, S. J., & Lisse, C. M. 2018, *Inferring the composition of disintegrating planet interiors from dust tails with future James Webb Space Telescope observations*, ArXiv e-prints

Bond, J. C., Lauretta, D. S., & O'Brien, D. P. 2010a, *Making the Earth: Combining dynamics and chemistry in the Solar System*, Icarus, 205, 321

Bond, J. C., Lauretta, D. S., Tinney, C. G., et al. 2008, *Beyond the iron peak: r- and s-process elemental abundances in stars with planets*, The Astrophysical Journal, 682, 1234

Bond, J. C., O'Brien, D. P., & Lauretta, D. S. 2010b, *The compositional diversity of extrasolar terrestrial planets. I. In situ simulations*, The Astrophysical Journal, 715, 1050

Borucki, W. J., Koch, D. G., Basri, G., et al. 2011, *Characteristics of Kepler planetary candidates based on the first data set*, The Astrophysical Journal, 728, 117

Boss, A. P. 1997, *Giant planet formation by gravitational instability.*, Science, 276, 1836

Bouchet, J., Mazevet, S., Morard, G., Guyot, F., & Musella, R. 2013, *Ab initio equation of state of iron up to 1500 GPa*, Physical Review B, 87, 094102

Boujibar, A., Andrault, D., Bouhifd, M. A., et al. 2014, *Metal-silicate partitioning of sulphur, new experimental and thermodynamic constraints on planetary accretion*, Earth and Planetary Science Letters, 391, 42

Boustie, M., Berthe, L., De Rességuier, T., & Arrigoni, M. 2008, *Laser shock waves: Funda-*

mentals and applications, in 1st International Symposium on Laser Ultrasonics: Science, Technology and Applications, Citeseer

Boyd, F. R. & England, J. L. 1960, *Apparatus for phase-equilibrium measurements at pressures up to 50 kilobars and temperatures up to 1750*degC, Journal of Geophysical Research, 65, 741

Boylan, J. 1996, *Smooth operators: carbon-graphite materials*, Materials World, 4, 707

Brewer, J. M., Fischer, D. A., Valenti, J. A., & Piskunov, N. 2016, *Spectral properties of cool stars: Extended abundance analysis of 1,617 planet-search stars*, The Astrophysical Journal Supplement, 225, 32

Broeg, C., Benz, W., Thomas, N., & Cheops Team. 2014, *The CHEOPS mission*, Contributions of the Astronomical Observatory Skalnate Pleso, 43, 498

Buchhave, L. A., Bizzarro, M., Latham, D. W., et al. 2014, *Three regimes of extrasolar planet radius inferred from host star metallicities*, Nature, 509, 593

Cameron, A. G. W. 1978, *Physics of the primitive solar accretion disk*, Moon and Planets, 18, 5

Carter, J. A., Agol, E., Chaplin, W. J., et al. 2012, *Kepler-36: A pair of planets with neighboring orbits and dissimilar densities*, Science, 337, 556

Carter-Bond, J. C., O'Brien, D. P., Delgado Mena, E., et al. 2012a, *Low Mg/Si planetary host stars and their Mg-depleted terrestrial planets*, The Astrophysical Journal Letters, 747, L2

Carter-Bond, J. C., O'Brien, D. P., & Raymond, S. N. 2012b, *The compositional diversity of extrasolar terrestrial planets. II. Migration simulations*, The Astrophysical Journal, 760, 44

Caspersen, K. J., Lew, A., Ortiz, M., & Carter, E. A. 2004, *Importance of shear in the bcc-to-hcp transformation in iron*, Physical Review Letters, 93, 115501

Cebulla, D. & Redmer, R. 2014, *Ab initio simulations of MgO under extreme conditions*, Physical Review B, 89, 134107

Charbonneau, D., Brown, T. M., Latham, D. W., & Mayor, M. 2000, *Detection of planetary transits across a Sun-like star*, The Astrophysical Journal Letters, 529, L45

Charbonneau, D., Brown, T. M., Noyes, R. W., & Gilliland, R. L. 2002, *Detection of an extrasolar planet atmosphere*, The Astrophysical Journal, 568, 377

Chi, H., Dasgupta, R., Duncan, M. S., & Shimizu, N. 2014, *Partitioning of carbon between Fe-rich alloy melt and silicate melt in a magma ocean - Implications for the abundance and origin of volatiles in Earth, Mars, and the Moon*, Geochimica et Cosmochimica Acta, 139, 447

Chiang, E. & Laughlin, G. 2013, *The minimum-mass extrasolar nebula: in situ formation of close-in super-Earths*, Monthly Notices of the Royal Astronomical Society, 431, 3444

Chust, T. C., Steinle-Neumann, G., Dolejš, D., Schuberth, B. S. A., & Bunge, H.-P. 2017, *MMA-EoS: A computational framework for mineralogical thermodynamics*, Journal of Geophysical Research (Solid Earth), 122, 9881

Cole, G. H. A. 1984, *Physics of planetary interiors*

Colonna, F., Fasolino, A., & Meijer, E. J. 2011, *High-pressure high-temperature equation of state of graphite from Monte Carlo simulations*, Carbon, 49, 364

Connolly, J. A. D. & Khan, A. 2016, *Uncertainty of mantle geophysical properties computed from phase equilibrium models*, Geophysical Research Letters, 43, 5026

Corgne, A., Wood, B. J., & Fei, Y. 2008, *C- and S-rich molten alloy immiscibility and core formation of planetesimals*, Geochimica et Cosmochimica Acta, 72, 2409

Cost, J. R., Janowski, K. R., & Rossi, R. C. 1968, *Elastic properties of isotropic graphite*, Philosophical Magazine, 17, 851

Cottenier, S. 2002, *Density functional theory and the family of (L)APW-methods: a step-by-step introduction* (Instituut voor Kern- en Stralingsfysica, K.U.Leuven, Belgium)

Cottenier, S., Probert, M. I. J., Van Hoolst, T., Van Speybroeck, V., & Waroquier, M. 2011, *Crystal structure prediction for iron as inner core material in heavy terrestrial planets*, Earth and Planetary Science Letters, 312, 237

Dasgupta, R. 2013, *Ingassing, storage, and outgassing of terrestrial carbon through geologic time*, Reviews in Mineralogy and Geochemistry, 75, 183

Dasgupta, R., Buono, A., Whelan, G., & Walker, D. 2009, *High-pressure melting relations in Fe-C-S systems: Implications for formation, evolution, and structure of metallic cores in planetary bodies*, Geochimica et Cosmochimica Acta, 73, 6678

Dasgupta, R., Chi, H., Shimizu, N., Buono, A. S., & Walker, D. 2013, *Carbon solution and partitioning between metallic and silicate melts in a shallow magma ocean: Implications for the origin and distribution of terrestrial carbon*, Geochimica et Cosmochimica Acta, 102, 191

Dasgupta, R. & Walker, D. 2008, *Carbon solubility in core melts in a shallow magma ocean environment and distribution of carbon between the Earths core and the mantle*, Geochimica et Cosmochimica Acta, 72, 4627

Daviau, K. & Lee, K. K. M. 2017, *Decomposition of silicon carbide at high pressures and temperatures*, Physical Review B, 96, 174102

de Kok, R. J., Brogi, M., Snellen, I. A. G., et al. 2013, *Detection of carbon monoxide in the high-resolution day-side spectrum of the exoplanet HD 189733b*, Astronomy & Astrophysics, 554, A82

Deeg, H. J. & Alonso, R. 2018, *Transit Photometry as an Exoplanet Discovery Method*, ArXiv e-prints

Delgado Mena, E., Israelian, G., González Hernández, J. I., et al. 2010, *Chemical clues on the formation of planetary systems: C/O Versus Mg/Si for HARPS GTO Sample*, The Astrophysical Journal, 725, 2349

Deng, L., Fei, Y., Liu, X., Gong, Z., & Shahar, A. 2013, *Effect of carbon, sulfur and silicon on iron melting at high pressure: Implications for composition and evolution of the planetary terrestrial cores*, Geochimica et Cosmochimica Acta, 114, 220

Deschamps, F. & Lin, J.-R. 2014, *Stagnant lid convection in 3D-Cartesian geometry: Scaling laws and applications to icy moons and dwarf planets*, Physics of the Earth and Planetary Interiors, 229, 40

Deschamps, F. & Sotin, C. 2001, *Thermal convection in the outer shell of large icy satellites*, Journal of Geophysical Research, 106, 5107

Désert, J.-M., Vidal-Madjar, A., Lecavelier Des Etangs, A., et al. 2008, *TiO and VO broad band absorption features in the optical spectrum of the atmosphere of the hot-Jupiter HD 209458b*, Astronomy & Astrophysics, 492, 585

Dewaele, A., Loubeyre, P., Occelli, F., et al. 2006, *Quasihydrostatic equation of state of iron above 2 Mbar*, Physical Review Letters, 97, 215504

Dorn, C., Khan, A., Heng, K., et al. 2015, *Can we constrain the interior structure of rocky exoplanets from mass and radius measurements?*, Astronomy & Astrophysics, 577, A83

Driscoll, P. E. & Barnes, R. 2015, *Tidal heating of Earth-like exoplanets around M Stars: Thermal, magnetic, and orbital evolutions*, Astrobiology, 15, 739

Dubrovinsky, L., Dubrovinskaia, N., Narygina, O., et al. 2007, *Body-centered cubic iron-nickel alloy in Earths core*, Science, 316, 1880

Duncan, M. S., Dasgupta, R., & Tsuno, K. 2017, *Experimental determination of CO_2 content at graphite saturation along a natural basalt-peridotite melt join: Implications for the fate of carbon in terrestrial magma oceans*, Earth and Planetary Science Letters, 466, 115

Dziewonski, A. M. & Anderson, D. L. 1981, *Preliminary reference Earth model*, Physics of the Earth and Planetary Interiors, 25, 297

Elkins-Tanton, L. T. 2012, *Magma oceans in the inner solar system*, Annual Review of Earth and Planetary Sciences, 40, 113

Elser, S., Meyer, M. R., & Moore, B. 2012, *On the origin of elemental abundances in the terrestrial planets*, Icarus, 221, 859

Fei, Y. & Brosh, E. 2014, *Experimental study and thermodynamic calculations of phase relations in the Fe-C system at high pressure*, Earth and Planetary Science Letters, 408, 155

Fei, Y., Murphy, C., Shibazaki, Y., Shahar, A., & Huang, H. 2016, *Thermal equation of state of hcp-iron: Constraint on the density deficit of Earth's solid inner core*, Geophysical Research Letters, 43, 6837

Fortier, A., Beck, T., Benz, W., et al. 2014, *CHEOPS: a space telescope for ultra-high precision photometry of exoplanet transits*, in Proceedings of the SPIE, Vol. 9143, Space Telescopes and Instrumentation 2014: Optical, Infrared, and Millimeter Wave, 91432J

Fortney, J. J., Marley, M. S., & Barnes, J. W. 2007, *Planetary radii across five orders of magnitude in mass and stellar insolation: Application to transits*, The Astrophysical Journal, 659, 1661

Fujiyoshi, T., Wright, C. M., & Moore, T. J. T. 2015, *Mid-infrared spectroscopy of SVS13: silicates, quartz and SiC in a protoplanetary disc*, Monthly Notices of the Royal Astronomical Society, 451, 3371

Fulton, B. J., Petigura, E. A., Howard, A. W., et al. 2017, *The California-Kepler survey. III. A gap in the radius distribution of small planets*, The Astronomical Journal, 154, 109

Garcia, R. F., Gagnepain-Beyneix, J., Chevrot, S., & Lognonné, P. 2011, *Very preliminary reference Moon model*, Physics of the Earth and Planetary Interiors, 188, 96

Ghiringhelli, L. M., Los, J. H., Meijer, E. J., Fasolino, A., & Frenkel, D. 2005, *Modeling the phase diagram of carbon*, Physical Review Letters, 94, 145701

Gillon, M., Triaud, A. H. M. J., Demory, B.-O., et al. 2017, *Seven temperate terrestrial planets around the nearby ultracool dwarf star TRAPPIST-1*, Nature, 542, 456

Giordano, D., Russell, J. K., & Dingwell, D. B. 2008, *Viscosity of magmatic liquids: A model*, Earth and Planetary Science Letters, 271, 123

Golubkova, A., Schmidt, M. W., & Connolly, J. A. D. 2016, *Ultra-reducing conditions in average mantle peridotites and in podiform chromitites: a thermodynamic model for moissanite (SiC) formation*, Contributions to Mineralogy and Petrology, 171, 41

Gomes, R., Levison, H. F., Tsiganis, K., & Morbidelli, A. 2005, *Origin of the cataclysmic Late Heavy Bombardment period of the terrestrial planets*, Nature, 435, 466

Grasset, O., Schneider, J., & Sotin, C. 2009, *A study of the accuracy of mass-radius relationships for silicate-rich and ice-rich planets up to 100 Earth masses*, The Astrophysical Journal, 693, 722

Grillmair, C. J., Burrows, A., Charbonneau, D., et al. 2008, *Strong water absorption in the dayside emission spectrum of the planet HD189733b*, Nature, 456, 767

Grillmair, C. J., Charbonneau, D., Burrows, A., et al. 2007, *A Spitzer spectrum of the exoplanet HD 189733b*, The Astrophysical Journal Letters, 658, L115

Hakim, K., Rivoldini, A., Van Hoolst, T., et al. 2018a, *A new ab initio equation of state of hcp-Fe and its implication on the interior structure and mass-radius relations of rocky super-Earths*, Icarus, 313, 61

Hakim, K., Spaargaren, R., Grewal, D. S., et al. 2018b, *Mineralogy, structure and habitability of carbon-enriched rocky exoplanets: A laboratory approach*, ArXiv e-prints

Hart, M. H. 1978, *The evolution of the atmosphere of the earth*, Icarus, 33, 23

Hashizume, K. & Sugiura, N. 1998, *Transportation of gaseous elements and isotopes in a thermally evolving chondritic planetesimal*, Meteoritics and Planetary Science, 33, 1181

Hatzes, A. P., Weiss, W. W., Rauer, H., & Grotsch-Noels, A. 2016, *V.3 Present and future space missions for ultra-precision photometry* (EDP Sciences), 241

Hauck, S. A., Margot, J.-L., Solomon, S. C., et al. 2013, *The curious case of Mercury's internal structure*, Journal of Geophysical Research (Planets), 118, 1204

Henry, G. W., Marcy, G. W., Butler, R. P., & Vogt, S. S. 2000, *A transiting "51 Peg-like" planet*, The Astrophysical Journal Letters, 529, L41

Hevey, P. J. & Sanders, I. S. 2006, *A model for planetesimal meltdown by ^{26}Al and its implications for meteorite parent bodies*, Meteoritics and Planetary Science, 41, 95

Hirose, K. & Fei, Y. 2002, *Subsolidus and melting phase relations of basaltic composition in the uppermostlower mantle*, Geochimica et Cosmochimica Acta, 66, 2099

Hirose, K., Labrosse, S., & Hernlund, J. 2013, *Composition and state of the core*, Annual Review of Earth and Planetary Sciences, 41, 657

Hoeijmakers, H. J., Ehrenreich, D., Heng, K., et al. 2018, *Atomic iron and titanium in the atmosphere of the exoplanet KELT-9b*, Nature, 560, 453

Hofmeister, A. M., Dong, J., & Branlund, J. M. 2014, *Thermal diffusivity of electrical insulators at high temperatures: Evidence for diffusion of bulk phonon-polaritons at infrared frequencies augmenting phonon heat conduction*, Journal of Applied Physics, 115, 163517

Holzapfel, W. B. 1996, *Physics of solids under strong compression*, Reports on Progress in Physics, 59, 29

Holzheid, A., Palme, H., & Chakraborty, S. 1997, *The activities of NiO, CoO and FeO in silicate melts*, Chemical Geology, 139, 21

Höning, D., Hansen-Goos, H., Airo, A., & Spohn, T. 2014, *Biotic vs. abiotic Earth: A model for mantle hydration and continental coverage*, Planetary Space Science, 98, 5

Höning, D. & Spohn, T. 2016, *Continental growth and mantle hydration as intertwined feedback cycles in the thermal evolution of Earth*, Physics of the Earth and Planetary Interiors, 255, 27

Huang, S.-S. 1959, *The problem of life in the universe and the mode of star formation*, Publications of the Astronomical Society of the Pacific, 71, 421

Huss, G. R., Meshik, A. P., Smith, J. B., & Hohenberg, C. M. 2003, *Presolar diamond, silicon carbide, and graphite in carbonaceous chondrites: implications for thermal processing in the solar nebula*, Geochimica et Cosmochimica Acta, 67, 4823

Ichikawa, H., Tsuchiya, T., & Tange, Y. 2014, *The P-V-T equation of state and thermodynamic properties of liquid iron*, Journal of Geophysical Research (Solid Earth), 119, 240

Ita, J. & Stixrude, L. 1992, *Petrology, elasticity, and composition of the mantle transition zone*, Journal of Geophysical Research, 97, 6849

Jansen, W. & Slaughter, M. 1982, *Elemental mapping of minerals by electron microprobe*, American Mineralogist, 67, 521

Javoy, M., Kaminski, E., Guyot, F., et al. 2010, *The chemical composition of the Earth: Enstatite chondrite models*, Earth and Planetary Science Letters, 293, 259

Johansen, A. & Lambrechts, M. 2017, *Forming planets via pebble accretion*, Annual Review of Earth and Planetary Sciences, 45, 359

Johansen, A., Mac Low, M.-M., Lacerda, P., & Bizzarro, M. 2015, *Growth of asteroids, planetary embryos, and Kuiper belt objects by chondrule accretion*, Science Advances, 1, 1500109

Johansen, A., Oishi, J. S., Mac Low, M.-M., et al. 2007, *Rapid planetesimal formation in turbulent circumstellar disks*, Nature, 448, 1022

Jugo, P. J., Luth, R. W., & Richards, J. P. 2005, *Experimental data on the speciation of sulfur*

as a function of oxygen fugacity in basaltic melts, Geochimica et Cosmochimica Acta, 69, 497

Jugo, P. J., Wilke, M., & Botcharnikov, R. E. 2010, *Sulfur K-edge XANES analysis of natural and synthetic basaltic glasses: Implications for S speciation and S content as function of oxygen fugacity*, Geochimica et Cosmochimica Acta, 74, 5926

Kasting, J. F., Whitmire, D. P., & Reynolds, R. T. 1993, *Habitable Zones around Main Sequence Stars*, Icarus, 101, 108

Kerley, G. I. & Chhabildas, L. C. 2001, *Multicomponent-multiphase equation of state for carbon*

Kite, E. S., Fegley, Jr., B., Schaefer, L., & Gaidos, E. 2016, *Atmosphere-interior exchange on hot, rocky exoplanets*, The Astrophysical Journal, 828, 80

Kite, E. S., Manga, M., & Gaidos, E. 2009, *Geodynamics and rate of volcanism on massive Earth-like planets*, The Astrophysical Journal, 700, 1732

Klarmann, L., Ormel, C. W., & Dominik, C. 2018, *Radial and vertical dust transport inhibit refractory carbon depletion in protoplanetary disks*, Astronomy & Astrophysics, 618, L1

Knibbe, J. S., Luginbühl, S. M., Stoevelaar, R., et al. 2018, *Calibration of a multi-anvil high-pressure apparatus to simulate planetary interior conditions*, EPJ Techniques and Instrumentation, 5, 5

Kobayashi, Y. 1974, *Anisotropy of thermal diffusivity in olivine, pyroxene and dunite*, Journal of Physics of the Earth, 22, 359

Kreidberg, L., Bean, J. L., Désert, J.-M., et al. 2014, *Clouds in the atmosphere of the super-Earth exoplanet GJ1214b*, Nature, 505, 69

Kruijer, T. S., Fischer-Gödde, M., Kleine, T., et al. 2013, *Neutron capture on Pt isotopes in iron meteorites and the Hf-W chronology of core formation in planetesimals*, Earth and Planetary Science Letters, 361, 162

Kuchner, M. J. & Seager, S. 2005, *Extrasolar carbon planets*, ArXiv Astrophysics e-prints

Kuiper, G. P. 1951, *On the origin of the solar system*, Proceedings of the National Academy of Science, 37, 1

Kushiro, I. & Walter, M. J. 1998, *Mg-Fe partitioning between olivine and mafic-ultramafic melts*, Geophysical Research Letters, 25, 2337

Laio, A., Bernard, S., Chiarotti, G. L., Scandolo, S., & Tosatti, E. 2000, *Physics of iron at Earth's core conditions*, Science, 287, 1027

Laughlin, G., Bodenheimer, P., & Adams, F. C. 1997, *The End of the Main Sequence*, The Astrophysical Journal, 482, 420

Lazar, C., Zhang, C., Manning, C. E., & Mysen, B. O. 2014, *Redox effects on calcite-portlandite-fluid equilibria at forearc conditions: Carbon mobility, methanogenesis, and reduction melting of calcite*, American Mineralogist, 99, 1604

Lazicki, A., Rygg, J. R., Coppari, F., et al. 2015, *X-ray diffraction of solid tin to 1.2 TPa*, Physical Review Letters, 115, 075502

Lee, J. & Morita, K. 2002, *Evaluation of surface tension and adsorption for liquid Fe-S alloys*, ISIJ International, 42, 588

Lee, J.-E., Bergin, E. A., & Nomura, H. 2010, *The solar nebula on fire: A solution to the carbon deficit in the inner solar system*, The Astrophysical Journal Letters, 710, L21

Léger, A., Rouan, D., Schneider, J., et al. 2009, *Transiting exoplanets from the CoRoT space mission. VIII. CoRoT-7b: the first super-Earth with measured radius*, Astronomy & Astrophysics, 506, 287

Lejaeghere, K., Bihlmayer, G., Björkman, T., et al. 2016a, *Reproducibility in density functional theory calculations of solids*, Science, 351

Lejaeghere, K., Cottenier, S., & Van Speybroeck, V. 2013, *Ranking the stars: A refined pareto approach to computational materials design*, Physical Review Letters, 111, 075501

Lejaeghere, K., Jaeken, J., Van Speybroeck, V., & Cottenier, S. 2014, *Ab initio based thermal property predictions at a low cost: An error analysis*, Physical Review B, 89, 014304

Lejaeghere, K., Vanduyfhuys, L., Verstraelen, T., Van Speybroeck, V., & Cottenier, S. 2016b, *Is the error on first-principles volume predictions absolute or relative?*, Computational Materials Science, 117, 390

Li, Y., Dasgupta, R., & Tsuno, K. 2015, *The effects of sulfur, silicon, water, and oxygen fugacity on carbon solubility and partitioning in Fe-rich alloy and silicate melt systems at 3 GPa and 1600* deg*C: Implications for core-mantle differentiation and degassing of magma oceans and reduced planetary mantles*, Earth and Planetary Science Letters, 415, 54

Li, Y., Dasgupta, R., Tsuno, K., Monteleone, B., & Shimizu, N. 2016, *Carbon and sulfur budget of the silicate Earth explained by accretion of differentiated planetary embryos*, Nature Geoscience, 9, 781

Lineweaver, C. H. & Norman, M. 2010, *The potato radius: A lower minimum size for dwarf planets*, ArXiv e-prints

Lodders, K. 2003, *Solar system abundances and condensation temperatures of the elements*, The Astrophysical Journal, 591, 1220

Lord, O. T., Walter, M. J., Dasgupta, R., Walker, D., & Clark, S. M. 2009, *Melting in the Fe-C system to 70 GPa*, Earth and Planetary Science Letters, 284, 157

Madden, J. H. & Kaltenegger, L. 2018, *A Catalog of Spectra, Albedos, and Colors of Solar System Bodies for Exoplanet Comparison*, ArXiv e-prints

Madhusudhan, N., Agúndez, M., Moses, J. I., & Hu, Y. 2016, *Exoplanetary atmospheres: Chemistry, formation conditions, and habitability*, Space Science Reviews, 205, 285

Madhusudhan, N., Lee, K. K. M., & Mousis, O. 2012, *A possible carbon-rich interior in super-Earth 55 Cancri e*, The Astrophysical Journal Letters, 759, L40

Madsen, G. K. H., Blaha, P., Schwarz, K., Sjöstedt, E., & Nordström, L. 2001, *Efficient linearization of the augmented plane-wave method*, Physical Review B, 64, 195134

Marois, C., Macintosh, B., Barman, T., et al. 2008, *Direct imaging of multiple planets orbiting the star HR 8799*, Science, 322, 1348

Marty, B., Alexander, C. M. O., & Raymond, S. N. 2013, *Primordial origins of Earth's carbon*, Reviews in Mineralogy and Geochemistry, 75, 149

Mayor, M. & Queloz, D. 1995, *A Jupiter-mass companion to a solar-type star*, Nature, 378, 355

McDade, P., Wood, B. J., Van Westrenen, W., et al. 2002, *Pressure corrections for a selection of piston-cylinder cell assemblies*, Mineralogical Magazine, 66, 1021

McDonough, W. F. & Sun, S.-s. 1995, *The composition of the Earth*, Chemical Geology, 120, 223

Metzger, P. T., Sykes, M. V., Stern, A., & Runyon, K. 2018, *The reclassification of asteroids from planets to non-planets*, ArXiv e-prints

Min, K. & Aluru, N. R. 2011, *Mechanical properties of graphene under shear deformation*, Applied Physics Letters, 98, 013113

Min, M., Waters, L. B. F. M., de Koter, A., et al. 2007, *The shape and composition of interstellar silicate grains*, Astronomy & Astrophysics, 462, 667

Miozzi, F., Morard, G., Antonangeli, D., et al. 2018, *Equation of state of SiC at extreme conditions: New insight into the interior of carbon rich exoplanets*, Journal of Geophysical Research (Planets), 123, 2295

Mizuno, H. 1980, *Formation of the giant planets*, Progress of Theoretical Physics, 64, 544

Mocquet, A., Grasset, O., & Sotin, C. 2014, *Very high-density planets: a possible remnant of gas giants*, Philosophical Transactions of the Royal Society of London Series A, 372, 20130164

Morard, G., Bouchet, J., Valencia, D., Mazevet, S., & Guyot, F. 2011, *The melting curve of iron at extreme pressures: Implications for planetary cores*, High Energy Density Physics, 7, 141

Morard, G. & Katsura, T. 2010, *Pressure-temperature cartography of Fe-S-Si immiscible system*, Geochimica et Cosmochimica Acta, 74, 3659

Morbidelli, A. & Raymond, S. N. 2016, *Challenges in planet formation*, Journal of Geophysical Research (Planets), 121, 1962

Morbidelli, A., Tsiganis, K., Crida, A., Levison, H. F., & Gomes, R. 2007, *Dynamics of the giant planets of the solar system in the gaseous protoplanetary disk and their relationship to the current orbital architecture*, The Astronomical Journal, 134, 1790

Mordasini, C. 2018, *Planetary population synthesis*, ArXiv e-prints

Morgan, W. C. 1972, *Thermal expansion coefficients of graphite crystals*, Carbon, 10, 73

Moriarty, J., Madhusudhan, N., & Fischer, D. 2014, *Chemistry in an evolving protoplanetary disk: Effects on terrestrial planet composition*, The Astrophysical Journal, 787, 81

Müller, A., Keppler, M., Henning, T., et al. 2018, *Orbital and atmospheric characterization of the planet within the gap of the PDS 70 transition disk*, ArXiv e-prints

Nabiei, F., Badro, J., Dennenwaldt, T., et al. 2018, *A large planetary body inferred from diamond inclusions in a ureilite meteorite*, Nature Communications, 9, 1327

Nakajima, T. & Sorahana, S. 2016, *Carbon-to-oxygen Ratios in M Dwarfs and Solar-type Stars*,

The Astrophysical Journal, 830, 159

Nisr, C., Meng, Y., MacDowell, A. A., et al. 2017, *Thermal expansion of SiC at high pressure-temperature and implications for thermal convection in the deep interiors of carbide exoplanets*, Journal of Geophysical Research (Planets), 122, 124

Noack, L., Höning, D., Rivoldini, A., et al. 2016, *Water-rich planets: How habitable is a water layer deeper than on Earth?*, Icarus, 277, 215

Ogihara, M., Kokubo, E., Suzuki, T. K., & Morbidelli, A. 2018, *Formation of close-in super-Earths in evolving protoplanetary disks due to disk winds*, Astronomy & Astrophysics, 615, A63

O'Neill, C. & Lenardic, A. 2007, *Geological consequences of super-sized Earths*, Geophysical Research Letters, 34, L19204

O'Neill, C., Lenardic, A., Weller, M., et al. 2016, *A window for plate tectonics in terrestrial planet evolution?*, Physics of the Earth and Planetary Interiors, 255, 80

O'Neill, H. S. C. & Eggins, S. M. 2002, *The effect of melt composition on trace element partitioning: an experimental investigation of the activity coefficients of FeO, NiO, CoO, MoO2 and MoO3 in silicate melts*, Chemical Geology, 186, 151

Ormel, C. W., Dullemond, C. P., & Spaans, M. 2010, *Accretion among preplanetary bodies: The many faces of runaway growth*, Icarus, 210, 507

Ormel, C. W. & Klahr, H. H. 2010, *The effect of gas drag on the growth of protoplanets. Analytical expressions for the accretion of small bodies in laminar disks*, Astronomy & Astrophysics, 520, A43

Ormel, C. W., Liu, B., & Schoonenberg, D. 2017, *Formation of TRAPPIST-1 and other compact systems*, Astronomy & Astrophysics, 604, A1

Palle, E. 2018, *The Detectability of Earth's Biosignatures Across Time*, ArXiv e-prints

Peplowski, P. N., Klima, R. L., Lawrence, D. J., et al. 2016, *Remote sensing evidence for an ancient carbon-bearing crust on Mercury*, Nature Geoscience, 9, 273

Perdew, J. P., Burke, K., & Ernzerhof, M. 1996, *Generalized gradient approximation made simple*, Physical Review Letters, 77, 3865

Perdew, J. P. & Wang, Y. 1992, *Accurate and simple analytic representation of the electron-gas correlation energy*, Physical Review B, 45, 13244

Perri, F. & Cameron, A. G. W. 1974, *Hydrodynamic instability of the solar nebula in the presence of a planetary core*, Icarus, 22, 416

Perryman, M., Hartman, J., Bakos, G. Á., & Lindegren, L. 2014, *Astrometric exoplanet detection with Gaia*, The Astrophysical Journal, 797, 14

Petigura, E. A. & Marcy, G. W. 2011, *Carbon and oxygen in nearby stars: Keys to protoplanetary disk chemistry*, The Astrophysical Journal, 735, 41

Petigura, E. A., Marcy, G. W., Winn, J. N., et al. 2018, *The California-Kepler survey. IV. Metal-rich stars host a greater diversity of planets*, The Astronomical Journal, 155, 89

Pickard, C. J. & Needs, R. J. 2009, *Stable phases of iron at terapascal pressures*, Journal of Physics Condensed Matter, 21, 452205

Pisani, C. 2012, *Quantum-mechanical ab-initio calculation of the properties of crystalline materials* (Springer Science & Business Media)

Poirier, J.-P. 2000, *Introduction to the physics of the Earth's interior* (Cambridge University Press), 326

Pollack, J. B., Hubickyj, O., Bodenheimer, P., et al. 1996, *Formation of the giant planets by concurrent accretion of solids and gas*, Icarus, 124, 62

Pourovskii, L. V., Mravlje, J., Ferrero, M., Parcollet, O., & Abrikosov, I. A. 2014, *Impact of electronic correlations on the equation of state and transport in ϵ-Fe*, Physical Review B, 90, 155120

Ragazzoni, R., Magrin, D., Rauer, H., et al. 2016, *PLATO: a multiple telescope spacecraft for exo-planets hunting*, in Proceedings of the SPIE, Vol. 9904, Space Telescopes and Instrumentation 2016: Optical, Infrared, and Millimeter Wave, 990428

Rai, N. & Westrenen, W. 2013, *Core-mantle differentiation in Mars*, Journal of Geophysical Research (Planets), 118, 1195

Rappaport, S., Levine, A., Chiang, E., et al. 2012, *Possible disintegrating short-period super-Mercury orbiting KIC 12557548*, The Astrophysical Journal, 752, 1

Rauer, H., Catala, C., Aerts, C., et al. 2014, *The PLATO 2.0 mission*, Experimental Astronomy, 38, 249

Raymond, S. N., Quinn, T., & Lunine, J. I. 2004, *Making other earths: dynamical simulations of terrestrial planet formation and water delivery*, Icarus, 168, 1

Raymond, S. N., Quinn, T., & Lunine, J. I. 2005, *Terrestrial planet formation in disks with varying surface density profiles*, The Astrophysical Journal, 632, 670

Reed, S. J. B. 2005, *Electron Microprobe Analysis and Scanning Electron Microscopy in Geology - 2nd Edition*, 206

Ricker, G. R., Winn, J. N., Vanderspek, R., et al. 2014, *Transiting Exoplanet Survey Satellite (TESS)*, in Proceedings of the SPIE, Vol. 9143, Space telescopes and instrumentation 2014: Optical, infrared, and millimeter wave, 914320

Ridden-Harper, A. R., Snellen, I. A. G., Keller, C. U., et al. 2016, *Search for an exosphere in sodium and calcium in the transmission spectrum of exoplanet 55 Cancri e*, Astronomy & Astrophysics, 593, A129

Rivoldini, A. & Van Hoolst, T. 2013, *The interior structure of Mercury constrained by the low-degree gravity field and the rotation of Mercury*, Earth and Planetary Science Letters, 377, 62

Rogers, L. A. 2015, *Most 1.6 Earth-radius planets are not rocky*, The Astrophysical Journal, 801, 41

Rohrbach, A., Ghosh, S., Schmidt, M. W., Wijbrans, C. H., & Klemme, S. 2014, *The stability of Fe-Ni carbides in the Earth#700s mantle: Evidence for a low Fe-Ni-C melt fraction in the*

deep mantle, Earth and Planetary Science Letters, 388, 211

Rohrbach, A. & Schmidt, M. W. 2011, *Redox freezing and melting in the Earth's deep mantle resulting from carbon-iron redox coupling*, Nature, 472, 209

Rubie, D. C., Jacobson, S. A., Morbidelli, A., et al. 2015, *Accretion and differentiation of the terrestrial planets with implications for the compositions of early-formed Solar System bodies and accretion of water*, Icarus, 248, 89

Sakai, T., Ohtani, E., Hirao, N., & Ohishi, Y. 2011, *Stability field of the hcp-structure for Fe, Fe-Ni, and Fe-Ni-Si alloys up to 3 Mbar*, Geophysical Research Letters, 38, L09302

Santos, N. C., Adibekyan, V., Dorn, C., et al. 2017, *Constraining planet structure and composition from stellar chemistry: trends in different stellar populations*, Astronomy & Astrophysics, 608, A94

Sata, N., Hirose, K., Shen, G., et al. 2010, *Compression of FeSi, Fe_3C, $Fe_{0.95}O$, and FeS under the core pressures and implication for light element in the Earth's core*, Journal of Geophysical Research (Solid Earth), 115, B09204

Schaefer, L., Jacobsen, S. B., Remo, J. L., Petaev, M. I., & Sasselov, D. D. 2017, *Metal-silicate partitioning and its role in core Formation and composition on super-Earths*, The Astrophysical Journal, 835, 234

Schäfer, U., Yang, C.-C., & Johansen, A. 2017, *Initial mass function of planetesimals formed by the streaming instability*, Astronomy & Astrophysics, 597, A69

Schlaufman, K. C. 2015, *A continuum of planet formation between 1 and 4 Earth radii*, The Astrophysical Journal Letters, 799, L26

Schmidt, M. W., Gao, C., Golubkova, A., Rohrbach, A., & Connolly, J. A. D. 2014, *Natural moissanite (SiC) – a low temperature mineral formed from highly fractionated ultra-reducing COH-fluids*, Progress in Earth and Planetary Science, 1, 27

Schoonenberg, D. & Ormel, C. W. 2017, *Planetesimal formation near the snowline: in or out?*, Astronomy & Astrophysics, 602, A21

Schubert, G., Cassen, P., & Young, R. E. 1979, *Subsolidus convective cooling histories of terrestrial planets*, Icarus, 38, 192

Schubert, G., Turcotte, D. L., & Olson, P. 2001, *Mantle convection in the Earth and planets* (Cambridge University Press), 956

Schuiling, R. D., Andriessen, B., Frapporti, G., et al. 1994, *Introduction to geochemistry* (University of Utrecht, Institute of Earth Sciences, Department of Geochemistry)

Schwarz, K., Blaha, P., & Trickey, S. B. 2010, *Electronic structure of solids with WIEN2k*, Molecular Physics, 108, 3147

Seager, S. 2013, *Exoplanet Habitability*, Science, 340, 577

Seager, S., Kuchner, M., Hier-Majumder, C. A., & Militzer, B. 2007, *Mass-radius relationships for solid exoplanets*, The Astrophysical Journal, 669, 1279

Seager, S., Turner, E. L., Schafer, J., & Ford, E. B. 2005, *Vegetation's red edge: A possible spectroscopic biosignature of extraterrestrial plants*, Astrobiology, 5, 372

Sha, X. & Cohen, R. E. 2010, *Elastic isotropy of ε-Fe under Earth's core conditions*, Geophysical Research Letters, 37, l10302

Sjöstedt, E., Nordström, L., & Singh, D. J. 2000, *An alternative way of linearizing the augmented plane-wave method*, Solid State Communications, 114, 15

Smythe, D. J., Wood, B. J., & Kiseeva, E. S. 2017, *The S content of silicate melts at sulfide saturation: New experiments and a model incorporating the effects of sulfide composition*, American Mineralogist, 102, 795

Solferino, G., Schmidt, M. W., & Bagdassarov, N. 2006, *Percolation threshold of iron-sulfide melts in olivine matrix: An experimental study with a centrifuging piston cylinder*, Geochimica et Cosmochimica Acta Supplement, 70, A602

Sotin, C., Grasset, O., & Mocquet, A. 2007, *Mass radius curve for extrasolar Earth-like planets and ocean planets*, Icarus, 191, 337

Southworth, J., Mancini, L., Madhusudhan, N., et al. 2017, *Detection of the atmosphere of the 1.6 M exoplanet GJ 1132 b*, The Astronomical Journal, 153, 191

Spohn, T. 1991, *Mantle differentiation and thermal evolution of Mars, Mercury, and Venus*, Icarus, 90, 222

Stacey, F. D. 2005, *High pressure equations of state and planetary interiors*, Reports on Progress in Physics, 68, 341

Stamenković, V., Noack, L., Breuer, D., & Spohn, T. 2012, *The influence of pressure-dependent viscosity on the thermal evolution of super-Earths*, The Astrophysical Journal, 748, 41

Stassun, K. G., Collins, K. A., & Gaudi, B. S. 2017, *Accurate empirical radii and masses of planets and their host stars with Gaia parallaxes*, The Astronomical Journal, 153, 136

Steenstra, E. S., Knibbe, J. S., Rai, N., & van Westrenen, W. 2016, *Constraints on core formation in Vesta from metal-silicate partitioning of siderophile elements*, Geochimica et Cosmochimica Acta, 177, 48

Steenstra, E. S., Seegers, A. X., Eising, J., et al. 2018, *Evidence for a sulfur-undersaturated lunar interior from the solubility of sulfur in lunar melts and sulfide-silicate partitioning of siderophile elements*, Geochimica et Cosmochimica Acta, 231, 130

Steenstra, E. S., Seegers, A. X., Putter, R., et al. submitted, *Metal-silicate partitioning systematics of siderophile elements at reducing conditions, part 1: a new experimental database*, Chemical Geology

Steinle-Neumann, G., Stixrude, L., & Cohen, R. E. 1999, *First-principles elastic constants for the hcp transition metals Fe, Co, and Re at high pressure*, Physical Review B, 60, 791

Steinle-Neumann, G., Stixrude, L., & Cohen, R. E. 2004, *Magnetism in dense hexagonal iron*, Proceedings of the National Academy of Science, 101, 33

Stewart, A. J., Schmidt, M. W., van Westrenen, W., & Liebske, C. 2007, *Mars: A new core-crystallization regime*, Science, 316, 1323

Stixrude, L. 2012, *Structure of iron to 1 Gbar and 40 000 K*, Physical Review Letters, 108, 055505

Stixrude, L. 2014, *Melting in super-earths*, Philosophical Transactions of the Royal Society of London Series A, 372, 20130076

Stixrude, L., Cohen, R. E., & Singh, D. J. 1994, *Iron at high pressure: Linearized-augmented-plane-wave computations in the generalized-gradient approximation*, Physical Review B, 50, 6442

Stixrude, L. & Lithgow-Bertelloni, C. 2005, *Thermodynamics of mantle minerals - I. Physical properties*, Geophysical Journal International, 162, 610

Stixrude, L. & Lithgow-Bertelloni, C. 2011, *Thermodynamics of mantle minerals - II. Phase equilibria*, Geophysical Journal International, 184, 1180

Tackley, P. J., Ammann, M., Brodholt, J. P., Dobson, D. P., & Valencia, D. 2013, *Mantle dynamics in super-Earths: Post-perovskite rheology and self-regulation of viscosity*, Icarus, 225, 50

Takahashi, S., Ohtani, E., Terasaki, H., et al. 2013, *Phase relations in the carbon-saturated C-Mg-Fe-Si-O system and C and Si solubility in liquid Fe at high pressure and temperature: implications for planetary interiors*, Physics and Chemistry of Minerals, 40, 647

Thiabaud, A., Marboeuf, U., Alibert, Y., Leya, I., & Mezger, K. 2015, *Elemental ratios in stars vs planets*, Astronomy & Astrophysics, 580, A30

Thorngren, D. P. & Fortney, J. J. 2018, *Bayesian analysis of hot-Jupiter radius anomalies: Evidence for ohmic dissipation?*, The Astronomical Journal, 155, 214

Thorngren, D. P., Fortney, J. J., Murray-Clay, R. A., & Lopez, E. D. 2016, *The mass-metallicity relation for giant planets*, The Astrophysical Journal, 831, 64

Tinetti, G., Drossart, P., Eccleston, P., et al. 2016, *The science of ARIEL (Atmospheric Remote-sensing Infrared Exoplanet Large-survey)*, in Proceedings of the SPIE, Vol. 9904, Space Telescopes and Instrumentation 2016: Optical, Infrared, and Millimeter Wave, 99041X

Todorov, K. O., Line, M. R., Pineda, J. E., et al. 2016, *The water abundance of the directly imaged substellar companion κ And b retrieved from a near infrared spectrum*, The Astrophysical Journal, 823, 14

Toplis, M. J. 2005, *The thermodynamics of iron and magnesium partitioning between olivine and liquid: Criteria for assessing and predicting equilibrium in natural and experimental systems*, Contributions to Mineralogy and Petrology, 149, 22

Tosi, N., Godolt, M., Stracke, B., et al. 2017, *The habitability of a stagnant-lid Earth*, Astronomy & Astrophysics, 605, A71

Tsiganis, K., Gomes, R., Morbidelli, A., & Levison, H. F. 2005, *Origin of the orbital architecture of the giant planets of the Solar System*, Nature, 435, 459

Tsuchiya, T. & Tsuchiya, J. 2011, *Prediction of a hexagonal SiO_2 phase affecting stabilities of $MgSiO_3$ and $CaSiO_3$ at multimegabar pressures*, Proceedings of the National Academy of Science, 108, 1252

Tsuno, K. & Dasgupta, R. 2015, *Fe-Ni-Cu-C-S phase relations at high pressures and temperatures - The role of sulfur in carbon storage and diamond stability at mid- to deep-upper mantle*, Earth and Planetary Science Letters, 412, 132

Tsuno, K., Ohtani, E., & Terasaki, H. 2007, *Immiscible two-liquid regions in the Fe O S system at high pressure: Implications for planetary cores*, Physics of the Earth and Planetary Interiors, 160, 75

Turcotte, D. L. & Oxburgh, E. R. 1967, *Finite amplitude convective cells and continental drift*, Journal of Fluid Mechanics, 28, 29

Tyler, W. W. & Wilson, A. C. 1953, *Thermal conductivity, electrical resistivity, and thermoelectric power of graphite*, Physical Review, 89, 870

Umemoto, K. & Wentzcovitch, R. M. 2011, *Two-stage dissociation in MgSiO $_3$ post-perovskite*, Earth and Planetary Science Letters, 311, 225

Unterborn, C. T., Dismukes, E. E., & Panero, W. R. 2016, *Scaling the Earth: A sensitivity analysis of terrestrial exoplanetary interior models*, The Astrophysical Journal, 819, 32

Unterborn, C. T., Kabbes, J. E., Pigott, J. S., Reaman, D. M., & Panero, W. R. 2014, *The role of carbon in extrasolar planetary geodynamics and habitability*, The Astrophysical Journal, 793, 124

Valencia, D., Ikoma, M., Guillot, T., & Nettelmann, N. 2010, *Composition and fate of short-period super-Earths. The case of CoRoT-7b*, Astronomy & Astrophysics, 516, A20

Valencia, D., O'Connell, R. J., & Sasselov, D. 2006, *Internal structure of massive terrestrial planets*, Icarus, 181, 545

Valencia, D., O'Connell, R. J., & Sasselov, D. D. 2007c, *Inevitability of plate tectonics on super-Earths*, The Astrophysical Journal Letters, 670, L45

Valencia, D., O'Connell, R. J., & Sasselov, D. D. 2009, *The role of high-pressure experiments on determining super-Earth properties*, Astrophysics and Space Science, 322, 135

Valencia, D., Sasselov, D. D., & O'Connell, R. J. 2007a, *Radius and structure models of the first super-Earth planet*, The Astrophysical Journal, 656, 545

van de Kamp, P. 1963, *Astrometric study of Barnard's star from plates taken with the 24-inch Sproul refractor.*, The Astronomical Journal, 68, 515

van de Kamp, P. 1982, *The planetary system of Barnard's star*, Vistas in Astronomy, 26, 141

van den Berg, A. P., Rainey, E. S. G., & Yuen, D. A. 2005, *The combined influences of variable thermal conductivity, temperature- and pressure-dependent viscosity and core mantle coupling on thermal evolution*, Physics of the Earth and Planetary Interiors, 149, 259

van den Berg, A. P., Yuen, D. A., Beebe, G. L., & Christiansen, M. D. 2010, *The dynamical impact of electronic thermal conductivity on deep mantle convection of exosolar planets*, Physics of the Earth and Planetary Interiors, 178, 136

Van Eylen, V., Agentoft, C., Lundkvist, M. S., et al. 2018, *An asteroseismic view of the radius valley: stripped cores, not born rocky*, Monthly Notices of the Royal Astronomical Society, 479, 4786

van Heck, H. J. & Tackley, P. J. 2011, *Plate tectonics on super-Earths: Equally or more likely than on Earth*, Earth and Planetary Science Letters, 310, 252

van Kan, J., Segal, A., & Vermolen, F. J. 2014, *Numerical methods in scientific computing* (VSSD)

van Kan Parker, M., Mason, P. R. D., & van Westrenen, W. 2011, *Trace element partitioning between ilmenite, armalcolite and anhydrous silicate melt: Implications for the formation of lunar high-Ti mare basalts*, Geochimica et Cosmochimica Acta, 75, 4179

van Lieshout, R., Min, M., & Dominik, C. 2014, *Dusty tails of evaporating exoplanets. I. Constraints on the dust composition*, Astronomy & Astrophysics, 572, A76

Veras, D., Mustill, A. J., Bonsor, A., & Wyatt, M. C. 2013, *Simulations of two-planet systems through all phases of stellar evolution: implications for the instability boundary and white dwarf pollution*, Monthly Notices of the Royal Astronomical Society, 431, 1686

Vidal-Madjar, A., Lecavelier des Etangs, A., Désert, J.-M., et al. 2003, *An extended upper atmosphere around the extrasolar planet HD209458b*, Nature, 422, 143

Vočadlo, L., Alfè, D., Gillan, M. J., et al. 2003, *Possible thermal and chemical stabilization of body-centred-cubic iron in the Earth's core*, Nature, 424, 536

Vočadlo, L., Wood, I. G., Gillan, M. J., et al. 2008, *The stability of bcc-Fe at high pressures and temperatures with respect to tetragonal strain*, Physics of the Earth and Planetary Interiors, 170, 52

Wagner, F. W., Sohl, F., Hussmann, H., Grott, M., & Rauer, H. 2011, *Interior structure models of solid exoplanets using material laws in the infinite pressure limit*, Icarus, 214, 366

Wagner, F. W., Tosi, N., Sohl, F., Rauer, H., & Spohn, T. 2012, *Rocky super-Earth interiors: Structure and internal dynamics of CoRoT-7b and Kepler-10b*, Astronomy & Astrophysics, 541, A103

Wagner, P. & Driesner, A. R. 1959, *High-Temperature Mechanical Properties of Graphite. I. Creep in Compression*, Journal of Applied Physics, 30, 148

Wahl, S. M. & Militzer, B. 2015, *High-temperature miscibility of iron and rock during terrestrial planet formation*, Earth and Planetary Science Letters, 410, 25

Walker, J. C. G., Hays, P. B., & Kasting, J. F. 1981, *A negative feedback mechanism for the long-term stabilization of the earth's surface temperature*, Journal of Geophysical Research, 86, 9776

Walsh, K. J., Morbidelli, A., Raymond, S. N., O'Brien, D. P., & Mandell, A. M. 2011, *A low mass for Mars from Jupiter's early gas-driven migration*, Nature, 475, 206

Wang, C., Hirama, J., Nagasaka, T., & Ban-Ya, S. 1991, *Phase equilibria of liquid Fe-S-C ternary system*, ISIJ International, 31, 1292

Wang, Y., Wen, L., & Weidner, D. J. 2013, *Composition of Mars constrained using geophysical observations and mineral physics modeling*, Physics of the Earth and Planetary Interiors, 224, 68

Watson, E. B., Wark, D. A., Price, J. D., & Van Orman, J. A. 2002, *Mapping the thermal structure of solid-media pressure assemblies*, Contributions to Mineralogy and Petrology, 142, 640

Wei, L., Kuo, P. K., Thomas, R. L., Anthony, T. R., & Banholzer, W. F. 1993, *Thermal conductivity of isotopically modified single crystal diamond*, Physical Review Letters, 70, 3764

Weiss, L. M. & Marcy, G. W. 2014, *The mass-radius relation for 65 exoplanets smaller than 4 Earth radii*, The Astrophysical Journal Letters, 783, L6

Whitehouse, L. J., Farihi, J., Green, P. J., Wilson, T. G., & Subasavage, J. P. 2018, *Dwarf carbon stars are likely metal-poor binaries and unlikely hosts to carbon planets*, Monthly Notices of the Royal Astronomical Society, 479, 3873

Williams, Q. & Knittle, E. 1997, *Constraints on core chemistry from the pressure dependence of the bulk modulus*, Physics of the Earth and Planetary Interiors, 100, 49

Wilson, H. F. & Militzer, B. 2014, *Interior phase transformations and mass-radius relationships of silicon-carbon planets*, The Astrophysical Journal, 793, 34

Winn, J. N. & Fabrycky, D. C. 2015, *The occurrence and architecture of exoplanetary systems*, Annual Review of Astronomy and Astrophysics, 53, 409

Wolstencroft, M., Davies, J. H., & Davies, D. R. 2009, *Nusselt-Rayleigh number scaling for spherical shell Earth mantle simulation up to a Rayleigh number of 10^9*, Physics of the Earth and Planetary Interiors, 176, 132

Wolszczan, A. & Frail, D. A. 1992, *A planetary system around the millisecond pulsar PSR1257 + 12*, Nature, 355, 145

Wu, S. Q., Ji, M., Wang, C. Z., et al. 2014, *An adaptive genetic algorithm for crystal structure prediction*, Journal of Physics: Condensed Matter, 26, 035402

Wyllie, P. J. 1981, *Plate tectonics and magma genesis*, Geologische Rundschau, 70, 128

Zapolsky, H. S. & Salpeter, E. E. 1969, *The mass-radius relation for cold spheres of low mass*, The Astrophysical Journal, 158, 809

Zuber, M. T., Solomon, S. C., Phillips, R. J., et al. 2000, *Internal structure and early thermal evolution of Mars from Mars Global Surveyor Topography and Gravity*, Science, 287, 1788

Zuckerman, B., Koester, D., Reid, I. N., & Hünsch, M. 2003, *Metal lines in DA white dwarfs*, The Astrophysical Journal, 596, 477

Zuckerman, B., Melis, C., Klein, B., Koester, D., & Jura, M. 2010, *Ancient planetary systems are orbiting a large fraction of white dwarf stars*, The Astrophysical Journal, 722, 725

Contribution from coauthors

The bibliographic information of the papers included in this thesis is listed here. The relative contribution of every coauthor is represented by their place in the author list.

Chapter 2: A new ab initio equation of state of hcp-Fe and its implication on the interior structure and mass-radius relations of rocky super-Earths
K. Hakim, A. Rivoldini, T. Van Hoolst, S. Cottenier, J. Jaeken, T. Chust, G. Steinle-Neumann
Icarus, 2018, 313, 61−78

Chapter 3: Mineralogy, structure and habitability of carbon-enriched rocky exoplanets: A laboratory approach
K. Hakim, R. Spaargaren, D. S. Grewal, A. Rohrbach, J. Berndt, C. Dominik, W. van Westrenen
Astrobiology (under review)

Chapter 4: Capturing the oxidation of silicon carbide in rocky exoplanetary interiors
K. Hakim, W. van Westrenen, C. Dominik
Astronomy & Astrophysics, 618, L6

Chapter 5: Thermal evolution of rocky exoplanets with a graphite outer shell
K. Hakim, A. van den Berg, A. Vazan, D. Höning, C. Dominik, W. van Westrenen
in preparation

Summary

In the third century BC, the Greek philosopher Epicurus scribed an almost prophetic statement in his letter to his disciple, Herodotus: “There is an infinite number of worlds, some like this world, others unlike it”. About four thousand planets outside our solar system (exoplanets) have been discovered in the past 25 years and tens of thousands or more are likely to be discovered in the next 25 years. A large fraction of these exoplanets are likely to have a solid or rocky surface, similar to the inner solar system planets; Mercury, Venus, Earth and Mars. Astronomical observations indicate that rocky exoplanets are much more diverse in their physics and chemistry than the planets of our solar system. For individual rocky exoplanets, however, the only information available at the moment is their mass and/or radius and there is no direct way to study their interiors. Nevertheless, it is possible to characterize them in a general sense. Some of the most intriguing questions are: What is the composition and structure of these diverse rocky exoplanets? What are their surfaces like? Can they sustain life?

Planets born orbiting their host stars are byproducts of the birth of the star itself. The formation of rocky planets takes place in the protoplanetary disk, a circumstellar nebula made of gas and solids (in the form of dust grains). These dust grains eventually become part of rocky planets as a result of accretion processes. The chemical composition of dust grains varies both with the distance from the newly-born star and with time. This chemical composition is strongly controlled by the relative abundances of major rock-forming elements such as magnesium, silicon and iron as well as carbon and oxygen. The bulk composition of a rocky planet depends on the chemical compositions of dust grains that acquired during formation.

Because the interiors of rocky planets are under immense pressures and temperatures, these dust grains undergo chemical reactions to produce a set of minerals in equilibrium. Due to gravity and the high temperatures associated with planetary accretion processes, the planets differentiate: denser minerals sink to the center of the planet and lighter minerals rise to the surface. This process leads to a stratified structure inside the planet. For a planet such as Earth or Mars, the inner layer is made of iron-rich metal and is called the core, and the outer layer comprises silicates and is called the mantle.

The heat acquired by a planet during its formation and produced during the natural decay of radioactive elements in its interior is slowly released during its evolution. Due to this internal heating, planetary interiors can remain dynamic for billions of years. The rate of

cooling of a planet depends on the physical and chemical properties of its different layers which determine the style and vigor of heat transport to the surface. The mantle can behave like a fluid over geological timescales. This leads to motion of material and transfer of heat resulting in convection, which is similar to the motion of water in a boiling pot (but extremely slow, at rates of centimeters per year). The material not taking part in convection transfers heat via conduction, which is the reason why the tail of a metallic spoon in the boiling pot becomes hot even though only the head is dipped.

Geosciences for exoplanets

In this thesis, I study the mineralogy, structure and evolution of chemically diverse rocky exoplanets using the tools mentioned below.

The deepest man-made hole on Earth reaches only 12 km below its surface, while the diameter of Earth is 12 742 km. Nonetheless, geoscientists still manage to study the Earth's interior using different tools from geophysics and geochemistry. Similarly, it is possible to study the interiors of rocky exoplanets using some of these tools. The high-pressure high-temperature conditions of planetary interiors can be reproduced in a high-pressure device using synthetic chemical powders to simulate interior bulk composition. Such experiments tell us about the minerals that form in the interiors of rocky exoplanets (Chapters 3 and 4). To describe the properties of these minerals we use the equation of state, which describes how the density of a mineral changes with pressure and temperature. The equation of state can either be measured directly from experiments or derived from the principles of quantum mechanics like we do in Chapter 2. With the information about mineral properties and physical laws, the stratified interior structure of rocky exoplanets is computed (Chapters 2, 3 and 5). For a generalized study of rocky exoplanets, theoretical mass-radius relations are also computed from the interior structure calculations (Chapter 2). The heat transport and thermal evolution in a rocky exoplanet are calculated using Rayleigh-Bénard convection (Chapter 5).

Mineralogy

Studies modeling the chemical evolution of protoplanetary disks have found that the carbon content in some rocky exoplanets can be up to 50% of the planet mass (Earth contains less than 0.01%). But the phase(s) in which this carbon is present are not known. We performed piston-cylinder experiments on chemical mixtures representative of carbon-enriched rocky exoplanets, exposing them to 1−2 GPa (10 000 times the atmospheric pressure) and 1523−1823 K, high enough to start melting rocks (Chapter 3). Our results show that these exoplanets, when fully differentiated (stratified), consists of a metallic core, a silicate mantle, and a graphite layer on top of the silicate mantle. Graphite (or diamond at higher pressures) is the dominant carbon-bearing phase in these exoplanets. The silicate mineralogy is similar to that in carbon-poor planets such as the Earth, and Mg/Si, Al/Si, Ca/Si ratios and oxygen fugacity (which essentially gives the oxygen content) determine the silicate phases and their compositions. Iron-rich metals show immiscibility (implying there would be a two-layer core

or a one-layer core) depending on the ratio of sulfur to iron and the core pressure. Our results show that if a rocky exoplanet contains more carbon than on the order of one per cent, graphite forms as a separate phase. Since the surface of these exoplanets may lack essential elements for life other than carbon such as oxygen, nitrogen, hydrogen and others, these exoplanets might be inhospitable for life.

Silicon carbide, another carbon-bearing phase discussed in several astronomical studies about carbon-enriched rocky exoplanets, which was present in the initial chemical mixture, disappeared by the end of our experiments. To understand the reason behind the vanishing of silicon carbide, we performed an experiment by reacting a silicon carbide layer with a layer representative of carbon-enriched rocky exoplanets (Chapter 4). Our experiment captures a reaction leading to the oxidation of silicon carbide in an exoplanetary interior. We show that, in order to stabilize silicon carbide in a planetary interior, all of the oxidized iron (Fe^{2+} and Fe^{3+}) should be reduced to Fe^{0}, suggesting future spectroscopic detection of Fe^{2+} or Fe^{3+} on the surface of rocky exoplanets may imply the absence of silicon carbide in the interior.

Structure

For the calculation of the interior structure of massive rocky exoplanets, equations of state of iron, the major constituent of the core, have been historically extrapolated to pressures more than an order of magnitude beyond their range of validity. In Chapter 2, we compute a new ab initio equation of state of solid iron up to pressures more than two orders of magnitude higher than the pressures reproducible in laboratories. The comparison of our equation of state with other equations shows that extrapolations lead to errors in the density of iron of up to 20% at a pressure of 10 TPa. This suggests that the implementation of extrapolated equations of state lead to a discrepancy of up to 20% in the masses of the most massive rocky exoplanets.

With the help of interior structure calculations, we quantify the effect of extreme core and mantle compositions and of the thermal profile on the mass-radius relations of massive rocky exoplanets (Chapter 2). Our results show that core and mantle compositions are capable of affecting the derived mass by up to 50%, whereas the temperature has a small effect of only a few per cent. Our application to Kepler-36b shows that its maximum core radius is 64% of the total radius.

We also perform interior structure calculations for rocky exoplanets with an iron-rich core, a silicate mantle and a graphite outer shell (Chapter 3). Our application to Kepler-37b, a planet with a known radius but unknown mass, shows that a model with 10% graphite has 7% less mass than the model with no graphite. This implies that the presence of graphite, due to its low density, can have a significant effect on the mass of the planet.

Evolution

Our experiments showed that it is possible for rocky exoplanets to consist of an iron-rich core, a silicate mantle, and a graphite outer shell (Chapter 3). But the thermal evolution of such planets is unknown. We apply a parameterized model of mantle convection to determine the heat transport in the graphite shell and the thermal evolution of these exoplanets (Chapter 5). We find that conduction is the dominant heat transport mechanism in graphite shells. Our results show that the outer graphite shell produces a thermal shielding effect which reduces the cooling rate of the planetary interior. This thermal shielding effect becomes significant for the long-term evolution of planets with a graphite outer shell thickness larger than 500 km. Our application to a known exoplanet, Kepler-37b, assuming that it is covered by a graphite shell, shows that the thermal shielding effect dominates over the effect of reduced internal heating. Plate tectonics and the presence of water on these exoplanets may increase the potential for habitability, especially for exoplanets with thin graphite shells.

The work presented in this thesis represents an effort to characterize rocky exoplanetary interiors by implementing laboratory and computational tools from geosciences. In my view, this is a first step towards establishing exogeoscience as a distinct discipline.

Samenvatting

In de derde eeuw voor Christus schreef de Griekse filosoof Epicurus een haast profetische stelling in zijn brief aan zijn discipel Herodotus: “Er is een oneindig aantal werelden, sommige zoals de onze, andere heel verschillend”. In de afgelopen 25 jaar zijn er ongeveer vierduizend planeten buiten ons zonnestelsel (exoplaneten) ontdekt, en in de komende 25 jaar zullen waarschijnlijk nog tienduizenden of meer ontdekkingen volgen. Een groot deel van deze exoplaneten heeft vermoedelijk een vast of rotsachtig oppervlakte, net als de planeten in het binnenste deel van het zonnestelsel; Mercurius, Venus, de aarde, en Mars. Astronomische waarnemingen hebben hebben een veel grotere diversiteit aangetoond in de natuur- en scheikundige eigenschappen vanrotsachtige exoplaneten dan van de planeten in ons zonnestelsel. Echter, de enige informatie die op dit moment beschikbaar is over individuele rotsachtige exoplaneten behelst hun massa en/of radius, en er is geen directe manier om hun binnenste te bestuderen. Niettemin is het mogelijk om exoplaneten in algemene zin te karakteriseren. Enkele intrigerende vragen zijn: Wat is de samenstelling en structuur van deze verschillende rotsachtige exoplaneten? Hoe ziet hun oppervlakte eruit? Zou er leven kunnen bestaan?

Planeten zijn een bijproduct van de geboorte van de sterren waar ze omheen draaien. De vorming van rotsachtige planeten vindt plaats in de protoplanetaire schijf, een circumstellaire wolk die uit gas en vaste deeltjes (in de vorm van stofkorrels) bestaat. De stofkorrels komen uiteindelijk terecht in de rotsachtige planeten door accretieprocessen. De chemische samenstelling van stofkorrels varieert met tijd en met de afstand tot de pasgeboren ster. Deze samenstelling is sterk afhankelijk van de relatieve chemische abundantie van belangrijke rotsvormende elementen zoals magnesium, silicium en ijzer, en ook van de hoeveelheid koolstof en zuurstof. De bulksamenstelling van een rotsachtige planeet hangt af van de chemische samenstellingen van de stofkorrels die de planeet heeft opgenomen tijdens haar vorming.

Omdat het binnenste van een rotsachtige planeet onder immense druk en temperatuur verkeert, ondergaan stofkorrels chemische reacties die tot een zekere evenwichtige combinatie van mineralen leiden. Vanwege de zwaartekracht en de hoge temperaturen die gepaard gaan met het planeetvormingsproces raken de planeten gedifferentieerd: zware materialen zinken naar beneden terwijl lichtere materialen naar boven komen. Dit proces leidt tot een gestratificeerde structuur in de planeet. In planeten zoals de aarde en Mars bestaat de binnenste laag, die we de kern noemen, uit ijzerrijk metaal. De buitenste laag bevat silicaten en wordt de mantel genoemd.

De hitte die een planeet verkrijgt tijdens haar vorming, en waar aan bijgedragen wordt door het natuurlijke verval van radioactieve elementen in haar binnenste, komt langzaam vrij tijdens de daaropvolgende evolutie. Het binnenste van een planeet kan miljarden jaren lang dynamisch actief blijven door deze interne hitte. De snelheid waarmee de planeet afkoelt hangt af van de natuur- en scheikundige eigenschappen van de verschillende lagen in de planeet, die de manier en kracht bepalen waarmee warmte naar het oppervlakte wordt getransporteerd. De mantel kan zich als een vloeistof gedragen op geologische tijdschalen, wat leidt tot de beweging van materiaal en warmteoverdracht in de vorm van convectie, net zoals in een pan met kokend water gebeurt (maar dan veel langzamer; we hebben het over snelheden van centimeters per jaar). Het materiaal dat niet meedoet aan de convectie draagt warmte over via geleiding, waardoor het uiteinde van een metalen lepel in de pan dat het water niet raakt, toch heet wordt.

Aardwetenschappen voor exoplaneten

In deze thesis bestudeer ik de mineralogie, structuur en evolutie van chemisch diverse rotsachtige exoplaneten, waarbij ik gebruik maak van methodes die ik hieronder beschrijf.

Het diepste gat dat door mensen op aarde is gemaakt reikt tot slechts 12 km onder het oppervlakte, terwijl de middellijn van de aarde 12 742 km is. Niettemin slagen aardwetenschappers erin het binnenste van de aarde te bestuderen door verschillende methodes uit de geofysica en geochemie te gebruiken. Het is ook mogelijk om de binnensten van rotsachtige exoplaneten te onderzoeken met een paar van deze methodes. De omstandigheden binnenin planeten, hoge druk en hoge temperatuur, kunnen worden nagebootst in een hogedrukapparaat met synthetische chemische poeders om de bulksamenstelling van planeten te simuleren. Zulke experimenten leren ons over de mineralen die zich bevinden in de binnensten van rotsachtige exoplaneten (Hoofdstuk 3 en 4). Om de eigenschappen van deze mineralen te beschrijven gebruiken we de toestandsvergelijking, die beschrijft hoe de dichtheid van mineralen verandert als functie van druk en temperatuur. De toestandsvergelijking kan zowel direct gemeten worden in experimenten, als afgeleid worden van de beginselen van de quantummechanica, zoals we in Hoofdstuk 2 doen. Met informatie over de mineraaleigenschappen en natuurkundige wetten kan de gelaagde structuur van rotsachtige exoplaneten berekend worden (Hoofdstuk 2, 3, en 5). Voor een algemene studie van rotsachtige exoplaneten worden theoretische massa-radiusrelaties bepaald uit de binnenstructuurberekeningen (Hoofdstuk 2). Het warmtetransport en de thermische evolutie in een rotsachtige exoplaneet kunnen worden berekend met Rayleigh-Bénardconvectie (Hoofdstuk 5).

Mineralogie

Studies waarin de chemische evolutie van protoplanetaire schijven wordt gemodelleerd laten zien dat het koolstofgehalte in sommige rotsachtige exoplaneten tot 50% van de planeetmassa kan zijn (ter vergelijking: de aarde bevat minder dan 0.01%). Echter, de fase waarin deze koolstof is geïncorporeerd is niet bekend. We hebben piston-cilinderexperimenten

uitgevoerd op chemische mengsels die representatief zijn voor koolstofrijke rotsachtige exoplaneten. We stelden deze mengsels bloot aan 1−2 GPa (10 000 keer de luchtdruk) en 1523−1823 K, hoog genoeg om gesteenten te laten smelten (Hoofdstuk 3). Onze resultaten tonen aan dat zulke exoplaneten, als ze helemaal gedifferentieerd (gestratificeerd) zijn, een metalen kern hebben, een silicaat mantel, en een grafietlaag bovenop de silicaat mantel. Grafiet (of diamant onder hogere druk) is de dominante koolstofhoudende fase in deze exoplaneten. De silicaat mineralogie is vergelijkbaar met die in koolstofarme planeten zoals de aarde, en Mg/Si, Al/Si, Ca/Si verhoudingen en zuurstofvluchtigheid (welke in essentie het zuurstofgehalte bepaalt), bepalen de silicaat fases en hun samenstelling. Ijzerrijke metalen vertonen onmengbaarheid (wat suggereert dat er een dubbellaagse of enkellaagse kern zou zijn), afhankelijk van de verhouding tussen zwavel en ijzer en de kerndruk. Onze resultaten laten zien dat als een rotsachtige exoplaneet meer koolstof bevat dan ongeveer één procent, grafiet een afzonderlijke laag vormt. Zulke exoplaneten zouden onherbergzaam voor leven kunnen zijn, omdat de oppervlaktes van deze exoplaneten andere essentiële elementen voor leven, zoals zuurstof, stikstof, waterstof, etc., missen.

Siliciumcarbide, een andere koolstofhoudende fase die wordt besproken in een aantal astronomische studies over koolstof-verrijkte rotsachtige exoplaneten, wat aanwezig was in het oorspronkelijke chemische mengsel, verdween aan het einde van onze experimenten. Om de reden voor de verdwijning van siliciumcarbide te begrijpen hebben we een experiment uitgevoerd waarin we een laag siliciumcarbide lieten reageren met een laag representatief voor koolstof-verrijkte rotsachtige exoplaneten (Hoofdstuk 4). Ons experiment bevatte een aanhoudende reactie die tot de oxidatie van siliciumcarbide in het binnenste van een exoplaneet leidt. We laten zien dat al het geoxideerde ijzer (Fe^{2+} en Fe^{3+}) gereduceerd moet worden tot FeO om het siliciumcarbide in het binnenste van een planeet te stabiliseren, wat suggereert dat toekomstige spectroscopische ontdekkingen van Fe^{2+} of Fe^{3+} op de oppervlaktes van rotsachtige exoplaneten een afwezigheid van siliciumcarbide in hun binnensten indiceren.

Structuur

Voor de berekening van de binnenstructuur van massieve rotsachtige exoplaneten zijn de toestandsvergelijkingen van ijzer, het belangrijkste bestanddeel van de kern, typisch geëxtrapoleerd tot waardes voor de druk die meer dan een orde van grootte groter zijn dan de hoogste waarde waarvoor de toestandsvergelijkingen geldig zijn. In Hoofdstuk 2 berekenen we een nieuwe ab initio toestandsvergelijking voor vast ijzer tot drukwaardes die meer dan twee orders van grootte hoger zijn dan nagebootst kan worden in het lab. De vergelijking tussen andere toestandsvergelijkingen en de onze laat zien dat extrapolaties tot fouten van ∼20% kunnen leiden in de dichtheid van ijzer bij een druk van 10 TPa. Dit suggereert dat de implementatie van geëxtrapoleerde toestandsvergelijkingen resulteren in een discrepantie van ∼20% in de massa's van de meest massieve rotsachtige exoplaneten.

Met behulp van binnenstructuur-berekeningen kwantificeren we de effecten van extreme kern- en mantelsamenstellingen en van het thermische profiel op de massa-radiusrelaties van massieve rotsachtige exoplaneten (Hoofdstuk 2). Onze resultaten tonen aan dat kern-

en mantelsamenstellingen de afgeleide massa tot ∼50% kunnen beïnvloeden, terwijl de temperatuur slechts een klein effect van een paar procent teweegbrengt. Onze toepassing op Kepler-36b laat zien dat haar maximale kernradius 64% van de totale radius is.

We voeren ook berekeningen van de binnenstructuur van rotsachtige exoplaneten met een ijzerrijke kern, een silicaat mantel en een grafiet buitenlaag uit (Hoofdstuk 3). Onze toepassing op Kepler-37b, een planeet met een bekende radius maar een onbekende massa, toont aan dat een model met 10% grafiet 7% minder massa heeft dan het model zonder grafiet. Dit betekent dat de aanwezigheid van grafiet, vanwege zijn lage dichtheid, een significant effect heeft op de massa van de planeet.

Evolutie

Onze experimenten hebben de mogelijkheid aangetoond dat rotsachtige exoplaneten bestaan uit een ijzerrijke kern, een silicaat mantel en een grafieten buitenste laag (Hoofdstuk 3). Maar de thermische evolutie van zulke planeten is tot noch toe niet bestudeerd. Wij passen een geparametriseerd model van mantelconvectie toe om het warmtetransport in de grafieten laag en de thermische evolutie van deze exoplaneten te bepalen (Hoofdstuk 5). We vinden dat geleiding het dominante warmtetransportmechanisme is in grafieten lagen. Onze resultaten tonen aan dat de buitenste grafieten laag een thermisch isolerend effect veroorzaakt, dat de koelsnelheid van het binnenste van de planeet verlaagt. Dit thermisch isolerende effect wordt belangrijk voor de lange-termijn evolutie van planeten met een grafieten buitenlaag die dikker is dan 500 km. Onze toepassing op een bekende exoplaneet, Kepler 37b, aannemende dat deze bedekt is met een grafieten laag, laat zien dat het thermisch isolerende effect sterker is dan het effect van verminderde interne opwarming. Platentektoniek en de aanwezigheid van water op deze exoplaneten zou de kans op leefbaarheid kunnen vergroten, in het bijzonder voor exoplaneten met dunne grafieten lagen.

Het werk dat in deze thesis wordt gepresenteerd representeert een poging om rotsachtige exoplaneten te karakteriseren middels experimentele en computationele technieken uit de aardwetenschappen. Naar mijn mening is dit een eerste stap in de oprichting van exo-aardwetenschappen als een aparte discipline.

Vertaler: Djoeke Schoonenberg

(Translator: Djoeke Schoonenberg)

सार

तीसरी शताब्दी ईसा पूर्व में, ग्रीक दार्शनिक एपिक्यूरस ने अपने शिष्य हेरोदोटस को लिखे अपने पत्र में लगभग एक भविष्यवाणी की थी - “विश्व की एक अनंत संख्या है, कुछ इस विश्व की तरह, अन्य इसके विपरीत।” पिछले २५ वर्षों में, हमारे सौर मंडल के बाहर लगभग चार हजार बहिर्ग्रह (एक्सोप्लेनेट) खोजें गए हैं और अगले २५ वर्षों में दस हजार या उससे भी अधिक की खोजे जाने की संभावना हैं। आंतरिक सौर मंडल ग्रहों, बुध, शुक्र, पृथ्वी और मंगल के समान इन बहिर्ग्रह की सतह ठोस या चट्टानी होने की संभावना है। खगोलीय अवलोकन से संकेत मिलता है कि हमारे सौर मंडल के चट्टानी ग्रहों की तुलना में चट्टानी बहिर्ग्रहों का भौतिकी और रसायन शास्त्र बहुत अधिक विविध है। व्यक्तिगत चट्टानी बहिर्ग्रह के लिए, तथापि, इस समय उपलब्ध एकमात्र जानकारी उनके द्रव्यमान और/या त्रिज्या की है और उनके आंतरिक अंशों का अध्ययन करने की कोई प्रत्यक्ष विधि उपलब्ध नहीं है। फिर भी, सामान्यत: इन ग्रहों की विशेषताओं का अध्ययन करना संभव है। कुछ सबसे रोचक प्रश्न हैं - इन विविध चट्टानी बहिर्ग्रहों की रचना और संरचना क्या है? उनकी सतह कैसी है? क्या उन ग्रहों पर जीवन का अस्तित्व संभव है?

एक सितारे के चारों ओर घूमने वाले ग्रह का जन्म उस सितारे के जन्म के साथ ही होता है। चट्टानी ग्रहों का गठन आदिग्रह चक्र (वायु और धूल-कणों से बनी एक परितारकीय निहारिका) में होता है। अभिवृद्धि प्रक्रियाओं के परिणामस्वरूप, ये धूल-कण अंतत: चट्टानी ग्रहों का हिस्सा बन जाते हैं। धूल-कणों की रासायनिक संरचना नवजात जन्मे तारे से दूरी और समय के साथ परिवर्तित होती है। यह रासायनिक संरचना चट्टान गठन के लिए आवश्यक तत्वों जैसे कि, मैग्नीशियम, लौह और सिलिकॉन के साथ-साथ ही कार्बन और ऑक्सीजन के सापेक्षक बहुतायत द्वारा नियंत्रित होता है। चट्टानी ग्रहों की थोक संरचना ग्रह-गठन के दौरान अधिग्रहित धूल-कणों की रासायनिक संरचनाओं पर निर्भर करती है। यही कारण है कि चट्टानी ग्रहों की कुल रासायनिक संरचना उनकी गठन प्रक्रिया में शामिल धूल-कणों की रासायनिक संरचना पर आधारित है।

चट्टानी ग्रहों के आतंरिक भागों में अत्यधिक दबाव और तापमान होता है। इस वजह से धूल-कणों पर रासायनिक प्रतिक्रिया होती है और खनिज पदार्थों का निर्माण होता है जो एक दूसरे के साथ रासायनिक संतुलन में होते हैं। गुरुत्वाकर्षण और ग्रहीय अभिवृद्धि प्रक्रियांओं से संलग्न उच्च तापमान के कारण ग्रहों के अंतर्गत विभिन्न स्तर बन जाते हैं - सघन खनिज पदार्थ ग्रह के गर्भ में रहता है और हलके खनिज पदार्थ ग्रह की सतह पर आते हैं। उदाहरण के लिए, पृथ्वी और मंगल जैसे ग्रहों में अंतरगर्भ (कोर) लौह-समृद्ध होता है और बाहरी परत या भूप्रावार (मैंटल) में सिलिकेट-युक्त खनिज पदार्थ होते हैं।

एक ग्रह द्वारा अपने गठन के समय और इसके आंतरिक भाग में रेडियोधर्मी तत्वों के प्राकृतिक क्षय के समय उत्पादित अधिग्रहित गर्मी को ग्रह की उत्क्रांति के दौरान धीरे-धीरे मुक्त किया जाता है। ग्रहों में आंतरिक ताप के कारण, उनके आंतरिक भाग अरबों वर्षों से गतिशील रह सकते हैं। एक ग्रह की शीतलन दर उसके भौतिक और रासायनिक गुणों पर निर्भर करती है। भूप्रावार भूवैज्ञानिक-काल पर तरल पदार्थ की तरह व्यवहार कर सकती है। इससे पदार्थ और ऊष्मा-स्थानांतरण की गति बढ़ जाती है जिसके परिणामस्वरू संवहन होता है, जो उबलते बर्तन में पानी की गति के समान होता है (लेकिन अत्यंत धीमी, सेंटीमीटर प्रति वर्ष की दर पर)। पदार्थ जो संवहन हस्तांतरण में भाग नहीं लेते हैं, चालन के माध्यम से ऊष्मान्तरण करते हैं। यही कारण है कि उबलते बर्तन में पूरा धातु का चम्मच गर्म हो जाता है भले ही मात्र उसका सिर डूबा हो।

बहिर्ग्रहों के लिए भूगर्भ विज्ञान

इस शोध-प्रबंध में, मैंने रासायनिक रूप से विविध चट्टानी बहिर्ग्रहों के खनिज विज्ञान, संरचना और उत्क्रांति का अध्ययन नीचे उल्लिखित उपकरणों का उपयोग करके किया है।

पृथ्वी का व्यास लगभग १२,७४२ कि.मी. है, परन्तु मनुष्य पृथ्वी की सतह से केवल १२ कि.मी. नीचे तक पहुँच सका है। फिर भी, भूगर्भ वैज्ञानिक भूगर्भ विज्ञान में विभिन्न उपकरणों का उपयोग करके पृथ्वी के आंतरिक भाग का अध्ययन करने में सफल रहे हैं। इसी तरह, इन उपकरणों में से कुछ का उपयोग कर चट्टानी बहिर्ग्रहों के आंतरिक भाग का अध्ययन संभव है। उच्च दबाव वाले उपकरण और कृत्रिम रासायनिक पाउडर की सहायता से, ग्रहों की उच्च तीव्रता और उच्च दबाव-उच्च तापमान स्थितियों को प्रयोगशाला में उत्पादित किया जा सकता है। ऐसे प्रयोग चट्टानी बहिर्ग्रहों के आंतरिक भाग में उपस्थित खनिजों के बारे में हमें बताते हैं (अध्याय ३ और ४)। इन खनिजों के गुणधर्मों को जानने के लिए हम अवस्था के समीकरण का उपयोग करते हैं, जो वर्णन करता है कि कैसे खनिजों का घनत्व दबाव और तापमान के साथ बदलता है। अवस्था के समीकरण को या तो सीधे प्रयोगों से मापा जाता है या क्वांटम मैकेनिक्स के सिद्धांतों से प्राप्त किया जाता है जैसे हम अध्याय २ में करते हैं।

भौतिकी नियम और खनिज पदार्थों के गुणों के जानकारी से चट्टानी बहिर्ग्रहों की स्तरीकृत आंतरिक संरचना का पता लगाया जा सकता है (अध्याय २, ३ और ५)। सामान्यतः चट्टानी बहिर्ग्रहों के एक सामान्यीकृत अध्ययन के लिए, उनकी आंतरिक संरचना को उनके द्रव्यमान और त्रिज्या से संबंधित हो सकता है (अध्याय २)। चट्टानी बहिर्ग्रहों में ऊष्मा परिवहन और ऊष्मीय उत्क्रांति की गणना रैले-बेनार्ड संवहन का उपयोग करके की जा सकती है (अध्याय ५)।

खनिज विज्ञान

आदिग्रह चक्रों की रासायनिक उत्क्रांति के अध्ययन में पाया गया है कि कुछ चट्टानी बहिर्ग्रहों में कार्बन मात्रा उनके द्रव्यमान के ५०% तक हो सकता है (पृथ्वी ०.०१% से कम धारण करती है)। लेकिन यह नहीं कहा जा सकता कि यह कार्बन किस रूप में है। इसलिए हमने कार्बन-समृद्ध चट्टानी बहिर्ग्रहों की रासायनिक रचना का प्रतिनिधित्व करने वाले कृत्रिम रासायनिक चूर्ण के साथ पिस्टन-सिलिंडर उपकरण में १-२ गिगापास्कल (जो वायुमंडलीय दबाव से १०,००० गुना अधिक है) और १५२३-१८२३ केल्विन (चट्टान पिघलाने में सक्षम) पर ले जाकर कई प्रयोग किये है (अध्याय ३)। हमारे परिणाम दिखाते हैं कि पूरी तरह से विभेदित (स्तरीकृत) होने पर इन बहिर्ग्रहों में धातु-समृद्ध अंतरगर्भ, सिलिकेट-युक्त भूप्रावार और भूप्रावार के शीर्ष पर ग्रेफाइट का आवरण होगा। ग्रेफाइट (अथवा उच्च दबाव पर हीरा) इन बहिर्ग्रहों में कार्बन का सबसे प्रभावी रूप है। सिलिकेट्स के खनिजशास्त्र और गुण कार्बन-अपर्याप्त ग्रहों के समान ही हैं, जैसे कि पृथ्वी में मैग्नीशियम/सिलिकॉन, ऐल्युमीनियम/सिलिकॉन, कैल्सियम/सिलिकॉन के अनुपात और ऑक्सीजन की मात्रा पर सिलिकेट्स का रूप और संरचना निर्धारित होता है। लौह-समृद्ध अंतरगर्भ में एक या दो परत होंगी ये सल्फर/लौह के अनुपात और अंतरगर्भ के दबाव पर निर्भर करता है। हमारे परिणाम दर्शाते हैं कि यदि एक चट्टानी बहिर्ग्रह में एक प्रतिशत से अधिक कार्बन होता है, तो कार्बन ग्रेफाइट के रूप में बनता है। चूंकि इन बहिर्ग्रहों की सतह में कार्बन को छोड़कर जीवन के लिए आवश्यक तत्व जैसे ऑक्सीजन, नाइट्रोजन, हाइड्रोजन और अन्य की कमी हो सकती है, ये जीवन के संरक्षण के लिए प्रतिकूल हो सकते है।

सिलिकॉन कार्बाइड युक्त कार्बन समृद्ध चट्टानी बहिर्ग्रहों की कई खगोलीय अध्ययनों में चर्चा की गई है। सिलिकॉन कार्बाइड जो हमारे प्रयोगों में प्रारंभिक रासायनिक मिश्रण में उपस्थित था, हमारे प्रयोगों के अंत में लुप्त हो गया। सिलिकॉन कार्बाइड के लुप्त हो जाने के पीछे कारण समझने के लिए, हमने एक सिलिकॉन कार्बाइड परत के साथ कार्बन समृद्ध चट्टानी बहिर्ग्रह के प्रतिनिधि परत पर प्रतिक्रिया करके एक प्रयोग किया (अध्याय ४)। हमारा प्रयोग एक बहिर्ग्रहीय आंतरिक भाग में सिलिकॉन कार्बाइड के ऑक्सीकरण की ओर अग्रसर होती एक निरंतर प्रतिक्रिया का अवलोकन करता है। हम प्रदर्शित करते हैं कि एक ग्रह के भीतर सिलिकॉन कार्बाइड को स्थिर करने के लिए सभी ऑक्सीकृत लौह (Fe^{2+} और Fe^{3+}) का Fe^{0} तक अपचयन होना चाहिए। भविष्य में स्पेक्ट्रोस्कोपिक अनुसन्धान द्वारा चट्टानी बहिर्ग्रहों की सतह पर Fe^{2+} या Fe^{3+} के शोध का अर्थ वह हो सकता है कि इन बहिर्ग्रहों के भीतर सिलिकॉन कार्बाइड की अनुपस्थिति है।

संरचना

भूगर्भ विज्ञान के इतिहास में, भारी चट्टानी बहिर्ग्रहों की आंतरिक संरचना की गणना के लिए लौह (अंतरगर्भ का प्रमुख घटक) की अवस्था के समीकरणों को उनकी वैधता सीमा से बाहर १० गुना अधिक दबावों के लिए बहिर्वेशित किया गया है। अध्याय २ में, हमने प्रयोगशालाओं में पुनरुत्पादनीय दबावों के १०० गुना अधिक दबावों के लिए लोहे के एक नवीन अवस्था के समीकरण की व्युत्पत्ति की है। हमारी अवस्था के समीकरण की तुलना अन्य समीकरणों के साथ करने से पता चलता है कि १० टेरापास्कल

के दबाव में लौह के घनत्व में २०% तक त्रुटि आ सकती है जिसका कारण अवस्था के समीकरण का बहिर्वेशन है। उसी प्रकार सबसे भारी चट्टानी बहिर्ग्रहों के द्रव्यमान में २०% तक त्रुटि आ सकती है।

अध्याय २ के अनुसार, आंतरिक संरचना के अध्ययन के आधार पर, हमने भारी चट्टानी बहिर्ग्रहों के द्रव्यमान-त्रिज्या संबंधों पर अंतरगर्भ और भूप्रावार की रासायनिक रचनाओं के प्रभाव और ऊष्मीय रूपरेखा के प्रभाव को मापा हैं। हमारे परिणाम बताते हैं कि अंतरगर्भ और भूप्रावार रचनाएं व्युत्पन्न द्रव्यमान को ५०% तक प्रभावित करने में सक्षम हैं, जबकि तापमान का प्रभाव केवल कुछ प्रतिशत है। केप्लर-३६ बी के लिए हमारा प्रयोग दर्शाता है कि इसके अंतरगर्भ की अधिकतम त्रिज्या कुल त्रिज्या की ६४% है।

हमने चट्टानी बहिर्ग्रहों के लिए लौह समृद्ध अंतरगर्भ के साथ सिलिकेट भूप्रावार और ग्रेफाइट बाहरी आवरण के आंतरिक संरचना की गणना भी की हैं (अध्याय ३)। केप्लर-३७ बी (एक ग्रह जिसकी त्रिज्या ज्ञात है लेकिन द्रव्यमान नहीं) के लिए हमारा अध्ययन दिखाता है कि १०% ग्रेफाइट वाला प्रतिरूप बिना ग्रेफाइट वाले प्रतिरूप की तुलना में ७% कम द्रव्यमान रखता है। इसका तात्पर्य है कि ग्रेफाइट की उपस्थिति, इसकी कम घनत्व के कारण, ग्रह के द्रव्यमान पर एक महत्वपूर्ण प्रभाव रखती है।

उत्क्रांति

हमारे प्रयोगों ने दर्शाया है कि कुछ चट्टानी बहिर्ग्रहों के भीतर लौह-समृद्ध अंतरगर्भ, सिलिकेट भूप्रावार और ग्रेफाइट बाहरी आवरण होने की संभावना है (अध्याय ३) लेकिन इस तरह के ग्रहों की ऊष्मीय उत्क्रांति अज्ञात है। हम ग्रेफाइट आवरण में ताप परिवहन और इन बहिर्ग्रहों के ऊष्मीय उत्क्रांति का निर्धारण करने के लिए भूप्रावार संवहन का एक मापदण्ड प्रतिरूप लागू करते हैं (अध्याय ५)। हम पाते हैं कि ग्रेफाइट बाहरी आवरण में चालन प्रमुख ताप परिवहन तंत्र है। हमारे परिणाम दिखाते हैं कि ग्रेफाइट बाहरी आवरण एक ऊष्मीय परिरक्षण प्रभाव पैदा करता है जो ग्रह के आंतरिक भाग की शीतलन दर को कम करता है। यह ऊष्मीय परिरक्षण प्रभाव ५०० कि.मी. से अधिक ग्रेफाइट आवरण वाले ग्रहों के दीर्घकालिक उत्क्रांति के लिए महत्वपूर्ण हो जाता है। हमारा अध्ययन एक ज्ञात बहिर्ग्रह केप्लर-३७ बी के लिए यह मानते हुए कि यह एक ग्रेफाइट आवरण द्वारा आच्छादित किया गया है, दिखाता है कि ऊष्मीय परिरक्षण प्रभाव कम दुर्बल आंतरिक तापन के प्रभाव पर प्रबल है। भूपट विवर्तनिकी और इन बहिर्ग्रहों पर पानी की उपस्थिति, विशेष रूप से पतले ग्रेफाइट आवरण वाले ग्रहों के लिए, जीवन के संरक्षण की क्षमता बढ़ सकती है।

इस शोध-प्रबंध में प्रस्तुत कार्य, भूगर्भ विज्ञान के प्रयोगशाला और अभिकलनात्मक उपकरण का कार्यान्वयन करके, चट्टानी बहिर्ग्रहीय आंतरिक भाग की विशेषता के लिए एक प्रयास का प्रतिनिधित्व करता है। मेरे दृष्टीकोण से, यह बहिर्भूगर्भ विज्ञान को एक विशिष्ट अनुशासन के रूप में स्थापित करने की दिशा में प्रथम पग है।

अनुवादक: डॉ वंदना सिंह कुशवाहा

(Translator: Dr. Vandana Singh Kushwaha)

सारांश

इ.स.पू. तिसऱ्या शतकात ग्रीक तत्त्ववेत्ता एपिक्युरस याने, त्याचा शिष्य हिरोडोटस याला लिहिलेल्या पत्रामध्ये, जणू एक भविष्यवाणीच केली होती, "या विश्वासारखी असलेली, अथवा नसलेली, अशी असंख्य विश्वं अस्तित्वात आहेत." आपल्या सूर्यमालेच्या बाहेर असणाऱ्या सुमारे चार हजार बाह्यग्रहांचा (एक्सोप्लॅनेट) मागील २५ वर्षात शोध लागला आहे आणि येत्या २५ वर्षात अश्या आणखी काही दशसहस्त्र ग्रहांचा शोध लागेल. या बाह्यग्रहांचा पृष्ठभाग बहुतांशी आपल्या सूर्यमालेतील बुध, शुक्र, पृथ्वी, मंगळ या ग्रहांसारखाच म्हणजे बहुतांशी घन आणि खडकाळ असावा. खगोलशास्त्रीय निरीक्षणांनुसार या बाह्यग्रहांचे भौतिक आणि रासायनिक गुणधर्म हे आपल्या सूर्यमालेतल्या ग्रहांच्या गुणधर्मांपेक्षा वेगळे असावेत. परंतु, अश्या खडकाळ बाह्यग्रहांबद्दल, त्याचं वस्तुमान आणि त्रिज्या याखेरीज, आणखी कुठलीच माहिती आणि तसेच त्यांच्या भूगर्भाचा अभ्यास करण्यासाठी कुठलीही सोपी पद्धत अद्याप उपलब्ध नाही. असे असले तरीही या ग्रहांच्या वैशिष्ट्यांचा अभ्यास केल्यास, या बाह्यग्रहांची भौतिक आणि रासायनिक संरचना कशी असेल? त्यांचा पृष्ठभाग कसा असेल? हे ग्रह जीवसृष्टीच्या संवर्धनासाठी अनुकूल असतील का? यासारखे काही अनुत्तरीत प्रश्न सोडविण्यास मदत होईल.

एका ताऱ्याभोवती फिरणाऱ्या ग्रहाचा जन्म त्या ताऱ्याच्या जन्मासोबतच होतो. अश्या खडकाळ ग्रहांची निर्मिती ही वायू आणि धूलीकणांपासून बनलेल्या परितारकीय निहारीकेमध्ये (आदिग्रह चक्र) होते. या ग्रहांच्या बनावटीमध्ये हे धूलीकण समाविष्ट होतात. या धूलीकणांचे रासायनिक गुणधर्म, हे त्यांचे नव्या जन्मलेल्या ताऱ्यापासूनचे असणारे अंतर आणि त्यांच्या उत्पत्तीपासून व्यतीत झालेला वेळ, यावर अवलंबून असतात. ही रासायनिक संरचना खडक निर्मितीसाठी आवश्यक असलेल्या मॅग्नेशियम, लोह आणि सिलिकॉन या मूलतत्वांशिवाय कार्बन आणि ऑक्सिजन या मूलतत्वांच्या सापेक्ष रासायनिक विपुलतेवरही अवलंबून असते. त्यामुळेच खडकाळ ग्रहांची एकूण रासायनिक संरचना ही त्यांच्या संवृद्धी प्रक्रियेदरम्यान त्यात समाविष्ट झालेल्या या धूलीकणांच्या रासायनिक रचनेवर आधारित असते.

खडकाळ ग्रहांच्या अंतर्गत भागांमध्ये प्रचंड दबाव आणि तापमान असतो. त्यामुळे धूलीकणांवर रासायनिक प्रतिक्रिया होते आणि खनिज पदार्थ तयार होतात जे एकमेकांशी समतोल राखतात. गुरुत्वाकर्षण आणि ग्रह संवृद्धीशी निगडित असणारे उच्च तापमान यांमुळे ग्रहांमध्ये वेगवेगळे स्तर निर्माण होतात – घन खनिजपदार्थ ग्रहाच्या गर्भात स्थिरावतात तर हलके खनिजपदार्थ ग्रहाच्या पृष्ठभागावर येतात. उदाहरणार्थ, पृथ्वी आणि मंगळाचा आंतर्गाभा (कोर) हा लोहयुक्त आहे आणि प्रावरणामध्ये (मँटल) सिलिकेट्स आढळतात.

ग्रहनिर्मितीच्या वेळी उपार्जित आणि गाभ्यातील किरणोत्सारी मूलतत्वांच्या अपक्षयातून तयार होणारी उष्णता ग्रहाची उत्क्रांती होताना हळू हळू बाहेर पडते. याच अंतर्गत उष्णतेमुळे, कित्येक लाखो–अब्ज वर्षं ग्रहांचा गाभा प्रवाही अथवा गतिक राहू शकतो. ग्रहांमधल्या स्तरांच्या भौतिक आणि रासायनिक गुणधर्मांवर ग्रहांचे शीतन अवलंबून असते. भूशास्त्रीय कालमानानुसार प्रावरण प्रवाही राहू शकते. यामुळे (खनिज)पदार्थांची हालचाल आणि उष्णतेचे प्रक्रमण होते. ग्रहांच्या अंतरंगात होणारे प्रक्रमण हे उकळत्या पाण्यात होणाऱ्या प्रक्रमणाप्रमाणे आहे (परंतु वर्षाला सेंटीमीटर इतक्या संथ गतीने). तसेच ज्याप्रमाणे एखादा धातूचा चमचा उकळत्या पाण्यात बुडवला असता चटकन तापतो तश्याचप्रकारचे उष्णतेचे संवहन हे प्रक्रमणामध्ये सहभागी न होणाऱ्या (खनिज)पदार्थांद्वारे होते.

बाह्यग्रहांसाठी भूगर्भशास्त्र

या शोधनिबंधामध्ये, मी खाली वर्णन केलेल्या पद्धतीने खडकाळ बाह्यग्रहांच्या खनिजशास्त्राचा, त्यांच्या संरचनेचा आणि उत्क्रांतीचा अभ्यास केला आहे.

पृथ्वीचा व्यास सुमारे १२,७४२ कि.मी. असून आजवर माणूस फक्त १२ कि.मी. खोल जाऊ शकला आहे. तरीही भूभौतिकशास्त्र व भूरसायनशास्त्रातील विविध पद्धतींचा वापर करून भूगर्भशास्त्रज्ञांना पृथ्वीच्या अंतरंगाचा अभ्यास करता येतो. यातीलच काही पद्धतींचा अवलंब करून खडकाळ ग्रहांच्या अंतरंगांचा अभ्यास करणे देखील शक्य आहे. एखादे उच्च–दाब यंत्र आणि कृत्रिम रासायनिक भुकटीच्या सहाय्याने ग्रहांच्या अंतरंगाची व तेथील उच्च–दाब–उच्च तापमान परिस्थितीची निर्मिती प्रयोगशाळेत करता येऊ शकते. खडकाळ ग्रहांच्या अंतरंगात कुठल्या खनिजपदार्थांची निर्मिती होऊ शकते हे आपल्याला अश्या प्रयोगांमधून समजते (प्रकरण ३ आणि ४). या खनिजपदार्थांच्या गुणधर्मांचा अभ्यास करताना अवस्था–समीकरणाचा वापर केला जातो, ज्यातून दाब आणि तापमानाचा खनिजांच्या घनतेवर होणारा परिणाम लक्षात येतो. या अवस्था–समीकरणाची उकल थेट प्रयोगांद्वारे अथवा प्रकरण २ मध्ये दिल्याप्रमाणे क्वान्टम स्थितिगतिशास्त्राद्वारे करता येते. भौतिकक्षेत्रातील नियम व खनिज पदार्थांचे गुणधर्म यांवरून खडकाळ ग्रहांच्या स्तरांचा सरासरी अंदाज बांधता येतो (प्रकरण २, ३ आणि ५). सर्वसाधारणपणे खडकाळ ग्रहांचा अभ्यास करताना, त्यांच्या अंतर्गत रचनेच्या आकलनानुसार, तात्विकदृष्ट्या त्यांचे वस्तुमान आणि त्रिज्या यांचा संबंध लावता येतो (प्रकरण २). खडकाळ ग्रहांवरील ऊष्मांतरण आणि त्यांची औष्णिक उत्क्रांती यांचे गणन रॅले–बेनार्ड प्रक्रमण प्रमेयाद्वारे करता येते (प्रकरण ५).

खनिजशास्त्र

आदिग्रह चक्रांच्या रासायनिक उत्क्रांतीचा अभ्यास करताना असे लक्षात आले आहे की काही खडकाळ बाह्यग्रहांच्या रचनेत कार्बनचे प्रमाण त्यांच्या वस्तुमानाच्या ५०% पर्यंत असू शकते (पृथ्वीसाठी हे प्रमाण ०.०१% पेक्षा कमी आहे). परंतु हा कार्बन कुठल्या स्वरूपात असेल हे नक्की सांगता येणार नाही. खडकाळ ग्रहांच्या कार्बनयुक्त अंतरंगाशी साधर्म्य असलेल्या रासायनिक मिश्रणावर १–२ गिगापास्कल क्षमतेचा दाब टाकून (वातावरणीय दाबाच्या १०,००० पट जास्त) आणि खडकांना वितळवेल इतके जास्त (सुमारे १५२३–१८२३ केल्व्हिन) तापमान साधून आम्ही काही पिस्टन–सिलेंडर प्रयोग केले आहेत (प्रकरण ३). आमच्या निरीक्षणांनुसार अश्या बाह्यग्रहांचे स्तरीकरण पूर्ण झाल्यावर सर्वात आतला स्तर (गाभा) हा धातूयुक्त असतो, त्यावर सिलिकेटचे प्रावरण व त्यावर ग्रॅफाईटचे कवच असते. ग्रॅफाईट (व उच्च दाबा खाली असताना हिरा) हे अश्या खडकाळ बाह्यग्रहांमधल्या कार्बनचे सर्वात प्रभावी स्वरूप असते. सिलिकेट्सचे खनिजशास्त्र व गुणधर्म हे पृथ्वी सारख्या, कार्बनची कमतरता असलेल्या ग्रहांप्रमाणेच, असतात आणि मॅग्नेशियम–सिलिकॉन, अल्युमिनियम–सिलिकॉन, कॅल्शियम–सिलिकॉन यांच्या गुणोत्तरांवरून तसेच ऑक्सिजनच्या आशुलोपतेनुसार (ज्यावरून उपलब्ध ऑक्सिजनची मात्रा समजते) या सिलिकेट्सचे स्वरूप आणि रचना ठरते. अंतर्गाभ्यावर असलेला दाब आणि सल्फर–लोह यांचे गुणोत्तर यानुसार लोह–युक्त धातू अमिश्रणीयता दर्शवतात (ज्यावरून गाभ्याचे १ किंव्हा २ स्तर असतील ते समजू शकते). आमच्या निरीक्षणांनुसार जर बाह्यग्रहांमध्ये कार्बनचे प्रमाण १% पेक्षा जास्त असेल तर ग्रॅफाईटची विलग प्रावस्था तयार होते. या बाह्यग्रहांच्या पृष्ठभागावर कार्बन वगळता, ऑक्सिजन, नायट्रोजन, हायड्रोजन व इतर जीवसृष्टीसाठी उपयुक्त मूलतत्वांची कमतरता असल्यामुळे हे ग्रह जीवसृष्टीच्या संवर्धनासाठी प्रतिकूल असू शकतात.

कार्बनयुक्त खडकाळ ग्रहांच्या खगोलशास्त्रीय संशोधनांमध्ये वर्णिलेली सिलिकॉन कार्बाइड ही कार्बनची अजून एक प्रावस्था. आमच्या प्रयोगामध्ये सुरुवातीच्या मिश्रणात असलेले सिलिकॉन कार्बाइड, प्रयोग संपताना पूर्ण नष्ट झाले होते. यामागचे कारण शोधण्यासाठी आम्ही एक प्रयोग केला ज्यामध्ये सिलिकॉन कार्बाइडचा स्तर आणि खडकाळ ग्रहांच्या कार्बनयुक्त रचनेचे प्रतिनिधित्व करणारा स्तर या दोहोंमधील रासायनिक अभिक्रियांचा अभ्यास आम्ही केला (प्रकरण ४). आमच्या प्रयोगांतून बाह्यग्रहांच्या अंतरंगात शक्य असलेली, सिलिकॉन कार्बाइडचे ऑक्सिडेशन घडवून आणणारी, अभिक्रिया लक्षात येते. आमच्या अभ्यासातून असेही निदर्शनास येते की ग्रहांच्या आंतरिक वातावरणात सिलिकॉन कार्बाइड स्थिर होण्यासाठी ऑक्सिडेशन झालेल्या संपूर्ण लोहाचे (Fe^{2+} आणि Fe^{3+}) क्षपण होणे (Fe^{0}) गरजेचे आहे, त्यामुळे भविष्यातील कोणत्याही पंक्तिदर्शनीक अभ्यासात एखाद्या ग्रहाच्या पृष्ठभागी Fe^{2+} किंवा Fe^{3+}

यांचा शोध लागल्यास त्या ग्रहाच्या अंतर्गत रचनेत सिलिकॉन कार्बाइडचा अभाव असू शकतो.

संरचना

भूगर्भशास्त्राच्या इतिहासात, मोठ्या खडकाळ बाह्यग्रहांच्या अंतर्गत संरचनेचा अभ्यास करताना, त्यांच्या गाभ्याचा मुख्य घटक असलेल्या लोहाच्या अवस्था समिकरणांचे, वैधतेपेक्षा १० पट जास्त दाब वापरून, बहिर्वेशन केले गेले आहे. प्रकरण २ मध्ये दिल्याप्रमाणे, प्रयोगशाळांमध्ये निर्माण करता येईल त्यापेक्षा १०० पट जास्त दाब वापरून आम्ही घन स्वरूपातल्या लोहासाठी एका नवीन अवस्था समीकरणाची रचना आणि गणना केली. आमच्या समीकरणाची मूळच्या समीकरणांशी तुलना केली असता असे लक्षात येते की १० टेरापास्कल इतका दाब असताना जुन्या समीकरणांप्रमाणे बहिर्वेशन केल्यास लोहाची घनता मोजण्यामध्ये २०% पर्यंत त्रुटी येते. म्हणजेच अवस्था समिकरणांचे बहिर्वेशन करून मोजमाप केलेल्या बहुतांश ग्रहांच्या वस्तुमानामध्ये देखील २०% पर्यंत त्रुटी असू शकते.

प्रकरण २ मध्ये दिल्याप्रमाणे, अंतर्गत संरचनेच्या अभ्यासाचा आधार घेत, आम्ही गाभा आणि प्रावरण यांच्या अत्यंत क्लिष्ट रचनेचा आणि औष्णिक पार्श्वरेखेचा, मोठ्या खडकाळ बाह्यग्रहांच्या वस्तुमान–त्रिज्या संबंधांवर काय परिणाम होऊ शकतो याचे आकलन केले. आमच्या निरिक्षणांनुसार गाभा आणि प्रावरण यांच्या रचनेचा ग्रहाच्या साधित वस्तुमानावर सुमारे ५०% पर्यंत प्रभाव पडू शकतो परंतु तापमानाचा परिणाम अगदी काही टक्केच होतो. आमच्या गणनेनुसार केप्लर–३६ब च्या गाभ्याची कमाल त्रिज्या संपूर्ण त्रिज्येच्या ६४% आहे.

प्रकरण ३ मध्ये दिल्याप्रमाणे, लोहयुक्त गाभा, सिलिकेटचे प्रावरण आणि ग्रॅफाईटचे बाह्य कवच असणाऱ्या खडकाळ बाह्यग्रहांच्या अंतर्गत संरचनेचा अभ्यास देखील आम्ही केला. यासाठी उदाहरण म्हणून त्रिज्या माहित असलेल्या परंतु वस्तुमान अज्ञात असलेल्या केप्लर–३७ब चा आम्ही विचार केला. आमच्या निकषांनुसार, १% ग्रॅफाईट असलेल्या प्रतिकृतीचे वस्तुमान हे ग्रॅफाईट नसलेल्या प्रतिकृतीपेक्षा ७% कमी असते. म्हणजेच निम्न घनतेच्या ग्रॅफाईटमुळे, ग्रहांच्या वस्तुमान मोजणीत लक्षणीय तफावत येऊ शकते.

उत्क्रांती

आमच्या प्रयोगांतून असे निदर्शनास येते की काही खडकाळ बाह्यग्रहांमध्ये लोहयुक्त गाभा, सिलिकेटचे प्रावरण आणि ग्रॅफाईटचे कवच असू शकते (प्रकरण ३). परंतु अश्या ग्रहांच्या औष्णिक उत्क्रांतीबद्दल अजून माहिती उपलब्ध नाही. प्रकरण ५ मध्ये दिल्याप्रमाणे या बाह्यग्रहांच्या औष्णिक उत्क्रांतीचा आणि ग्रॅफाईट कवचातून होणाऱ्या ऊष्मांतरणाचा अभ्यास करण्यासाठी आम्ही प्रावरणातून होणाऱ्या प्रक्रमणाची प्रमाणित प्रतिकृती वापरली आहे. या अभ्यासातून असे निदर्शनास येते की, ग्रॅफाईट कवचातून ऊष्मांतरण हे मुख्यत्वे संवहन प्रक्रियेद्वारे होते आणि ग्रॅफाईटच्या कवचामुळे औष्णिक परिरक्षण होऊन ग्रहांच्या आतील भागाच्या शीतनाचा वेग मंदावतो. ग्रॅफाईटच्या बाह्य कवचाची जाडी ५०० कि.मी. पेक्षा जास्त असल्यास या औष्णिक परिरक्षणाचा ग्रहांच्या दीर्घ–कालीन विकासावर लक्षणीय परिणाम होतो. उदाहरणार्थ, आमच्या निकषांनुसार जर केप्लर–३७ब वर ग्रॅफाईटचे कवच आहे असे गृहीत धरले तर औष्णिक परिरक्षणाचा होणारा परिणाम हा ग्रहाच्या अंतर्गत उष्णतेच्या परिणामापेक्षा जास्त असेल. भूपट्ट विवर्तनिकी आणि पाण्याची उपलब्धता असल्यास अश्या, विशेषतः ग्रॅफाईटचे पातळ कवच असलेल्या, बाह्यग्रहांवर जीवसृष्टीच्या संवर्धनाची क्षमता वाढू शकेल.

प्रस्तुत शोधनिबंधात, भूगर्भशास्त्राशी निगडित, संगणकीय तसेच प्रयोगशाळांमधील, विविध पद्धतींचा वापर करून, खडकाळ बाह्यग्रहांच्या अंतर्गत रचनेचा अभ्यास करण्यात आला आहे. बाह्य–भूगर्भशास्त्र अशी विशिष्ट शाखा प्रस्थापित होण्यासाठी हे पहिले पाऊल ठरू शकेल.

अनुवादक : डॉ विश्वास रवींद्र अभ्यंकर

(Translator: Dr. Wishwas Ravindra Abhyankar)

The end or just a new beginning?

Did you open this section without reading rest of the thesis? Okay, okay, don't feel guilty. This is the most interesting part anyway :)

I believe that any person, in addition to exhibiting personal attributes, reflects the environments of the past and the present, that is, the society and the people. Here, I would like to thank the souls who have supported me during the last four years as well as those who shaped the course of my life to make me capable of reaching here. Of course, the list is long (but not exhaustive, excuses for that). So, brace yourselves, it is going to be a long ride.

First, I would like to thank Carsten and Wim for putting their trust in me with this interdisciplinary project. There were quite a few ups and downs during this PhD and both of you always encouraged me to keep going. I have learned a lot from both of you. Carsten, since day one I could easily resonate with your energy. Thank you for letting me walk into your office without appointments. I would always cherish our scientific and non-scientific discussions. Wim, without your open-mindedness about talking business with two astronomers, this project wouldn't have been possible. Thank you for your witty comments on my manuscripts, they always made me smile during stressful moments. Regarding working in the laboratory, what I am going to miss the most is my love and hate relationship with Freddy.

Next, I would like to express my gratitude to my collaborators, Tim and Tilio. Thank you, Tim, for giving me the opportunity to do my master thesis on exoplanets (other choice was Titan but I really wanted exoplanets), that is where it essentially began for me. Tilio, I always have valued your rapid and witty replies to my emails and I hope I get to drink more coffee with you at ROB. A special thanks to Stefaan for providing the equation of state data for iron, which was crucial for our paper. Gerd and Thomas, I really appreciate your contributions to the phase relations data for super-Earth mantles. Thanks Tilly and Sergei for your help with the microprobe in Utrecht and thanks Fraukje for managing visits to the microprobe lab. Arno and Jasper, thank you for hosting me in Münster in your laboratory multiple times. Although results were not in our favor, I will truly cherish the experience of learning and operating some cool machines, and also German efficiency! Rob, thank you for your contribution with carbon experiments, I wish you all the best for your future. Thanks Allona for being the only interior modeling person in my vicinity and making yourself available when I would drop by your office for quick chats, especially for my last project. Thanks a lot, Arie, for rigorously collaborating in my thermal evolution project. I have learned a

lot from you. Dennis, it was really nice to meet someone with similar research interests. I regard your inputs vital for improving my last paper.

Chris, although I never had the chance to collaborate with you but thank you for keeping your door open for me to have discussions on several topics. Sebastiaan, thank you for hosting me in Chicago during my visit. I would also like to thank the exoplanets and disks group members, Lucia, Tomas, Rik, Gaby, Kamen, Melissa, Vatsal, Djoeke, Jacob, Jean-Michel, Jayne, Lorenzo, Michiel, Lucas, Rens, Beibei, for bringing together some amazing expertise which helped me learn a lot. Thanks Rens and Annemieke for keeping my knowledge broad by involving me in the ISM course. Alex, thank you for being open to talk to on several topics, also thanks for organizing the presentation skills course.

I would also like to thank my PEPSci colleagues in Leiden, Utrecht, Groningen, and Delft for several fun meetings, lunches and dinners without which I would not know anything about astrochemistry, planetary science or biology. Thanks Claudia, for being my lunch buddy during my visits to Utrecht. Also, thanks to Vincent, Katya, Andrew, Christian, Lucas, Edgar, Bram, Teresa, Alex, and several others!

Before I start thanking Amsterdammers, I would like to thank people in Leuven who were the first astronomers I encountered in my life. Thank you Christoffel for accepting someone without a physics background to your master's program. I would always remember our discussion about the orbit of Neptune and dinosaurs. Conny, I really value your way of interaction with students, it is really encouraging to stay in academia. My stay in IvS wouldn't have been fun without Vincent, Marie, Charis, Michiel, Cem, Timothy and Bram.

My interdisciplinary project made my stay in Amsterdam a superposition of two quantum states: API at UvA and Earth Science Dept at VU. I am really going to miss the lunch and coffee breaks at VU with Jurrien, Mélissa, Clément, Yue, Steffi, Dennis, Onno, Paolo, Lorenzo, Alice, Janne, Héloïse, and others. Jurrien, I will never be able to erase from my memory your scream in the flight simulator in Houston. Mélissa, thank you for such passionate discussions about every planetary body in our solar system, and of course about science, climate change, administration, people, and also the one you hate the most, politics! Clément, never forget me when you become the next Damian Peach! Yue, thanks for all the fun ideas for group hangouts. Steffi, thanks for being the missing link in our lab, I am sure I will catch up with you in Switzerland. Also, many thanks to Fenny for all the administrative work which is much more complicated at VU.

Now it gets to the difficult part – API. This place is really special. I haven't been to many scientific departments in the world, but I can confidently state that there is no department which matches the social and cultural diversity and integrity as API. You can walk out in the corridor and always find at least one soul to hear you out. The amount of non-science activities going on at API gives a perfect way to relieve your stress and makes you focus on your work better. People say you don't make real friends after a certain age. But coming to Amsterdam changed that for me.

Martin is the Gandalf of API, standing in the way of every newcomer screaming you shall not pass. But once you kick his posterior, you get past The Ice Wall and reach Hogwarts,

where you get to become a Jedi. Thank you, Martin, for being the person who says no to every plan I make and still joins it anyway. Oscar, you are like a classic movie which is ahead of its time and appreciated only a generation later. To answer your question from several years ago: you started your PhD too early. Nevertheless, we had a lot of fun during the times you were here. But I totally miss your hyperactivity! Macla, I think we survived because our love and hate feeling is mutual. Since the day I met you I also wanted to kill you, especially when it's about card games. I am truly amazed by your positivity. Thank you so much for everything you do :) Thanks Macla, Oscar and Esperanza and your family for hosting us in Colombia, I would like a chance to visit again, soon! Alice, what can I say? You are stubborn and strict yet the most fun-loving and mischievous person, it is a mystery to me how you manage to be both at once. Thank you for sharing piparelle with me. You are a true friend. I hope to visit Mount Etna soon (and perhaps also you? :P). Thanks Macla and Alice, for being a constant support over these four years. Also, we need to plan that beer trip! Ciccio, you are so natural at being an API. Thanks for being an integral part from a distance. Since a year, you have got more reasons to keep visiting! Ning, thanks for being part of Vandana's and my life in Amsterdam! Ylva, you have an infectious enthusiasm, thanks for so many wonderful memories. Vlad, thanks for being the social glue, I had a feeling that the social nature of API was dying until you arrived. I will always remember (forget) your tea. Smriti, you were my first Indian connection in Amsterdam. And because of you, Maithili was my second Indian connection. Thank you both for all the Indian food and chats over the years. Alicia, you are an amazing friend, you have no limits on the effort you put in for the people you care about, thank you! Koushik, our KGP and Chauki connection was an instant click. Dario, thanks for being the pollo we always needed but not wanted. Until now no one has managed to fill the pollo you left behind! Adam C., thanks for your craziness which usually scares the people but occasionally also brings smile on their face. Daniele, from just a Roman guy to the Nature guy, you have gone a long way. Hope to catch up with you in Canada. Amruta, thanks for being the only Marathi-speaking person in the corridor (also for the Oort Canal). Gullo, thanks for being our El Capitan for the Batavieren races. Manos, you were probably my first API connection (we met almost a year before I arrived in Amsterdam). Thanks for those Oreos :) Riley, the athlete in you made us participate and win several API tournaments, thanks for that. Stefano, thanks for being a creative genius. Georgi and Chris, thanks for being the backbenchers in the class who make fun of every soul. Susan, thank you for all the help with housing related matters and also for checking my stress level every now and then. Milena, thanks a lot for all extreme conversations and the help with administrative stuff. Thanks to Yuri for making the score sheets for 7 Up and 7 Down. Liliana, I am grateful to you for sparing my life after the Mexican cake smash. Theo and Chiara, thanks for killing Martin all those years. Samayra, thanks for practicing to pronounce my name for the past four years; give it another four years and you will be there! Marieke, thanks for being my unexpected secretary when I was not around — this has led to a lot of funny stories :) Lucia, it was fun to discuss all sorts of things from carbon to beers! Djoeke, thank you for being my go-to planet person, and also for translating my thesis summary! Claire, thanks for your omnipresence in all events :) we still need to play mini-golf, again. Dimitris, yes, seriously stop shooting those videos! Adam I. and Natalie, thanks for making the evenings in API

so lively. Difeng, I hope you finally removed the hair from Natalie's potato. Also thanks to Bertrand, Rachel, Hanneke, Mathieu, Eva, Eleanor, Mark, Laura, Nina, Vatsal, Frank, Rachel, Maria, Aastha, Martijn, Tom, Liam, Juan, Silvia, Jure, Milena, Susan, Renée, Jason, Lucas, Leon, Tobi, Fe, Athira, Lorenzo, Ines, Ben, all new APIs who are still absorbing the intense social environment, and several of you whom I am forgetting at the moment (excuses!), for being around for sports, beers, whiskey breaks, international dinners, Sinterklaas and Christmas parties, and what not!

Thanks for several wonderful memories in Amsterdam, Bhagyashree and Wishwas (also for translating my thesis summary to Marathi), and Aish and Swapneel. Thanks to my Leuven friends, Vamsi, Rochan (also thanks for playing the role of a cupid), Manoj, Finub and others, for the amazing trips exploring Belgium and beyond; more destinations await us. Thanks to all those friends whom I met during different walks of my life and and have influenced the decisions in my life in one way or another. Especially to my Mumbai flatmates, Mayank, Shobhit, Abhijeet, Arpit, Rohit, Rahul; my KGP friends, Vipul, Vasi, Rohan, Pankaj (thanks for making an awesome cover), Shashank, Jayant, Asit, Romil, Rajat, Kuldeep, Shaun, Agro, Shishir; my school friends, Pranjal, Prakash, Vivek, Ravi and Mayank.

Thanks to my extended family members who take pride in each of my accomplishments: Maushi-Kaka, Sameer, Satish kaka-kaku, Sanika, Aatya-Fua, Mayank-Suchita, Manju didi and jiju, Suresh kaka-kaku, Sameer, Raju mama-mami, Chaitali, Aayushi, Babu mama-mami, Tanaya-Devika, Nana and Aaji-Ajoba. My talented in-laws: Ajeet bhaiya and Shruti bhabhi, Amit bhaiya and Nishi, Archana didi and Akhilesh jijaji, Rachna didi and Prateek jijaji, and the chillar party :) Thank you papaji and mummyji for being a source of inspiration for me.

Mummy and Pappa, although the two of you are different personalities, I cannot start thanking you one by one because you have been always one unit for me. I will always carry the moral values and principles you have imbibed in me. When I was quitting my successful job in Mumbai to pursue astronomy in a foreign land, both of you did not blink an eye and thought that it was a brilliant idea and that I would definitely succeed. So thank you for believing in my abilities more than anyone. Mummy, thanks for giving me all the support during my failures. Pappa, thanks for those little science projects we did together during my childhood, and for bringing me those audio books by Jayant V. Narlikar on space and astronomy, I guess the mystery to why I chose astronomy over anything else lies here.

Vandana, we met by chance and yet it felt it was meant to be. I cannot imagine the last few years without your presence in my life. Our common love for chai, food, cooking, movies and travelling is what brought us together but the peace and happiness you add in my life is what has kept us together :) Thank you for being the person you are. Also, thanks for translating my thesis summary to Hindi. Plenty more memories await us. I would like to quote you here: "Whatever our souls are made of, yours and mine are the same."

Life is short but the world is getting smaller day by day. I am sure I will cross paths with many of you in the future. So, I refuse to say goodbye just yet!

Kaustubh

A

"We don't read and write poetry because it's cute. We read and write poetry because we are members of the human race. And the human race is filled with passion. And medicine, law, business, engineering, these are noble pursuits, and necessary to sustain life. But poetry, beauty, romance, love, these are what we stay alive for."

— Robin Williams, Dead Poets Society